

Hans-Joachim Kunze

SPRINGER SERIES ON ATOMIC, OPTICAL AND PLASMA PHYSICS 56

Introduction to Plasma Spectroscopy



Springer

Springer Series on
ATOMIC, OPTICAL, AND PLASMA PHYSICS 56

Springer Series on
ATOMIC, OPTICAL, AND PLASMA PHYSICS

The Springer Series on Atomic, Optical, and Plasma Physics covers in a comprehensive manner theory and experiment in the entire field of atoms and molecules and their interaction with electromagnetic radiation. Books in the series provide a rich source of new ideas and techniques with wide applications in fields such as chemistry, materials science, astrophysics, surface science, plasma technology, advanced optics, aeronomy, and engineering. Laser physics is a particular connecting theme that has provided much of the continuing impetus for new developments in the field. The purpose of the series is to cover the gap between standard undergraduate textbooks and the research literature with emphasis on the fundamental ideas, methods, techniques, and results in the field.

Please view available titles in *Springer Series on Atomic, Optical, and Plasma Physics* on series homepage <http://www.springer.com/series/411>

Hans-Joachim Kunze

Introduction to Plasma Spectroscopy

With 87 Figures

Professor em. Dr. Hans-Joachim Kunze
Ruhr-Universität
Institut für Experimentalphysik V
44780 Bochum, Germany
E-mail: hans-joachim.kunze@rub.de

Springer Series on Atomic, Optical, and Plasma Physics ISSN 1615-5653
ISBN 978-3-642-02232-6 e-ISBN 978-3-642-02233-3
DOI 10.1007/978-3-642-02233-3
Springer Heidelberg Dordrecht London New York

Library of Congress Control Number: 2009931048

© Springer-Verlag Berlin Heidelberg 2009

This work is subject to copyright. All rights are reserved, whether the whole or part of the material is concerned, specifically the rights of translation, reprinting, reuse of illustrations, recitation, broadcasting, reproduction on microfilm or in any other way, and storage in data banks. Duplication of this publication or parts thereof is permitted only under the provisions of the German Copyright Law of September 9, 1965, in its current version, and permission for use must always be obtained from Springer-Verlag. Violations are liable to prosecution under the German Copyright Law.

The use of general descriptive names, registered names, trademarks, etc. in this publication does not imply, even in the absence of a specific statement, that such names are exempt from the relevant protective laws and regulations and therefore free for general use.

Cover design: SPi Publisher Services

Printed on acid-free paper

Springer is part of Springer Science Business+Media (www.springer.com)

To Regina, Stefanie and Martina

Preface

This book is based on lectures given at the Ruhr-University of Bochum for graduate and postgraduates students starting their studies on plasma physics, but it is as well directed at established researchers who are newcomers to spectroscopy and need quick access to the diagnostics of plasmas ranging from low to high density technical systems at low temperatures as well from low to high density hot plasmas. Basic ideas and fundamental concepts are briefly introduced as is typical instrumentation from the X-ray to the infrared spectral regions. Examples, techniques, and methods illustrate the possibilities. The list of cited references is certainly not complete. Preference is given to either more recent publications since they usually refer to previous work or to reviews. I am grateful to Hans R. Griem and Andreas Dinklage for reading the manuscript and suggestions for improvement.

Bochum,
July 2009

Hans-Joachim Kunze

*There is no lift to success,
you have to climb the stairs.
Emil Oesch*

Contents

1	Introduction	1
2	Quantities of Spectroscopy	5
2.1	Radiometric Quantities	5
2.2	Measured Quantities	6
2.3	Local Quantities	9
2.3.1	Homogeneous Plasmas	9
2.3.2	Axially and Spherically Symmetric Plasmas	9
2.3.3	Plasmas Without Symmetry	11
2.4	Radiance of Plasmas with Re-Absorption	12
3	Spectroscopic Instruments	15
3.1	General Considerations	15
3.2	Dispersing Elements	17
3.2.1	Prisms	17
3.2.2	Gratings	18
3.2.3	Crystals	24
3.2.4	Interferometers	27
3.3	Windows, Filters, Mirrors, Optics	28
3.3.1	Windows	28
3.3.2	Filters	30
3.3.3	Mirrors	33
3.3.4	Optics	34
3.4	Spectrometer Designs	38
3.4.1	Prism Spectrometers	38
3.4.2	Spectrometers with a Plane Grating	39
3.4.3	Spectrometers with a Concave Grating	41
3.4.4	Spectrometers with Transmission Grating	43
3.4.5	Crystal Spectrometers	44
3.4.6	Interferometric Spectrometers	47
3.5	Alignment and Apparatus Function	49

4 Detectors	53
4.1 General Properties	53
4.2 Photoemissive Detectors	55
4.2.1 Photocells	55
4.2.2 Photomultipliers	57
4.2.3 Channel Photomultipliers and Microchannel Plates	61
4.3 Semiconductor Detectors	63
4.3.1 Photoconductors	63
4.3.2 Photodiodes	66
4.3.3 Array Detectors	68
4.4 Photoionization Detectors	69
4.4.1 Ionization Chambers	69
4.4.2 Proportional Chambers	70
4.4.3 Multiwire Proportional Chambers	71
4.4.4 Gas Amplification Detectors	72
4.5 Miscellaneous Detectors	73
5 Calibration	75
5.1 Wavelength Calibration	75
5.2 Sensitivity Calibration	76
5.2.1 Some General Considerations	76
5.2.2 UV to Near-Infrared	78
5.2.3 Vacuum-Ultraviolet	79
5.2.4 X-ray Region	83
6 Radiative Processes in Plasmas	85
6.1 Overview	85
6.2 Line Radiation	87
6.2.1 Emission and Absorption by Atoms and Ions	87
6.2.2 Emission by Molecules	92
6.2.3 Theoretical Considerations and Scaling Laws	94
6.3 Continuum Radiation	98
6.3.1 Recombination Radiation and Photoionization	98
6.3.2 Bremsstrahlung	104
6.3.3 Negative Ion and Molecular Continua	109
6.3.4 Rate Coefficients for Radiative Recombination	110
7 Collisional Processes	115
7.1 Introductory Remarks	115
7.2 Collisional Excitation and Deexcitation by Electron Impacts	116
7.3 Electron Impact Ionization and Three-Body Recombination	126
7.4 Dielectronic Recombination and Autoionization	129
7.5 Charge Exchange Processes	132
7.6 Ion and Atom Impact Excitation and Ionization	133

8	Kinetics of the Population of Atomic Levels in Plasmas	135
8.1	Introductory Remarks	135
8.2	Thermodynamic Equilibrium Relations	136
8.3	Local Thermodynamic Equilibrium	139
8.4	Corona Equilibrium	142
8.5	Collisional Radiative Models	146
9	Line Broadening	153
9.1	Profile Functions	153
9.2	Broadening Mechanisms	155
9.2.1	Natural Broadening	155
9.2.2	Doppler Broadening	156
9.2.3	Pressure Broadening by Neutral Particles	157
9.2.4	Stark Broadening	158
9.2.5	Effects of Collective Fields	170
9.2.6	Magnetic Field Effects	174
9.2.7	Broadening due to Self-Absorption	176
10	Diagnostic Applications	179
10.1	Verification of Atomic Data	179
10.2	Measurements of Particle Densities	180
10.2.1	Particle Densities from Line Emission	180
10.2.2	Particle Densities Employing Injected Fast Beams	182
10.2.3	Density of Molecules	182
10.2.4	Actinometry	183
10.2.5	Particle Densities from Absorption Measurements	183
10.2.6	Ratio of Particle Densities from the Spectra of Helium-like Ions	184
10.3	Temperature Measurements	186
10.3.1	Atom, Molecule, and Ion Temperature	186
10.3.2	Electron Temperature	187
10.4	Measurements of the Electron Density	195
10.4.1	Electron Densities from Line Profiles	195
10.4.2	Electron Densities from the Ratio of Lines	198
10.4.3	Electron Densities from the Continuum Emission at Long Wavelengths	200
10.4.4	Electron Densities from Other Spectroscopic Observations	201
10.5	Electric and Magnetic Field Measurements	202
10.5.1	Magnetic Fields	202
10.5.2	Electric Fields	203
A	Appendix	205
A.1	List of Symbols	205

XII Contents

B Appendix	211
B.1 Data Centers	211
C Appendix	213
C.1 Atomic Constants and Quantities	213
C.2 Some Atomic Relations	214
References	215
Index	237

Introduction

Spectroscopic methods offer a large variety of possibilities to diagnose plasmas in the laboratory and in space, the apparatus required being one of the least complicated in many cases. Astronomical objects are the sun, the stars, and the interstellar matter. Plasmas in the laboratory range at low temperatures from low-density plasmas as nowadays mostly used for plasma processing to high density arcs and plasma torches at atmospheric pressure; at high temperatures pulsed but long-lived low density plasmas in magnetically confined fusion devices such as tokamaks and stellarators are at one end, short-lived inertially confined pellets having densities up to 100 times solid-state density represent the other end.

Specifically we talk of plasma *emission* spectroscopy if electromagnetic radiation emitted by the plasma is recorded, spectrally resolved, analyzed and interpreted in terms of either parameters of the plasma or characteristic parameters of the radiating atoms, ions or molecules. It is the most straightforward approach since only one port in otherwise closed systems is needed for radiation to escape. An inherent drawback is certainly the fact that the radiation detected and hence all information obtainable is integrated along the line of sight. This also holds for the supplementary approach of *absorption* spectroscopy. There radiation – in the most general case continuum radiation – is directed through the plasma, and the modification of the spectrum of the transmitted radiation by absorption and also by scattering contains the information on the plasma and its constituents. The application of fixed wavelength and tunable lasers as radiation sources utilizing both absorption and various scattering processes in the plasma is widespread and has developed into a field of its own described as laser spectroscopy. It is not a subject of this book and we refer to the relevant literature, for example to [1], or specifically with respect to the diagnostics of plasmas to [2]. Scattering by plasma electrons known as incoherent and collective Thomson scattering, one of the most powerful plasma diagnostic techniques [3–6] is also only mentioned here.

Most spectroscopic methods utilize the radiation emitted by atoms, ions, or molecules being present in the specific plasma either as impurities or being

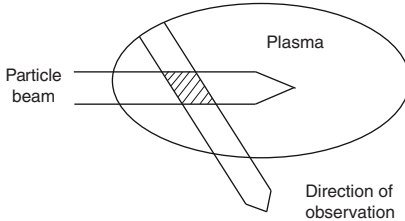


Fig. 1.1. Injection of a particle beam into a plasma

intentionally added to the plasma for specific purposes such as radiation cooling or diagnostics. In recent years, the injection of atomic beams has been advanced: they enter the plasma more or less on a straight path till they are ionized. As Fig. 1.1 reveals, observation of the emission from the beam particles now yields *local* information from the hatched region, background radiation naturally still being collected along the line of sight.

The present monograph intends to give an introduction to plasma spectroscopy, and the two books by Griem [7, 8] remain the standard references for this field. The monograph by Fujimoto [9] emphasizes the theoretical framework for the population density distribution in plasmas. For a general introduction to spectroscopic principles and techniques, the monograph [10] may be consulted. Spectroscopic methods are also discussed in books on plasmas diagnostics [11, 12].

Spectral Regions

With increasing temperature of a plasma the maximum of the continuum radiation and the strong lines emitted occur at shorter wavelengths, and typically plasma spectroscopy has to cover the spectral range from the infra-red down to X-rays. Although the physical concepts underlying the emission of radiation are more or less the same over this spectral range, different experimental techniques have to be employed, resulting in a corresponding partition into several spectral ranges.

380–750 nm is the visible. This spectral region is well defined by the sensitivity curve of the eye. Radiation is transmitted through air with practically no losses; this also holds for the adjacent regions toward shorter and longer wavelengths. The *infra-red* IR extends from the *near infra-red* to the *far infra-red* FIR adjacent to the microwave region, which starts around wavelengths of 1 mm, but transmission through air can be influenced by absorption within molecular bands of water vapor, carbon dioxide and other molecular constituents or pollutants. In addition, absorption by windows has to be considered, which also occurs when going to wavelengths below the visible. Flint glass, for example, starts to absorb already around 380 nm, and for

shorter wavelengths windows of quartz are advised; ordinary quartz cuts off at around 210 nm, but best quartz is satisfactory down to just below 180 nm. The spectral range 200–380 nm is known as the *ultraviolet* UV.

Below 200 nm electromagnetic radiation is absorbed by air, first by oxygen starting at around 195 nm and then by nitrogen at 145 nm, and transmission through air occurs again only below 0.15 nm, where 30% of the radiation starts to be transmitted through 1 m of air at atmospheric pressure. To avoid this absorption in air, the spectrographic system and path of the radiation from the plasma have to be evacuated. For that reason, the spectral range 200–0.15 nm has been named the *vacuum-ultraviolet or vacuum-UV* VUV. Traditionally, this range is subdivided according to the optics which has to be employed. *Vacuum-UV* is thus specifically used for the range 200–105 nm, where transparent window materials (LiF cuts off at 105 nm) and hence also lens optics exist.

The range 105–0.15 nm is customarily named *extreme-ultraviolet* EUV or XUV, and it includes *the soft X-rays* from 30 to 0.15 nm.

Below 0.15 nm the region of the *hard X-rays* starts, where it is more practical to use the photon-energy unit in kilo electron volts instead of the wavelength. Hard x-rays overlap with the broad range of γ -rays from about 10 keV to 250 MeV; γ -quanta are typically emitted by nuclei.

Spectroscopic Units

The electromagnetic radiation flux from a surface element plotted as function of frequency ν or wavelength λ is known as *spectrum*. Both are related to each other by

$$\lambda_{\text{vac}} = c/\nu , \quad (1.1)$$

where c and λ_{vac} are velocity of light and wavelength in vacuum, respectively, and ν is in Hertz ($1 \text{ Hz} = 1 \text{ s}^{-1}$). The most common wavelength units are the nanometer (nm), the Ångström ($1 \text{ \AA} = 10^{-1} \text{ nm}$) and the micrometer (μm). The wavenumber σ defined by

$$\sigma = 1/\lambda_{\text{vac}} = \nu/c \quad (1.2)$$

is more commonly used at long wavelengths, especially when dealing with molecular transitions. Its unit is the inverse meter, but in practice wavenumbers are usually expressed in inverse centimeters (cm^{-1}). This unit has been named Kayser (K), $1 \text{ K} = 1 \text{ cm}^{-1}$.

At short wavelengths the photon energy $E = h\nu$ is preferred in the unit electron volt (eV). Wavelength in vacuum – we omit the subscript “vacuum” from hereon – and energy are thus related by

$$\frac{h\nu}{\text{eV}} \frac{\lambda_{\text{vac}}}{\text{nm}} = 1239.842 . \quad (1.3)$$

Wavelengths of atoms and their ionization stages may be found in a number of reference publications and as well in data banks: one easily accessible and extremely useful data bank is that of the National Institute of Standards and Technology NIST at Gaithersburg, USA [13]: the data have been critically evaluated and compiled, and energy levels, configurations, and transition probabilities are also given. Since the energy E of the levels is given in the unit cm^{-1} ($1 \text{ eV} \Rightarrow 8065.541 \text{ cm}^{-1}$), the wavenumber of a transition and thus its vacuum wavelength is simply obtained from the difference of the energies of upper $E(p)$ and lower level $E(q)$: $\sigma = E(p) - E(q) = 1/\lambda$. It is common practice that wavelengths above 200 nm (λ_n) are quoted in dry air containing 0.03% CO₂ at 101 325 Pa at a temperature of 288.15 K. Both wavelengths are related to each other by

$$\lambda_n = \lambda/n . \quad (1.4)$$

Here, n is the index of refraction of air at the above conditions, which is given by [14]

$$n = 1 + 6432.8 \times 10^{-8} + \frac{2949\,810}{146 \times 10^8 - \sigma^2} + \frac{25\,540}{41 \times 10^8 - \sigma^2} , \quad (1.5)$$

where σ is the wavenumber in cm^{-1} .

For molecular spectra the monographs by Herzberg are still the main source [15, 16]. A molecular database HITRAN is continuously being developed at the Harvard-Smithsonian Center for Astrophysics in Cambridge, USA [17].

Quantities of Spectroscopy

2.1 Radiometric Quantities

The total energy emitted by a plasma as electromagnetic radiation per unit time is called its *radiative loss* and plays a crucial role in all power balance considerations. As a physical quantity it is a *radiant flux* Φ (through the surface of the plasma), and its unit is watt (W). It is also called *radiant power*. *Radiant flux density* ϕ refers to the flux per unit area $\phi = d\Phi/dA$ with the unit W m^{-2} , irrespective of whether the radiation is emitted from an area, crosses an imaginary surface in space, or falls onto an area A . In this latter case, it is customary to call this flux density at the surface *irradiance* E . The energy deposited per unit area during a given time is the *fluence* $H = \int Edt$, with the unit J m^{-2} .

The SI quantity *radiance* L is defined as the radiant flux per unit projected area per solid angle Ω [18]. Figure 2.1 illustrates the geometry, where θ is the angle between the normal of the surface element dA and the direction of the radiation.

$$L = \frac{d^2\Phi}{dA \cos \theta d\Omega} \quad (2.1)$$

Its unit is $\text{W m}^{-2} \text{sr}^{-1}$. Again, it also applies to real and imaginary surfaces. Although the radiance is the correct SI unit, the rather familiar word *intensity* is still being used instead in much of the plasma spectroscopy literature. Confusion is unavoidable when authors use intensity for the radiation flux density. It is advisable, therefore, to check the unit whenever “intensity” is encountered. The official SI quantity *radiant intensity* I is the flux per solid angle emitted from a source which makes it a property of a source rather than of a radiating surface: $I = d\Phi/d\Omega$, the unit being W sr^{-1} . In the field of physical optics the word “intensity” refers to the magnitude of the Poynting vector.

For completeness the *radiant energy density* u (unit J m^{-3}) should be mentioned, which is usually employed in atomic and thermodynamic

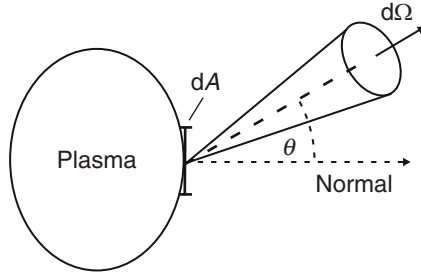


Fig. 2.1. Definition of radiance

considerations. In case of isotropic radiation, for example, it is given by relation (a), and for collimated radiation in the other limit by relation (b):

$$(a) \quad u = \frac{4\pi}{c} L \quad (b) \quad u = \frac{1}{c} L \quad (2.2)$$

The *local* emission at the position \mathbf{r} in the plasma is characterized by the *emission coefficient* $\varepsilon(\mathbf{r})$:

$$\varepsilon(\mathbf{r}) = \frac{d^2\Phi(\mathbf{r})}{dV \, d\Omega}, \quad (2.3)$$

where $d\Phi(\mathbf{r})$ is the radiant flux from the volume element dV at \mathbf{r} . This assumes that the emission is isotropic. It can, of course, also be non-isotropic, when a specific direction is given by electric or magnetic fields or by fast particle beams. The unit of the emission coefficient is $\text{W m}^{-3} \text{ sr}^{-1}$.

With the exception of bolometric measurements usually *spectral quantities* are measured and they are denoted by the pertinent subscript λ (or ν or ω). They are *derivative quantities* and they yield the total quantity when integrated over wavelength or frequency or an interval, respectively. For example:

$$\varepsilon(\mathbf{r}) = \int_o^\infty \varepsilon_\lambda(\mathbf{r}, \lambda) d\lambda \quad \text{or} \quad \varepsilon(\mathbf{r}, \lambda_0, \Delta\lambda) = \int_{\lambda_0 - \Delta\lambda/2}^{\lambda_0 + \Delta\lambda/2} \varepsilon_\lambda(\mathbf{r}, \lambda) d\lambda. \quad (2.4)$$

2.2 Measured Quantities

In the most straightforward case radiation from a plasma (for simplicity we take a plane surface with surface element dA_p) falls on a detector with surface element dA_d positioned at a distance s , see Fig. 2.2. The quantity thus recorded is a flux Φ given according to (2.1) by

$$\Phi = \iint L \cos\theta \, dA_p \, d\Omega = \iint L \cos\theta \, dA_p \frac{\cos\beta \, dA_d}{s^2}, \quad (2.5)$$

where integration is over plasma and detector surfaces. For small angles this flux reduces to

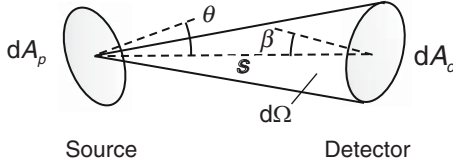


Fig. 2.2. Geometry of surface elements of source and detector

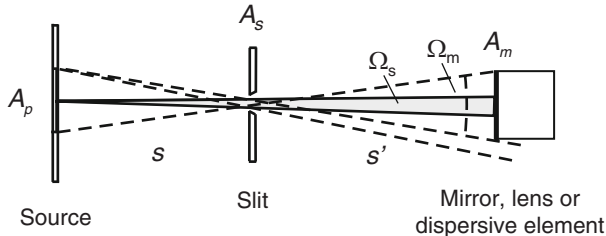


Fig. 2.3. Measured radiation

$$\Phi = L A_p \Omega_d = L \frac{A_p A_d}{s^2} . \quad (2.6)$$

Ω_d is the solid angle subtended by the detector area A_d .

For spectrally resolved measurements the radiation flux is limited by the area A_s of the entrance slit of a spectrographic instrument and by the size of a mirror, a lens, a dispersing element, or a real or virtual aperture (cross section A_m). Figure 2.3 illustrates this geometry, and it is obvious that the cross section A_m determines the area A_p of the source surface from which radiation is collected through the slit. Thus, the flux can be written

$$\Phi = L A_p \Omega_s = L A_p \frac{A_s}{s^2} = L A_s \frac{A_m}{s'^2} = L A_s \Omega_m . \quad (2.7)$$

The quantity $A_s \Omega_m$ is called the *throughput* or *étendue* of the instrument (it is conserved as we will see later), and the flux Φ is simply obtained as if the emitting surface with radiance L were in the plane of the entrance slit. (Keep in mind that this only holds if the emitting surface is larger than A_p .)

This is readily exploited in quantitative measurements: a standard radiator of known radiance L_0 is placed close to the entrance slit, or in principle at any distance where its size is still sufficient to fill the solid angle Ω_m . The flux $\Phi_\lambda(\lambda) \Delta\lambda = L_{0\lambda}(\lambda) \Delta\lambda A_s \Omega_m$ over a spectral interval $\Delta\lambda$ will produce a signal S_0 at the exit of a detector. Keeping all settings constant, the respective flux in the same spectral interval from an unknown radiator may give the signal S_x , hence

$$L_{x\lambda}(\lambda) = \frac{S_x}{S_0} L_{0\lambda}(\lambda) . \quad (2.8)$$

This is an extremely simple relation: the ratio of the signals yields the unknown spectral radiance $L_{x\lambda}(\lambda)$, and it is this quantity which is obtained in the measurement.

A plasma, on the other hand, emits throughout its volume, but the above considerations may also be applied directly, if we replace the radiating surface of Fig. 2.3 by a slice of plasma of thickness ds . $A_p(s)$ just has to be smaller than the cross section of the plasma at the distance s . With *no absorption* within the plasma (2.3) and (2.7) yield with $dV = dA_p(s) ds$

$$\Phi = \iiint \varepsilon(s) dA_p(s) ds d\Omega = \left(\int \varepsilon(s) ds \right) A_p \Omega_s = L A_s \Omega_m \quad (2.9)$$

$$\text{with } L = \int \varepsilon(s) ds, \quad (2.10)$$

where L is the radiance at the surface of the plasma and will also be again the effective radiance in the plane of the entrance slit.

For a correctly designed optical system, reduced to a lens of diameter D in Fig. 2.4, we have for object and image size y and y' with object and image distance s and s' , respectively,

$$\frac{y/2}{y'/2} = \frac{s}{s'}, \quad (2.11)$$

and hence

$$\frac{y^2}{s^2} D^2 = \frac{y'^2}{s'^2} D^2 \implies A_p \Omega_p = A_p' \Omega_p'. \quad (2.12)$$

The throughput is conserved. Since also the radiant flux Φ remains constant, (2.9) and (2.12) yield directly the well known law

$$L = L' \quad (2.13)$$

i.e., the radiance is an invariant of an optical system with no absorption.

In case the cross section of the plasma is smaller than the area A_p at the position s (Fig. 2.3), the full throughput is not utilized. In this case, the plasma should be imaged onto the entrance slit employing a lens or a spherical mirror. These considerations also apply when a large plasma is to be investigated spatially resolved. Figure 2.5 illustrates such an arrangement. The lens

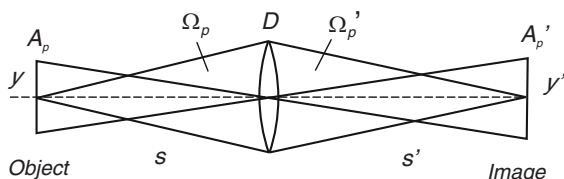


Fig. 2.4. Imaging by a lens

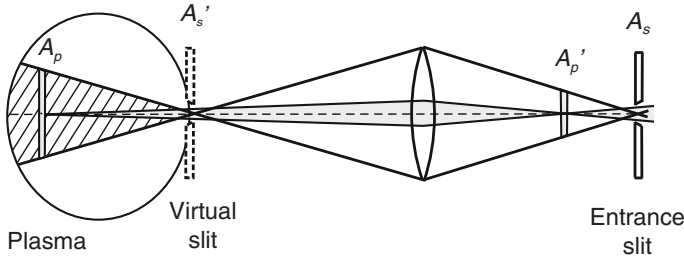


Fig. 2.5. Spatially resolved measurements

produces a virtual image (area A'_s) of the entrance slit, and only radiation from the shaded region is collected by the lens and the virtual slit and hence also by the entrance slit. This geometry corresponds exactly to that of Fig. 2.3 with a radiance $L = \int \varepsilon ds$ at the position of the virtual slit and according to (2.13) also at the entrance slit: the quantity obtained is the *local* radiance at the surface of the plasma, given by the integral of the emission coefficient ε along the line of sight. One must, of course, select a lens of sufficient diameter, that the full throughput is used in the spectrographic instrument.

2.3 Local Quantities

2.3.1 Homogeneous Plasmas

The discussions in the preceding sections showed that the quantity measured is always the local radiance at the surface of the plasma, which is given by integration of the emission coefficient along the line of sight when absorption of radiation within the plasma is not important. Hence, only an average emission $\bar{\varepsilon}$ can be quoted

$$\bar{\varepsilon} = \frac{L}{s_2 - s_1}, \quad (2.14)$$

where $s_2 - s_1$ is the depth of the plasma along the line of sight. For a homogeneous plasma this corresponds to the true emission coefficient ε .

2.3.2 Axially and Spherically Symmetric Plasmas

In cases of axially symmetric plasma columns (cylinders), the derivation of local emission coefficients $\varepsilon(r)$ is possible if the radiance of the plasma is measured over the cross section of the column. Integration along a chord parallel to the x-axis yields, after substituting $x^2 = r^2 - y^2$ (Fig. 2.6), the one-dimensional profile of the radiance

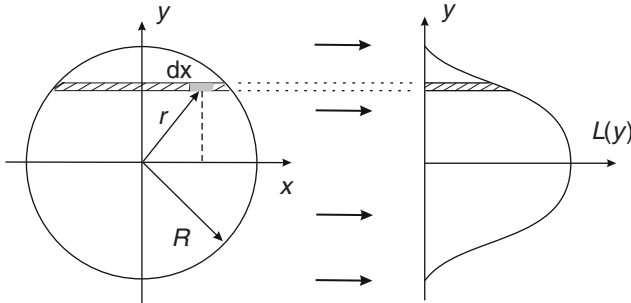


Fig. 2.6. Radiance parallel to the y -axis of a cylindrically symmetric plasma column

$$L(y) = 2 \int_0^{x_{max}} \varepsilon(r) dx = 2 \int_0^{\sqrt{R^2 - y^2}} \varepsilon(r) dx = 2 \int_y^R \frac{\varepsilon(r) r dr}{\sqrt{r^2 - y^2}}. \quad (2.15)$$

Equation (2.15) is of the Abel type, and the local emission coefficient $\varepsilon(r)$ is recovered by the Abel inversion which can be written analytically as

$$\varepsilon(r) = -\frac{1}{\pi} \int_r^R \frac{dL(y)}{dy} \frac{dy}{\sqrt{y^2 - r^2}}. \quad (2.16)$$

Since the spatial derivative dL/dy enters the inversion, it is obvious that the results are very sensitive to noise and errors in the measured radiance $L(y)$. Unfortunately, the errors in the derivative accumulate over the integration interval $[r, R]$, and the resulting uncertainty is most severe on the axis $r = 0$. Hence, appropriate smoothing of the data can be essential for the quality of the inversion. An inversion algorithm without differentiation has been proposed by [19], and other improved inversion methods are mentioned in [8]. In cases of strongly spatially structured emission profiles, the finite solid angle of the radiation collecting optics has to be taken into account [20].

The two-dimensional radiance $L(y, z)$ in the $y-z$ plane is readily analyzed only in the case of spherically symmetric plasmas. Because of the symmetry it usually suffices to analyze the radiance $L(y, 0)$ obtained by integration in the plane ($z = 0$), to which the above cylindrical solution can be applied. Physically, it corresponds to a one-dimensional analysis employing a narrow slit in front of the plasma.

In the X-ray region, the pinhole camera is the standard imaging system. It is simple, and the typical arrangement is shown in Fig. 2.7. Integration of the emission coefficient $\varepsilon(r)$ is now along differing tilted chords. The chordal heights p , or impact parameters, are calculated from the known geometric dimensions of the system, and the recorded radiances can then readily be transformed to the respective radiance distribution of parallel recording needed for the standard Abel inversion.

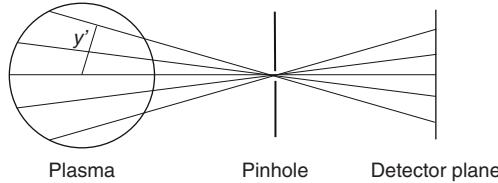


Fig. 2.7. Schematic arrangement of a pinhole camera

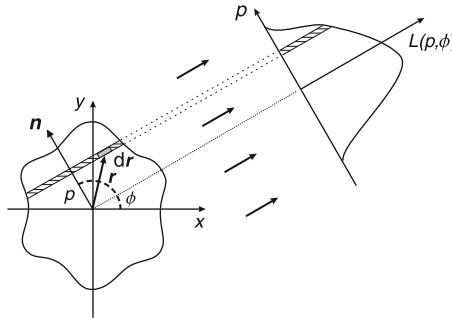


Fig. 2.8. Coordinate system for the Radon transform

2.3.3 Plasmas Without Symmetry

One special case of nonaxisymmetry exists in tokamaks which employ a limiter and have a circular poloidal cross-section: the magnetic flux surfaces and hence the density contour lines are very close to a set of nested eccentric circles, the shift of the circle centers being known as the Shafranov shift Δ . With the transformation $r^2 = (x + \Delta)^2 + y^2$, Abel inversion as discussed in Sect. 2.3.2 can again be executed, and specific methods have been developed [21–23]. In [24] the technique was extended to plasmas of elliptic shape which is transformed mathematically to a concentric circular shape for the Abel inversion.

The mathematical problems associated with the general reconstruction of the local emission $\varepsilon(\mathbf{r})$ throughout the plasma are essentially identical to those encountered in computer-aided tomography, drawing on the same mathematical techniques [25]. The radiance of the plasma has to be recorded in numerous directions, and the Radon transformation and its inverse then provide the mathematical basis for the reconstruction. We shall consider here only the two-dimensional Radon transform, the extension to three dimensions being straightforward. Figure 2.8 illustrates the geometry and the definition of the coordinates. Integration is along straight lines given by ($\mathbf{n} = \{\cos \phi, \sin \phi\}$ is a unit vector perpendicular to these lines)

$$\mathbf{r} \cdot \mathbf{n} - p = x \cos \phi + y \sin \phi - p = 0 \quad (2.17)$$

yielding the radiance

$$L(p, \phi) = \int_{-\infty}^{\infty} \int_{-\infty}^{\infty} \varepsilon(x, y) \delta(x \cos \phi + y \sin \phi - p) dx dy, \quad (2.18)$$

where $\delta(\cdot)$ is the Dirac delta function. Because of the symmetry $L(p, \phi) = L(-p, \phi + \pi)$ only angles 0 to π are needed. Mathematically, $L(p, \phi)$ is the Radon transform of $\varepsilon(x, y)$

$$L(p, \phi) = \mathcal{R}_2\{\varepsilon(x, y)\}. \quad (2.19)$$

For the execution of the inverse Radon transformation to obtain the emission $\varepsilon(x, y)$ within the plasma,

$$\varepsilon(x, y) = \mathcal{R}_2^{-1}\{L(p, \phi)\}, \quad (2.20)$$

a number of algorithms and numerous techniques are available, see for example [26]. The quality of the obtained reconstruction certainly depends on the number of views of the plasma (different angle ϕ), or precisely on the number of $L(p, \phi)$ values. Unfortunately, these are usually limited due to experimental constraints, as for example by the plasma vessel and its ports. The reconstruction is facilitated and improved, if additional information on the plasma shape or its overall structure is available and can be utilized.

2.4 Radiance of Plasmas with Re-Absorption

We now consider that some radiation is re-absorbed within the plasma and introduce a wavelength-dependent absorption coefficient $\kappa(x, \lambda)$. It is defined such that in the direction x the change of the spectral radiance $L_\lambda(x, \lambda)$ by a thin slab due to absorption is given by

$$dL_\lambda(x, \lambda) = -\kappa(x, \lambda) L_\lambda(x, \lambda) dx. \quad (2.21)$$

The unit of $\kappa(x, \lambda)$ is m^{-1} . The designation $\kappa_\lambda(x)$, which is sometimes found in the literature, should not be used since a subscript usually indicates differentiation. If we add the emission by the plasma slab (2.10), the total change of the radiance becomes

$$dL_\lambda(x, \lambda) = \varepsilon_\lambda(x, \lambda) dx - \kappa(x, \lambda) L_\lambda(x, \lambda) dx. \quad (2.22)$$

Figure 2.9 illustrates the geometry. Division by dx leads to

$$\frac{dL_\lambda(x, \lambda)}{dx} = \varepsilon_\lambda(x, \lambda) - \kappa(x, \lambda) L_\lambda(x, \lambda). \quad (2.23)$$

known as *equation of radiative transfer*.

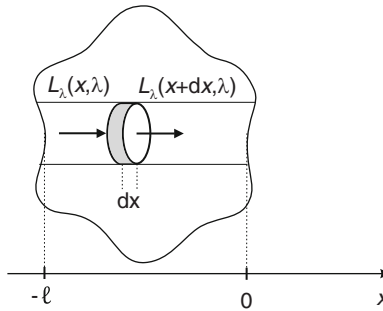


Fig. 2.9. Geometry of radiation transport

It is customary to introduce the *optical depth* τ measured back into the plasma by

$$d\tau = -\kappa(x, \lambda) dx. \quad (2.24)$$

As new variable τ replaces x by

$$\tau(x, \lambda) = - \int_0^x \kappa(x', \lambda) dx' \quad (2.25)$$

with $\tau = 0$ at the plasma surface ($x = 0$). The magnitude of the total optical depth (also called as optical thickness) $\tau(-\ell, \lambda)$ determines the significance of radiative transport at the wavelength λ . Equation (2.23) can now be written as

$$\frac{dL_\lambda(x, \lambda)}{d\tau} = L_\lambda(x, \lambda) - \frac{\varepsilon_\lambda(x, \lambda)}{\kappa(x, \lambda)} = L_\lambda(x, \lambda) - S_\lambda(x, \lambda). \quad (2.26)$$

Integration is along the line of sight (or more precisely, along an actual ray trajectory) into the plasma.

The ratio $\varepsilon_\lambda(x, \lambda)/\kappa(x, \lambda) = S_\lambda(x, \lambda)$ is known as *source function*. In calculating the source function in the most general cases, induced emission and scattering of radiation have to be considered. Fortunately, in many diagnostic applications scattering does not play a role.

The solution of (2.26) for the case of no radiation incident on the plasma at $x = -\ell$ gives the radiance at the plasma surface

$$L_\lambda(0, \lambda) = \int_0^{\tau(-\ell, \lambda)} S_\lambda(\tau, \lambda) e^{-\tau} d\tau. \quad (2.27)$$

The limit (2.10) of an optically thin plasma ($\tau \ll 1$) is recovered by expanding $e^{-\tau}$ and keeping only the first term:

$$L_\lambda(0, \lambda) \cong \int_0^{\tau(-\ell, \lambda)} S_\lambda(\tau, \lambda) d\tau = \int_{-\ell}^0 \varepsilon_\lambda(x, \lambda) dx. \quad (2.28)$$

An analytic solution of (2.26) is readily given for a homogeneous plasma, $S_\lambda(x, \lambda) = S_\lambda(\lambda)$:

$$L_\lambda(0, \lambda) = S_\lambda(\lambda) \left[1 - e^{-\tau(-\ell, \lambda)} \right]. \quad (2.29)$$

For optically thick, $\tau(-\ell, \lambda) \gg 1$, inhomogeneous plasmas we make the transition $\tau(-\ell, \lambda) \rightarrow \infty$ and integrate (2.26) by parts:

$$\begin{aligned} L_\lambda(0, \lambda) &= - \int_0^\infty S_\lambda(\tau, \lambda) e^{-\tau} d\tau \\ &= S_\lambda(\tau = 0, \lambda) + \frac{S_\lambda(\tau, \lambda)}{d\tau} \Big|_{\tau=0} + \frac{d^2 S_\lambda(\tau, \lambda)}{d\tau^2} \Big|_{\tau=0} + \dots \end{aligned} \quad (2.30)$$

Alternatively, one can develop $S_\lambda(\tau, \lambda)$ as a MacLaurin power series and obtains [27]

$$S_\lambda(\tau, \lambda) = S_\lambda(\tau = 0, \lambda) + \frac{S_\lambda(\tau, \lambda)}{d\tau} \Big|_{\tau=0} (\tau - 0) + \frac{1}{2} \frac{d^2 S_\lambda(\tau, \lambda)}{d\tau^2} \Big|_{\tau=0} (\tau - 0)^2 + \dots \quad (2.31)$$

Provided the higher terms do not contribute too much, the comparison of both equations yields

$$L_\lambda(0, \lambda) \simeq S_\lambda(\tau = 1, \lambda), \quad (2.32)$$

i.e., the spectral radiance is about equal to the source function at the optical depth $\tau(\lambda) \simeq 1$. Since τ varies with wavelength, the observed spectral radiance corresponds to different positions in the plasma. In astronomy, (2.32) is known as Eddington–Barbier relation.

3

Spectroscopic Instruments

3.1 General Considerations

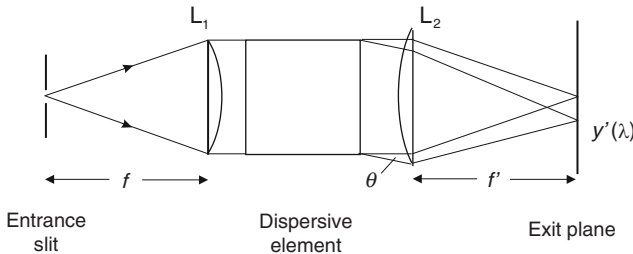
The selection of a spectrographic system including the detector is governed by several aspects:

- Wavelength region of interest
- Low or high-resolution studies, survey spectra, line intensities only or detailed line profiles
- Weak or strong emitter, which usually is equivalent to having a plasma of low or high density
- Low or high time resolution, which basically determines the detector and only to a lesser degree the throughput of the system
- Stigmatic or astigmatic image of the plasma in the exit plane

Spectrometers with the exception of instruments for the X-ray region typically consist of:

- An entrance slit (width w_{en} , area A_E)
- A dispersive element
- An optical system, which forms a spectrally dispersed image of the entrance slit in the exit plane
- A detector in the exit plane

Figure 3.1 illustrates a schematic layout. Dispersing elements are prisms, gratings, interferometers, and crystals. The imaging system consists usually of a lens L_1 (or mirror M_1) collimating the radiation from the entrance slit, and a lens L_2 (or mirror M_2) focusing the radiation in the exit (image) plane. Mirrors have the advantage of no chromatic aberration and can also be used at shorter wavelengths where glasses, quartz, and crystals absorb the radiation. Unfortunately, their reflectivity decreases at short wavelengths; this can be remedied to some degree by reducing the number of reflecting surfaces and employing spherical or even toroidal gratings which combine focusing and dispersing properties. The optical system (L_1, L_2) or (M_1, M_2) becomes unnecessary.

**Fig. 3.1.** Schematic of a spectrometer

The dispersing elements are characterized by their *angular dispersion* [28] defined by

$$\frac{d\beta}{d\lambda}, \quad (3.1)$$

where $d\beta$ is the difference in angle of the emergent radiation corresponding to a difference $d\lambda$ in wavelength. The unit is rad/nm.

Since a beam of parallel radiation impinging on the lens L_2 under the angle θ is focussed at $y' = -f' \tan \theta$ in the focal plane, the *linear dispersion*, i.e., the separation of different wavelengths in the focal plane usually in mm/nm, is given by (with $d\theta = d\beta$)

$$\frac{dy'}{d\lambda} = -\frac{f'}{\cos^2 \theta} \frac{d\beta}{d\lambda}. \quad (3.2)$$

The *reciprocal linear dispersion* or *plate factor* $d\lambda/dy'$ in nm/mm or Å/mm is more commonly used in practice. Explicit expressions for these quantities will be given in the following chapters.

The *resolving power* \mathcal{R} characterizes the minimum separation $\delta\lambda$ of the central wavelengths of two closely spaced equally intense lines, which are considered to be just resolved. \mathcal{R} can as well be expressed in terms of wavenumber or frequency, and it is defined as

$$\mathcal{R} = \frac{\lambda}{\delta\lambda} = \frac{\sigma}{\delta\sigma} = \frac{\nu}{\delta\nu}. \quad (3.3)$$

The optical system of the spectrometer forms an image of the entrance slit in the exit plane, and for monochromatic radiation (spectral width approaching zero) the shape of the “line” produced is called the *instrument function* or *apparatus profile*. It is not a perfect geometrical image of the slit of width w_{en} , but the image is broadened by mechanical defects, optical aberrations and diffraction at the rim of the dispersing element. Narrowing the width of the entrance slit at the expense of lowering the throughput narrows the “line” width and the theoretical maximum of the resolving power corresponding to the diffraction-limited instrument function is finally approached. Two equally intense lines are considered still resolvable if the maximum of the diffraction

pattern of each line falls on the first minimum of the other (Rayleigh's criterion); the dip between the two maxima is about 20%. In cases, where the instrument function has no diffraction shape, this dip to peak ratio is taken as resolution criterion. For quantitative studies of line widths, it is necessary to determine experimentally the respective instrument function for each setting of the entrance slit.

Since the throughput $A_E \Omega$ depends on the area of the entrance slit, the radiation-collecting power of spectrometric instruments is characterized by the so-called f-number or aperture ratio f/D , where f is the focal length of the collimating lens L_1 and D is its diameter matched to the size of the dispersing element.

An array detector or a photographic plate in the image plane allows recording of a spectral range, and one commonly calls this whole setup a *spectrograph*. If a slit in the exit plane selects a spectral line or a narrow spectral region, the instrument becomes a *monochromator*. Moving the slit with the detector or rotating the dispersing element yields a scanning monochromator. For specific applications several slits with detectors may be placed in the exit plane, which is easily done with fibers, for example. Such a setup is called a *polychromator*.

Stray light at the exit plane of a spectroscopic instrument can be a problem when weak continuous radiation, for example, is studied in the presence of strong line radiation: it causes a background in the exit plane and must be experimentally quantified and/or reduced to a tolerable level. Stray light has several causes, the most trivial one being leakage of light through the housing. Serious causes are reflection and scattering of radiation, that entered through the entrance slit, from walls and from surfaces of optical components (lenses, mirrors, prisms, and gratings) of the instrument, as can readily be seen in the visible when illuminating a spectroscopic instrument and inspecting the interior with the cover off and the room light turned down. Dust is especially harmful, and all optical components should be kept clean. One option to drastically reduce stray light is to select a double or even a triple monochromator where two or three instruments are in series, the exit slit of one instrument being the entrance slit of the next one. The resulting relative stray light level in the exit plane is simply the product of the stray light levels of each instrument.

3.2 Dispersing Elements

3.2.1 Prisms

Prisms have been largely superseded by gratings as dispersing element but are still in use because of several advantages, see Sect. 3.4.1 and [10]. Figure 3.2 shows the path of a ray through the principal section of a single prism of base length B and prism angle γ . Refraction at both surfaces results in a deviation β which depends on the wavelength λ because of the dispersion of

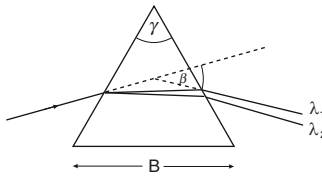


Fig. 3.2. Dispersion by a prism with index of refraction n

the prism material $dn/d\lambda \neq 0$. Composite prisms have been designed with special characteristics [28].

Prisms are usually aligned that the rays pass through the prism symmetrically, that is, with equal refraction at each surface. In this case, the deviation β is minimum and the angular dispersion is given by [29]

$$\frac{d\beta}{d\lambda} = \frac{\sin(\gamma/2)}{[1 - n^2 \sin^2(\gamma/2)]^{1/2}} \frac{dn}{d\lambda}. \quad (3.4)$$

It increases with prism angle γ but does not depend on the size of the prism. Application of Rayleigh's criterion yields the resolving power

$$\mathcal{R} = B \frac{dn}{d\lambda}. \quad (3.5)$$

When the beam does not fill the prism, B is the difference in the extreme paths through the prism. In cases of two or more prisms in tandem, B is the sum of the bases. A large number of materials are available and may be selected, for specific applications even in a variety of designs and optical arrangements [28], although equilateral prisms with $\gamma = 60^\circ$ are most common.

3.2.2 Gratings

Diffraction gratings have higher resolving power and dispersion and can be used in a much larger spectral region [31, 32]. Reflection gratings are the most common ones, although transmission gratings are also in use at long wavelengths in the infra-red and at short wavelengths in the soft X-ray region. The standard reflection grating is on a plane or concave surface and consists of equally spaced identical structures usually called *grooves*. The groove profile affects the intensity distribution of the diffracted radiation. Gratings are produced by two methods: by mechanical ruling, in which a diamond burnishes the grooves individually into the well-annealed substrate, or by interference methods, where respective fringe patterns are formed by two laser beams and expose a photosensitive layer on the surface of the grating blank. The shape of the grooves in the first case is triangular, and the total surface of the ruled "master grating" is finally coated with a thin reflecting metallic layer, in most cases aluminum, or gold and platinum for use at short wavelengths. Replicas

are made from expensive master gratings with epoxy resin castings. Gratings produced by the interference method are called *holographic* gratings and the shape of the grooves after development of the photoresist is sinusoidal (see below).

For a beam of parallel radiation incident at the angle α onto a grating, the principal maxima of the diffracted radiation, which give the *spectral lines*, are at angles β determined by the fundamental grating equation discussed in nearly every textbook on optics:

$$m \lambda = d (\sin \alpha + \sin \beta). \quad (3.6)$$

α and β are positive when measured on the same side of the grating normal, m the diffraction order and d is the groove spacing. Manufacturers usually quote the groove density $1/d$ in grooves per millimeter. The subsidiary maxima between the principal maxima are insignificant. $\beta = -\alpha$ gives zero order. m is positive for $-\beta < \alpha$ and the respective spectrum is called inside spectrum; $-\beta > \alpha$ yields m negative and the outside spectrum.

Figure 3.3 shows the typical profile of a ruled grating. Because of this shape the diffracted power is influenced and concentrated into a direction β_B that corresponds to the specular reflection at the facets of the triangular grooves. These facets make an angle ϑ with the plane of the grating, and the condition becomes

$$\alpha - \vartheta = \vartheta - \beta_B. \quad (3.7)$$

The maximum occurs at one wavelength λ_B (in each order m of the spectrum):

$$m\lambda_B = 2d \sin \vartheta \cos(\alpha - \vartheta). \quad (3.8)$$

For $m = 1$ and $\alpha = 0$

$$\lambda_{B1} = d \sin 2\vartheta; \quad (3.9)$$

λ_{B1} is called blaze wavelength, ϑ is the blaze angle, and the technique of shaping the grooves is called blazing. It is obvious that the blaze wavelength at higher orders is at λ_{B1}/m . Gratings are usually supplied with an arrow on the backside to show the direction of the concentrated radiation. The efficiency curve of a grating gives the diffracted power relative to the incident power as function of wavelength. Its maximum reaches 70–80% at λ_{B1} , and the useful

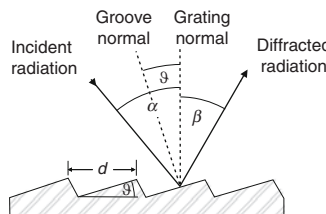


Fig. 3.3. Profile of a ruled diffracting grating

range of a grating is approximately between $\lambda_{B1}/2 \leq \lambda \leq 2\lambda_{B1}$. Holographic gratings have no blaze because of the symmetry of the grooves, but the range of the diffraction efficiency can be controlled to some extent by the modulation depth of the grooves, and ion etching techniques are now being employed to change the sinusoidal profiles to triangular. Some more details on efficiency curves are given on p. 22.

The angular dispersion follows from (3.6) to

$$\frac{d\beta}{d\lambda} = \frac{m}{d \cos \beta}, \quad (3.10)$$

and if grating and focusing lens L_2 (Fig. 3.1) are aligned on the optical axis, $\alpha = 0$ and $\theta = \beta$, the linear dispersion becomes

$$\frac{dy'}{d\lambda} = - \frac{m f'}{d \cos^3 \beta}. \quad (3.11)$$

The Rayleigh criterion leads to a simple relation for the theoretical resolving power of a grating

$$\mathcal{R} = m N, \quad (3.12)$$

where N is the total number of illuminated grooves on the surface of the grating. Introducing the illuminated width $W = N d$ of the grating,

$$\mathcal{R} = W \frac{m}{d} \quad (3.13)$$

shows that for a given groove spacing d , the achievable width W limits the resolving power \mathcal{R} . The same resolution is possible with small groove spacing and low diffraction order or with large groove spacing and high diffraction order. This is utilized in a special grating design known as echelle grating, Fig. 3.4. The grooves form right-angled steps and the radiation is incident perpendicular onto the narrow sides of the grooves, which have the reflective coating. Observation of the diffracted radiation with these gratings is usually in the direction of the incident radiation ($\beta = \alpha$, because the diffracted beam is at the same side of the grating normal as the incident beam); this arrangement is known as Littrow-grating mount.

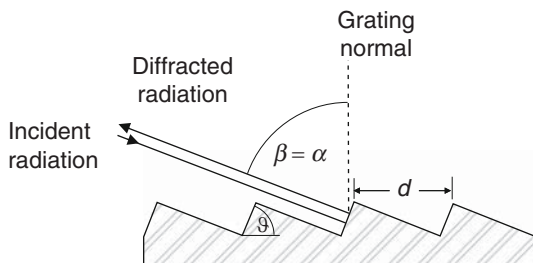


Fig. 3.4. Echelle grating

$$m \lambda = 2d \sin \alpha = 2d \sin \vartheta. \quad (3.14)$$

These gratings are used in high orders and allow thus a high resolving power. Unfortunately, many orders will overlap and spectral filters are employed to isolate the desired order, or the orders are separated by introducing cross-dispersion with an additional dispersing element [10]. One defines the *free spectral range* $|\Delta\lambda|_F$ of a grating as the wavelength band where radiation from adjacent orders does not overlap:

$$m (\lambda + |\Delta\lambda|_F) = (m + 1) \lambda \quad \text{gives} \quad (3.15)$$

$$|\Delta\lambda|_F = \frac{\lambda}{m}. \quad (3.16)$$

Concave Gratings

The decreasing reflectivity of metals at short wavelengths leads to a decreasing efficiency of the gratings (and of mirrors). To reduce the number of reflecting surfaces concave gratings are employed: their focusing properties were originally pointed out by Rowland in 1881. The standard concave grating is of spherical shape, the grooves are equidistant. Figure 3.5 illustrates the characteristics, which are best explained employing the Rowland circle. For a grating of radius R , it is the circle of radius $R/2$ that passes through the center of the grating surface, with the grating tangent to the circle and the grooves perpendicular to the plane of the circle. If a point source (in a spectrograph an entrance slit with low height) is positioned on the Rowland circle, focusing is on this circle for all wavelengths (tangential focus), but strong astigmatism perpendicular to the plane of the circle is characteristic of the concave grating. The length z_1 of the tangential (meridional) focus of any point on the entrance slit is given by

$$z_1 = L (\sin^2 \beta + \sin \alpha \tan \alpha \cos \beta), \quad (3.17)$$

where L is the length of the illuminated grooves of the grating. A contribution z_2 due to the finite height h of the entrance slit has to be added to obtain the total height $z = z_1 + z_2$ of the astigmatic image:

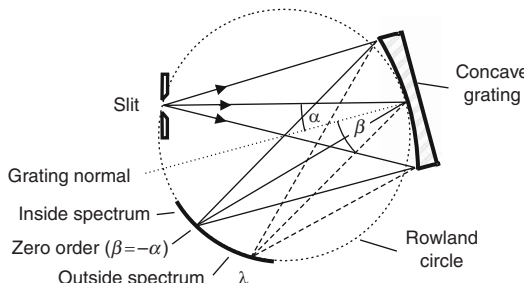


Fig. 3.5. Concave grating

$$z_2 = h \frac{\cos \beta}{\cos \alpha}. \quad (3.18)$$

Also, the image is not a straight line but curved, the curvature being concave toward the entrance slit [30]. The general focusing properties have been analyzed in a number of publications, see for example [31–33].

The angular dispersion of the concave grating is identical to that of the plane grating (3.10). With $dl = R d\beta$, the linear dispersion along the Rowland circle l becomes

$$\frac{dl}{d\lambda} = \frac{dl}{d\beta} \frac{d\beta}{d\lambda} = \frac{m R}{d \cos \beta}. \quad (3.19)$$

Toroidal and Varied Line Spacing Gratings

The astigmatism of the spherical concave grating does not allow simultaneous spatially resolved measurements of a plasma which require that any point of the exit slit is an image of the respective point on the entrance slit. The astigmatism can, however, be drastically reduced by employing toroidal gratings [34], which have different radii for the meridional plane and the plane perpendicular to it, the sagittal plane. Nowadays, the grating designer has additional possibilities to also correct other aberrations and to tailor the grating even to individual requirements: grooves can be curved and their spacing can be varied across the grating surface [35, 36]. The theory is well developed and described, for example, in [33]. The performance of a new grating design is usually checked by ray tracing which delivers respective spot diagrams in the exit plane. A rather successful design with extensive application is the spherically concave grating of Harada et al. [37] with varied spacing and curved grooves: the spectral image is not on the Rowland circle but in a *plane*. This allows to employ array detectors with a plane surface. Varied line spacing (VLS) gratings are now offered by most manufacturers.

Efficiency of Reflection Gratings

The selection of a grating depends on the specific application, and efficiency curves (efficiency plotted vs. wavelength) are usually supplied by the manufacturers. The maximum efficiency at the blaze wavelength is first determined by the reflectivity of the coating of the surface (see also Sect. 3.3.3). In the ultra-violet, visible, and infra-red spectral regions, aluminum coatings are typical; overcoating with magnesium fluoride (MgF_2) helps to maintain the reflectivity in the UV over time. Platinum (Pt), iridium (Ir), and osmium (Os) offer higher reflectivity in the VUV, gold (Au) in the infra-red. The efficiency behavior is discussed in detail in [32], and many efficiency curves are found there.

The efficiency depends also on the polarization of the incident radiation. It differs for radiation polarized parallel to the grating grooves (p-plane) and radiation polarized perpendicular to the grooves (s-plane). For completely

unpolarized radiation, the efficiency curve is exactly halfway between the p- and s-efficiency curves. Anomalies – sharp peaks or troughs – are often observed in efficiency curves of the s-polarization. They first were seen by R.W. Wood in 1902 and are referred to as Wood's anomalies.

At wavelengths below 30 nm the reflectivity of metals becomes too small at normal incidence and gratings are employed at large angles of incidence, (grazing incidence) which increases the reflectivity. One utilizes the fact that an electromagnetic wave (angular frequency ω) incident obliquely at a grazing angle ϕ (the complement to the angle of incidence, $\phi = 90^\circ - \alpha$) is totally reflected when

$$\omega \sin \phi \leq \omega_{pe}, \quad (3.20)$$

where ω_{pe} is the plasma frequency of the quasi-free electrons with density n_e in the metal. The minimum wavelength (*cutoff*), above which radiation is reflected, may thus be expressed as

$$\lambda_{\min} = 2\pi \sqrt{\frac{\epsilon_0 m_e c^2}{n_e e^2}} \sin \phi, \quad (3.21)$$

or as numerical value equation

$$\frac{\lambda_{\min}}{\text{nm}} = 3.34 \times 10^{16} \left(\frac{n_e}{\text{m}^{-3}} \right)^{-1/2} \sin \phi. \quad (3.22)$$

For a gold coated grating with $n_e = 4.66 \times 10^{30} \text{ m}^{-3}$ the lowest reflected wavelength is 0.54 nm for a grazing incidence angle of 2° [30].

For specific applications in the extreme-ultraviolet wavelength region (for example good image quality employing normal incidence) multilayer coatings of a grating allow an alternative. Multilayers are designed for a specific wavelength (see Sect. 3.3.3) which matches with the grating. The bandwidth is typically 5–10 % of the design wavelength [38, 39].

Sometimes a choice between a mechanically ruled and a holographic grating is possible. Here, it is advised to simply consult the data sheets of the manufacturers. In general, the efficiency of the holographic grating will be somewhat lower than that of the ruled grating, but holographic gratings are completely free of “ghost” lines because of their perfect groove spacing. Periodic imperfections during the ruling process introduce an additional periodicity which leads to these ghost lines. Due to modern feedback control techniques during ruling their intensity now is kept between 10^{-6} and 10^{-4} of that of the parent line. Examples may be seen in [32]. Furthermore, also the stray light level of the holographic grating is much lower than that of a ruled grating.

Transmission Gratings

Transmission gratings are generally for use at near-normal incidence and, for the near-UV, visible, and the near-IR spectral regions. The grooves are

either ruled into a transparent substrate or are made as plastic film replicas on the substrate [32]. They are almost completely free of polarization effects. Triangular grooves provide again a *blazing* effect and concentrate the radiation into a specified wavelength band.

Techniques developed in microelectronics make it possible to fabricate high line-density, thin-film-backed, or free-standing transmission gratings for the soft X-ray region [40]. A simple setup and ease of alignment promote their use, so far mostly in the spectroscopy of laser-produced plasmas [41], and references therein. The achievable resolution is moderate, but adequate for survey spectra. Free-standing gold gratings with 5,000 lines/mm are commercially available. The feasibility of such gratings was demonstrated to extend to the 10 keV range [42].

3.2.3 Crystals

For very short wavelengths, crystals are the only available dispersing elements. X-rays impinging on a crystal are coherently scattered by the regularly positioned atoms and, at a given angle of incidence, constructive interference (diffraction) takes place for only one wavelength (or multiples of a wavelength) and in one direction in the plane of incidence, the diffraction angle being equal to the angle of incidence. Bragg recognized [43] that these conditions are equivalent to reflections at lattice planes parallel to the diffracting surface. In contrast to gratings diffraction thus is from the volume of the crystal. The geometry is illustrated in Fig. 3.6, and the famous Bragg relation is readily derived:

$$m\lambda = 2d_{hkl} \sin \theta. \quad (3.23)$$

h, k, l are the Miller indices describing the lattice planes, d_{hkl} the net spacing of the planes, m is the order of diffraction, and θ is the Bragg angle (complement of the angle of incidence). It is obvious that for lines emitted from a point source the Bragg condition is fulfilled on circles on the surface of the crystal (Fig. 3.7) and the radiation forms a cone after reflection for each wavelength. Depending on the position of the detector plane relative to the crystal the “spectral lines” on the detector are thus sections of a circle, an ellipse, a parabola or a hyperbola. Each wavelength is reflected from a different part of the crystal.

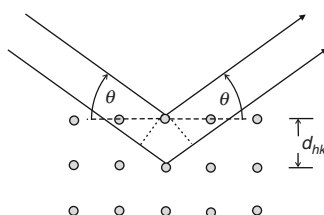


Fig. 3.6. Bragg reflection by a crystal

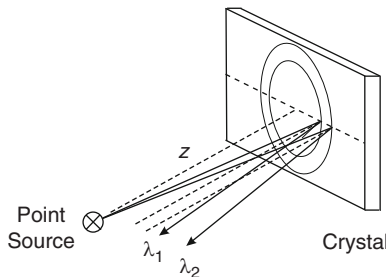


Fig. 3.7. Bragg reflection of a point source

Table 3.1. Examples of some typically employed crystals

Crystal	Miller indices	2d (nm)	Note
Quartz	50̄52	0.1624	
Quartz	1011	0.6592	
Topaz	303	0.2712	
LiF	200	0.4027	
HOPG		0.6708	
ADP	101	1.0648	
Mica	002	1.984	
KAP	001	2.6579	
OHM		6.35	
Lead stearate		10.04	
Multilayers		by specification	

The wavelength range of interest determines first the selection of a crystal: the double lattice spacing $2d$ must exceed the longest wavelength. Crystals can be cut in different lattice planes (hkl), or ($hkil$) with $i = -(h + k)$ for hexagonal crystals, and a wide range of crystals is thus available [44–46]. Table 3.1 lists some typically employed crystals. The first one has the shortest $2d$ of any practical crystal. Mica is very versatile and easily bent. Organic crystals like OHM (octadecyl hydrogen maleate) conclude the list of true crystals for very large lattice spacing. In pseudo crystals consisting of multiple layers of Langmuir–Blodgett metal soap films (e.g., lead stearate) on a substrate, the lattice spacing is also determined by the internal structure whereas for multilayer films produced by sputtering or evaporation $2d$ can, in principle, be adjusted to any value. Many details are found in [47], see also Sect. 3.3.3. Thus, the use of Langmuir–Blodgett films has diminished in favor of multilayer films.

The property to consider next is the reflectivity of the crystals. It varies from crystal to crystal, is different for various lattice planes and depends also on the Bragg angle and thus on the wavelength. The inherent angular spread of the diffracted radiation $\Delta\theta_{1/2}$ is characterized by the ‘‘rocking curve’’ (reflection curve), which is usually obtained by scanning the crystal about the Bragg angle and measuring the reflected radiant flux of a well-collimated

incident monochromatic beam. $\Delta\theta_{1/2}$ is defined as the full width at half-maximum of the reflection curve and is commonly in the range of $0.2^\circ - 0.4^\circ$, but can be less; for quartz it is $\sim 0.05^\circ$. For multilayers the rocking curve is much wider than for crystals, at least one order-of-magnitude [48]. This width determines the resolving power $\lambda/\delta\lambda$ of a crystal. Differentiation of Bragg's law (3.23) yields

$$\mathcal{R} = \frac{\lambda}{\delta\lambda} = \frac{\tan\theta}{\Delta\theta_{1/2}} \quad (3.24)$$

Best resolution thus occurs at large Bragg angles.

An integrated reflectivity is defined as the integral of the reflectivity over all angles of incidence; its unit is radian. It is typically between 10^{-5} and 10^{-4} rad and decreases by more than one order-of-magnitude from first to second order [46]. Mica is an exception, having good reflectivity at higher odd orders [49]. Crystals should, of course, not contain elements with absorption edges in the wavelength region of interest to avoid abrupt variations in the reflectivity. Peak reflectivity, integrated reflectivity, and $\Delta\theta_{1/2}$ characterize a crystal.

The “highly oriented pyrolytic graphite (HOPG)” crystal is an example of a mosaic crystal. The mosaic structure leads to a much higher angular width of the reflection, “mosaic spread,” and thus to a substantially higher integrated reflectivity compared to perfect crystals, although the peak reflectivity can be lower [50].

The reflectivity naturally depends on the polarization, it differs for π and σ polarized X-rays (electric field vector in the plane of incidence and perpendicular to it, respectively). At the Brewster angle α_B determined by Brewster's law, $\tan\alpha_B = n$, the reflectivity for the π component is practically zero. With $n \approx 1$ for X-rays, the Brewster angle is 45° . Hence, for investigations of the polarization of X-rays at a wavelength λ the Bragg angle must also be around 45° . This demands crystals with a $2d$ spacing as close as possible to that given by Bragg's law (3.23), i.e., $2d \approx 1.41 \lambda$, must be chosen.

Curved Crystals

Crystals are easily bend in one dimension introducing focusing properties analogous to those of concave gratings but imposing the additional condition of equal angles of incidence and reflection. Hence, only one wavelength of the emission from a point source on the Rowland circle (radius one half the radius of the bent crystal) is refocused on this circle, but the irradiance is greatly enhanced. First designs had been implemented by Johann [51]. A rather simple low-cost technique to bend the crystals to any desired curvature was introduced by Brogren [52]: the plane-parallel thin crystal plate is placed between two pairs of steel rods, all parallel to each other. Pressing these rods against each other bends the crystal plate. Further properties will be discussed in Sect. 3.4.5.

Today advanced techniques allow to bend crystals in two dimensions. Both spherically and toroidally bent crystals are in use. High precision machining and polishing make it possible to attach crystals to the mount simply by “optical contact,” i.e. adhesion by van-der-Waals forces. Astonishing resolution is thus obtained with good crystals.



3.2.4 Interferometers

The Fabry–Perot interferometer is the dispersing element with the highest possible dispersing power. It consists of two separate plates with reflecting surfaces, aligned parallel to each other thus forming a plane-parallel air gap. The outer surfaces of the plates are coated with antireflection layers. For specific applications it may be simply a solid plane-parallel glass or fused quartz plate with coated reflecting surfaces (Fabry–Perot etalon). Figure 3.8 symbolizes a Fabry–Perot system: a plane parallel air slab (index of refraction n_{air}) with partially reflecting surfaces of reflectivity R . A plane monochromatic wave incident under the angle α is split by successive reflections into coherent waves of decreasing amplitude. These partial waves add, the intensity distribution of the transmitted wave being given by the phase difference between two partial waves after two reflections. The optical path difference Δs between two such waves is simply

$$\Delta s = 2 d n_{air} \cos \alpha , \quad (3.25)$$

and the corresponding phase difference δ becomes

$$\delta = \frac{2\pi\Delta s}{\lambda} = \frac{4\pi d n_{air} \cos \alpha}{\lambda} . \quad (3.26)$$

Adding all partial waves gives the flux Φ_T of the transmitted wave relative to that of the incident wave Φ_0 [10, 29]

$$\frac{\Phi_T}{\Phi_0} = \frac{1}{1 + F \sin^2(\delta/2)} \quad (3.27)$$

with $F = 4 R / (1 - R)^2$. The right-hand side of (3.27) is known as Airy distribution. Applying Rayleigh’s criterion to the case of near normal incidence ($\alpha \approx 0^\circ$) yields a resolving power

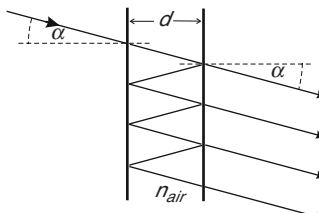


Fig. 3.8. Fabry–Perot gap

$$\mathcal{R} = \frac{\lambda}{\delta\lambda} = \frac{4\pi n_{air} d}{\lambda} \frac{\sqrt{R}}{1-R}, \quad (3.28)$$

which indeed can be very large. Fabry–Perot interferometers are characterized by a rather small *free spectral range* $\Delta\lambda_F$, i.e., a small separation of two successive maxima of the same wavelength; for normal incidence it is given by

$$\Delta\lambda_F = \frac{\lambda^2}{2 n_{air} d}. \quad (3.29)$$

Wavelengths of waves, which are separated by more than $\Delta\lambda_F$, cannot be related to each other. A useful parameter in this context is also the *finesse* \mathcal{F} :

$$\mathcal{F} = \frac{\pi\sqrt{R}}{1-R}. \quad (3.30)$$

It gives the ratio of free spectral range to full half-width of an interference fringe of the Airy distribution.

3.3 Windows, Filters, Mirrors, Optics

3.3.1 Windows

Laboratory plasmas are usually confined by vessels, and windows restrict the spectral range of radiation exiting the vessel. Attention must be paid naturally also to the material of all optical components to be sure that they do not absorb spectral regions of interest. Figure 3.9 illustrates the transmission of some commonly employed materials [53]. BK7 (a) is a borosilicate crown glass with high homogeneity, which is widely used in the visible and infrared. Suprasil (b) is a sample of a number of available synthetic fused silica materials (synthetic quartz glass) with good transmission in the UV and in

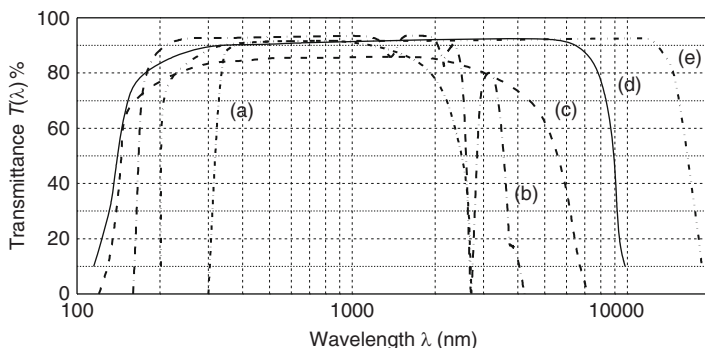


Fig. 3.9. Transmission of window materials: (a) BK7 ($d = 10$ mm); (b) Suprasil ($d = 10$ mm); (c) Sapphire ($d = 1$ mm); (d) CaF_2 ($d = 10$ mm); (e) NaCl ($d = 10$ mm)

the IR up to $2.5\mu\text{m}$. The strong water absorption band at $2.7\mu\text{m}$ depends on the concentration of water. Sapphire (c) is one of the hardest materials with high-mechanical strength and chemical resistance; it is a single crystal of Al_2O_3 . CaF_2 (d) exhibits good transmission from 170 nm to $7.8\mu\text{m}$. It is slightly soluble in water. One of the most useful windows in the infra-red is sodium chloride (rock salt)(e). It is sensitive to moisture and the surface may be exposed only to dry air. The spectral transmittance $T(\lambda)$ (sometimes also called external transmittance) is defined as the ratio of transmitted spectral radiant flux to incident spectral radiant flux and includes the reflection losses at the surfaces of the window (or vessel wall). According to Fresnel the reflectance $R(\lambda)$ is given at each boundary vacuum-material or air-material for normal incidence by

$$R(\lambda) = \left(\frac{n-1}{n+1} \right)^2, \quad (3.31)$$

where n is the index of refraction of the material at the specific wavelength. R is about 4% for quartz and most glasses. High-quality optics surfaces are usually coated with antireflection layers. Short- and long-wavelength cutoffs are obvious. Close to those the transmittance depends strongly on the thickness d of the window. The internal transmittance $T_{int}(\lambda) \simeq T(\lambda)[1 + 2R(\lambda)]$ scales by the Beer-Lambert law as

$$T_{int}(\lambda) = e^{-\alpha(\lambda)d} = \left(e^{-\alpha(\lambda)d_0} \right)^{d/d_0}, \quad (3.32)$$

where $\alpha(\lambda)$ is the absorption coefficient of the material. Absorption coefficients for many materials can be found in [53], for example. One should keep in mind that the short-wavelength cutoffs shift to longer wavelengths with increasing temperature [54].

As already discussed in Chap. 1 the transmission through air must certainly be accounted for. It can be manipulated to some extent by reducing the air pressure in the optical path (down to vacuum) or by filling in another gas that does not absorb in the spectral region of interest. Figure 3.10 displays the transmission through air and also through helium and argon [55].

Some materials lose transmittance after exposure to intense radiation from hot plasmas or even to plasma particles. Windows should be checked therefore from time to time. One-well known example is LiF, the material with the lowest cut-off: surface damage leads to coloring and decreasing transmission. Other investigations are reported, for example, in [56–59].

In the soft X-ray region, the first choice of window material is polyimide (better known by the trade name Kapton). It has a high tensile and flexural strength, and the transmittance of a $1\mu\text{m}$ thick foil is shown in Fig. 3.11. The transmission of Lexan (polycarbonate) is similar, its tensile and flexural strengths are smaller. Since most windows have to be rather thin [60], the foils are usually supported by a backing (solid mesh or grid).

The standard material for windows in the X-ray region is beryllium. Figure 3.11 shows the transmission of a 10 and a $100\mu\text{m}$ thick window. Be has

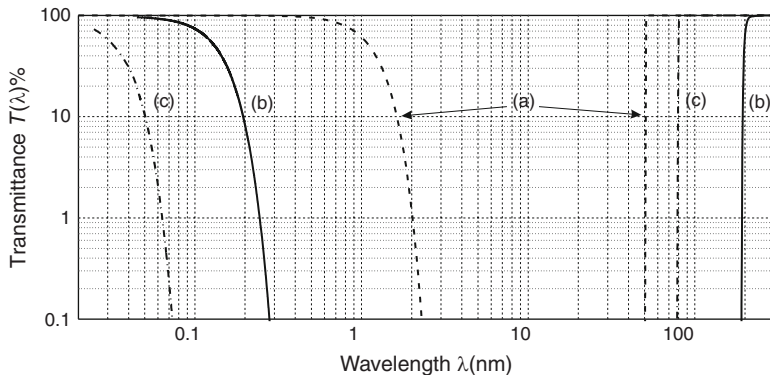


Fig. 3.10. Transmission through 100 cm of gas at 101.325 kPa and 295 K: (a) He, (b) air, and (c) Ar

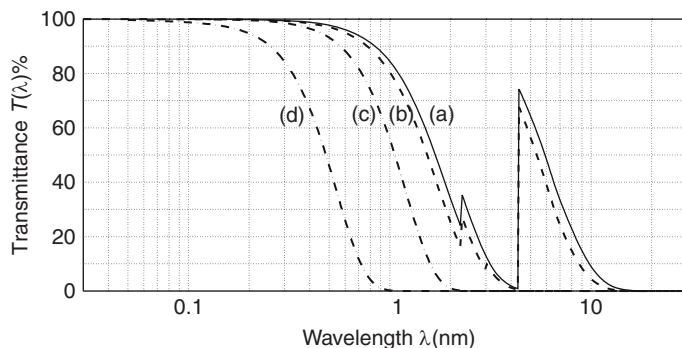


Fig. 3.11. Transmission through 1 μm thick windows of Lexan (a) and Kapton (b), and of Be 10 μm thick (c) and 100 μm thick (d) [64]

to be handled with care because it is brittle and toxic. For that reason proper slight coating is advised which does not change the transmission but facilitates handling and protects the surface.

3.3.2 Filters

Filters transmit radiation in specified wavelength regions and are characterized as short pass, long pass, band pass, interference, notch, and neutral density filters. In the ultraviolet, visible, and infra-red spectral region colored-glass filters are the most common. Absorption is caused by doping glass with simple or complex ions, or with colloids. Long pass filters transmit the longer wavelength region and can have a sharp cut-off, which can be shifted via the thickness of the filter. Curves (a–c) of Fig. 3.12 display examples. Such filters are conveniently employed when the second order of radiation of shorter

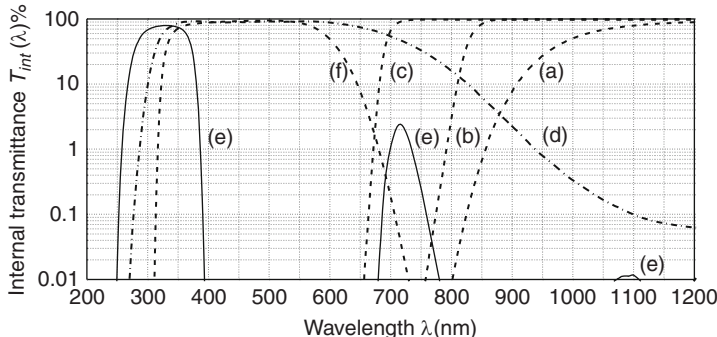


Fig. 3.12. Examples of the internal transmission through some colored-glass filters, all 3 mm thick: (a), (b), and (c) are long pass filters specified as RG1000, RG830, and RG695, respectively; (d) is a short pass filter KG1, and (e) and (f) are band pass filters UG11 and BG40, respectively [61]

wavelength has to be blocked. Curve (d) is an example of a short pass filter, and (e) and (f) are band pass filters. Details are found in the data sheets of suppliers. For specific applications liquid filters can be a substitute and are readily made; they consist usually of a quartz cuvette filled with a liquid of desired absorption properties.

Long exposures to high fluxes of ultraviolet radiation change the transmission of filter glasses (and of liquid filters) and should be controlled. The effect is known as solarization.

At wavelengths shorter than 200 nm, the dielectric window materials discussed in Sect. 3.3.1 are long pass absorption filters as well [62]. With decreasing wavelength thin films of metals and semiconductors, unbacked or supported by a thin organic film, take over. Typical thicknesses range from about 10–200 nm and reach micrometer and much more in the X-ray region. Sharp absorption edges at the short wavelength sides of transmission regions are characteristic. They correspond to threshold absorption by respective inner shell electrons and are given by the ionization energy of that shell. A survey [63] for the VUV region illustrates the possibilities. Absorption coefficients to calculate the transmission for the X-ray region are found in [55]. The transmission curves of the windows shown in Fig. 3.10 as well as those of Fig. 3.13 are examples. The absorption coefficients of [55] have been made accessible on the internet and transmission curves can be calculated online [64].

Foils of two metallic elements with successive atomic numbers are combined in Ross filter systems. Both foils are separately exposed to the full radiation and, as is obvious from Fig. 3.13, transmit all radiation of high photon energies and of a band with a sharp edge. The transmitted radiation is detected, and the difference of the signals corresponds just to the transmission in the narrow band shown in (c). The thickness of the foils should be adjusted

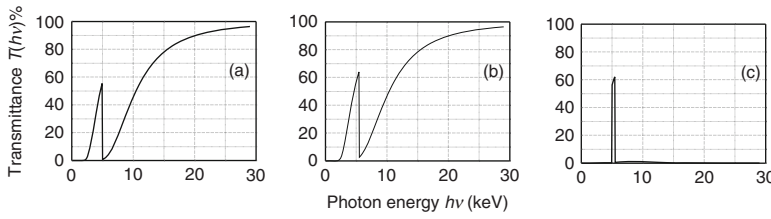


Fig. 3.13. Example of a Ross filter system: (a) transmittance through $15.4\ \mu\text{m}$ of Ti, (b) through $10\ \mu\text{m}$ of V, and (c) difference of transmittances

for lowest out-of-band transmission, for which in some cases additional foils of other materials might be helpful. In the above case, Ti, $15.4\ \mu\text{m}$ and V, $10\ \mu\text{m}$ thick are selected, the width of the transmission band is about $500\ \text{eV}$ at a photon energy of $5.3\ \text{keV}$. The noise of the final signal is naturally determined by the noise of the total signals in each channel, and hence such a system is best employed when detection of strong line radiation in the transmission band is the goal.

Thin metallic foils are prone to tiny pinholes, which transmit radiation of all wavelengths, i.e., also of the visible spectral region. It is advisable, therefore, to combine several thin foils to arrive at a desired thickness.

Neutral density filters have nearly constant spectral transmission over some larger spectral range, for example from 400 to $700\ \text{nm}$. Very often they are characterized by the optical density D , which is related to the transmittance T by

$$D = \lg(1/T). \quad (3.33)$$

In combinations the densities of the filters simply add. In the soft X-ray and X-ray region thin foils of micro-mesh with a well-defined number of holes per square centimeter and thus well-defined transmission are a convenient substitute for not available neutral density filters.

Narrow band transmission in the wavelength region above $200\ \text{nm}$ is achieved with interference filters. The basic element is nothing else but a Fabry–Perot etalon consisting of a dielectric layer between two semireflective layers (see Sect. 3.2.4). The thickness is usually selected to $nd = \lambda_0/2$ or λ_0 , where λ_0 is the wavelength of maximum transmission and n is the index of refraction of the dielectric. This results in a large free spectral range of $\Delta\lambda_F = \lambda_0$ or $\lambda_0/2$, respectively. Higher orders of shorter wavelength are thus readily eliminated by broad band absorption filters. At the long wavelength side multilayer blocking structures limit the transmission. Peak transmission, half-width of the transmission curve and magnitude of blocking the out-of-band radiation characterize an interference filter. Truly narrow band transmission is achieved by several cavities in series in one filter assembly. Band widths range from 10 to $0.1\ \text{nm}$. Tilting the filter shifts the transmission band to shorter wavelengths: according to (3.26) for constant δ the wavelength has to decrease with increasing angle α .

The extension of such transmission filters into the VUV region below 200 nm is limited by the lack of suitable dielectric materials. Only very special designs are feasible [65]. This is different for reflection filters; they are discussed in Sect. 3.3.3 on mirrors.

Notch filters are usually interference filters that have a deep narrow rejection band while providing high, flat transmission for the rest of the spectrum. The center wavelength also shifts to shorter wavelengths when the filter is tilted.

Polarization of the emitted radiation is analyzed employing linear polarization filters. Details are found in all textbooks on optics. Most popular and of highest quality are Glan–Taylor and Glan–Thompson systems, which consist of two specifically cut prisms of birefringent material. However, the acceptance angle is small and they have to be placed into a section where the beam of radiation is rather parallel. Easy to use also in diverging or converging beams of radiation are polyvinil films that have been stretched so as to align the chains of molecules: the films become dichroic and are easily cut to any desired size. Below 200 nm a few transmitting polarizers made of window materials mentioned in Sect. 3.3.1 become feasible, till toward shorter wavelengths and in the X-ray region only reflecting polarizers remain, [66] and Sect. 3.2.3.

3.3.3 Mirrors

Thin metal coatings on plane or spherical substrates are the standard mirrors over a wide range of wavelengths. Thin layers are sufficient, the reflectance $R(\lambda)$ even decreases if the layers become too thick. Figure 3.14 illustrates the normal incidence reflectance of some common mirror materials. The curves should be considered as giving only some guide lines, since the reflectance depends also on the method of deposition and drops with age, especially when exposed to air. This is especially severe for aluminum in the VUV, where the change is due to the formation of an oxide layer and occurs within hours [67].

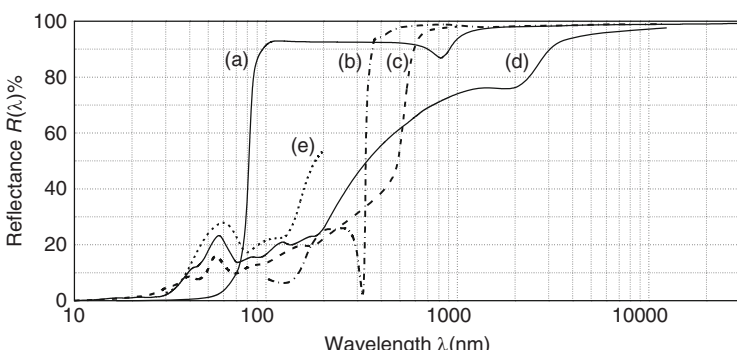


Fig. 3.14. Normal incidence reflectance of metal coatings (evaporated): (a) aluminum [68]; (b) silver [69]; (c) gold [69]; (d) platinum [70]; (e) osmium [71]

It can be avoided by some protective overcoating (usually a thin layer of SiO₂ or MgF₂), which even enhances the reflectivity. Silver tarnishes by forming silver sulfide on its surface, and again a protective layer remedies this in the visible and infra-red. Aluminum has good reflectivity over a wide range of wavelengths from the infra-red down into the VUV. Osmium has one of the highest reflectance values of any single material in the region 40–70 nm.

The severe decrease of the reflectance at short wavelengths can be avoided by going to larger angles of incidence as discussed in Sect. 3.2.2 on the efficiency of gratings. Hunter [72] presents and analyzes reflectance curves for a number of materials for angles of incidence $\alpha = 0^\circ$ and $\alpha = 89^\circ$.

Where large angles of incidence are not practical, multilayer systems are the solution especially for the soft-X-ray region. The principal element is a quarter-wave double-layer: in the ideal case it consists of two non-absorbing materials with high and low indices n_1 and n_2 of refraction which are deposited on top of each other. The respective optical paths are

$$n_i d_i = \lambda/4, \quad (3.34)$$

where d_i is the thickness of the respective layer. Reflection at the optically denser medium occurs with a phase change of 180° and at the optically thinner medium with no phase change, resulting in a total phase shift of 360° of the amplitudes reflected from adjacent boundaries. This produces a standing wave pattern inside the double layer. For a sufficient number of double layers the reflectance approaches 100%, which can be realized rather closely in the visible and infra-red spectral regions. One has to keep in mind that all layers contribute to the reflection.

At wavelength below 110 nm, however, no absorption-free materials are available. As a consequence, the ideal design is modified such as to make the weakly absorbing layer wider and to place it around the antinode, and to narrow the absorbing layer and to shift it to the node. In this way, one can optimize the reflectivity and minimize the total absorption. An example of optimized design are mirrors for EUV lithography at 13.5 nm, where a reflectance of 70% with a bandwidth of 2% has been achieved with Mo/Si double layers. Details and general design principles for multilayer stacks are found in [73, 74], and online design is offered at [64]. In the X-ray region, finally, only crystals remain as narrow-band mirrors, see Sect. 3.2.3.

3.3.4 Optics

For the wavelength region above 110 nm, a variety of materials including those discussed for windows in Sect. 3.3.1 are available for optical components such as lenses, composite and corrected objectives, and prisms. Details on characteristics and especially on their imaging properties are found in every book on optics, see for example [29]. This also holds for spherical and cylindrical mirrors, the surfaces of which are coated by thin metal films or

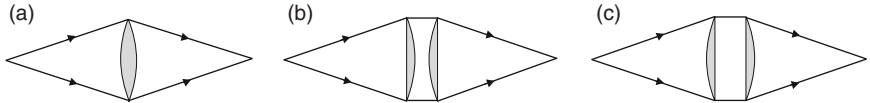


Fig. 3.15. Illustration of good and poor simple imaging

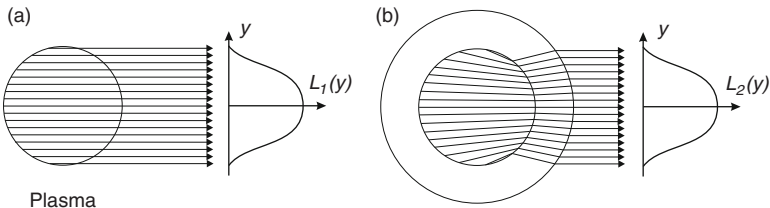


Fig. 3.16. (a) Emission along parallel chords with no wall. (b) Emission along chords in the plasma which leave the discharge vessel as parallel rays corresponding to (a). The index of refraction was chosen to $n = 1.55$ and the ratio of the radii to $5/3$, which corresponds, for example, to capillary discharge tubes of 3 mm inner diameter and 5 mm outer diameter

multilayer stacks (see Sect. 3.3.3) as required for their specific application down into the soft X-ray region. The advantage of mirrors is the absence of chromatic aberration, which can indeed be large for simple lenses when covering a wide spectral range, for example from the ultraviolet to the infra-red. Achromats then are a necessity for imaging a plasma onto a spectrographic system. Chromatic images of sufficient quality are very often obtained with simple lens systems if the Coddington shape factor is properly selected [29, 78]. Figure 3.15 shows examples. For transferring an image 1:1 a single symmetric biconvex lens (a) is rather close to the minimum of spherical aberration. Splitting the system into two plano-convex lenses as in (b) eases not only focusing without varying the object-image distance but also decreases spherical aberration. Both lenses, however, placed the wrong way as illustrated in (c) as is done erroneously very often, increases the spherical aberration dramatically. Replacing the plano-convex lenses of (b) by achromatic telescope objectives which are corrected for imaging objects located at infinite distance results in high-quality images.

The distortion of the image by a thick wall of the discharge vessel should be considered in side-on observations, especially when Abel inversion (p. 10) is performed to obtain local emission coefficients. The experimental procedure is pretty much facilitated nowadays by employing a CCD detector in the exit plane of a stigmatic spectrograph, where each point of the entrance slit is imaged to one point of the exit plane, of course dispersed along the wavelength axis there. Since the cross-section of the plasma column is imaged onto the entrance slit, each point thus corresponds to the integration of the spectral emission coefficient along a specific chord. Figure 3.16a displays the respective rays when the thickness of the wall is negligible. In the case of a thick wall,

however, the deviation of rays by the wall is serious as shown in (b) for a capillary discharge tube cited often in the literature. Fortunately, the deviation is such that the distance from the center (chordal height) remains the same, thus introducing no error if the effect is neglected: the radiance distribution is the same as without wall, i.e., $L_1(y) = L_2(y)$. The detailed analysis [75] reveals that the chordal height of the deviated rays in the plasma is exactly d/n_{plasma} , where d is the distance of the ray from the optical axis outside the tube and n_{plasma} is the index of refraction of the plasma. A neglect of the wall is dramatic, however, for nonsymmetrical plasmas. Ray-tracing [29] is advised, therefore. Distortions must also be analyzed if absorption in the wall or in the plasma takes place.

Polished stainless steel walls as used, for example, in plasma processing have a substantial reflectivity in the visible which is wavelength dependent. This increases the recorded emission and may introduce errors if not properly accounted for [76].

When the demand of sufficient reflectivity at short wavelengths requires large angles of incidence for mirrors, astigmatism, coma, and spherical aberration become severe. Coma and spherical aberration can be reduced by decreasing the aperture, which unavoidably reduces the collecting power of the mirror. Astigmatism is battled by single aspheric mirrors or by pairs of cylindrical mirrors. The Kirkpatrick–Baez arrangement is one example [77], see Fig. 3.17. It consists of two concave cylindrical mirrors with perpendicular axes of revolution. Other arrangements, which are very common in the observation of astronomical plasmas, utilize inside reflections from conicoidal surfaces and are known as Wolter systems [73, 79]. Nesting a number of such surfaces inside each other increases the collecting power.

Similar in principle are recent developments, which exploit grazing-incidence reflection inside single or bundles of straight or tapered capillary tubes made of glass or quartz [80]. An elegant variant is the use of microchannel plates (MCPs) with square pores. The imaging properties have been analyzed in detail in [81]. Figure 3.18 illustrates the principle. All rays from a point source which are reflected from the midplane of the pores are focused in one point. In reality focusing is certainly not perfect, only one quarter of the rays goes into the true image; two quarters form a cross image and one quarter a diffuse halo. The complete image is described by a respective point spread function. Cases of nonideal microchannel plate X-ray optics are analyzed in [82], and recent developments pushed their use to hard X-rays of around 50 keV [83].

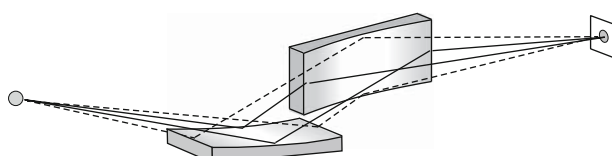


Fig. 3.17. Principle of the Kirkpatrick–Baez system

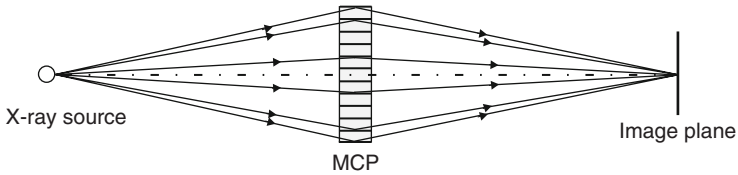


Fig. 3.18. Principle of focusing by a microchannel plate

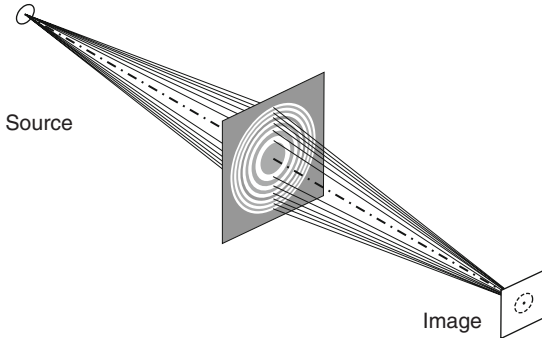


Fig. 3.19. Imaging by a Fresnel zone plate

The highest spatial resolution in X-ray imaging is obtained with Fresnel zone plates which are circular diffraction gratings with radially decreasing line width. They were well known in the visible [29], but modern fabrication techniques recently facilitated their use into the EUV and X-ray spectral regions. They are either free standing thin rings (usually of gold), bridged by a few spokes holding the rings together, or they consist of absorbing or phase shifting rings on a thin transparent substrate. Diffraction occurs at the rings (Fig. 3.19), and their spacing is selected such that the diffracted waves interfere constructively for one wavelength at the desired distance creating an image there. The areas of the zones are approximately equal. Object and image distance obey the ordinary lens formula with the focal length f given by

$$f \simeq \frac{r_n^2}{n\lambda} \simeq \frac{r_1^2}{\lambda}, \quad (3.35)$$

where r_n is the outer radius of zone n . Details on zone plates for the X-ray region are given in [73]. Since the image is formed by diffraction, the spatial resolution is given by Rayleigh's criterion.

Some applications or instruments require collimated radiation of small angular spread. In the X-ray region, this is achieved in one dimension with so-called Soller collimators (slits), Fig. 3.20a; they consist of a set of closely spaced thin metal plates. For hard X-rays, where radiation hitting the plates is fully absorbed (no reflections between the plates), geometrical considerations are quite adequate: the collimator's transmission as function of angle

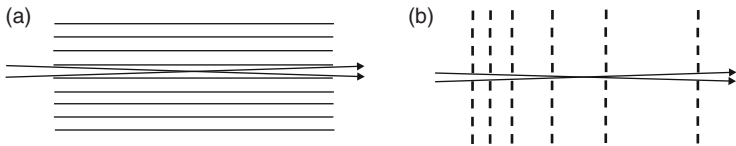


Fig. 3.20. (a) Soller collimator (slit) and (b) stacked-grid collimator

is triangular with the angular spread (full-width at half-maximum FWHM) given by $\Delta\theta_{1/2} = w/H$, where w is the distance of the plates and H is their length.

With increasing wavelength, reflections between the plates start to broaden the angular spread, and already in the soft X-ray region and especially in the EUV stacked-grid collimators are employed therefore, Fig. 3.20b. The separation of the grids must be properly chosen, and even broadening by diffraction has to be taken into account: in principle, each grid is nothing else but a low-resolution diffraction grating [84]. Two-dimensional collimators can be described as two one-dimensional ones.

3.4 Spectrometer Designs

In this chapter, we discuss some of the most common designs; their main characteristics are independent whether the instrument is used as *spectrograph* or *monochromator* (Sect. 3.1). In the ideal case, imaging should be stigmatic, i.e., each point of the entrance slit is focused as a point in the exit plane. In case of astigmatism, the output surface is taken to be the astigmatic focal surface on which the focal lines are in the direction of the geometric slit image.

Instruments for use at wavelengths below 200 nm must have a vacuum-tight housing equipped with sufficiently strong vacuum pumps to remove the gas which continuously diffuses in through the entrance slit from the plasma vessel. In some cases, a differentially pumped section in front of the instrument can become indispensable.

3.4.1 Prism Spectrometers

Prism instruments are relatively cheap, simple to construct and to align, they have no overlapping orders, and the image of the entrance slit is reasonably stigmatic. They are practically everlasting and are easily cleaned. Some disadvantages like the curved image of the entrance slit in the exit plane and the nonlinear wavelength scale are readily compensated electronically when using a CCD camera as detector. On the other hand, the achievable resolving power remains low and limited.

Figure 3.21 shows the standard arrangement which consists of the prism, two telescope achromats, and the entrance slit [28]. A number of different

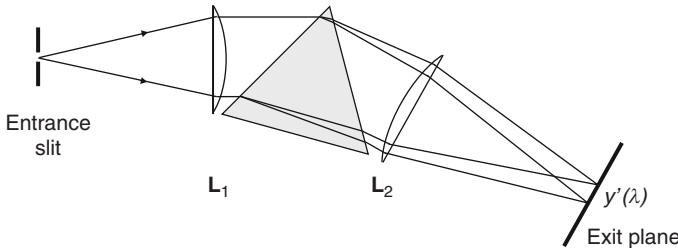


Fig. 3.21. Prism spectrometer

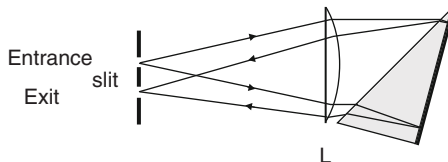


Fig. 3.22. Prism spectrometer in Littrow mounting

mountings can be used like, for example, a train of several prisms of different glass composition (direct-vision prisms) to have the central wavelength in the direction of the incident radiation.

A compact design is obtained by employing the Littrow mounting or auto-collimation. One lens functions both as collimator and focuser, and a reflecting coating at the rear face of a 30° prism (Fig. 3.22) assures that the refracted radiation nearly retraces back to the entrance slit. The total dispersion is that of a 60° prism. Since the planes of entrance slit and of spectral image coincide, such arrangements are best used as monochromators with entrance and exit slits close-by. A small mirror just in front of the focal plane can intercept the dispersed rays and direct them sideways to an exit slit positioned there; this eases attaching the detector. Scanning of the wavelength is by turning the prism mount. The curved image of the entrance slit limits the usable height depending, of course, on the desired resolution. Also, the stray light level is more troublesome for this mounting than for others.

3.4.2 Spectrometers with a Plane Grating

The Littrow mount is also used with plane gratings. Figure 3.23 displays the principle of the configuration with a concave mirror instead of the lens and a deflecting plane mirror before the exit slit. This mirror can be avoided if entrance slit and exit slit (or image plane) are offset slightly along the direction of the grating grooves. The concave mirror is either spherical or off-axis paraboloidal. The wavelength is changed by turning the grating.

Many designs use the Ebert–Fastie mount, see Fig. 3.24. A large single spherical mirror is again collimator and focuser, but in comparison to the

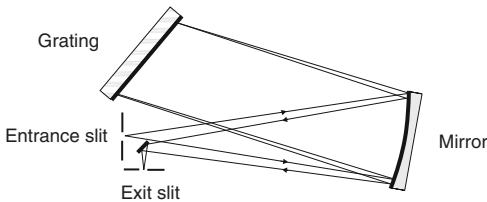


Fig. 3.23. Grating spectrometer in Littrow mounting

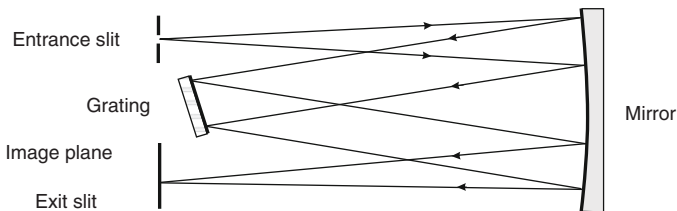


Fig. 3.24. Ebert–Fastie spectrometer

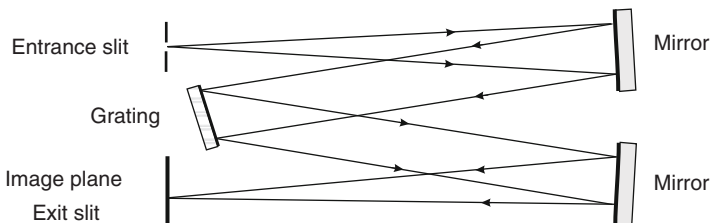


Fig. 3.25. Czerny–Turner mount

Littrow mount, coma is much reduced. Instruments with high f-number are available, unfortunately the curvature of the slit image is severe in these cases and limits the usable slit height. Improvements are possible by using curved slits.

Most commonly employed is the Czerny–Turner mount shown in Fig. 3.25. The single mirror is replaced by two adjacent mirrors and, if these are off-axis spherical and properly tilted [32], coma can be canceled. Astigmatism is rather small as well. Many designs use deflecting plane mirrors behind the entrance slit and before the image plane for convenience.

The size of collimating and focusing mirror must be carefully selected, and attention has to be paid to their positioning. Otherwise, diffracted radiation may hit the first collimating mirror again [85], then it is diffracted a second time at different angles and produces finally an undefined second spectrum in the image plane. If found, such *re-entry* spectra can be eliminated by properly placed masks.

Monochromators of the Ebert–Fastie and the Czerny–Turner mount are very often used in tandem (two or three) to reduce the stray light level and to obtain higher spectral purity, see Sect. 3.1. The exit slit of one monochromator is the entrance slit of the next one. Single units may simply be coupled, or are arranged as one unit in one housing.

Both the Ebert–Fastie and the Czerny–Turner mounts can be designed for use with an echelle grating (p. 20) close to the Littrow mode. High spectral resolution in high orders is achieved, but because of the small free spectral range many orders overlap. This is remedied by a cross-dispersing prism placed before the image plane, which separates the orders of diffraction. However, only recently application of gated CCD cameras (see p. 68) as detector combined with suitable software for the combination of the spectra of different orders has made these echelle spectrometers to powerful and versatile instruments [86]: spectra of large spectral ranges are produced.

3.4.3 Spectrometers with a Concave Grating

Spectrometers with concave gratings may be divided into two categories: normal incidence and grazing incidence instruments according to the angle of incidence. Figure 3.5 of the concave grating also illustrates the typical normal incidence mount (small α): grating, entrance slit and spectral image along the Rowland circle. Because they have only one reflecting surface these instruments are well suited for short wavelengths (VUV), where the reflectance of metal mirrors drops. The spectral lines are astigmatic. When entrance slit and grating are fixed (i.e., the angle of incidence is kept constant) the setup is termed Paschen–Runge mounting [32].

Close to the grating normal (small β) a plane area detector can be used without much loss of resolution; the dispersion is nearly linear, and coma and astigmatism are small. At larger β the detector should be curved.

An exit slit converts the instrument into a monochromator. Usually this slit is also kept fixed for compactness of the instrument, and the wavelength is changed by rotating the grating. Unfortunately, the spectral image moves out of focus, and this has to be compensated by simultaneously translating the grating. One specific design known as Seya–Namioka mounting avoids this, (Fig. 3.26): if entrance and exit slit are positioned symmetrically ($\beta = -\alpha$) on the Rowland circle and separated by 70.25° , the image degradation is at a minimum [87]. Replacing the spherical grating with a toroidal one of properly selected minor radius reduces the rather large astigmatism. Other modifications of the Seya–Namioka concept have been reported. In one approach, a cylindrical mirror is mounted in the exit arm within the Rowland circle compensating for the astigmatism and providing a single tight focus [88].

The most compact design for spherical gratings is the Eagle mount, which can be considered as the equivalent of the Littrow mount for plane gratings: $\beta \simeq \alpha$, i.e., in autocollimation the diffracted radiation nearly retraces back to the entrance slit. If entrance and exit slits are located side by side (Fig. 3.27)

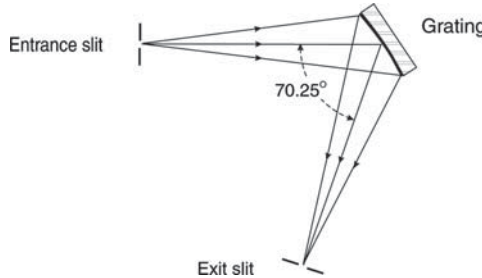


Fig. 3.26. Seya-Namioka monochromator

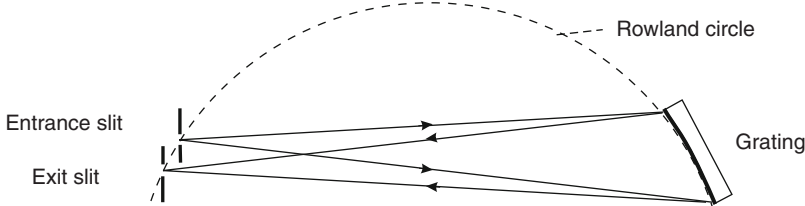


Fig. 3.27. Eagle mounting

one talks of *in-plane* mounting; in *off-plane* Eagle instruments both slits are placed symmetrically above and below the plane of the Rowland circle. When changing the central wavelength, the grating must naturally be rotated *and* translated. With an area detector in the exit plane the instrument turns into a spectrograph.

For large plasmas the Wadsworth mounting can offer some attractive features. A respective concept is presented in [89]. The concave spherical grating is illuminated by parallel rays and a fully stigmatic image is produced for each wavelength on a parabolic surface, located at approximately $R/2$, where R is the radius of curvature of the grating. Collimation of the incident radiation in the VUV can be done mechanically by properly stacked grids (see also Sect. 3.3.4).

Although the major application of concave gratings is in the VUV, useful designs especially of high-throughput instruments are commercially offered also for the visible spectral region.

Below 30 nm concave gratings are used in grazing incidence arrangements. The typical geometric setup is seen in Fig. 3.28. For highest resolution entrance slit, grating, and image plane must be carefully aligned on the Rowland circle, which can be a rather tedious task for small grazing incidence angles ϕ . The lowest reflected wavelength is given by (3.22). If high resolution is not required, a rather simple design places a plane detector in a plane perpendicular to the

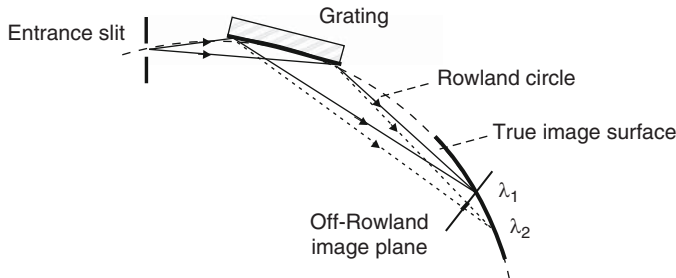


Fig. 3.28. Grazing incidence mount

focused radiation as indicated in the figure (off-Rowland mode). Due to the narrow cones of the focused radiation, the obtained resolution can be sufficient for survey spectra [90].

Grazing incidence instruments employing gratings of varied line spacing (p. 22) are increasingly used now, since their focal surface is indeed flat over a large spectral region, which also eases alignment. Astigmatism is still a problem, but it can be sufficiently reduced by employing a combination of a cylindrical and a spherical mirror to properly image the plasma onto the entrance slit of the instrument and to compensate thus for the astigmatism of the varied line spacing grating [91]. For instruments with a standard spherical grating this can be achieved with a single toroidal mirror [92].

Finally, high-efficiency instruments have been designed also with toroidal gratings with varied line spacing and curved lines to obtain a flat image plane *and* to minimize aberrations (p. 22). Such designs are not restricted to grazing incidence systems but possible for instruments of any angle of incidence. They are usually customer designed with the help of ray tracing techniques [93].

3.4.4 Spectrometers with Transmission Grating

Most systems using a transmission grating are straightforward to construct and easy to align. Their application has spread therefore especially in the soft X-ray region. The most common gratings are produced filling the opening of a pinhole or a slit with the grating bars parallel to the slit. Figure 3.28 illustrates the setup of a pinhole transmission grating. Perpendicular to the dispersion plane (i.e., in the y -direction) spatial resolution is simultaneously obtained by the pinhole effect. The characteristics of such a system have been studied both experimentally and theoretically [94]. Larger free-standing transmission gratings, which have a perpendicular support structure, have also been mounted, for example, with a Kirkpatrick–Baez system (p. 36) [95] to obtain spatial resolution and also higher spectral resolution by simply using more lines per millimeter (3.12) (Fig. 3.29).

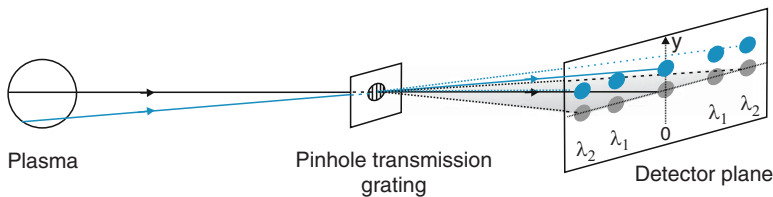


Fig. 3.29. Principle of a pinhole transmission grating spectrograph

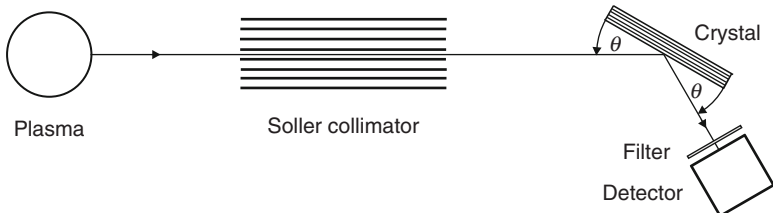


Fig. 3.30. Crystal monochromator

3.4.5 Crystal Spectrometers

For the investigation of point plasmas (laser-produced plasmas or micro-pinches) spectrographs employing a plane crystal are extremely simple and are readily built, Fig. 3.7: a detector just has to be placed into the cones of the radiation reflected from the crystal [96].



Plane highly oriented mosaic crystals offer an interesting variant: rays from a monochromatic point source converge to a point after reflection from the crystal at a distance equal to the distance source-crystal before they finally diverge [97]. This is known as *mosaic focusing*, and the properties of a corresponding spectrometer, for example employing HOPG crystals, were studied in detail in [98].

X-ray monochromators are, in general, in use for recording the time evolution of the emission from extended plasmas at selected wavelengths. A typical setup can be seen in Fig. 3.30: Soller collimator (slit), flat crystal, and detector. The resolution according to (3.24) is no longer given solely by the rocking curve of the crystal, the angular spread of the collimator has to be taken also into account. Turning the crystal varies the reflected wavelength. To fulfil the Bragg condition, turning the crystal by $\Delta\theta$ requires turning the detector arm by $2\Delta\theta$. The turn table for the system thus demands a so-called $\theta/2\theta$ drive; they are commercially available. Since long wavelength radiation (especially visible light) is reflected as well by the crystal or its backing, the detector has to be insensitive to this radiation, and/or filters absorbing long wavelengths are to be placed into the path of the radiation, see Sect. 3.3.2. Finally, in some systems the Soller collimator is placed behind the crystal in the detector arm to reduce any fluorescence radiation possibly produced in the crystal.

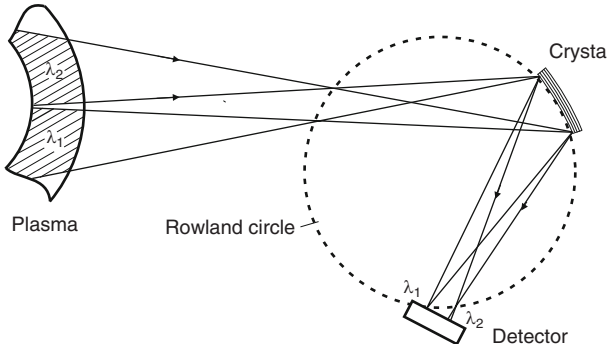


Fig. 3.31. Johann spectrometer

Hot fusion plasmas pose the problem of high fluxes of neutrons and γ -rays, which may swamp the detector. The design of double-crystal monochromators allows for proper shielding, and a corresponding system has been successfully installed and used at the fusion device JET at Culham [99]. The lattice planes of both crystals have to be parallel within an angular margin much smaller than the width of the rocking curve. An additional feature, the possibility of swiveling the first crystal around an axis parallel to the optical axis between the two crystals, even allows spatial scanning of the plasma [100].

The most commonly employed spectrographs for the investigation of inertially and magnetically confined plasmas utilize the so-called Johann mount with a cylindrically bent crystal [51, 101–103]. Since only one wavelength and the corresponding shorter wavelengths in higher orders of the radiation from a point source on the circle are focused again in one point on the Rowland circle (radius $R/2$, radius of the bent crystal R , see p. 21), the plasma has to be placed off the circle to obtain a spectrum. Extended plasmas are usually placed outside the Rowland circle, and the resulting focusing properties are shown in Fig. 3.31. It is obvious that each recorded wavelength is emitted from a different plasma region, here indicated by the shaded areas λ_1 and λ_2 . For optimum resolution X-ray photons should hit the detector perpendicularly, which requires an off-Rowland mount of the detector as shown in the figure. This naturally results in some broadening of the spectral lines. However, even for lines on the Rowland circle focusing of the Johann geometry is not perfect [51]. Additional broadening is associated with the height of the crystal as well as with its illuminated length relative to the radius of curvature. This Johann error is due to the fact that the diffracting planes do not touch the Rowland circle; the distance is largest at the ends, and this limits the meaningful length of the crystal.

Selecting the $2d$ spacing of the crystals such that the Bragg angle for the radiation of interest is close to the Brewster angle of 45° polarizes the reflected radiation (Sect. 3.2.3). The combination of two identical instruments with the spectrometer planes perpendicular to each other makes up a so-called

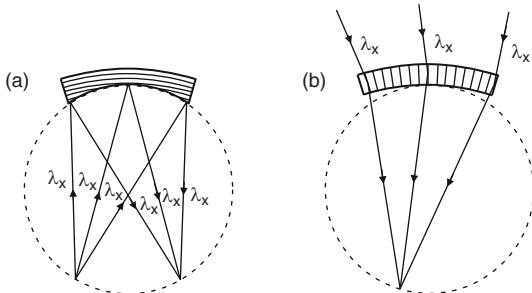


Fig. 3.32. Crystal spectrometer mounts: (a) Johansson mount, (b) Cauchois mount

polarimeter system, which is used to study the polarization of the emitted radiation [104, 105].

As two-dimensional detectors became available, spectrometers employing spherically and toroidally bent crystals in the Johann mount added another dimension, i.e., spatial imaging. They allow spatially resolved spectroscopic studies [106, 107].

For highest resolution Johansson [108] advanced a mount shown in Fig. 3.32a, which circumvents the Johann error. The crystal is bent cylindrically again to a radius R but also cylindrically ground to a radius $R/2$; its surface thus touches the Rowland circle. Spectrometers with two-dimensionally curved and ground Johansson crystals are considered in [109]. Hard X-rays demand small Bragg angles and the scheme proposed by Cauchois (Fig. 3.32b) is well suited for that spectral region [110, 111]. Diffraction is in transmission, the reflecting planes are perpendicular to the surface, and focusing is on the Rowland circle. In addition to the Johann error, another defocusing defect originates in the fact that the lattice spacing d of the crystal planes changes in radial direction with bending of the crystal.

Focusing along the plane of dispersion (Johann mount) is also called horizontal focusing in contrast to vertical focusing, where the crystal is bent perpendicular to the direction of dispersion. Such a scheme was realized by van Hám̄os [112]. The crystal forms a cylindrical surface, and source and detector are on the cylindrical axis, Fig. 3.33. In the dispersion direction, the crystal works like a flat crystal: different wavelengths are diffracted toward different points along the axis. Since all rays of the same wavelengths hitting the crystal at the same arcs are focused to the same points on the axis, the system has a large collection solid angle. For a long crystal the reflected wavelength band can be rather wide. A slit placed perpendicular to the dispersion plane allows spatially resolved studies. This spectrometer type has been used successfully for the investigation of large magnetically confined plasmas [115] and of small laser-produced plasmas [116]. Modifications of the van Hám̄os scheme also employ conically bent crystals: in arrangements due to Hall [113] the apex of the circular cone is located in the detector plane, in the configuration by Pikuz et al. source and imaging plane are positioned on the cone axis [114].

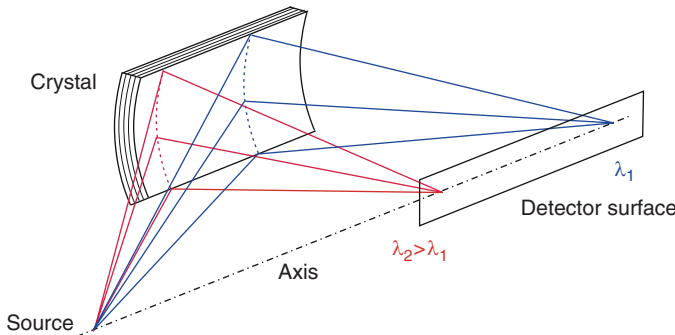


Fig. 3.33. Scheme of the van Hám̄os spectrometer

Further designs noteworthy to mention are a vertical-geometry Johann spectrometer [117] and a vertical dispersion double-crystal system with the two flat crystals in the nonparallel setting [118].

3.4.6 Interferometric Spectrometers

Two types of interferometric arrangements play a role in plasma spectroscopy, the Fabry–Perot and the Michelson interferometer. Descriptions of the instruments and their use are given in [10, 119, 120]. Although the typical spectral range of application is from the UV to the IR, extensions into the VUV have also been reported.

Fabry–Perot Interferometric Spectrometers

Replacing the dispersing element of Fig. 3.1 with a Fabry–Perot interferometer or etalon (Sect. 3.2.4) makes up the Fabry–Perot interferometric spectrometer. A point source (or a pinhole in case of an extended plasma) results in a single image point, the irradiance being determined by an Airy distribution (3.27) for each wavelength. The image of an extended plasma is a circular fringe pattern, each fringe representing the loci of constant α (3.26). The maxima of the fringes are at $\delta = m \cdot 2\pi$, i.e.,

$$m \lambda = 2d n_{air} \cos \alpha, \quad (3.36)$$

where m is the order of interference. m is highest in the center and decreases outward.

Due to the narrow free spectral range $\Delta\lambda_F$ narrow band pass filters are mandatory to avoid overlapping fringes of different orders of other wavelengths. It is obvious that these spectrometers have a higher throughput than dispersive systems as a direct consequence of a large aperture. Furthermore, they are instruments of very high resolving power (3.28). In the imaging mode

an array detector (CCD camera) may be positioned in the image plane, and the circular fringe pattern is readily analyzed. Naturally, the resolving power is now limited by the pixel size.

Placing the detector at the center of the ring system behind a circular aperture and changing the separation of the Fabry–Perot plates allows easy scanning of the spectrum, of course only in a narrow spectral interval. Scanning can be rapid: for that purpose one plate is usually attached to a hollow cylinder of piezoelectric material [121]. Precise scanning is also possible by changing the air pressure in the container of the interferometer and thus the index of refraction n_{air} between the plates (pressure scanning).

Michelson Interferometers

The Michelson interferometer is the instrument of Fourier transform spectroscopy (FTS). The schematic setup is found in nearly every introductory textbook on modern physics, Fig. 3.34. Radiation from a point source is collimated by the first lens L_1 , and the parallel beam is split into two by a beam splitter. The beams reflected normally by the mirrors M_1 and M_2 are recombined and interfere, the irradiance at the focal plane of the second lens L_2 , where the detector is placed, depending on the phase difference of both beams. A compensating plate renders the path in glass of both beams equal. Displacing mirror M_2 changes the path difference and thus the phase difference of the beams, and the detector records an interferogram directly as function of the displacement. Since this interferogram is nothing else but the Fourier transform of the spectrum, performing the inverse Fourier transform gives the spectrum [122]. The high-resolving power is essentially limited only by the distance Δs the mirror can be moved, thus truncating the interferogram. This truncation results in side lobes in the Fourier transform of the spectral lines. A mathematical trick, multiplication of the integrand by a specific function, suppresses these maxima. However, this procedure called apodization

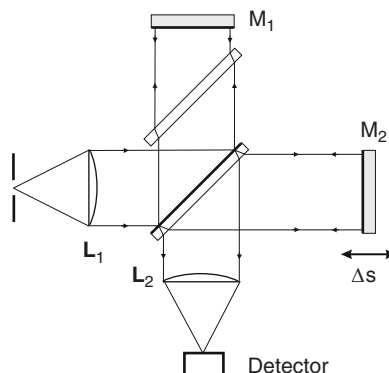


Fig. 3.34. Schematic of scanning Michelson interferometer

also broadens the lines. More details are found in [119]. The truncation limits the resolution to $\delta\lambda = \lambda^2/2\Delta s$ which leads to a resolving power (3.3)

$$\mathcal{R} = \frac{2\Delta s}{\lambda}. \quad (3.37)$$

In the infra-red spectral region, where detector noise can be crucial, further advantages bear most strongly. First to mention is the high throughput. Second, the Fourier transform spectrometer looks at all of a spectrum all of the time, whereas a dispersive scanning spectrometer records only one wavelength at a time while rejecting all others. This results in improved signal-to-noise ratios, the effect being known as multiplex or Fellgett's advantage.

Extension into the VUV is discussed in [119], and a Michelson interferometer for the X-ray region has also been demonstrated recently in [123].

A new design of a Fourier transform spectrometer employs an electro-optical path-modulation technique at a fixed delay instead of a moving mirror [124]. The spectral information of a line (isolated by a narrow-band filter) is transferred to the temporal frequency domain at harmonics of the modulation frequency and can be recorded by a single photodetector. Multiple delay instruments have also been tested. Imaging systems employing a CCD camera synchronized to the modulation frequency of the interferometer yield two-dimensional radiance and flow patterns of a line and the temperature field from its Doppler width [125].

3.5 Alignment and Apparatus Function

The maximum possible radiant flux through a spectrometric instrument is given by the throughput. To avoid any loss, attention must be paid to carefully align the instrument with respect to the plasma and/or the optical system, which images a selected part of the plasma surface onto the entrance slit of the spectrometer. The aperture stop of the spectrometer remains the effective aperture stop of the whole system, and no other optical component limits the flux thus becoming the effective stop. For alignment, a laser beam can be used to define the optical axis of the full optical system and to center all components. In most cases, this requires to open the spectrometer housing to assure that all its components are indeed also on this axis. A recommended practical routine, which is useful in many cases for both good alignment and optimum illumination, is to place a visible light source in the image plane of the spectrometer at the position of zero order and simply to build up the system backward: the radiation cone emanating from the entrance slit is of optimum shape and all components can be selected and placed accordingly.

From Fig. 3.1, it is obvious that in the geometric limit, which holds for wide entrance slits (width w_{en}), the shape of a monochromatic wave in the exit plane is a direct image of the entrance slit. The shape of this *spectral line* is rectangular of width w'_{en} , if any curvature of the slit image, which

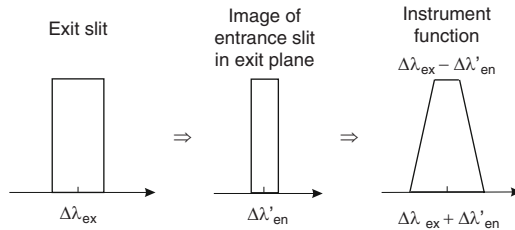


Fig. 3.35. Instrument function of a monochromator

can be serious for high slits in Ebert–Fastie mountings, for example, can be ignored. The width w_{en} thus determines the spectral bandpass as well as the throughput. If used as monochromator, the width of the exit slit w_{ex} should be larger than w'_{en} in order not to lose any flux. Scanning now the exit slit across the spectral image leads to a trapezoidal shape of the *recorded line* representing the instrument function or apparatus profile for this specific setting of entrance and exit slits. Using the linear dispersion of the instrument (3.2) the widths w may be expressed in terms of the corresponding wavelength intervals, i.e., $w'_{\text{en}} \rightarrow \Delta\lambda'_{\text{en}}$ and $w_{\text{ex}} \rightarrow \Delta\lambda_{\text{ex}}$. Figure 3.35 illustrates this instrument function of a monochromator. The full width at half maximum is $\text{FWHM} = \Delta\lambda_{\text{ex}}$. For equal slit widths, $\Delta\lambda_{\text{ex}} = \Delta\lambda'_{\text{en}}$, the instrument function is a triangle with $\text{FWHM} = \Delta\lambda_{\text{ex}} = \Delta\lambda'_{\text{en}}$. Selecting $\Delta\lambda_{\text{ex}} < \Delta\lambda'_{\text{en}}$ the instrument function becomes a trapezoid with $\text{FWHM} = \Delta\lambda'_{\text{en}}$.

When narrowing the entrance slit, aberrations and finally diffraction effects determine its image in the exit plane. This image is the instrument function (apparatus profile) when used as spectrograph. It has to be determined for each width of the entrance slit. For scanning monochromators the selected exit slit width, of course, must be included as illustrated earlier.

If the instrument function at a wavelength λ_0 is described by $\mathcal{I}(\lambda - \lambda_0)$ and an emission line has a line shape given by $\mathcal{L}(\lambda - \lambda_0)$, the observed profile of that line in the image plane of the spectrometer is a convolution of both functions:

$$\begin{aligned}\mathcal{L}^*(\lambda - \lambda_0) &= \mathcal{I}(\lambda - \lambda_0) * \mathcal{L}(\lambda - \lambda_0) \\ &= \int_{-\infty}^{\infty} \mathcal{I}(\lambda' - \lambda_0) \mathcal{L}(\lambda - \lambda') d\lambda'.\end{aligned}\quad (3.38)$$

All three functions are normalized to 1. To retrieve the true spectral profile $\mathcal{L}(\lambda - \lambda_0)$ from the measured one $\mathcal{L}^*(\lambda - \lambda_0)$ by de-convolution seems formally straightforward in the Fourier domain, since there (3.38) is simply

$$\tilde{\mathcal{L}}^* = \tilde{\mathcal{I}} \times \tilde{\mathcal{L}} \quad \text{and} \quad \tilde{\mathcal{L}} = \frac{\tilde{\mathcal{L}}^*}{\tilde{\mathcal{I}}}, \quad (3.39)$$

where the tilde indicates the respective Fourier transform. However, this leads to dividing small numbers by each other or even to division by zero;

furthermore, small experimental errors including noise in $\mathcal{L}^*(\lambda - \lambda_0)$ may produce large errors in $\mathcal{L}(\lambda - \lambda_0)$: the solution becomes unstable. A number of de-convolution algortihms have been developed, see for example [126, 127].

Since most lines emitted by plasmas are pretty well described by a Voigt function (see Sect. 9.1), the following approach usually leads to success: a Voigt function is convolved with the instrumental function and the optimum parameters of the Voigt function are determined by a least-square fit to the experimental profile.

The instrument function of a Fourier transform spectrometer is a normalized sinc function, and the procedures for retrieving the original line profiles [10] correspond to those outlined for dispersive instruments.

Detectors

4.1 General Properties

Detectors for spectroscopy can be classified according to their application. One class converts radiant flux $\Phi(\lambda)$ in a spectral interval $\Delta\lambda$ into a current signal I , Fig. 4.1, the magnitude of which depends on the wavelength. The conversion efficiency is described by the spectral sensitivity $S(\lambda)$ which is defined as the ratio of output current of the detector to incident radiant flux,

$$S(\lambda) = \frac{I}{\Phi(\lambda)}, \quad [S] = \frac{\text{A}}{\text{W}}. \quad (4.1)$$

$S(\lambda)$ is also known as responsivity of the detector. The time response of the detector is crucial in case of rapidly varying radiation. This response is characterized either by the rise time T_r or by the bandwidth f_{bw} . The rise time refers to the time of the output current I to rise from 10 to 90% of the peak value if the input radiation is described by a step function. The bandwidth is defined as the cut-off frequency in Hertz at which the amplitude of the current is reduced to $1/\sqrt{2}$ of the value at low frequencies. Both are connected with each other by the relation:

$$f_{bw} T_r \cong 0.35. \quad (4.2)$$

We denote the frequency of electric circuits with “f” in contrast to the frequency of electromagnetic waves, which we continue to denote by ν .

Some detectors have an internal delay time which must be taken into account when correlating signals. The output current in the absence of incident flux is called dark current; it limits measurements at low flux levels. In most cases it is essentially thermal in origin and may hence be reduced by cooling the detector. The linearity of the system is another important characteristic. To quote the maximum linear output current is one possibility, the dynamic range is the other quantity used in that context. It is defined as the ratio of maximum to minimum detectable linear output current. Noise will

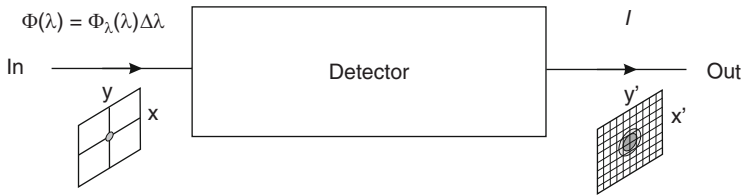


Fig. 4.1. Schematic of a detector

be discussed with individual detectors. In some applications the time stability could also be important as well as the life time of the detector, i.e., its deterioration (aging) with time.

Array detectors record the spectrum (object) in the exit plane (x, y) of a spectrograph and produce a digitized image (x', y'), which can be viewed on a screen or further processed by a computer. The most widely used systems at present are *charged coupled device arrays* (briefly called CCDs or CCD detectors). They gradually replaced photographic emulsions which were the standard array detectors till the turn of the century. Their spatial resolution was limited by the grain size; the spatial resolution of a CCD is now given correspondingly by the size of the radiation-sensitive cells (picture elements or briefly *pixels*). Their spectral sensitivity is certainly also wavelength dependent. The dynamic range is given here by the maximum possible output count rate in a pixel to dark current count rate. Binning of pixels along one direction (usually the y' -axis) corresponds to summation of the emission in that direction and is equivalent to a one-dimensional detector array. Linear photodiode arrays were highly in use before CCDs reached the present state of development. At very low radiation levels binning of pixels along the wavelength coordinate may also become necessary to improve the signal-to-noise ratio at the expense of spectral resolution.

The imaging quality of an array detector is characterized by a respective point-spread function $F(x', y')$, which describes the intensity distribution of a point object $f(x_0, y_0)$ in the image (x', y') plane of the detector,

$$f(x_0, y_0) \quad \Rightarrow \quad F(x' - x'_0, y' - y'_0). \quad (4.3)$$

Convolution with the instrument function of the spectrograph gives the instrument function of the entire spectrographic system.

In case of rapidly changing plasmas, the possible exposure or gate times of the array detector are further important characteristics. Detectors which record a series of consecutive images are known as *framing cameras*, and frame rate and possible total number of frames play a role. Gate times hit a lower limit and for ultra-fast plasma events one has to turn to *streak cameras* which achieve at present a time resolution of the order of 100 fs. Their entrance is a narrow slit aligned parallel to the wavelength axis (x-axis) of the spectrum, and the system sweeps the image with time in the exit plane along the ordinate which thus becomes the time coordinate.

4.2 Photoemissive Detectors

4.2.1 Photocells

The vacuum photocell (phototube, photodiode) is one of the simplest forms of radiation detectors. Figure 4.2 illustrates the principle and includes the simple electric circuit [128]. Radiant flux impinging on a photocathode (C) releases photoelectrons by the *external* photoelectric effect, which are accelerated toward an anode (A). The resulting *photocurrent* I_c is monitored either by a current meter or by the voltage produced across the load resistor R . I_c initially rises with the applied anode voltage, but soon reaches a plateau region; the anode voltage for operation must be chosen in that regime. There I_c is linearly dependent on the incident radiant flux Φ . At very high flux levels an upper limit is given either by space-charge effects or by deterioration of the cathode. Some sensitive photocathodes even age without illumination.

The most widely used photocathodes are semi-transparent thin films deposited on the vacuum side of the entrance window as depicted earlier: the electrons are emitted from the rear side. Opaque cathodes are opposite the window, and the electrons are emitted from the illuminated side.

Dark current I_d and noise determine the lower level of radiation that can be detected. In general, the major contribution to the dark current is thermal emission of electrons from the cathode, although leakage currents and electrons released from the inside of the tube by radioactive radiation of the environment can also contribute.

Noise influences the accuracy of the measurement. Two intrinsic sources are:

- Shot noise of the current. The rms-value $\sqrt{\overline{I^2}}$ of any current I is simply given by

$$\overline{\Delta I^2} = 2 e I \Delta f, \quad (4.4)$$

where $\Delta f \leq f_{bw}$ is the bandwidth selected for the measurement and e is the elementary charge.

- Johnson noise of the load resistor R . It depends on the temperature T and is given by the Nyquist relation

$$\overline{\Delta I_R^2} = \frac{4 k_B T \Delta f}{R}. \quad (4.5)$$

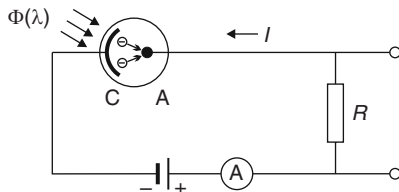


Fig. 4.2. Vacuum photocell with electric circuit

k_B is the Boltzmann constant. The noise contributions are independent of each other and simply add. The total noise level therefore can be written as

$$\overline{\Delta I^2} = 2e \left(\frac{2k_B T}{eR} + I_c + I_d \right) \Delta f. \quad (4.6)$$

With the spectral sensitivity $S(\lambda)$ of the photocell the photocurrent is given by $I_c = S(\lambda) \Phi(\lambda)$.

For recording rapidly changing fluxes the load resistor must match the impedance of a cable, which is typically 50Ω . In this case, the dark current can be neglected. Johnson noise of the resistor becomes smaller than the shot noise of the photocurrent for

$$I_c > \frac{2k_B T}{eR}, \quad \text{i.e.,} \quad \Phi(\lambda) > \frac{1}{S(\lambda)} \frac{2k_B T}{eR}. \quad (4.7)$$

It is convenient to introduce the *quantum efficiency* $\eta(\lambda)$ for photoemissive detectors, which gives the fraction of electrons released from the photocathode by one incident photon:

$$\eta(\lambda) = \frac{I_c}{\Phi(\lambda)} \frac{hc}{e\lambda} = S(\lambda) \frac{hc}{e\lambda}. \quad (4.8)$$

The flux necessary for detection according to (4.7) thus is

$$\Phi(\lambda) > \frac{1}{\eta(\lambda)} \frac{2k_B T}{e^2 R} \frac{hc}{\lambda}. \quad (4.9)$$

For a quantum efficiency $\eta = 0.2$ and a load resistor $R = 50\Omega$ one obtains $\Phi > 13\text{ mW}$ at a wavelength $\lambda = 500\text{ nm}$. In case of stationary plasmas with steady-state emission, the load resistor naturally can be increased by many orders-of-magnitude and thus the lowest detectable flux is decreased correspondingly. However, it is obvious that for the majority of spectroscopic studies photocells are not well suited, and photomultipliers with internal amplification discussed in Sect. 4.2.2 are the detectors of choice.

The *spectral range* is primarily determined by the photocathode material, but further restricted by the transmission of the window. The work function of the material fixes the long-wavelength end, since the photon energy must be larger than the work function for an electron to be released. At short wavelengths the window transmission cuts off, see Sect. 3.3.1. To go beyond the lowest cut-off, which is nominally LiF at 105 nm , windowless configurations are possible, and there the wavelength limit is given by absorption in the cathode material. For example, gold has a quantum efficiency around 10% between 40 and 100 nm [30]. The detectors are easily built; units with Al photocathodes have been successfully employed on tokamaks in the photon energy range 10 eV to 10 keV [129].

The most widely used photocathode materials are silver–oxygen–cesium Ag–O–Cs, antimony–cesium SbCs₃, and bi- and trialkali compounds like Sb–K–Cs, Sb–Rb–Cs, and Sb–Na–K–Cs. Gallium arsenide GaAs and indium gallium arsenide InGaAs cathodes cover a wider spectral range than others from the ultraviolet into the near-infra-red spectral region. Cesium telluride CsTe and cesium iodide CsI cathodes are not sensitive to visible light, and are therefore referred to as solar blind. Maximum quantum efficiencies are typically between 10 and 25%.

Several designation systems for the spectral response were or are still in use like, e.g., the S-numbers. However, to select the optimum cathode for specific or for general applications, it is advisable to consult the detailed data sheets of the manufacturers.

4.2.2 Photomultipliers

Photomultiplier tubes (PMTs) surmount the noise limitations of photocells by internal amplification of the photocurrent I_c . The principle is illustrated in Fig. 4.3: amplification is accomplished by a series of *dynodes* D between photocathode C and anode A. Each is kept on a potential which increases in steps from the cathode to the anode. Electrons released from the photocathode (potential V_c) are accelerated and focused by the electric field toward the properly shaped and positioned first dynode on potential V_1 and, at sufficient energy $e(V_1 - V_c)$, release secondary electrons from the dynode. The average number of released electrons divided by the number of incoming electrons is defined as the secondary-emission coefficient δ and depends on the dynode material, its surface, the angle of incidence, and on the kinetic energy of the primary electrons. For commonly used dynode materials, δ has values between 4 and 14 at 200 eV [130]. The process is repeated from dynode to dynode till the electron avalanche reaches the anode at potential V_A . A system with n dynodes is called an n-stage photomultiplier tube. For the special case of equal secondary-emission coefficients and perfect collection efficiency of all secondary electrons, the total gain G is given by $G = \delta^n$.

The voltage for the electrodes is usually supplied by a linear resistive voltage divider, Fig. 4.4, the cathode being at negative potential. The power

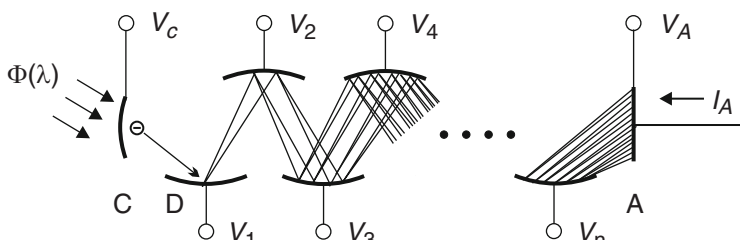


Fig. 4.3. Principle of the photomultiplier tube PMT

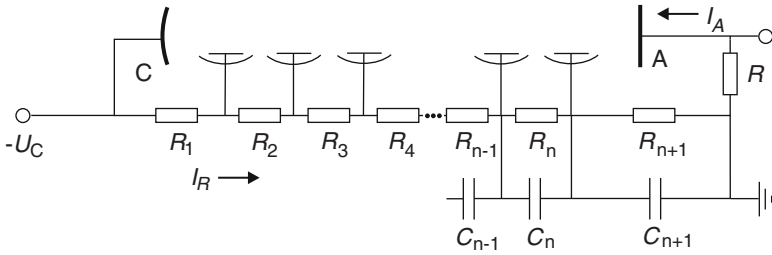


Fig. 4.4. Voltage divider suitable for pulsed operation

supply has to be well regulated in order to guarantee stability of amplification. As a rule of thumb, the anode current I_A must *never* be larger than 1% of the current I_R through the resistors of the voltage divider; otherwise the voltages between the last stages drop because of too large currents from the dynodes and, at constant supply voltage $-U_c$, the voltages between the first stages increase, which results in an overall change of the amplification. When designing the voltage divider, attention should also be paid to the ohmic heat produced in order to avoid heating the photomultiplier assembly. Manufacturers specify the maximum anode current which is typically less than $100\ \mu\text{A}$: higher currents cause fatigue and lower the lifetime. For most photomultipliers most stable performance is at currents below $10\ \mu\text{A}$. Anode current and incident radiant flux are proportional to each other over typically eight orders-of-magnitude, the deviations being usually less than 3%.

At low anode-current levels, a large load resistor R is usually selected in order to have a high-level voltage output. For the reasons discussed earlier, attention must be paid to keep the voltage across R much smaller than the voltage between last dynode and anode. The influence on the frequency response is discussed later.

For pulsed measurements much higher anode currents are possible as long as the *mean* anode current remains below the above maximum permitted value. The necessary charge for the high electron currents from the last dynodes must be supplemented, of course, which is done by capacitors parallel to the resistors of the voltage divider. Their minimum capacitance can be estimated from the peak current I_i from each dynode i and the pulse duration Δt . Demanding the voltage change between two electrodes to be less than 1% requires $\Delta Q = I_i \Delta t = C_{i+1} \Delta(V_{i+1} - V_i) < C_{i+1} 0.01 I_R R_{i+1}$. The last capacitor, for example, thus must have

$$C_{n+1} > 100 \frac{I_A \Delta t}{I_R R_{n+1}}. \quad (4.10)$$

The load R is usually matched to the impedance of a cable (e.g., $50\ \Omega$), which is negligibly small compared to R_{n+1} .

Space charge effects start to limit the linearity at high currents, and it is customary therefore to apply higher voltages to the last few stages, which

extends the linear range. Corresponding recommendations of the manufacturers should be followed to achieve optimum performance. Already small magnetic fields can deflect photoelectrons and primary electrons from their normal trajectories and thus cause severe reductions of the amplification. Under most operating conditions a mu-metal shield will remedy this. However, when measurements are carried out, for example, on pulsed power devices with high fields, additional shielding is necessary.

The spectral sensitivity of the cathode is identical to that of a photocell with the first dynode as anode. All relevant considerations remain valid. Multiplying the “photocell” sensitivity with the gain yields the spectral sensitivity of the photomultiplier as function of the applied voltage $-U_c$.

The shape of the current pulse at the anode in response to a delta-function type radiation pulse is broadened and delayed. The delay is due to the finite transit time of the electron avalanche through the tube. It depends on the applied voltage and on the specific photomultiplier configuration and is in the range of 20–100 ns for most commonly used tubes. Broadening is essentially caused by the transit-time spread due to different paths of the electrons. Data sheets usually quote the rise time T_r , the corresponding bandwidth f_{bw} is given by (4.2). Typical rise times are between 1.5 and 15 ns. In case maximum gain is not needed, a simple approach allows to achieve a faster rise time: one dynode is selected as anode, the later dynodes and the original anode are ignored, and the voltages between the used dynodes are increased. In this way, it was possible to obtain a rise time of 0.36 ns with a rather inexpensive tube 1P28 [131].

Increasing the load resistance R leads to a deterioration of the frequency response. The bandwidth is finally determined by

$$f_{bw}^* = \frac{1}{2\pi RC_A}, \quad (4.11)$$

where C_A is the capacitance of the anode to all other electrodes and includes stray capacitances of the wiring.

Shot noise of dark current I_d and of photocurrent I_c give the major contributions to the noise of the anode current, since both are amplified by the gain G . Fluctuations of the secondary emission enhance this noise by a factor $\delta/(\delta - 1)$ [132]. In contrast to the vacuum photocell, Johnson noise of the load resistor is negligible. Equation (4.6) becomes for the photomultiplier

$$\overline{\Delta I_A^2} = 2eG^2(I_c + I_d) \frac{\delta}{\delta - 1} \Delta f, \quad (4.12)$$

resulting in a the signal-to noise ratio

$$\frac{I_A}{\sqrt{\overline{\Delta I_A^2}}} = \frac{I_c}{\sqrt{2e\Delta f(I_c + I_d)\frac{\delta}{\delta - 1}}} = \frac{I_A}{\sqrt{2e\Delta f G(I_A + I_{Ad})\frac{\delta}{\delta - 1}}}, \quad (4.13)$$

where I_{Ad} is now the dark current at the anode. At low currents, cooling will reduce that component of I_{Ad} , which results from thermal emission. The

dark current can increase by several orders-of-magnitude through excitation of the photocathode, when the tube is exposed to daylight under nonoperational conditions. This effect is temporary, but it takes many hours till the dark current returns to its original value. Handling under subdued lighting conditions is therefore recommended.

Many useful details on photomultipliers can be found in handbooks which are issued by the major manufacturers and which are available on the internet through their website.

Extension of the spectral sensitivity into the vacuum-UV and X-ray spectral regions is achieved by suitable scintillators in front of a photomultiplier. Scintillator materials absorb photons from the UV to the X-ray region and emit fluorescence radiation in the visible and UV. It is detected by the photomultiplier, which has to be selected such that its spectral sensitivity range matches the spectrum of the fluorescent emission. The quantum efficiency of the scintillator is certainly a selection criterion, as well as the decay time of the fluorescent radiation. It determines the time resolution of the scintillator-photomultiplier detector.

Although it is convenient and in some cases unavoidable to have the scintillator separated, for example, inside the vacuum chamber or directly on the vacuum window and the photomultiplier outside behind the window, a lower collection efficiency of the fluorescent radiation is the consequence. In case of low light levels one should strive, therefore, to have the scintillating material coated directly onto the entrance window of an end-on tube, which yields an optimum collection solid angle approaching 2π . In this case, the tube window will be the exit window of the vacuum housing. The thickness of the scintillator has to be optimized for complete absorption of the incoming photons but still good transmission of the visible light. Some materials have a rather constant quantum efficiency η from the UV to the EUV (e.g., 65% for sodium salycilate [30]), where η is defined here as the number of fluorescent photons into the solid angle 4π divided by the number of absorbed photons. In the X-ray region this changes, the number of visible fluorescent photons becomes proportional to the energy $h\nu$ of the incoming photons.

Suitable materials are discussed in [30, 133–135]. Both organic and inorganic scintillators are available, single crystals of thallium-activated sodium iodide NaI(Tl) being most commonly used for hard X-rays since they have the highest quantum efficiency. Like other inorganic scintillators NaI(Tl) crystals are, however, deliquescent and vulnerable to shock and impact, and their decay time is 230 ns. Hence, in spite of their lower quantum efficiency organic scintillators like sodium salycilate, p-terphenyl and plastic scintillators are preferred in most investigations of plasmas, definitely for the soft X-ray and VUV region. They are easier to handle. Plastic scintillators can be shaped into any form, and sodium salycilate and p-terphenyl can be evaporated as a thin film onto windows or the photomultiplier. Their decay times are in the range of nanoseconds. Plastic scintillators consist of a solid solution of organic scintillating molecules in polymerized solvent. Adding special dopant

materials quenches the decay, unfortunately at the expense of lowering the fluorescent output, but pulse durations down to 100 ps have been reached.

4.2.3 Channel Photomultipliers and Microchannel Plates

In the channel photomultiplier CPM, the discrete dynode structure of standard photomultiplier tubes between photocathode and anode is replaced by a channel electron multiplier CEM, Fig. 4.5. This extremely simple system consists of a hollow tube (the “channel”) whose inside wall acts as both a continuous dynode system and a continuous voltage divider. Electrons from the transmissive photocathode enter the tube and when striking the wall produce secondary electrons which are accelerated along the tube toward the anode end. En route this process repeats till the electron avalanche is collected by the anode.

The channel wall must have suitable secondary emission properties and correct conductivity to provide the continuous increase of the electrical potential from the cathode to the anode end. The surface layer is a semiconductor and can be produced by coating the wall. Another often-used technique is to make the tube of lead glass, which appropriately treated in a hydrogen furnace produces the required surface. Some walls also have suitable photo-emissive properties, or an additional thin layer with desired characteristics is even coated onto the inner wall, and this makes the separate photocathode redundant: photons strike the inner wall directly, releasing the first electrons. These photodetectors are also simply referred to as CEMs. They have spectral sensitivities from the VUV down into the X-ray region.

Amplifications in excess of 10^8 are possible and the output current reaches several μA . At such currents the electron density especially at the end of the channel becomes high and residual or liberated absorbed gas molecules are readily ionized: these positive ions are accelerated opposite to the electrons and can reach the front end where they release electrons leading to spurious signals. Curving the tube multiply reduces the distance an ion can travel and eliminates this “ion-feedback.” CEMs have rather low dark currents equivalent to 0.1–0.5 primary electrons per second, and they are also rather insensitive to magnetic fields.

The electrical performance characteristics of a channel electron multiplier are essentially determined by the ratio of channel length to channel diameter,

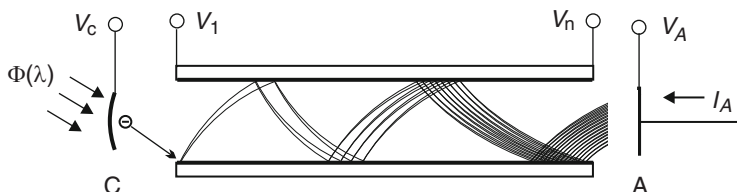


Fig. 4.5. Channel photomultiplier

and this just called for miniaturization. Indeed, this was most successfully accomplished with the design of microchannel plates MCPs [136], which are arrays of the order of 10^7 miniature channel electron multipliers oriented parallel to each other and formed into the shape of a thin disc. The channel diameters are typically between 10 and 25 μm , although smaller ones down to 2 μm pores have been reported. The spatial resolution is given by the pitch, i.e., the center-to-center spacing of the pores. For optimization, the channels are usually inclined by a bias angle with respect to the surface normal.

Thin metallic electrodes of inconel or nichrome are vacuum-deposited on both input and output surfaces; all channels are thus connected in parallel. The plates are delicate, and exposure to moisture can cause warping and cracking. Hence, attention should be paid to the handling and storage instructions supplied by the manufacturers.

The thickness of the plates is typically between 0.25 and 1 mm, resulting in extremely short transit times and transit time spreads. This allows ultrafast detector systems, when a microchannel plate is placed between a photocathode and anode. Cathode and MCP are arranged in close proximity, and rise times down to 65 ps have been reported. The gain of a single microchannel plate is usually kept below 10^4 , since otherwise ion feedback starts to become a problem. Higher gains are achieved by cascading two or three plates. Figure 4.6 shows such a MCP-PMT with two plates arranged with opposite bias angle.

The output is a two-dimensional electron image which preserves the spatial distribution of the input radiation. This allows to built PMTs with a limited number of independent anodes. Systems with two-dimensional matrix anodes as well as others with only linearly arranged anodes are commercially available. They permit the observation of adjacent spectral intervals in the exit plane of a spectrometer.

The other wide-spread application of microchannel plates is image converter and image intensifier. The anode is replaced by a phosphor, the most

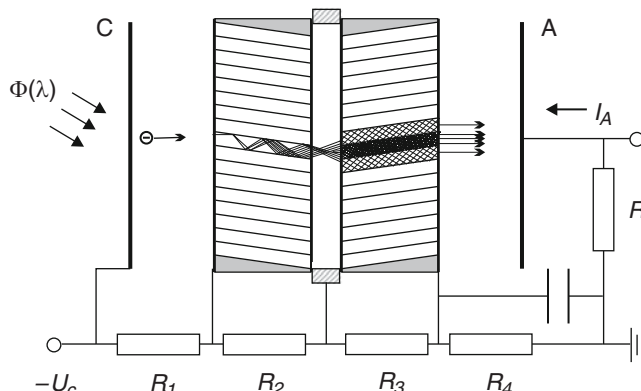


Fig. 4.6. Two-stage MCP photomultiplier tube

common ones being P20 emitting in the green and P11 emitting in the blue. Much faster response is obtained with P47 phosphor, of course at much lower efficiency. The radiating phosphor then is imaged by a high-power optical system onto an optical multichannel analyzer [96, 137] or a CCD camera (p. 68) for appropriate readout. The phosphor can be even on a fiberoptic faceplate, serving simultaneously as vacuum to air interface; in this case, the camera can be attached directly to the fiberoptic end. For detection in the VUV and X-ray region the separate photocathode is simply omitted (open front end), and the photoelectric effect on the channel walls provides the first electrons. To enhance the quantum efficiency the front face of the MCP can be coated with a suitable material; among several possibilities, the most common ones are CsI [138, 139] for the VUV and KBr for the X-ray region [140]. Open-end plates must certainly be operated at recommended vacuum pressures. Like CEMs, they are rather immune to magnetic fields.

Other readout schemes for microchannel plates are in use, but less common in plasma spectroscopic systems. For detectors on space missions, for example, cross delay line anodes are preferred which determine the position of the charge clouds leaving the MCP by measuring the time difference between the arrival of the pulses at both ends of the delay lines [141].

Gating of MCPs for recording rapidly changing radiation is rather straightforward. For gating times above about 100 ns, the voltage applied to one stage of a two-stage plate is simply pulsed, for times down to about 1 ns it is better to pulse the accelerating voltage between MCP and phosphor. Extremely short gate times of about 100 ps have been achieved by shaping the plate electrodes as part of a strip transmission line [142]. Commercially available are also multi-frame systems consisting of multichannel plates sectioned into several strips, which can be gated independently and thus allow recording of a spectrum at several selected times [143].

4.3 Semiconductor Detectors

Semiconductor detectors are based on the *internal* photoelectric effect [130, 144]: photons are absorbed and excite electrons from the valence band or donor levels into the conduction band, or from the valence band into acceptor levels; the free charge carriers thus produced in the material increase the conductivity. The change of the resistance is a measure of the absorbed flux. In diode systems, the absorption is in the vicinity of a *p–n* junction and modifies the current–voltage characteristic .

4.3.1 Photoconductors

Figure 4.7 shows the level structure of undoped and doped semiconductors. In undoped materials (a) intrinsic photoconduction occurs by absorption of photons exciting electrons from the valence band into the conduction band.

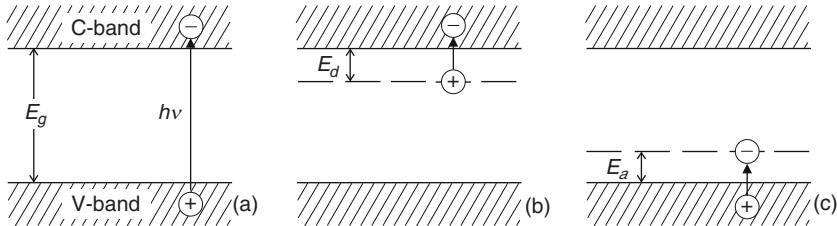


Fig. 4.7. Structure of the energy levels in semiconductors: (a) undoped and (b, c) doped materials

The long-wavelength limit is given by the width of the forbidden gap E_g , i.e., $\lambda \leq h c / E_g$. To extend the spectral sensitivity further into the infra-red, extrinsic photoconductivity in materials (normally germanium and silicon) doped with impurities is exploited. The excitation energy from donor levels E_d (b) or from the valence band into acceptor levels E_a (c) is much smaller than E_g . Unfortunately, the sensitivity at long wavelengths requires cooling of the detectors, and due to the relatively small number of available impurity levels the effective absorption coefficient is also lower.

At constant illumination, the generation of free charge carriers must be balanced by their recombination, which can be characterized by the effective lifetime τ of these carriers. For an extrinsic n -type photoconductor this leads to

$$g = \frac{\Delta n_e}{\tau}, \quad (4.14)$$

where Δn_e is the density of the excited electrons and g the rate of their generation. Introducing the quantum efficiency η and the volume V , in which the incident flux $\Phi(\lambda)$ is absorbed, one may write

$$\Delta n_e = \frac{\eta(\lambda) \Phi(\lambda)}{h\nu} \frac{\tau}{V}. \quad (4.15)$$

Since the conductivity σ is given by $\sigma = -e \mu_e n_e$, where μ_e is the mobility of the free electrons, the change of the conductivity, and thus of the resistance R_d due to illumination becomes

$$\frac{\Delta R_d}{R_d} = -\frac{\Delta \sigma}{\sigma} = -\frac{\Delta n_e}{n_e} = \frac{\tau}{n_e V} \frac{\eta(\lambda) \Phi(\lambda)}{h\nu}. \quad (4.16)$$

A simple circuit for measuring ΔR_d of a photoconductor and hence the incident flux $\Phi(\lambda)$ is shown in Fig. 4.8. With the battery (bias) voltage U_b the output voltage U across the load resistor R is $U = U_b R / (R + R_d)$, and the voltage change ΔU caused by the absorbed radiation becomes for $\Delta R_d \ll R_d$

$$\Delta U = -U_b \frac{R \Delta R_d}{(R + R_d)^2} = -U_b \frac{R / R_d}{(1 + R / R_d)^2} \frac{\tau}{n_e V} \frac{\eta(\lambda) \Phi(\lambda)}{h\nu}. \quad (4.17)$$

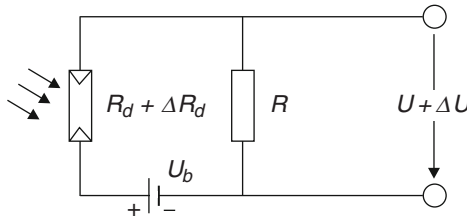


Fig. 4.8. Electrical circuit of photodetector

Matching detector and load resistance, $R_d = R$, yields the largest voltage signal ΔU , and the spectral sensitivity $S^*(\lambda)$ of an n -type photoconductive detector simplifies in this case to

$$S^*(\lambda) = \frac{-\Delta U}{\Phi(\lambda)} = \frac{U_b}{4} \frac{\tau}{n_e V} \frac{\eta(\lambda)}{hc} \lambda, \quad [S^*] = \frac{V}{W}. \quad (4.18)$$

In principle, the lifetime τ of the photon-generated electrons can be larger than their transit time τ_t through the semiconductor between its electrodes. Conceptually, one can think that they traverse the semiconductor $G = \tau/\tau_t$ times before they recombine. G is called the photoconductive gain [144].

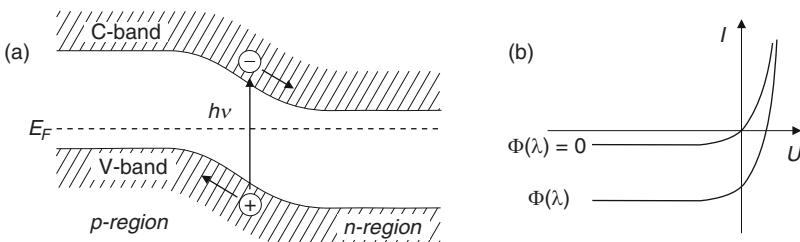
Equation (4.18) indicates, that in the ideal case the spectral sensitivity S^* should increase toward the long-wavelength cut-off and that it depends linearly on the bias voltage. The equation also guides the manufacturer in the optimization of detectors: long carrier lifetime, small volume V , and low initial carrier density n_e . On the other hand, τ limits the frequency response to a bandwidth $f_{bw} = 1/(2\pi\tau)$, and hence for a fast detector it should be short. The carrier density n_e without illumination is due to thermal excitation, and cooling decreases n_e , thus increasing S^* .

Several sources contribute to the noise level, which determines the ultimate accuracy of any detection: Johnson or thermal noise of photoconductor and load resistor (4.5), generation-recombination noise in the photon-generated and thermally excited carriers, and $1/f$ noise which dominates at low frequencies [144]. As discussed earlier, Johnson noise reduces with cooling of the detector, and ideally the generation-recombination noise of only photon-excited carriers should remain dominant. In the limit, there will be still background radiation incident on the detector causing noise without external illumination, and such a detector is called a background-noise-limited infra-red photodetector (BLIP).

Table 4.1 shows examples of photoconductors, their approximate useful spectral range and the temperature T of operation. The first three columns present intrinsic semiconductors. HgCdTe offers the greatest wavelength range and permits the highest operating temperature at long wavelengths. It is an alloy, and the spectral range can be changed by adjusting the stoichiometry of the system. The last three columns give some extrinsic photoconductors.

Table 4.1. Photoconductors

Intrinsic semiconductors			Extrinsic semiconductors		
Material	Spectral range μm	T K	Material	Spectral range μm	T K
CdS	0.5–0.9	295	Ge:Au	1–9	77
PbS	0.6–3.0	295	Ge:Cu	6–28	4.2
PbS	0.7–3.8	77	Ge:Zn	7–40	4.2
PbSe	0.9–5.2	295	Ge:Sb	40–140	4.2
InSb	0.5–6.5	195	Si:As	3–15	20
HgCdTe	2–30	77			

**Fig. 4.9.** (a) Energy diagram of a p - n junction and (b) current–voltage characteristics of a photodiode

4.3.2 Photodiodes

In photodiodes the sensitive detector volume is the p - n transition region between a p -type and an n -type semiconductor. Figure 4.9a shows the respective energy diagram with conduction and valence bands. The Fermi level is indicated by the Fermi energy E_F . The transition region is characterized by a depletion of charge carriers: diffusion of holes from the p -region into the n -region and in the opposite direction of electrons into the p -region leads to the buildup of an electric double layer and a corresponding electric field, which drives an opposite current that finally compensates the diffusion current. Depletion regions can be made large.

Electrons and holes produced by absorption of photons in the depletion region result in a current which depends on the applied voltage. Figure 4.9b illustrates the current–voltage characteristic $I = f(U)$ for an arbitrary flux $\Phi(\lambda)$ and for no illumination. As detectors, these diodes are operated with reversed bias voltage $U < 0$. The current becomes independent of the voltage as long as it is large enough.

$$I = -e \frac{\eta(\lambda) \Phi(\lambda)}{h\nu} + I_d , \quad (4.19)$$

where I_d is the dark current. Noise of the dark current, which also here limits the sensitivity, can again be significantly reduced by cooling.

Table 4.2. Photodiodes

Material	Spectral range μm	T K	Material	Spectral range μm	T K
Si	0.4–1.1	295	InAs	0.6–3.2	77
Ge	0.5–1.8	295	InSb	0.6–5.6	77
InGaAsP	1.0–1.7	295	HgCdTe	2–15	77
InAs	0.9–5.2	295	PbSnTe	8–12	77

A high-quantum efficiency $\eta(\lambda)$ (typically 80%) is one of the advantages of photodiodes. They are compact, rugged, and insensitive to magnetic fields. The bandwidth of the frequency response is given by an equation similar to (4.11), i.e., it is essentially determined by the load resistance and the capacitance of the depletion layer. Since its width increases with increased reversed bias voltage, thus decreasing the capacitance, photodiodes can be made very fast till the drift time of the carriers through the depletion layer determines the final cut-off.

Several variations of the basic type of photodiode discussed earlier have been developed and are used in spectroscopy. The $p-i-n$ diodes are an extension of the $p-n$ junction: an undoped zone (i) of the intrinsic semiconductor separates the p - and n -regions, which are produced by having the respective dopants diffused into the intrinsic semiconductor. Absorption is now in the i -zone, which can be made very wide and thus allows a fast response. Photodiodes with bandwidths of gigahertz are possible.

Schottky-barrier photodiodes allow the highest frequency operation ($>100\text{ GHz}$). They consist of a metal-semiconductor junction in which the metal layer is thin enough to transmit the incident radiation. Absorption occurs at the junction, the majority carriers being responsible for the photocurrent.

Manufacturers offer a large variety of photodiodes. The most important semiconductor material is silicon; p -region and n -region are obtained by the respective doping. Germanium diodes have a wider spectral sensitivity but a larger dark current. Table 4.2 displays examples of photodiodes. The alloy HgCdTe is included, whose bandgap depends on its stoichiometry.

For the vacuum-ultraviolet and soft X-ray spectral regions silicon photodiodes with thin oxide layers proved to be stable and suitable detectors for absolute flux measurements [145, 146].

Reverse-biased $p-i-n$ diodes of silicon and germanium make also excellent energy-resolving detectors of single X-ray photons from about 1 keV to few hundreds of keV. The diode is nearly fully depleted and thus provides a large detector volume. The photons interact in the intrinsic region and produce there tracks of electron-hole pairs. 3.6 eV are needed to generate one electron-hole pair in silicon, and 2.98 eV in germanium. The recorded current pulse of a single photon is a direct measure of its energy, which thus can be obtained via pulse-height analysis. A variant is the lithium-drifted silicon, Si(Li), detector,

where a large sensitive volume is created by having lithium atoms drifted into slightly *p*-doped silicon. The energy resolution is certainly limited, typically to about 150 eV, but no spectrograph is needed. The resolution suffices for measurements of the continuum radiation of long-lived hot plasmas like those of tokamaks [147, 148].

4.3.3 Array Detectors

Photodiode arrays consist of a linear arrangement of many small photodiodes (usually up to 1,024) which in practice are integrated on a single chip. They are of the *p–n* type and if made of silicon they have typically a sensitivity in the range 200–1,000 nm. Infra-red detectors for 1–2.5 μm are made of InGaAs. They may be used at room temperature, cooling leads to lower detector noise.

Basic devices are direct-readout configurations, where one output connection is provided for each photodiode. The practically useful number of elements is thus limited, and multiplexed arrays are the most common ones: the photodiode array is hybridized to a silicon complementary metal-oxide-semiconductor (CMOS) readout integrated circuit.

Two-dimensional charge coupled device (CCD) detectors developed rapidly during the last 2 decades. The basic elements (pixels) are made up of metal-oxide-semiconductor (MOS) capacitors on a doped silicon substrate; silicon dioxide is the insulator. By applying a voltage electrons and holes created by absorption of photons are collected and change the charge on each MOS capacitor. After a controlled integration time a proper sequence of clock voltage pulses transfers the charge packets through the array of capacitors till they reach the last capacitor of a row, where the respective voltage changes are read by an A/D converter and stored in a memory for further processing.

An advanced CCD architecture employs a serial multiplication register placed between the usual shift register and the output amplifier. In this additional register, existing of many stages, electrons are accelerated by a high electric field and generate further electrons by impact ionization. Although the amplification in each stage is small (lower than 2%) when executed over a large number of stages a substantial gain is achieved in these electron multiplying charge coupled device (EMCCD) detectors.

Front illuminated CCDs are usually optimized for the visible region, back illuminated ones with a thinned substrate for the UV. In the VUV, such directly illuminated CCDs are not commonly used because of a poor quantum efficiency. This is different for X-rays: with a deep depletion region single photon sensitivity is achieved. The back-illuminated version provides the best quantum efficiency for the soft to medium X-ray region. For hard X-rays only indirect detection schemes are meaningful: the X-rays are converted to visible light by a phosphor on a fiber optic taper which delivers the image to the CCD detector. Alternatively, these schemes employ an image converter or image intensifier (p. 62) instead of fiber optic [149]. Both provide also a shutter.

The readout time of CCD detectors is typically in the range of 1 ms. New technologies with faster readout are pursued. Pixel array detectors (PADs), for example, promise readout times of 1 μ s or even shorter [150]. These detectors consist of two layers: in a high-resistivity pixellated silicon diode layer the X-rays are absorbed and create electron–hole pairs. Each detector pixel is electrically coupled with a readout pixel of the second layer, which is a CMOS chip.

4.4 Photoionization Detectors

The fundamental process utilized in these detectors is ionization of gases by photons and subsequent measurement of the produced charges. The probability of absorbing the incident photons within the gas volume may approach 100% if gas type and dimensions of the device are properly chosen. A long-wavelength limit is naturally given by the ionization energy of the gas atoms or molecules. Such detectors are thus suited for the X-ray region, but application to the vacuum–ultraviolet is feasible with proper gas filling [30]. Two schemes used in spectroscopy are ionization chambers and proportional counters.

4.4.1 Ionization Chambers

Typical ionization chambers either consist of a rectangular gas cell with two plane electrodes and a thin window or have cylindrical geometry with one electrode (usually the anode) being a wire on the axis, and the second electrode (cathode) being the outer chamber wall. For the vacuum–UV the window is replaced by a small aperture through which the gas escapes and has to be replenished continuously. A differential pumping section may, therefore, be necessary on the entrance side.

The mode of operation is such that only the *primary* ionization produced by the photons absorbed in the gas is measured. The scheme is obvious from Fig. 4.10 displaying a parallel plate chamber. Each absorbed photon produces one electron–ion pair as long as the photon energy is below the threshold for multiple ionization. Above that threshold, multiple ionization can be accounted for as respective cross-sections are known [151]. For the

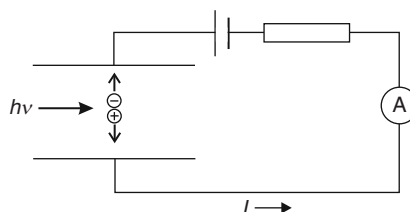


Fig. 4.10. Scheme of the ionization chamber

X-ray region one has to bear in mind that the ejected electron itself has enough energy for collisional ionization of further atoms, and additional electron–ion pairs are thus produced. For each suitable gas one defines an average energy w required to produce an electron–ion pair such that the ratio $\gamma = h\nu/w$ gives the average number of pairs produced by one photon. For argon, for example, $w = 26.2 \text{ eV}$ [134].

Electrons and ions drift towards the electrodes in the electric field in between them, and a current I is recorded in the circuit. On the one hand, the field ought to be high enough that the ions reach the cathode before recombination, but on the other hand it must still be sufficiently low that the electrons do not acquire en route the energy needed for ionizing new atoms in the gas. The electron pulse arrives at the anode in short time, while the ion pulse will be weaker but much longer due the low drift velocity of the ions.

For measuring quasi-continuous fluxes ionization chambers are used, however, in the current mode which integrates over all pulses. If all photons of energy $h\nu$ are absorbed in the chamber, an incident radiant flux Φ_0 results in the current

$$I = \gamma \frac{\Phi_0}{h\nu} e. \quad (4.20)$$

These detectors are thus almost ideal for absolute flux measurements; $\gamma \simeq 1$ in the VUV. If absorption of the flux is not complete, the absorbed radiation is obtained via the Beer–Lambert law and (4.20) may be written as

$$I = \gamma \frac{\Phi_0 [1 - \exp(-\sigma nd)]}{h\nu} e, \quad (4.21)$$

where σ is the absorption cross-section of the gas [55, 64], n the density of atoms or molecules, and d is the length of the chamber.

Filling is usually with inert gases, but a number of molecular gases have also been used, especially in the VUV [30]. The chambers must be carefully designed and several variants are available. One example is the double ionization chamber developed by Samson [152], which allows measurement of flux and absorption.

4.4.2 Proportional Chambers

When increasing the voltage applied to an ionization chamber the electrons gain enough energy to ionize further atoms, and at sufficiently high voltages an electron avalanche will finally develop. Within some voltage range known as *proportional regime* the magnitude of the current pulse varies linearly with the voltage and the amplification is typically 10^3 – 10^5 . At still higher voltages, a discharge develops and the device becomes a Geiger–Müller counter. Proportional chambers can be used in the photon counting or in the current mode. Counting rates can be as high as 10^6 s^{-1} .

Proportional chambers have cylindrical symmetry with a thin anode wire on the axis. As a consequence, the electric field increases strongly around the

wire and the electron avalanche thus develops close to the wire. This leads to a very localized charge increase on the wire, and charge readout at both ends of the wire (known as method of charge division) allows to determine the position on the wire and thus the axial position of absorption of the original photon in the tube [153].

At constant voltage the current pulse depends on the energy of the photons through γ , and pulse height analysis will allow some limited energy resolution [153]:

$$\frac{\Delta(h\nu)}{h\nu} \simeq \frac{10.8}{\sqrt{h\nu}}. \quad (4.22)$$

4.4.3 Multiwire Proportional Chambers

For the spectroscopy of hot magnetically confined fusion plasmas multiwire proportional chambers (MWPCs) are the most widely employed detectors in the exit plane of the X-ray spectrographs, see for example [105, 154]. In principle, they are many single wire units closely spaced in parallel. The present designs consist of a grid of uniformly spaced anode wires sandwiched between two cathode planes. The cathode on the entrance side after the window is usually a wire grid, too; the second cathode can be a series of strips or again a wire grid, Fig. 4.11.

Absorption of the photons is in the drift region after the first cathode; the very localized electron pulses on the anode wires induce image pulses on the cathode wires or strips that are the basis of position encoding; early designs also utilized readout from anode wires. The introduction of effective readout systems by Charpak et al. [155] started the widespread use. The method of charge division mentioned in Sect. 4.4.2 is one possibility, although the most highly developed and most frequently used techniques utilize a delay line [156, 157]: all cathode wires or strips feed the nodes of the line, and the difference of the arrival times at both ends yields the position. For the analysis, the time information is converted into position by time-to-digital converters (TDCs), which are a crucial part of the detectors. By determining the centroid of the cathode charges, a position resolution approaching 0.1 mm is possible.

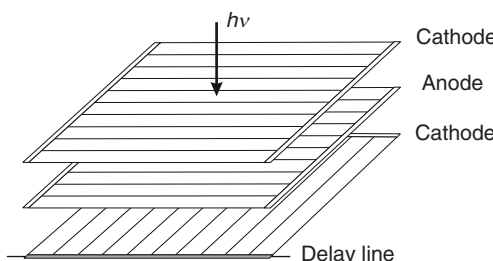


Fig. 4.11. Scheme of a multiwire proportional chamber

The detectors have extremely low noise levels and an excellent dynamic range of about 10^6 ; they can be built of almost any shape and size. Parallax effects certainly must be considered when mounting on a spectrometer. Typical count rates are in the range of $10^5\text{--}10^6\text{ s}^{-1}$. The absorption of the X-rays in the chamber can be optimized by selecting the filling gas [64, 157], once the targeted spectral range is known. Commonly used gases are again argon, krypton and xenon with some quench gas added to prevent the electron avalanche from becoming self-sustaining.

Two orthogonally mounted cathode planes as shown in Fig. 4.11 allow two-dimensional position encoding if the charge induced on the first cathode plane is utilized as well. In another variant the second cathode plane is made up of an array of cathode elements instead of strips, which can be read in two dimensions.

4.4.4 Gas Amplification Detectors

A novel concept for electron amplification in gas detectors was introduced in 1997 by Sauli [158] and triggered the development especially of two-dimensional detector schemes. They are very promising and could replace some day multiwire proportional chambers since they are cheaper and quite robust against radiation damage.

The basic element, known as gas electron multiplier GEM, is an insulating polymer foil, metalized on both sides and punched with an array of holes, which are typically of bi-conical shape, Fig. 4.12(left). A voltage applied between both sides of the foil produces very high fields in the holes, and electrons produced by the incident X-rays in the upper gas volume drift into the channels where they are accelerated and multiply by collisional ionization: an avalanche develops over a very short distance and moves towards the electrodes in the lower volume. Electron multiplication up to 10^3 is possible.

Figure 4.12(right) illustrates one variant of a two-stage array detector. A suitable resistor chain provides the voltages to the cathode, the two GEMs and to a matrix of readout pads, which are hit by the electron avalanches. The intrinsic advantage is obvious: the multiplication region is separate from the readout electrodes. A time resolution in the microsecond domain seems feasible.

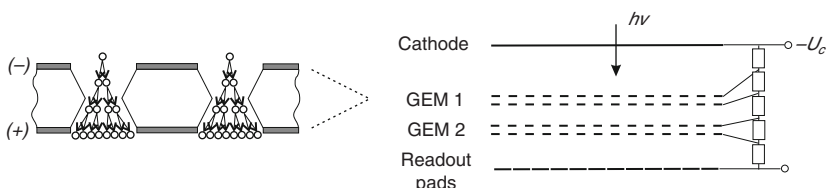


Fig. 4.12. Scheme of gas electron multiplier between cathode and anode (left); scheme of two-stage array detector (right)

4.5 Miscellaneous Detectors

Thermal Detectors

The *bolometer* is a thermal detector most widely used in the far infra-red. Absorption of radiation heats the detector element which changes its electrical resistance. This change is readily measured. Bolometers have a nearly constant sensitivity over a wide spectral range. Their frequency response is essentially determined by the heat capacity C_Q of the detector and the overall thermal conductance to a heat sink. In analogy to (4.11) the bandwidth becomes

$$f_{\text{bw}}^* = \frac{1}{2\pi R_Q C_Q}, \quad (4.23)$$

where R_Q is the overall thermal resistance.

For the X-ray region, the corresponding thermal detector is the *microcalorimeter*, where the “thermometer,” usually a thermistor, is separate from the absorber [159]. Operated at low temperatures below 100 mK it allows the measurement of single X-ray photons with an energy resolution of about 0.1% or better [160].

Image Plates

The usefulness of image plates in the VUV and X-ray spectral regions has been investigated only in recent years [161–163]. Image plates have a response that is linear to the fluence over a wide dynamic range of five orders-of-magnitude, their sensitivity is greater than that of conventional photographic glass plates, and they can be reused.

Image plates are film-like sheets coated with BaFBr with a trace amount of Eu²⁺ added as luminescence centers. Incident photons ionize Eu²⁺, the photoelectron is ejected into the conduction band, where it becomes trapped in a metastable F center. The exposed plates are finally scanned with a narrow beam of a red HeNe laser, which excites the trapped photoelectrons into the conduction band. There they recombine with the Eu³⁺ ions emitting photons at 390 nm which are recorded. At present, the film readers limit the spatial resolution to about 35 μm. Exposing the plates to visible light erases the residual image for reuse.

Streak Cameras

Very rapidly changing radiation is recorded with streak cameras (p. 54) which are commercially available from the X-ray to the infra-red spectral region. Mounted in the exit plane of a spectrograph they record a spectrum of small height but sweep it in addition continuously in the direction perpendicular to the wavelength axis. The core element between the photocathode on the

entrance side and a two-dimensional detector (for example a MCP) on the exit side of the camera is a pair of sweep electrodes: a rising voltage deflects the accelerated photoelectrons, the deflection angle increasing with time. This converts the variation with time into a spatial distribution.

Present streak cameras offer high sensitivity that supports even photon counting. For the detailed spectroscopy of laser-produced plasmas they are more or less indispensable.

Calibration

5.1 Wavelength Calibration

Commercial spectrographic systems are usually supplied with some wavelength calibration, but it is essential that the experimenter performs his own calibration for reliable measurements. A number of sources emitting well-known emission lines are available, and the best values of their wavelengths may be taken from data banks accessible on the internet. Data have been critically evaluated for many decades by the National Institute of Standards and Technology (NIST) of the USA [13], see also p. 4. Special data bases have been established by the astronomy and fusion communities (Appendix B).

For the UV to the infra-red spectral region most commercial spectral lamps are of the hollow-cathode discharge type. Hydrogen and helium lamps are certainly intriguing because of their simple spectra, and mercury lamps because of strong lines in the UV. Optimal calibration is achieved if traces of these or other suitable elements can be added to the plasma to be investigated. For all spectral regions such in situ calibration is inherently possible in a number of cases since many plasmas contain already small amounts of impurities from the walls such as carbon, oxygen, and their ions whose spectra are very well known down to the soft X-ray region. In all cases, however, attention must be paid to possible Doppler shifts, which can be serious even for heavy ions in hot plasmas.

Care must be exercised with many lamps, because the radiation can cause serious damage to the eyes even leading to blindness.

For the VUV spectral region, the emission lines of a high-current hollow-cathode discharge [164], which is used for sensitivity calibration, see p. 80, are very well documented. A hollow-cathode-triggered pinch source, which was developed for EUV lithography applications [165], has also been successfully adopted with different gas fillings for the wavelength calibration and alignment of advanced instruments down to about 2.37 nm [166]. It is simple, has high-intensity and is relatively stable. Laser-produced plasmas of suitable composition are another possibility and can provide a point source down into

the X-ray region. Spectrographs for large volume fusion devices (Fig. 3.31) require large-area sources, and seeding the plasma with known elements for calibration is again probably the most simple approach. A large-area source utilizing K, L, and M transitions of different elements for calibration was developed and investigated [167].

5.2 Sensitivity Calibration

5.2.1 Some General Considerations

The absolute sensitivity calibration of a spectrographic system is best done for the complete system and not separately for the individual components. The considerations as discussed in Sect. 2.2 apply: the standard source of known radiance should be placed such that the radiation fills the full solid angle Ω_m of the spectroscopic system and that the identical part of the entrance slit, preferably the total slit, is illuminated as in the measurements.

One distinguishes primary and secondary radiance standards. Primary standards are the blackbody radiator for the infrared to the visible region, and synchrotrons for the short wavelength range. The spectral radiance of a blackbody is determined by Planck's law and it is a function of temperature and wavelength only. It is independent of the angle between the direction of emission and the normal of the surface (Lambert's law). In principle, a blackbody is realized by a suitably designed furnace ("hohlraum") with a small hole from which the radiation escapes. The hole has to be small enough not to disturb the radiation inside the hohlraum, which is in thermodynamic equilibrium with the walls.

According to Planck the spectral radiance $L_\lambda^B(\lambda, T)$ of the blackbody is given by

$$L_\lambda^B(\lambda, T) = \frac{2hc^2}{\lambda^5} \frac{1}{e^{h\nu/k_B T} - 1}, \quad (5.1)$$

which may be written as numerical value equation

$$L_\lambda^B(\lambda, T) = \frac{1.1910 \times 10^{20}}{(\lambda/\text{nm})^5} \frac{1}{e^{h\nu/k_B T} - 1} \frac{\text{W}}{\text{m}^2 \text{ nm sr}}. \quad (5.2)$$

The precision of the temperature determines the uncertainty of the spectral radiance. Fixed-points of the International Temperature Scale ITS like the melting temperatures of gold (1337.33 K) and platinum (2041.4 K) are the most commonly used reference standards. Metal–carbon eutectics are presently investigated for higher temperature fixed-points [168–170]. Most national metrological laboratories maintain a series of blackbody sources and provide calibration services.

Attention has to be paid to stray light (p. 17) when the calibration is done at wavelengths far from the maximum emission of the standard source.

Electron storage rings are the radiometric standard source for shorter wavelengths, although their emission covers the region from the infrared to the X-rays: the emitted synchrotron radiation can be calculated exactly when the energy of the electrons, the electron current and the magnetic field at the tangent point under observation are known [171]. Some metrological institutions have such a storage ring or have access to one.

In contrast to the thermal radiation of a blackbody the synchrotron radiation is completely polarized in the plane of the electron orbits with the E -vector parallel to the orbital plane. Outside this plane vertical polarization components exist. Drawbacks for the calibration of a complete spectroscopic system are certainly the facts that the synchrotron radiation is emitted into a small cone and that the system has to be moved to the location of the synchrotron [172, 173].

The sensitivity calibration is easily transferred from one spectral region to another by the *branching ratio method* employing a suitable and sufficiently large plasma source of spectral radiance $L_\lambda(\lambda)$ [174]: one considers the emission of two optically thin lines from a common upper level.

We define the spectral sensitivity of the complete spectrographic system S_{sys} in analogy to (4.1) and obtain with (2.9) and the emission coefficient ε of a line defined by (6.5)

$$S_{sys}(\lambda) = \frac{I}{\Phi(\lambda)} = \frac{I}{L_\lambda(\lambda)\Delta\lambda A_s\Omega_m} = \frac{I}{\left(\int \frac{h\nu}{4\pi} A(p \rightarrow q) n(p) ds\right) A_s\Omega_m}, \quad (5.3)$$

where $A(p \rightarrow q)$ is the transition probability from level (p) to level (q) , and $n(p)$ is the population density of the upper level (p) . For two lines from the same upper level to levels (q) to levels (q') (Fig. 5.1) this leads to

$$S_{sys}(\lambda_2) = S_{sys}(\lambda_1) \frac{I_2}{I_1} \frac{\lambda_2}{\lambda_1} \frac{A(p \rightarrow q)}{A(p \rightarrow q')} . \quad (5.4)$$

The accuracy is essentially determined by the accuracy of the transition probabilities A , see Sect. 6.2. Since the emission to the lowest level is usually affected first by self-absorption, this must definitely be checked. Line pairs with two lines close in wavelengths may allow multiple jumps, and larger

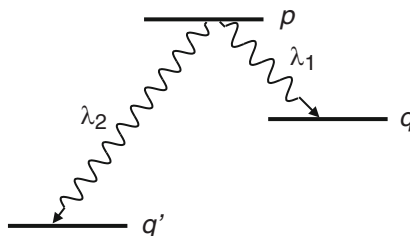


Fig. 5.1. Branching ratio method: lines from the same upper level

wavelengths regions can thus be covered. The extension of the branching ratio method to the emission of molecular bands is discussed in [175].

In cases of two-dimensional (spatial) recording in the exit plane of the spectroscopic system any sensitivity variations along the Y-direction have to be accounted for, too, in the calibration procedure. Causes can be, for example, vignetting in the optical path or pixel to pixel variations in array detectors. Corrections in the latter case are summarized as “flat fielding.”

Finally, fast gated systems should be calibrated also under gating conditions, since detectors like image intensifiers may show the *irisng effect*: due to the finite travel time of the gating pulse from the edge to the center there will be a delay in switching between center and edge.

5.2.2 UV to Near-Infrared

Tungsten Strip Lamp

Secondary standard sources are readily available for this spectral region and have usually been calibrated against a primary standard source. The most commonly used secondary standard is the tungsten strip lamp: a strip of tungsten is mounted in a glass envelope with a window of fused silica or of sapphire in some cases. Vacuum lamps are usually for temperatures from 1,100 to 2,000 K; lamps filled with argon are used for temperatures from 1,600 to 2,700 K, since the gas slows down evaporation of tungsten. Heating of the strip is by a highly stabilized current. Because the temperature varies considerably along the filament, calibration is done nominally for a small central part, maybe of 1 mm height, which hence should be used in the measurements only. This is certainly a restriction in some cases. It is also advised to mount especially gas-filled lamps in the same position as the calibration was done, because changing heat conduction in the lamp may change the temperature.

The spectral radiance $L_\lambda(\lambda, T)$ is obtained by multiplying the blackbody radiance with the spectral emissivity $\epsilon(\lambda, T)$ of tungsten and with the spectral transmittance $T(\lambda)$ (Sect. 3.3.1) of the window:

$$L_\lambda(\lambda, T) = T(\lambda) \epsilon(\lambda, T) L_\lambda^B(\lambda, T). \quad (5.5)$$

T is the *true* temperature at the center of the strip. The emissivity is a rather weak function of wavelength and temperature: it varies between 0.41 and 0.48 in the wavelength range from 250 to 700 nm and temperatures from 1,600 to 2,700 K [176, 177]. Uncertainties of the spectral radiance of calibrated lamps are typically around $\pm 1\%$.

Tungsten strip lamps age and re-calibration becomes necessary after some use. In cases where high precision is not striven for, one may calibrate a lamp in the laboratory employing a pyrometer. This is usually done at the wavelength $\lambda_0 = 650$ nm. The procedure yields a temperature called brightness temperature T_b , defined in the following way: a blackbody at T_b has the same spectral radiance at $\lambda_0 = 650$ nm as the tungsten strip lamp at T :

$$\epsilon(\lambda_0, T) L_\lambda^B(\lambda_0, T) = L_\lambda^B(\lambda_0, T_b). \quad (5.6)$$

The true temperature T is thus readily obtained from the brightness temperature. In the limit $h\nu_0 \gg k_B T$ the relation between the two temperatures becomes

$$\frac{1}{T_b} = \frac{1}{T} \left\{ 1 - \frac{k_B T}{h\nu_0} \ln [\epsilon(\lambda_0, T)] \right\}. \quad (5.7)$$

Low Current Carbon Arc

The low-current carbon arc with the electrodes mounted at right angles to each other is a simple and easy to use secondary radiation standard, which can be reproduced anywhere. The spectral radiance of the anode has been studied by a number of authors, e.g., [178–181], and the emission from it was found to be surprisingly reproducible if the arc was operated just below the hissing point. The diameter of the electrodes is not critical. The spectral radiance is tabulated from 190 nm to 15 μm . In the spectral range above 270 nm $L_\lambda(\lambda)$ is approximated by (5.5) as emitter with $T = 3,830 \text{ K}$ and emissivity $\epsilon = 0.965$, [181]. Below 270 nm emission from the arc stream in front of the anode adds to the emission from the incandescent anode and finally dominates. In some spectral regions emission from molecular bands is observed, e.g., from CN bands in the region 370–420 nm and from C₂ bands in the region 450–474 nm; these spectral regions are, therefore, not suitable for calibration purposes. The accuracy is quoted to reach $\pm 5\%$.

Sources Using Integrating Spheres

The small usable surface element of tungsten strip lamps is a shortcoming in some applications, and this is overcome by placing a lamp suitably inside an integrating sphere. Such hollow spheres known as Ulbricht spheres have a diffusely reflecting internal surface of special photometer paint: light inside the sphere is reflected many times so that it is spatially uniform across an exit port and nearly Lambertian, i.e., the radiance is also independent of the angle between surface normal and direction of emission. The exit port can be made large, if only its size relative to the internal surface is kept sufficiently small. Lamps employed are usually tungsten halogen lamps. Complete systems are offered by several companies; they must be calibrated against a standard source, since their spectrum is due to emission from all emitting elements of the lamp which can be at different temperatures.

5.2.3 Vacuum-Ultraviolet

Wall-Stabilized Arcs

Wall-stabilized arcs operated in hydrogen were initially studied for their potential as a primary source standard, since the optically thin continuum

emission of the hydrogen plasma can be calculated if plasma temperature and electron density are known. The achieved uncertainties were $\pm 5\%$ above 140 nm, $\pm 14\%$ at 124 nm [182], and $\pm 15\%$ for the spectral region 53–92 nm [183]. Several laboratories then concentrated their efforts on operating arcs in argon and to develop such discharges as secondary source standards. They are referred to as argon mini-arcs, and the emission is observed also along the axis. They have either a MgF₂ window [184, 185] or employ a windowless differential pumping system [186]. Windows age, but they are interchangeable and their transmission can be measured separately.

The spectrum consists of a strong continuum with impurity lines becoming increasingly important below 170 nm. These lines are excluded from the radiance calibration of the source. The spectral radiance of the continuum of the mini-arc is much higher than that of the carbon arc and that of deuterium lamps which are discussed in the sect. “Deuterium lamps.” [185]. Absolute radiance values are reported from 95 nm, respectively from 115 nm in case of a window, up to 330 nm. The uncertainty in the spectral radiance is around $\pm 5\%$ for the wavelength region above 150 nm, and around $\pm 10\%$ for wavelengths below.

One disadvantage is naturally the small size of the emitting plasma core, as well as the small usable solid angle. The diameter of the calibrated plasma is typically around 0.30 mm, the spectral radiance is constant to within $\pm 1\%$ for f-numbers as large as f/9.

Deuterium Lamps

Deuterium lamps emit a line-free continuum from 165 to 350 nm (see Chap. 6.3.3) and are suited as a secondary radiance source standard. In addition, they are relatively cheap and are easy to handle. The uncertainty of the spectral radiance is $\pm 4\%$ [187, 188]. Employing a MgF₂ window, the possible use was extended to the spectral region 115–165 nm, where the emission of molecular lines dominates [189].

One shortcoming is the rapid wavelength-dependent aging with time of operation [190]. However, more suitable lamps are becoming available, and monitoring a lamp extends the time till recalibration [191].

High-Current Hollow-Cathode Discharge

An interesting standard source is the high-current hollow-cathode discharge developed by [164] and calibrated against the synchrotron radiation of an electron storage ring [192]. The source is known as DKK source, named after the principal developers Danzmann, Kock, and Kühne. It operates with an aluminum cathode and different buffer gases (He, Ne, Ar, Kr) at a constant current. Between 13 and 125 nm the spectral radiance of lines from atoms and ions of the buffer gas and sputtered aluminum is surprisingly reproducible to

within $\pm 10\%$ (2σ value). A modular design allows easy exchange of the cathode insert, and the old emission values are reproduced to within the above uncertainty. The short-term stability is $\pm 5\%$ over a period of 40 h. The emission profile of the source is essentially flat across a diameter of 1.2 mm, into a solid angle of 10^{-4} sr.

Penning Discharge

The radiance of lines from a Penning discharge has been studied and calibrated by comparison with a primary standard [193]. For wavelengths shorter than 120 nm the Penning discharge is a source of intense lines from neutral to multiply ionized atoms of the cathode material. For wavelengths below 20 nm the radiance is higher by 2–3 orders-of-magnitude than from the DKK source; above 30 nm lines from both sources provide a good overlap. Stable operation is possible for 5 h.

Electron Cyclotron Resonance Source

An interesting alternative to the earlier given sources may be an electron cyclotron resonance (ECR) plasma source whose properties and behavior are currently being investigated [194]. The stability of the source is similar and its lifetime is longer, but no final assessment as to its suitability as standard source has been reached.

BRV Source

A vacuum spark discharge originally described by Balloffet, Roman, and Vodar [195] and hence known as BRV source is a pulsed source of continuum radiation from the visible to below 5 nm. The discharge is between an anode pin of heavy metal (uranium) and a disc cathode, and it is initiated by a trigger spark in vacuum, i.e., at pressures below 10^{-2} Pa. The emission between 40 and 600 nm has been investigated and the potential as radiometric standard has been assessed [196].

The radiation output varies strongly from pulse to pulse and its duration is shorter with decreasing wavelength. Hence, only the time integrated radiance is useful. In general, however, the source is not completely satisfactory as a standard, better alternatives are available.

Laser-Produced Plasmas

The potential of laser-produced plasmas as radiometric standard sources has been studied by several groups. They are produced by focusing Q-switched or mode-locked lasers onto solid targets, preferably of rare earth elements or heavy metals like gold or tungsten, e.g., [197, 198]. Although the reproducibility was as good as 5% and they are better suited than the BRV source between

40 and 80 nm [199], laser-produced plasmas did not yet establish themselves as radiometric standard.

Plasmas with Optically Thick Lines

If plasmas are increasingly seeded with impurities, lines and especially resonance lines from the atoms and their ions ending at the respective ground states become increasingly optically thick: their spectral radiance grows against the blackbody limit given by the Planck function (5.2) corresponding to the temperature of the plasma. This spectral radiance thus can be calculated and, provided the temperature of the plasma is well known and constant along the line of sight, gives a radiometric standard [200], strictly speaking even a primary standard. A calibration of optically thick lines from carbon and nitrogen in an argon wall-stabilized arc against synchrotron radiation yielded excellent consistency [201].

For general applications, the problem is definitely the accuracy of the temperature determination. Furthermore, for a precise assessment of how well the spectral radiance of the line touches the blackbody curve, a measurement of the spectral line profile may become necessary.

Branching Ratio Method

The branching ratio method discussed on p. 77 offers a highly convenient and in situ calibration possibility if the plasma to be studied either emits already suitable line pairs or can be seeded with suitable impurities. One preferably selects one line in the visible, where calibration is readily performed, the other in the VUV region of interest. Care has to be exercised if the short-wavelength line is a resonance line since these are affected by self-absorption in many cases. Anyhow, it should be checked by varying the concentration of the seeded impurities.

At sufficiently high plasma densities the method can be extended to line pairs from different sublevels, if it is verified that their population is proportional to their statistical weight. For many ions, this is usually the case in high-density pinch plasmas [202–204].

Because of its simplicity the method has been widely applied on many plasmas. The major limitation is a shortage of suitable line pairs with sufficiently accurate transition probabilities. On the other hand, the situation continuously improves as data bases evolve [13]. Lists of line pairs of atoms and ions of the hydrogen, helium, lithium, and beryllium isoelectronic sequences are given in [205] along with their pertinent data. The transition probabilities for the above ions are the best known ones.

An example of a sensitivity calibration of a grazing incidence instrument over a large spectral range employing branching ratios of magnetic multipole transitions in addition to some of the above line pairs is found in [206]. The spectrometer was attached to a tokamak.

A possible extension to molecules making use of Franck–Condon factors of molecular bands was first demonstrated with the CO molecule in [207]. Bands of N₂ were employed in [208].

5.2.4 X-ray Region

Extension of the branching ratio method into the X-ray region below 1 nm appears intriguing and straightforward, but unfortunately no suitable line pairs with a long-wavelength line in the visible are available.

A large-area X-ray source, whose radiance can readily be determined, was specifically developed for the absolute calibration of spectrometers in the X-ray region [167]. It consists of a large-area metal anode plate, which can easily be exchanged for the production of different *characteristic* X-ray lines. The cathode is a system of stretched thin gold-covered tungsten wires arranged parallel to the anode. They are heated and the emitted electrons are accelerated toward the anode, where they lead to the typical emission of X-rays. The emission is proportional to the electron current and it is observed through the cathode mesh.

The radiance of the lines of the source is obtained from the spectrum derived via pulse-height analysis of the emitted photons recorded with a Si(Li) detector, p. 68, of known spectral quantum efficiency. Aperture of the detector and subtended solid angle must be determined as well. K-, L-, and M-lines of a number of elements were used, the background continuum was less than 10% of the total line integral in all cases.

Radiative Processes in Plasmas

6.1 Overview

All plasmas emit and absorb electromagnetic radiation and Fig. 6.1 shows, as an example, the characteristics of the emission spectrum of a dense laboratory hydrogen plasma with some impurities at the electron temperature of $k_{\text{B}}T_{\text{e}} = 10 \text{ eV}$. The dashed line is the blackbody limit drawn for comparison.

We identify the following contributions:

- Bremsstrahlung (dot-dashed contribution), a continuum radiation, is emitted when the electrons experience deflection in the electric field of the ions. At long wavelengths the optical depth becomes large and the bremsstrahlung approaches the blackbody limit (Planck function).
- Recombination radiation, also a continuum but characterized by edges. It is emitted when electrons recombine with ions.
- Line radiation corresponds to transitions of electrons between levels in atoms and ions, and at low temperatures also in molecules. Lines may become optically thick especially at long wavelengths and then they also reach the blackbody limit.

The schematic energy level diagram of a nonhydrogenic ion in Fig. 6.2 illustrates the transitions. It is evident why they are also termed *free-free*, *free-bound* and *bound-bound* transitions, respectively, transitions from doubly excited states included. By absorption of radiation each transition is possible in the reverse direction.

The maximum emission of the (optically thin) bremsstrahlung is at λ_{\max} given by (Sect. 6.3.2)

$$\lambda_{\max} k_{\text{B}}T_{\text{e}} = \frac{hc}{2}, \quad \text{respectively} \quad \frac{\lambda_{\max}}{\text{nm}} \frac{k_{\text{B}}T_{\text{e}}}{\text{eV}} = 620. \quad (6.1)$$

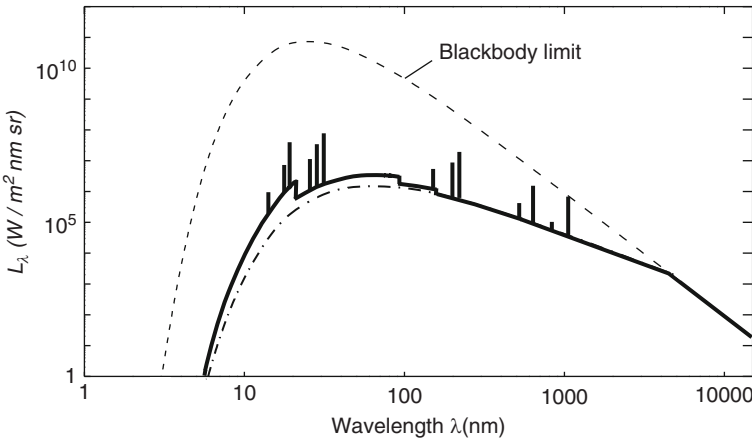


Fig. 6.1. Simulated spectrum of a dense hydrogen plasma of $k_B T_e = 10 \text{ eV}$ with impurities, $n_e = 10^{19} \text{ cm}^{-3}$, thickness 1 mm

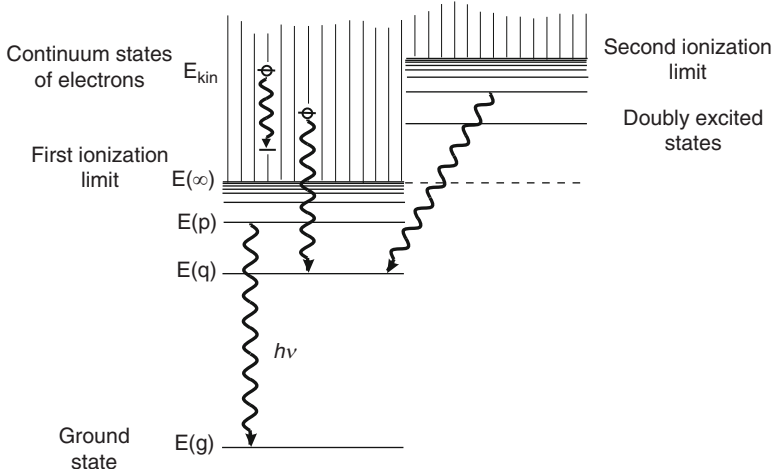


Fig. 6.2. Schematic energy level diagram of a non-hydrogenic ion

In contrast, the maximum of the blackbody radiator is according to Wien's displacement law at

$$\frac{\lambda_{max}}{\text{nm}} \frac{k_B T}{\text{eV}} = 249.7. \quad (6.2)$$

In rapidly heated plasmas or in plasmas with injected heavy impurities also innershell transitions emitting characteristic X-ray lines of atoms and ions are possible since energetic electrons produce innershell vacancies as well as ionization of the outer electrons.

Introductions to atomic and molecular structure and spectra are found in most textbooks on modern physics and in a number of specific monographs like, for example [209–213].

6.2 Line Radiation

6.2.1 Emission and Absorption by Atoms and Ions

A spectral line is emitted when a bound electron undergoes a transition from an upper level (p) of energy $E(p)$ to a lower level (q) of energy $E(q)$. Energy conservation gives the frequency of the line

$$\nu_{pq} = \frac{E(p) - E(q)}{h}. \quad (6.3)$$

The transition is *spontaneous* and the decay is simply proportional to the density $n_z(p)$ of the species of charge (z) in the upper state,

$$-\frac{dn_z(p)}{dt} \Big|_{p \rightarrow q} = A(p \rightarrow q) n_z(p). \quad (6.4)$$

The constant $A(p \rightarrow q)$ is a characteristic atomic constant for that specific transition and known as atomic transition probability (unit s^{-1}) or Einstein coefficient of spontaneous emission. With each transition a photon is emitted, and the emission coefficient ε of the line thus is given by

$$\varepsilon(p \rightarrow q) = \frac{h\nu_{pq}}{4\pi} A(p \rightarrow q) n_z(p). \quad (6.5)$$

This fundamental spectroscopic equation reveals that the population densities $n_z(p)$ of the excited states of the atomic species are the quantities obtained from measurements of the radiance of lines, after the local emission coefficient has been retrieved (see Sect. 2.3), and provided that the transition probabilities are known. The sum of all transition probabilities $A(p \rightarrow)$ from one upper level to *all* lower levels gives the lifetime τ_p of the upper level against spontaneous emission

$$\tau_p = \frac{1}{\sum_{q < p} A(p \rightarrow q)} = \frac{1}{A(p \rightarrow)}. \quad (6.6)$$

All lines are broadened, their shape described by a normalized *line shape* or *profile function* $\mathcal{L}(\nu)$ (see Sect. 9.1). The spectral emission coefficient of a line hence is written

$$\varepsilon_\nu(p \rightarrow q) = \frac{h\nu_{pq}}{4\pi} A(p \rightarrow q) n_z(p) \mathcal{L}(\nu). \quad (6.7)$$

Its unit is $[\varepsilon_\nu] = \text{W}/(\text{m}^3 \text{Hz})$.

Emission is also induced by electromagnetic wave fields, the respective rate being proportional to the spectral radiant energy density u_ν (2.2):

$$-\frac{dn_z(p)}{dt} \Big|_{p \rightarrow q} = B(p \rightarrow q) u_\nu n_z(p). \quad (6.8)$$

The inverse process is absorption,

$$-\frac{dn_z(q)}{dt} \Big|_{q \rightarrow p} = B(q \rightarrow p) u_\nu n_z(q). \quad (6.9)$$

$B(p \rightarrow q)$ and $B(q \rightarrow p)$ are known as Einstein coefficients of induced emission and (induced) absorption, respectively, and u_ν is to be regarded *constant* in the frequency interval of the line profile.

Relations between the Einstein coefficients are obtained by considering the atomic system in thermodynamic equilibrium, where transition rates in opposite direction must balance; the population densities obey the Boltzmann distribution, and the radiation field is given by Planck's law [210]. The two conditions

$$g(p)B(p \rightarrow q) = g(q)B(q \rightarrow p) \quad \text{and} \quad (6.10)$$

$$A(p \rightarrow q) = \frac{8\pi h\nu_{pq}^3}{c^3} B(p \rightarrow q) \quad (6.11)$$

follow, where $g(p)$ and $g(q)$ are the statistical weights of upper and lower level, respectively. When using the angular frequency ω or the wavelength λ instead of ν in (6.9), i.e.,

$$B(q \rightarrow p) u_\nu = B'(q \rightarrow p) u_\omega = B''(q \rightarrow p) u_\lambda, \quad (6.12)$$

where $u_\nu d\nu = u_\omega d\omega = u_\lambda d\lambda$, one obtains $B' = 2\pi B$ and $B'' = (\lambda^2/c)B$, and relation (6.11) becomes

$$A(p \rightarrow q) = \frac{\hbar \omega_{pq}^3}{\pi^2 c^3} B'(p \rightarrow q) \quad \text{and} \quad A(p \rightarrow q) = \frac{8\pi hc}{\lambda_{pq}^5} B''(p \rightarrow q). \quad (6.13)$$

The different definitions of the B-coefficient are possible pitfalls and can lead to errors; the reader is advised, therefore, to check the definition employed by an author before any use.

As discussed in Sect. 2.4, in practice the absorption coefficient $\kappa(x, \nu)$ is the quantity used, which is defined as the fractional decrease of the spectral radiance $L_\nu(x, \nu)$ (2.21) by a plasma slab of thickness dx at the position x :

$$dL_\nu(x, \nu) = -\kappa(x, \nu) L_\nu(x, \nu) dx \quad (6.14)$$

The unit of $\kappa(x, \nu)$ is m^{-1} . For a line at the central frequency ν_{qp} , the line absorption coefficient may be written as (we omit the spatial coordinate x in the following)

$$\kappa(x, \nu) = \kappa^L(\nu_{qp}) \mathcal{L}(\nu) \quad \text{with} \quad \int_{\text{line}} \mathcal{L}(\nu) d\nu = 1, \quad (6.15)$$

where $\mathcal{L}(\nu)$ is the line shape function and $\kappa^L(\nu_{qp})$ is the integrated line absorption coefficient. Its unit is m^{-1}Hz . The spectral flux absorbed in a plasma

slab of thickness Δx corresponds, according to (6.9), to the absorption of $B(q \rightarrow p) u_\nu n_z(q) \Delta x$ photons. Hence, this relation multiplied with $h\nu_{qp}$ is equal to the right-hand side of (6.14) after integration of the absorption coefficient $\kappa(\nu)$. u_ν respectively L_ν are taken to be constant across the line.

$$\begin{aligned} B(q \rightarrow p) u_\nu(\nu_{qp}) n_z(q) \Delta x h\nu_{qp} &= L_\nu(\nu_{qp}) \Delta x \int_{\text{line}} \kappa(\nu) d\nu \\ &= \kappa^L(\nu_{qp}) L_\nu(\nu_{qp}) \Delta x. \end{aligned} \quad (6.16)$$

With $u_\nu(\nu_{qp}) = L_\nu(\nu_{qp})/c$ according to (2.2), this results in

$$\kappa^L(\nu_{qp}) = \frac{h\nu_{qp}}{c} B(q \rightarrow p) n_z(q). \quad (6.17)$$

The integrated line absorption coefficients for the spectral radiance in angular frequency and wavelength units are obtained in full analogy as

$$\kappa^L(\omega_{qp}) = \frac{\hbar\omega_{qp}}{c} B'(q \rightarrow p) n_z(q) = 2\pi \kappa^L(\nu_{qp}). \quad (6.18)$$

$$\kappa^L(\lambda_{qp}) = \frac{h}{\lambda_{qp}} B''(q \rightarrow p) n_z(q) = \frac{\lambda_{qp}^2}{c} \kappa^L(\nu_{qp}). \quad (6.19)$$

In plasmas especially of higher density an appreciable number of atoms/ions can be in the upper level (p) of the transition and stimulated emission must be taken into account. This occurs into the same direction as the incident radiation thus resulting in an effective reduction of the absorption. The *net* integrated line absorption coefficient $\kappa_{\text{net}}^L(\nu_{qp})$ for equal absorption and emission profiles hence is

$$\begin{aligned} \kappa_{\text{net}}^L(\nu_{qp}) &= \frac{h\nu_{qp}}{c} [B(q \rightarrow p) n_z(q) - B(p \rightarrow q) n_z(p)] \\ &= \kappa^L(\nu_{qp}) \left[1 - \frac{g(q) n_z(p)}{g(p) n_z(q)} \right]. \end{aligned} \quad (6.20)$$

If upper and lower level are in local thermodynamic equilibrium (Sect. 8.2), the density ratio is given by the Boltzmann factor, and

$$\kappa_{\text{net}}^L(\nu_{qp}) = \kappa^L(\nu_{qp}) \left[1 - \exp \left(-\frac{h\nu_{qp}}{k_B T_e} \right) \right]. \quad (6.21)$$

The absorption coefficient divided by the density of the species in the lower level gives the cross-section for the absorption process:

$$\sigma(\nu) = \frac{\kappa(\nu)}{n_z(q)} = \frac{\kappa^L(\nu_{qp})}{n_z(q)} \mathcal{L}(\nu) = \sigma^L(\nu_{qp}) \mathcal{L}(\nu), \quad (6.22)$$

with the units $[\sigma(\nu)] = \text{m}^2$ and $[\sigma^L(\nu_{qp})] = \text{m}^2 \text{Hz}$, respectively.

An immediate idea on the strength of a transition is conveyed by another quantity, the *oscillator strength*, or more precisely the *absorption oscillator strength*. It is also simply called the *f-value*. It is derived by comparison with the classical description of the absorption process; it is dimensionless and represents the fraction of one classical oscillator (electron) actually effective in the absorption process.

$$B(q \rightarrow p) = \frac{e^2}{4\epsilon_0 m_e} \frac{1}{h\nu_{qp}} f(q \rightarrow p). \quad (6.23)$$

With the classical electron radius

$$r_e = \frac{1}{4\pi\epsilon_0} \frac{e^2}{m_e c^2} = 2.81794 \times 10^{-15} \text{ m}, \quad (6.24)$$

one arrives at

$$\begin{aligned} \kappa^L(\nu_{qp}) &= \pi c r_e f(q \rightarrow p) n_z(q), \\ \kappa^L(\omega_{qp}) &= 2\pi^2 c r_e f(q \rightarrow p) n_z(q), \\ \kappa^L(\lambda_{qp}) &= \pi \lambda_{qp}^2 r_e f(q \rightarrow p) n_z(q), \end{aligned} \quad (6.25)$$

and, for example,

$$\sigma^L(\nu_{qp}) = 2.654 \times 10^{-6} f(q \rightarrow p) \text{ m}^2 \text{ Hz}. \quad (6.26)$$

The emission oscillator strength $f(p \rightarrow q)$ is defined by

$$gf = g(q) f(q \rightarrow p) = -g(p) f(p \rightarrow q), \quad (6.27)$$

but it is rarely used. Some data compilations simply give the quantity gf . Combining (6.11) and (6.23) results in the relation

$$\begin{aligned} f = f(q \rightarrow p) &= \frac{1}{8\pi^2 c r_e} \frac{g(p)}{g(q)} \lambda_{pq}^2 A(p \rightarrow q) \\ &= 1.4992 \times 10^{-14} \frac{g(p)}{g(q)} \left(\frac{\lambda_{pq}}{\text{nm}} \right)^2 \frac{A(p \rightarrow q)}{\text{s}^{-1}}. \end{aligned} \quad (6.28)$$

By its definition, f should be smaller than one, approaches one for the strongest resonance transitions and for a system with a single optical electron above a closed shell in its ground-state (g) a sum rule holds:

$$\sum_p f(g \rightarrow p) = 1. \quad (6.29)$$

An important f -sum rule for all radiative transitions from one level (q) is known as Thomas–Reiche–Kuhn sum rule,

$$\sum_{p>q} f(q \rightarrow p) + \sum_{r<q} f(q \rightarrow r) = N, \quad (6.30)$$

where N equals the number of electrons involved in the transitions. The sum of the absorption oscillator strengths has to include transitions into the continuum, and the downward transitions are negative. Detailed discussions and further sum rules are found in [8, 211].

In theoretical calculations usually the *line strength* S is preferred, which is symmetric in both directions. It is the square of the transition matrix element of the multipole operator $\mathsf{T}^{(k)}$ of order k [214, 215]:

$$S(q, p) = S(q \rightarrow p) = S(p \rightarrow q) = |\langle \Psi_q | \mathsf{T}^{(k)} | \Psi_p \rangle|^2, \quad (6.31)$$

where Ψ_q and Ψ_p are the initial-state and final-state wave functions of levels (q) and (p) .

Two types of radiative transitions occur, electric and magnetic multipole transitions, ($\mathsf{Q}^{(k)}$ and $\mathsf{M}^{(k)}$ are the operators, respectively), although in neutral atoms only electric dipole transitions (operator $\mathsf{Q}^{(1)} = e\mathbf{r}$) are strong and observable. They are called, therefore, *allowed* transitions. In addition to the other electric and magnetic multipole transitions also *intercombination* transitions (transitions between states of different multiplicity) are weak or even forbidden. These statements do not hold for heavy high-Z atoms because of breakdown of LS-coupling and for highly ionized atoms, see Sect. 6.2.3.

Line strengths are usually quoted in atomic units, which are given in Table 6.1 for three transitions. a_0 is the Bohr radius and μ_B is the Bohr magneton.

The oscillator strengths are:

$$\text{E1 : } g(q)f(q \rightarrow p) = 3.0376 \times 10^1 \frac{S(p, q)/(a_0 e)^2}{\lambda_{pq}/\text{nm}}, \quad (6.32)$$

$$\text{M1 : } g(q)f(q \rightarrow p) = 4.044 \times 10^{-4} \frac{S(p, q)/(\mu_B)^2}{\lambda_{pq}/\text{nm}}, \quad (6.33)$$

$$\text{E2 : } g(q)f(q \rightarrow p) = 2.518 \times 10^{-1} \frac{S(p, q)/(a_0 e)^4}{(\lambda_{pq}/\text{nm})^3}. \quad (6.34)$$

For all transitions conservation laws lead to specific selection rules for the total angular momentum J and for the angular of momentum L , Table 6.2. The rules for L are strictly valid only in the *LS* coupling scheme of atoms and ions.

Table 6.1. Atomic units of line strengths

Transition	Designation	Atomic unit
Electric dipole transition	E1	$(a_0 e)^2 = 7.1882 \times 10^{-59} \text{ m}^2 \text{C}^2$
Magnetic dipole transition	M1	$\mu_B^2 = 8.6007 \times 10^{-47} \text{ J}^2 \text{T}^{-2}$
Electric quadrupole transition	E2	$(a_0 e)^4 = 5.1671 \times 10^{-117} \text{ m}^4 \text{C}^4$

Table 6.2. Selection rules [210, 211]

E1	$\Delta L = 0, \pm 1$	$\Delta S = 0$	$\Delta J = 0, \pm 1$	$0 \rightarrow 0$	forbidden for L and J
M1	$\Delta L = 0$	$\Delta S = 0$	$\Delta J = 0, \pm 1$	$0 \rightarrow 0$	forbidden for L and J
E2	$\Delta L = 0, \pm 2$	$\Delta S = 0$	$\Delta J = 0, \pm 1 \pm 2$	$0 \rightarrow 0$	forbidden for L and J
				$\frac{1}{2} \rightarrow \frac{1}{2}$	forbidden for J
				$0 \rightarrow 1$	forbidden for L and J

Line strengths S and hence transition probabilities A are atomic properties (6.31) but may certainly change if the strong electromagnetic field of a high-density plasma starts to modify the wave function Ψ_p of the upper level (p) [217]. In general, this occurs at rather high plasma densities with the exception of forbidden components of a line, where mixing of the wave functions leads to a change of A even at low densities, p. 169. A related high-density effect is the lowering of the free-bound continuum, Chap. 8.

Apparent changes of transition probabilities were reported in a series of studies of the ratio of lines from the same upper level emitted from laser-produced plasmas [218]. The effect termed “quenching of Einstein A coefficients” could, however, be attributed to density gradients and Stark broadening [217]. Measurements at similar plasma conditions employing emission from the homogeneous part of a well-diagnosed pinch plasma [219] confirmed that the claimed effect does not exist, at least at the densities reported.

6.2.2 Emission by Molecules

In low-temperature plasmas and close to the walls of fusion devices neutral molecules and molecular ions are present. Because of their complex structure – states due to electronic excitation as well as the ground state are split into vibrational levels, and these again into rotational ones – molecular spectra are rich in lines. Each level (p) is specified by its electronic state (quantum numbers α), vibrational and rotational quantum numbers v and J , respectively.

The spectrum in the visible and ultraviolet regions corresponds essentially to electronic transitions accompanied also by a change of vibrational and molecular energies. As a consequence the electronic spectra show up as electronic-vibrational *bands* which, for each pair of vibrational levels, consist of rotational lines from different rotational branches (P-, Q-, and R-branch). Emission between rotational levels of the same vibrational and electronic state is typically in the microwave region, between vibrational levels in the infra-red.

In principle, all general considerations of Chap. 5 are also valid for single molecular transitions. Transition probabilities, oscillator, and line strengths are defined identically to those of atoms (6.28), (6.31), (6.32). Electric dipole

transitions are dominating; the dipole operator is now a function of the electronic and nuclear coordinates, and the wave functions of the levels (p) and (q), neglecting electron and nuclear spin, are factorized into electronic, vibrational, and rotational functions. Accordingly, the line strength is the product of three factors: an electronic part given by the coupling of the two electronic states $|R_e(\alpha', \alpha'')|^2$, where R_e is the electronic transition matrix element, a factor known as Franck–Condon factor $q(v', v'')$ depending on the spatial overlap of vibrational wave functions, and the Hönl–London factor $S(\mathcal{J}', \mathcal{J}'')$, which determines the relative strength within a band.

In molecular spectroscopy it is customary to mark the quantum numbers of the upper level with one prime, those of the lower level with two primes. For a diatomic molecule, the line strength for the transition between two levels (p) and (q) with the rotational quantum numbers \mathcal{J}' and \mathcal{J}'' hence is written [10]

$$\begin{aligned} S(p, q) &= S(\alpha'v'\mathcal{J}', \alpha''v''\mathcal{J}'') \\ &= |R_e(\alpha', \alpha'')|^2 q(v', v'') S(\mathcal{J}', \mathcal{J}''). \end{aligned} \quad (6.35)$$

The Franck–Condon factors give the relative band strength and are normalized to

$$\sum_{v'} q(v', v'') = 1. \quad (6.36)$$

The Hönl–London factors are normalized by

$$\sum_{\mathcal{J}'} S(\mathcal{J}', \mathcal{J}'') = g(2\mathcal{J}'' + 1), \quad (6.37)$$

where the electronic degeneracy g takes care of the multiplicity by the electron spin and Λ -doubling [10, 216]. Summation is over all g sublevels of a given \mathcal{J}'' and over all upper levels with which they can combine.

In some diagnostic applications and in the analysis of pertinent astronomical observations, very often the *band strength* is employed, which describes the sum of all transitions between two vibrational levels (α', v') and (α'', v'') of two electronic states α' and α'' . It is rather formally defined by

$$S(\alpha'v', \alpha''v'') = |R_e(\alpha', \alpha'')|^2 q(v', v''). \quad (6.38)$$

One has to keep in mind, however, that the correct emission coefficient (6.5) of a band is obtained by summation over all rotational components, i.e., by

$$\varepsilon(\alpha'v' \rightarrow \alpha''v'') = \frac{1}{4\pi} \sum_{\mathcal{J}'} [h\nu_{\alpha'v'\mathcal{J}', \alpha''v''\mathcal{J}''} A(\alpha'v'\mathcal{J}' \rightarrow \alpha''v''\mathcal{J}'') n(\alpha'v'\mathcal{J}')], \quad (6.39)$$

where $n(\alpha'v'\mathcal{J}')$ are the population densities in the upper rotational levels. With the total population density in the upper vibrational state $(\alpha'v')$ given by

$$n(\alpha'v') = \sum_{\mathcal{J}'} n(\alpha'v'\mathcal{J}'), \quad (6.40)$$

the emission coefficient of a band can be written in a form

$$\varepsilon(\alpha'v' \rightarrow \alpha''v'') \simeq \frac{h\bar{\nu}}{4\pi} A(\alpha'v' \rightarrow \alpha''v'') n(\alpha'v') \quad (6.41)$$

only with the following approximations: a properly weighted mean frequency $\bar{\nu}$ (wavelength respectively) has to be introduced enabling the summation of the rotational lines since in addition to ν in (6.39) an even stronger dependence $A(\alpha'v'\mathcal{J}' \rightarrow \alpha''v''\mathcal{J}'') \sim \nu^3 S(\alpha'v'\mathcal{J}', \alpha''v''\mathcal{J}'')$ across the band is seen, when combining (6.28) and (6.32). Furthermore, this weighting depends on the distribution of the population over the rotational levels, and hence $A(\alpha'v' \rightarrow \alpha''v'')$ is actually temperature-dependent through $\bar{\nu}$. Available data on transition probabilities may be found in [17] and [212].

6.2.3 Theoretical Considerations and Scaling Laws

The most extensive critical compilation of atomic transition probabilities including a bibliographic database is available at the website of the National Institute of Standards and Technology of the USA [13]. Theoretical transition probabilities obtained in various approximations are compared with each other, as are experimental values obtained by several methods. The comparison of both theory and experiment, where possible, allows a rather good assessment of the final uncertainty given for the listed data. Critical factors for this task are discussed, for example, in [220].

The typical experimental methods are:

- Measurement of radiometrically calibrated line emission from plasma sources, for which the population model (Chap. 8) has been well identified and self-absorption is excluded
- Life-time measurements by excitation of upper levels with tunable laser radiation and observation of the radiative decay
- Life-time measurements by excitation of fast ions in passing through thin foils and observing the emission along the path of the ions (beam foil technique)
- Life-time measurements of long-lived metastable levels by electron beam excitation in electron-beam ion-trap facilities

Transition probabilities partially without critical assessment are also collected and/or deposited in a number of data centers which are listed in Appendix B.1.

For the theoretical calculations of the line strengths (6.31) and hence of the transition probabilities the wave functions of upper and lower level must be known, and their uncertainties enter quadratically. For any atom or ion, with the exception of single electron hydrogen and hydrogen-like ions, the wave functions can be found only by approximation methods, since the mutual interaction between the atomic electrons leads to a mixing of wave functions for each state. In the most common approximation, each wave function is taken to be a linear combination of wave functions of this state and related

states of the same total angular momentum and spin quantum number and of the same parity. The mixing coefficients are obtained by variational methods, e.g., the Hartree–Fock self-consistent field approach or the Dirac Hartree–Fock method for highly ionized species, where relativistic effects become important [215]. Another approach uses a simple basis of hydrogen-like wave functions and treats the interaction and relativistic effects as perturbation in a $1/Z$ expansion, where Z is the nuclear charge [221, 222].

Scaling laws and regularities along isoelectronic sequences not only provide extremely useful information where data are missing, but also give insight into the changing emission characteristics. For hydrogenic species with one electron the solution of the Schrödinger equation yields analytic functions for the wave functions and hence direct scaling for the line strengths. We neglect the small influence of the reduced mass and give, for the sake of completeness, also the scaling for the transition energy ΔE , respectively the wavelength $\Delta\lambda_{\text{vac}}$:

$$(\Delta E)_Z = Z^2 (\Delta E)_H , \quad (6.42)$$

$$(\Delta\lambda_{\text{vac}})_Z = \frac{1}{Z^2} (\Delta\lambda_{\text{vac}})_H , \quad (6.43)$$

$$S_Z = \frac{1}{Z^2} S_H \quad (6.44)$$

$$f_Z = f_H , \quad (6.45)$$

$$A_Z = Z^4 A_H . \quad (6.46)$$

For nuclear charges $Z > 20$ relativistic corrections become noticeable.

Table 6.3 displays the data for the main lines of hydrogen in order to obtain an idea of typical magnitudes. n_p and n_q are the principal quantum number of upper and lower levels; wavelengths, transition probabilities, and oscillator strengths are averages weighted over the fine structure.

With increasing principal quantum number n_p the lifetime of the levels increases, an effect which is crucial when considering the population of highly excited levels (see Chap. 8). The corresponding total transition probability to all lower level becomes [7]

$$A_Z(n_p \rightarrow) \approx 1.6 \times 10^{10} \frac{Z^4}{n_p^{9/2}} . \quad (6.47)$$

Table 6.3. Hydrogen values [223]

Transition	$n_p \rightarrow n_q$	$\Delta\lambda$ nm	$A_H(n_p \rightarrow n_q) \text{ s}^{-1}$	$f(n_q \rightarrow n_p)$
L_α	$2 \rightarrow 1$	121.567	4.699×10^8	0.4161
L_β	$3 \rightarrow 1$	102.573	5.575×10^7	0.0791
L_γ	$4 \rightarrow 1$	97.254	1.278×10^7	0.0290
$H_\alpha(\text{air})$	$3 \rightarrow 2$	656.280	4.410×10^7	0.6407
$H_\beta(\text{air})$	$4 \rightarrow 2$	486.132	8.419×10^6	0.1193

Since high-lying levels become more and more hydrogenic even in multi-electron species, this relation is a good approximation in general. Averaging the hydrogenic oscillator strength over fine structure and magnetic sublevels results in the useful relation which is accurate for large n_p and n_q :

$$\bar{f}(n_q \rightarrow n_p) \approx \frac{32}{3\sqrt{3}\pi} \left(\frac{1}{n_q^2} - \frac{1}{n_p^2} \right)^{-3} \frac{1}{n_q^5} \frac{1}{n_p^3}. \quad (6.48)$$

\bar{f} decreases rapidly with increasing principal quantum numbers of both the upper and the lower state.

Systematic trends for allowed transitions along isoelectronic sequences in multi-electron species are indicated by conventional perturbation theory, when the oscillator strength for a fixed transition is expanded in a power series of the inverse nuclear charge Z of the ion [210, 225, 226]:

$$f = f_0 + f_1 Z^{-1} + f_2 Z^{-2} + \dots \quad (6.49)$$

For large Z the f -value approaches f_0 , which is the oscillator strength computed in the hydrogen approximation. Hence for transitions with a change of the principal quantum number, ($\Delta n \neq 0$), trends are in many cases according to the hydrogen scaling, (6.42)–(6.46). For ($\Delta n = 0$)–transitions, on the other hand, the hydrogen value is $f_0 = f_H = 0$, and the trend is given by the second term f_1 . One expects, therefore,

$$\lambda_Z \propto \frac{1}{Z}, \quad f_Z \propto \frac{1}{Z}, \quad A_Z \propto Z. \quad (6.50)$$

Deviations from the above trends are especially expected for low Z , where the expansion (6.49) is often not useful, and for very high Z , when relativistic effects play a role. Figure 6.3 shows the f -values for two resonance transitions of the lithium isoelectronic sequence. The data employed were taken from the NIST compilation [13]. The transition $2s \rightarrow 3p$ is an example of a deviation

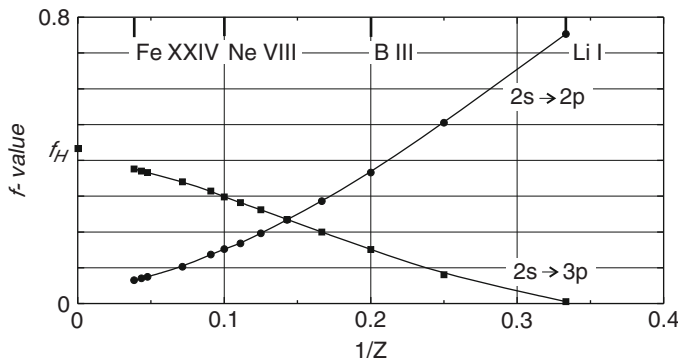


Fig. 6.3. Oscillator strength in the lithium isoelectronic sequence

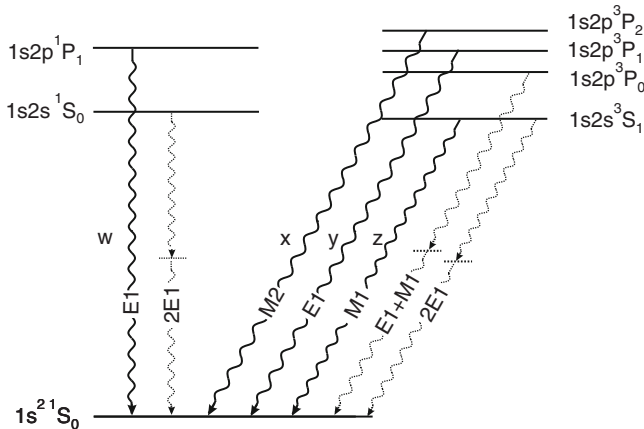


Fig. 6.4. Schematic energy level diagram (not to correct scale) of helium-like ions

from the expected scaling: it is due to severe cancellation in the transition integral. Nevertheless, the smoothness illustrates the usefulness of such graphs for finding unknown f -values simply by interpolation.

Transitions other than electric dipole transitions have usually extremely small transitions probabilities and are called *forbidden*. The upper level thus becomes metastable, if no other radiative decay route is possible. With increasing nuclear charge of atoms and ions this changes rapidly because of relativistic effects and increasing spin-orbit interaction that leads to a breakdown of LS-coupling and to mixing of wave functions. We illustrate such transitions in helium-like ions, since these ions are frequently employed in the diagnostics of hot plasmas, see p. 184 and p. 192. At low nuclear charge Z , the energy pattern splits into a singlet and a triplet term system, and Fig. 6.4 shows the relevant level diagram with the ground state and the $n = 2$ singly excited states in LS-notation, although one has to keep in mind that for very high charge jj -coupling would be more appropriate. The labels w, x, y, and z were introduced by Gabriel [227] for the transitions indicated in the figure, and they are now commonly adopted.

The *resonance transition* $1s2p\ 1P_1 \rightarrow 1s^2\ 1S_0$ is designated by (w) and its transition probability scales as $A_Z(2^1P_1 \rightarrow 1^1S_0) \propto Z^4$ according to (6.46).

The *intercombination line* $1s2p\ 3P_1 \rightarrow 1s^2\ 1S_0$ labeled (y) is not allowed in pure LS-coupling because of the change of the spin quantum number $\Delta S = 1$, but its transition probability increases rapidly with nuclear charge as pointed out above: $A_Z(2^3P_1 \rightarrow 1^1S_0) \propto Z^{10}$ for low Z , $A_Z(2^3P_1 \rightarrow 1^1S_0) \propto Z^8$ for large Z and $\propto Z^4$ for very large Z .

The *forbidden lines* $1s2p\ 3P_2 \rightarrow 1s^2\ 1S_0$ and $1s2s\ 3S_1 \rightarrow 1s^2\ 1S_0$ correspond to a magnetic quadrupole $M2$ and a magnetic dipole transition $M1$; they are labeled (x) and (z) and their transition probabilities scale as $A_Z(2^3P_2 \rightarrow 1^1S_0) \propto Z^8$ and $A_Z(2^3S_1 \rightarrow 1^1S_0) \propto Z^{10}$.

Table 6.4. Transition probabilities A_Z in helium-like ions in s^{-1} [229]

Transition	Label	He I	Ar XVII	Fe XXV	Kr XXXV
$1s2p\ ^1P_1 \rightarrow 1s^2\ ^1S_0$	w	1.80×10^9	1.07×10^{14}	4.57×10^{14}	1.51×10^{15}
$1s2p\ ^3P_1 \rightarrow 1s^2\ ^1S_0$	y	1.79×10^2	1.80×10^{12}	4.42×10^{13}	3.92×10^{14}
$1s2p\ ^3P_2 \rightarrow 1s^2\ ^1S_0$	x	3.27×10^{-1}	3.14×10^8	6.51×10^9	9.34×10^{10}
$1s2s\ ^3S_1 \rightarrow 1s^2\ ^1S_0$	z	1.27×10^{-4}	4.79×10^6	2.08×10^8	5.82×10^9

The $1s2s\ ^1S_0$ state can decay to the ground state only by a two-photon transition (2E1), the scaling being $A_Z(2\ ^1S_0 \rightarrow 1\ ^1S_0) \propto Z^6$. However, the magnitude of the transition probability remains low enough for all Z that this decay never plays a role for the population kinetics of the levels in laboratory plasmas. Such a two-photon decay channel exists also for the $2\ ^3S_1$ state, its probability scaling with Z^{10} ; its magnitude, however, is several orders lower than that of the single-photon M1 transition.

The two-photon (E1+M1) decay of the $1s2p\ ^3P_1$ level to the ground state is negligible for all Z . A discussion of all preceding transitions is given in [228], and relativistic calculations of the transition probabilities up to $Z=100$ are found in [229]. For illustration, transition probabilities are shown for some helium-like ions in Table 6.4.

Finally, magnetic dipole transitions between levels within the ground state of ions having configurations of the types $2s^22p^k$ and $3s^22p^k$ with $k = 1\dots 5$ are mentioned because of their relevance in diagnostic applications, see p. 181. The vast majority of the lines is in the convenient near ultraviolet to near infrared spectral region, and despite their very low transition probabilities, which are typically in the range $A_Z = 1\dots 1,000 \text{ s}^{-1}$, they are observable in hot plasmas of fusion devices (for example [230]) and in the solar corona due to the high densities in the ground state. The best-known examples are the green and red solar lines of Fe:

$$3s^23p\ ^2P_{3/2} \rightarrow 3s^23p\ ^2P_{1/2} \text{ in Fe XIV at } 530.286 \text{ nm, } A_Z = 59.4 \text{ s}^{-1} \text{ [231]}, \\ 3s^23p\ ^52P_{1/2} \rightarrow 3s^23p\ ^52P_{3/2} \text{ in Fe X at } 637.45 \text{ nm, } A_Z = 69.4 \text{ s}^{-1}.$$

A specific compilation of such lines up to molybdenum is found in [232]. The transition probabilities depend only on the quantum numbers L , S , and J of the initial and final state in the nonrelativistic LS -coupling scheme, but relativistic calculations taking into account configuration interaction are necessary in many cases, e.g., [233].

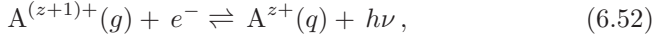
6.3 Continuum Radiation

6.3.1 Recombination Radiation and Photoionization

Capture of a free electron of energy E_{kin} into an excited level (q) of an ion results in the emission of a photon of energy $h\nu$ given by (see Fig. 6.2)

$$h\nu = E_{\text{kin}} + [E(\infty) - E(q)]. \quad (6.51)$$

It is obvious that due to the continuous energy distribution of the electrons also the emission spectrum is continuous but must show discontinuities according to the discrete atomic level structure. The inverse process is photoionization, and both are connected with each other by the principle of detailed balance, which is discussed in Chap. 8. Both processes are written symbolically



where A^{z+} represents an ion of charge (z) and (g) its ground state. Hence, the standard approach is to calculate the cross-section for recombination from that for photoionization. The cross-section for excitation (absorption) between discrete states can be written as (by combining (6.17), (6.22), and (6.25)):

$$\sigma^L(\nu_{qp}) = \frac{h\nu_{qp}}{c} B(q \rightarrow p) = \pi c r_e f(q \rightarrow p); \quad \text{with } [\sigma^L(\nu_{qp})] = \text{m}^2 \text{Hz}. \quad (6.53)$$

For photoionization the upper states (p_{con}) are in the continuum, and for calculation of the transition matrix elements (6.31) the wave functions of the free electrons in an energy interval $dE_{\text{kin}} = h\nu$ have to be taken. Introducing the differential or continuous oscillator strength $df(q \rightarrow p_{\text{con}})/d\nu$ for the bound-free transitions, the equivalent to (6.53) becomes [234]

$$\sigma(q \rightarrow p_{\text{con}}) = \pi c r_e \frac{df(q \rightarrow p_{\text{con}})}{d\nu}; \quad \text{with } [\sigma(q \rightarrow p_{\text{con}})] = \text{m}^2. \quad (6.54)$$

These cross-sections must connect continuously across the ionization limit with the discrete cross-sections of the bound-bound transitions. This is clearly exemplified in [215].

For hydrogenic ions already an early semiclassical calculation by Kramers yielded rather reasonable results. He considered the transition from a lower elliptical orbit to an upper hyperbolic orbit of the free electron and invoked the correspondence principle [235]. The cross-section, averaged over the angular momentum states l belonging to one principal quantum number n_q of the initial level, is now known as Kramers cross-section and is simply given by

$$\sigma^{Kr}(n_q \rightarrow E_{\text{kin}}) = \frac{64\alpha}{3\sqrt{3}} \frac{Z^4}{n_q^5} \left(\frac{E_R}{h\nu} \right)^3 \pi a_0^2 \quad \text{with } \nu \geq \nu_{n_q\infty}, \quad (6.55)$$

where $\nu_{n_q\infty}$ is the sharp threshold frequency for ionization given by the ionization energy of that level, $h\nu_{n_q\infty} = E(\infty) - E(n_q)$, and ν is given by (6.51). α is the fine structure constant, a_0 is the first Bohr radius, and πa_0^2 is the unit of atomic cross-sections; its magnitude is

$$\pi a_0^2 = 8.7974 \times 10^{-21} \text{ m}^2. \quad (6.56)$$

The energy E_R is the Rydberg energy, i.e., the ionization energy of the hydrogen atom for infinite nuclear mass m_N ,

$$E_R = \frac{m_e e^4}{8 \epsilon_0^2 h} = \frac{hc}{4\pi} \frac{\alpha}{a_0} = 13.606 \text{ eV}. \quad (6.57)$$

The correct ionization energy E_H of the hydrogen atom is obtained by replacing the electron mass m_e with its reduced mass ($m_e m_N / (m_e + m_N)$); however, as the difference is very small, the distinction between E_R and E_H is usually ignored.

It is common to describe the quantum-mechanically calculated accurate cross-section as the product of Kramers cross-section and a correction factor $G_{n_q}^{\text{bf}}(\nu)$ known as bound-free Gaunt factor:

$$\sigma(n_q \rightarrow E_{\text{kin}}) = \sigma^{Kr}(n_q \rightarrow E_{\text{kin}}) G_{n_q}^{\text{bf}}(\nu). \quad (6.58)$$

With the pertinent Gaunt factor $G_{n_q l}^{\text{bf}}(\nu)$ the cross-section for sublevels $n_q l$ is obtained by

$$\sigma(n_q l \rightarrow E_{\text{kin}}) = \sigma^{Kr}(n_q \rightarrow E_{\text{kin}}) G_{n_q l}^{\text{bf}}(\nu). \quad (6.59)$$

Tables of the Gaunt factor are given by [236]. With population densities according to the statistical weight of the sublevels the l -averaged cross-section is obtained by

$$\sigma(n_q \rightarrow E_{\text{kin}}) = \frac{1}{n_q^2} \sum_l (2l+1) \sigma(n_q l \rightarrow E_{\text{kin}}). \quad (6.60)$$

Kramers cross-section suggests a dependence with $\sigma \propto 1/\nu^3$ above the ionization limit for each n_q . The true dependence, however, may scale between $1/\nu^{8/3}$ and $1/\nu^{7/2}$ [224]. The maximum cross-section at each ionization threshold $\nu_{n_q \infty}$ is given by

$$\sigma^{Kr}(n_q \rightarrow E_{\text{kin}} = 0) = 0.090 \frac{n_q}{Z^2} \pi a_0^2, \quad (6.61)$$

bearing in mind, as mentioned earlier, that it connects continuously with the bound-bound excitation cross-section. Scaling of cross-sections is as

$$Z^2 \sigma\left(\frac{\nu}{Z^2}\right) \approx \text{const.} \quad (6.62)$$

Two- and more-electron systems require detailed calculations which are reported in the literature, see for example [211, 237–239]. In these atoms/ions, the cross-sections of low-lying levels may deviate strongly from the hydrogenic values but as high-lying excited levels become more and more hydrogenic, Kramers cross-section tends to become a good approximation as even the Gaunt factors are close to one.

In plasmas of high density, one certainly must take into account the lowering of the ionization energy, p. 137, and the downshift of the ionization threshold due to merging of spectral lines from line broadening, p. 151; details are found in Chap. 5.5 of [8]. For the sake of completeness, we also mention

that at high photon energies innershell-ionization will occur for many-electron atoms.

The Milne relation connects the cross-sections of radiative recombination and photoionization, (p. 137). For recombination of an ion of charge $(z+1)$ in its ground state (g) with an electron of energy E_{kin} into the level (q) of the ion with charge (z) it is written

$$\sigma_{z+1}(E_{\text{kin}} \rightarrow q) = \frac{g_z(q)}{g_{z+1}(g)} \frac{1}{2m_e c^2} \frac{(h\nu)^2}{E_{\text{kin}}} \sigma_z(q \rightarrow E_{\text{kin}}). \quad (6.63)$$

$g_{z+1}(g)$ and $g_z(q)$ are the statistical weights of the levels. The number of recombination events into the level (q) per unit time in the unit volume by free electrons in the energy interval E_{kin} to $E_{\text{kin}} + \Delta E_{\text{kin}}$ is given by

$$\Delta \frac{dn_z(q)}{dt} = n_{z+1}(g) n_e f_e(E_{\text{kin}}) \Delta E_{\text{kin}} v \sigma_{z+1}(E_{\text{kin}} \rightarrow q), \quad (6.64)$$

where $f_e(E_{\text{kin}})$ is the energy distribution function of the plasma electrons and $v = \sqrt{2E_{\text{kin}}/m_e}$ is their velocity in the above energy interval. The corresponding emission coefficient thus follows:

$$\begin{aligned} \varepsilon_{\nu}^{\text{fb}}(\nu) \Delta \nu &= \frac{h\nu}{4\pi} \Delta \left(\frac{dn_z(q)}{dt} \right) \\ &= \frac{h\nu}{4\pi} n_{z+1}(g) n_e f_e(E_{\text{kin}}) \Delta E_{\text{kin}} v \sigma_{z+1}(E_{\text{kin}} \rightarrow q), \end{aligned} \quad (6.65)$$

with ν determined by E_{kin} through (6.51) and $h \Delta \nu = \Delta E_{\text{kin}}$. Since for a fixed frequency (ν) recombination into all levels $(q) \geq (q_{\min})$ with an ionization energy $E(\infty) - E(q) \leq h\nu$ will contribute, the spectral emission coefficient for recombination radiation becomes after substituting (6.63)

$$\varepsilon_{\nu}^{\text{fb}}(\nu) = \frac{h^4 \nu^3}{4\pi m_e c^2} n_{z+1}(g) n_e \sum_{q \geq q_{\min}} \frac{g_z(q)}{g_{z+1}(g)} \frac{f_e(E_{\text{kin}})}{\sqrt{2m_e E_{\text{kin}}}} \sigma_z(q \rightarrow E_{\text{kin}}), \quad (6.66)$$

with summation over all higher lying levels $(q) \geq (q_{\min})$ and E_{kin} determined for each level (q) again by (6.51).

Due to the high collision frequency among the electrons, the energy distribution is Maxwellian in most cases:

$$f_e(E_{\text{kin}}) dE_{\text{kin}} = \frac{2}{\sqrt{\pi}} \frac{E_{\text{kin}}^{1/2}}{(k_B T_e)^{3/2}} \exp\left(-\frac{E_{\text{kin}}}{k_B T_e}\right) dE_{\text{kin}} \quad \text{with} \quad (6.67)$$

$$\int_0^{\infty} f_e(E_{\text{kin}}) dE_{\text{kin}} = 1. \quad (6.68)$$

The spectral emission coefficient thus is

$$\begin{aligned}\varepsilon_{\nu}^{\text{fb}}(\nu) &= \frac{h^4 \nu^3}{(2\pi m_e)^{3/2} c^2} \frac{n_{z+1}(g) n_e}{(k_B T_e)^{3/2}} \exp\left(-\frac{h\nu}{k_B T_e}\right) \\ &\times \sum_{q \geq q_{min}} \frac{g_z(q)}{g_{z+1}(g)} \exp\left(\frac{E(\infty) - E(q)}{k_B T_e}\right) \sigma_z(q \rightarrow E_{\text{kin}}).\end{aligned}\quad (6.69)$$

In high-density plasmas the ionization energy $[E(\infty) - E(q)]$ of the levels (q) has to include any relevant lowering as mentioned earlier.

For recombination of bare nuclei ($z + 1 = Z$) into their hydrogenic ions (z) we substitute the ionization energy by

$$E(\infty) - E(q) = \frac{Z^2 E_R}{n_q^2} = h\nu_{n_q \infty} \quad (6.70)$$

and obtain for the spectral radiance with (6.55), (6.57), $g_z(n_q) = 2n_q^2$, $g_{z+1}(g) = 1$ and $n_{z+1}(g) = n_Z$

$$\begin{aligned}\varepsilon_{\nu}^{\text{fb}}(\nu) &= \frac{64\sqrt{\pi}(\alpha a_0)^3 E_R}{3\sqrt{3}} \times n_Z n_e Z^4 \left(\frac{E_R}{k_B T_e}\right)^{3/2} \exp\left(-\frac{h\nu}{k_B T_e}\right) \\ &\times \sum_{n_q \geq n_{qmin}} \frac{1}{n_q^3} \exp\left(\frac{Z^2 E_R}{n_q^2 k_B T_e}\right) G_{n_q}^{\text{bf}}(\nu).\end{aligned}\quad (6.71)$$

Griem [7] splits the sum over n_q into two parts: the first sum is done up to a principal quantum number n'_q above which adjacent levels are so close that they may be approximated by a continuum. Hence, the second sum starting at $(n'_q + 1)$ can be replaced by an integral.

In wavelength units the spectral radiance reads with $\varepsilon_{\lambda} = \varepsilon_{\nu} c / \lambda^2$

$$\begin{aligned}\varepsilon_{\lambda}^{\text{fb}}(\lambda) &= \frac{64\sqrt{\pi}c(\alpha a_0)^3 E_R}{3\sqrt{3}} \times n_Z n_e Z^4 \left(\frac{E_R}{k_B T_e}\right)^{3/2} \frac{1}{\lambda^2} \exp\left(-\frac{hc}{\lambda k_B T_e}\right) \\ &\times \sum_{n_q \geq n_{qmin}} \frac{1}{n_q^3} \exp\left(\frac{Z^2 E_R}{n_q^2 k_B T_e}\right) G_{n_q}^{\text{bf}}(\lambda).\end{aligned}\quad (6.72)$$

Figure 6.5 illustrates the recombination spectrum of an optically thin hydrogen plasma of $k_B T_e = 5$ eV with the Gaunt factors set to unity. The edge structure imposed by recombination into the different shells (n_q) is characteristic. Due to the $1/n_q^3$ factor, recombination into the ground state gives by far the strongest contribution. At short wavelengths (large ν) the exponential term $\exp(-h\nu/k_B T_e)$ determines the spectrum, at long wavelengths a $1/\lambda^2$ dependence emerges between the edges.

The total emission coefficient $\varepsilon^{\text{fb}}(\rightarrow n_q)$ due to recombination into levels of principal quantum number n_q is readily obtained by integrating (6.71) from

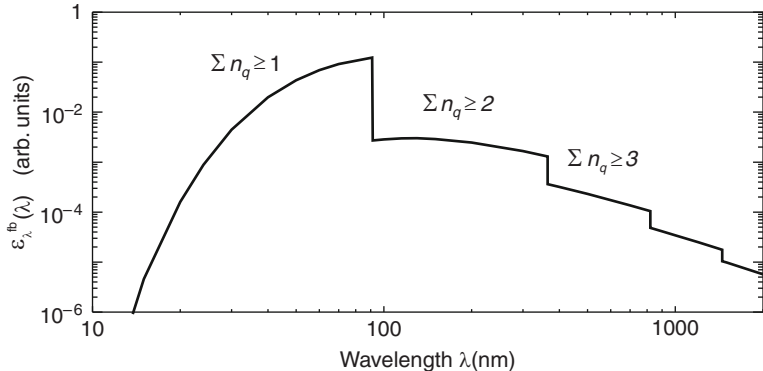


Fig. 6.5. Emission coefficient of radiative recombination of a hydrogen plasma of $k_B T_e = 5 \text{ eV}$

$\nu = Z^2 E_R / n_q^2 h$ to $\nu = \infty$ and the Gaunt factors set to unity:

$$\varepsilon^{\text{fb}}(\rightarrow n_q) \approx \frac{64\sqrt{\pi}(\alpha a_0)^3 E_R}{3\sqrt{3}} n_Z n_e Z^4 \left(\frac{E_R}{k_B T_e} \right)^{3/2} \frac{k_B T_e}{h} \frac{1}{n_q^3}. \quad (6.73)$$

Summation over all shells (n_q) leads to the Riemann zeta function

$$\sum_{n_q=1}^{\infty} \frac{1}{n_q^3} = \zeta(3) = 1.2020\dots \quad (6.74)$$

and thus to the total emission coefficient by recombination into all levels of a hydrogenic ion

$$\begin{aligned} \varepsilon^{\text{fb}} &= 1.2020 \varepsilon^{\text{fb}}(\rightarrow n_q = 1) \\ &\approx 1.2020 \frac{64\sqrt{\pi}(\alpha a_0)^3 E_R^2}{3\sqrt{3} h} n_Z n_e Z^4 \left(\frac{E_R}{k_B T_e} \right)^{1/2} \\ &\approx 1.08 \times 10^{-38} Z^4 \left(\frac{E_R}{k_B T_e} \right)^{1/2} \frac{n_Z}{\text{m}^{-3}} \frac{n_e}{\text{m}^{-3}} \frac{W}{\text{m}^3 \text{sr}}. \end{aligned} \quad (6.75)$$

Here again Z is the nuclear charge, (z) the charge of the ion, and $(z+1)$ corresponds to the Roman number spectroscopic symbol.

The emission decreases with $1/\sqrt{k_B T_e}$, and the fraction emitted by recombination into all levels $n_q \geq 2$ is only 20% of that emitted by recombination into the ground state. The correct emission coefficient for hydrogenic ions is finally obtained by adding a multiplicative Gaunt factor to (6.75).

The total intrinsic power loss per unit volume from a plasma of completely stripped ions by recombination into hydrogenic ions is obtained by integration over the solid angle

$$P^{\text{fb}} = 4\pi \varepsilon^{\text{fb}}. \quad (6.76)$$

With respect to the energy balance this leads to an electron energy loss constant by radiative recombination

$$\begin{aligned}
\Lambda_{\text{loss}}^{\text{fb}} &= -\frac{1}{\frac{3}{2} n_e k_B T_e} \frac{d(\frac{3}{2} n_e k_B T_e)}{dt} \\
&\approx \frac{4\pi \varepsilon^{\text{fb}}}{\frac{3}{2} n_e k_B T_e} \\
&\approx 4.15 \times 10^{-20} Z^4 \left(\frac{E_R}{k_B T_e} \right)^{3/2} \frac{n_Z}{\text{m}^{-3}} \text{s}^{-1}. \tag{6.77}
\end{aligned}$$

For a deuterium fusion plasma of $k_B T_e = 10 \text{ keV}$ and a density of $n_e = n_Z = 10^{20} \text{ m}^{-3}$ this gives a loss constant of $\Lambda_{\text{loss}}^{\text{fb}} \approx 2.08 \times 10^{-4} \text{ s}^{-1}$ corresponding to a loss time of $\tau_{\text{loss}}^{\text{fb}} = 1/\Lambda_{\text{loss}}^{\text{fb}} \approx 4.8 \times 10^3 \text{ s}$.

For all ions of charge state (z) other than hydrogen-like ones, in principle, specific calculations of the photoionization cross-sections for all levels are needed as pointed out already, and/or they have to be determined experimentally. Then one uses (6.69). However, in analogy to the Gaunt factor approach for hydrogenic ions it is customary to employ the semiclassical Kramers relation for recombination to hydrogenic ions and to multiply this emission coefficient with a factor $\xi^{\text{bf}}(z, T_e, \nu)$ or $\xi^{\text{bf}}(z, T_e, \lambda)$, which takes into account the atomic structure of the final ion and produces the correct emission coefficient with its discontinuities (edges). For frequencies smaller than the ionization energy, the sum of (6.72) may be replaced by an integral, and one obtains for recombination of an ion of charge (z) [8]

$$\begin{aligned}
\varepsilon_{\lambda}^{\text{fb}}(\lambda) &= \frac{32\sqrt{\pi} c (\alpha a_0)^3 E_R}{3\sqrt{3}} \times n_z(g) n_e z^2 \left(\frac{E_R}{k_B T_e} \right)^{1/2} \\
&\times \frac{1}{\lambda^2} \exp\left(1 - \frac{hc}{\lambda k_B T_e}\right) \xi^{\text{bf}}(z-1, T_e, \lambda), \tag{6.78}
\end{aligned}$$

which is valid for $h\nu \leq E_{z-1,\text{ion}}$, the ionization energy of the recombined ion. $\xi^{\text{bf}}(z-1, T_e, \lambda)$ is called Biberman factor. One has to keep in mind that certainly any shift of the series limit and a reduction of the ionization energy must be accounted for in $E_{z-1,\text{ion}}$. ξ^{bf} -factors for rare gas plasmas are given specifically, for example, in [240].

6.3.2 Bremsstrahlung

Deflection of electrons in the field of ions leads even in the classical picture to the emission of radiation, which corresponds quantum mechanically to transitions between continuum states (Fig. 6.1). The spectrum of all the free-free transitions in the plasma is continuous and the radiation is labeled *bremsstrahlung*.

For the derivation of the emission coefficient $\varepsilon_{\lambda}^{\text{ff}}(\lambda)$ we start with the recombination into hydrogenic ions of plasmas with a Maxwellian energy distribution. Following [7] and [27] we consider only the second part of the sum

over all levels in (6.72), where the separation of the levels is very close and the sum can be replaced by an integral. With $G_{n_q}^{\text{bf}}(\lambda) = 1$ one obtains

$$\begin{aligned} \sum_{n'_q+1}^{\infty} \frac{1}{n_q^3} \exp\left(\frac{Z^2 E_R}{n_q^2 k_B T_e}\right) &\Rightarrow \int_{n'_q+1}^{\infty} \frac{1}{n_q^3} \exp\left(\frac{Z^2 E_R}{n_q^2 k_B T_e}\right) dn_q \\ &= -\frac{k_B T_e}{2 Z^2 E_R} \int_{\frac{Z^2 E_R}{(n'_q+1)^2 k_B T_e}}^0 \exp(x) dx. \end{aligned} \quad (6.79)$$

Integration to the ionization limit ($n_q \rightarrow \infty$, respectively $x = 0$) gives recombination into bound states, and hence integration into the region $x < 0$ must correspond to transitions into free states with a total contribution

$$-\frac{k_B T_e}{2 Z^2 E_R} \int_0^{-\infty} \exp(x) dx = \frac{k_B T_e}{2 Z^2 E_R}. \quad (6.80)$$

Executing this integration from $x = 0$ thus gives all transitions between free states which is nothing else but bremsstrahlung.

Adding also a Gaunt factor G^{ff} to (6.72), the emission coefficient for bremsstrahlung in a fully ionized plasma of completely stripped ions of charge $z = Z$ thus is

$$\begin{aligned} \varepsilon_{\lambda}^{\text{ff}}(\lambda) &= \frac{32\sqrt{\pi} c (\alpha a_0)^3 E_R}{3\sqrt{3}} \times n_Z n_e Z^2 \left(\frac{E_R}{k_B T_e}\right)^{1/2} \\ &\times \frac{1}{\lambda^2} \exp\left(-\frac{hc}{\lambda k_B T_e}\right) G^{\text{ff}}(T_e, \lambda). \end{aligned} \quad (6.81)$$

Gaunt factors are found again in Karzas and Latter [236]. The numerical value of the pre-factor is

$$\frac{32\sqrt{\pi} c (\alpha a_0)^3 E_R}{3\sqrt{3}} = 4.108 \times 10^{-46} \text{ W m}^4 \text{ sr}^{-1}. \quad (6.82)$$

In analogy to the recombination radiation, (6.81) is slightly modified for ions of arbitrary charge z in the plasma by replacing the Gaunt factor by a corresponding Biberman ξ^{ff} -factor and n_Z by n_z , i.e., all ions in that ionization stage:

$$\begin{aligned} \varepsilon_{\lambda}^{\text{ff}}(\lambda) &= \frac{32\sqrt{\pi} c (\alpha a_0)^3 E_R}{3\sqrt{3}} \times n_z n_e z^2 \left(\frac{E_R}{k_B T_e}\right)^{1/2} \\ &\times \frac{1}{\lambda^2} \exp\left(-\frac{hc}{\lambda k_B T_e}\right) \xi^{\text{ff}}(z, T_e, \lambda). \end{aligned} \quad (6.83)$$

For employing continuum radiation in the diagnostics of plasmas it is important to realize that at short wavelengths practically only the exponential factor $\exp(-h\nu/k_B T_e)$ determines the shape of the spectrum as it does

for recombination radiation, and at long wavelengths it also scales with $1/\lambda^2$. The ratio of both emission coefficients from plasmas with completely stripped ions and the Gaunt factors set to 1 is

$$\frac{\varepsilon_{\lambda}^{\text{fb}}}{\varepsilon_{\lambda}^{\text{ff}}} = 2 \frac{E_{Z,\text{ion}}}{k_B T_e} \sum \frac{1}{n_q^3} \exp\left(\frac{E_{Z,\text{ion}}}{n_q^2 k_B T_e}\right), \quad (6.84)$$

with $E_{Z,\text{ion}} = Z^2 E_R$ being the ionization energy of the recombined hydrogen-like ion.

At long wavelengths ($h\nu \ll E_{Z,\text{ion}}$) only recombination into levels of high principal quantum numbers n_q contributes, and because of the $(1/n_q^3)$ -factor $\varepsilon_{\lambda}^{\text{fb}}$ can be neglected. At short wavelengths, on the other hand, recombination radiation definitely dominates for $k_B T_e < 3E_{Z,\text{ion}}$.

Integration over wavelength or frequency gives the total emission coefficient

$$\begin{aligned} \varepsilon^{\text{ff}} &= \frac{32\sqrt{\pi}(\alpha a_0)^3 E_R^2}{3\sqrt{3}h} n_Z n_e Z^2 \left(\frac{k_B T_e}{E_R}\right)^{1/2} \\ &= 4.51 \times 10^{-39} Z^2 \left(\frac{k_B T_e}{E_R}\right)^{1/2} \frac{n_Z}{\text{m}^{-3}} \frac{n_e}{\text{m}^{-3}} \frac{\text{W}}{\text{m}^3 \text{sr}}. \end{aligned} \quad (6.85)$$

The total power loss per unit volume is given in analogy to (6.76) by $P^{\text{ff}} = 4\pi \varepsilon^{\text{ff}}$, and the electron energy loss constant due to bremsstrahlung becomes ,

$$\Lambda_{\text{loss}}^{\text{ff}} \approx 1.73 \times 10^{-20} Z^2 \left(\frac{E_R}{k_B T_e}\right)^{1/2} \frac{n_Z}{\text{m}^{-3}} \text{s}^{-1}. \quad (6.86)$$

For the deuterium fusion plasma of p. 104 ($k_B T_e = 10 \text{ keV}$ and $n_e = n_Z = 10^{20} \text{ m}^{-3}$) the loss time now is $\tau_{\text{loss}}^{\text{ff}} \approx 15.6 \text{ s}$, i.e., losses by bremsstrahlung are much stronger.

Although the Gaunt factors are about unity, averaged Gaunt factors may be added to the hydrogenic approximations (6.75) and (6.85) for higher accuracy [8]. Biberman factors, which by many authors are simply also designated Gaunt factors, are added accordingly when these equations are used for ions of charge z .

In each plasma usually several ionization stages of a species (i) are present, and hot completely ionized hydrogen plasmas contain highly ionized impurities. Bremsstrahlung due to several ions is readily accounted for since the various contributions are additive. Equation (6.83) becomes

$$\begin{aligned} \varepsilon_{\lambda}^{\text{ff}}(\lambda) &= \frac{32\sqrt{\pi} c (\alpha a_0)^3 E_R}{3\sqrt{3}} \times n_e \left(\sum_{i,z} z_i^2 n_z^i \right) \left(\frac{E_R}{k_B T_e} \right)^{1/2} \\ &\times \frac{1}{\lambda^2} \exp\left(-\frac{hc}{\lambda k_B T_e}\right) \bar{\xi}^{\text{ff}}, \end{aligned} \quad (6.87)$$

where an averaged Biberman (Gaunt) factor has been added for completeness.

For fusion plasmas it is common to compare bremsstrahlung emission at long wavelengths, where recombination radiation is negligible, with that of a pure hydrogen plasma without impurities and to characterize the ratio by an effective charge z_{eff} :

$$\varepsilon_{\lambda}^{\text{ff}}(\lambda) = z_{\text{eff}} \varepsilon_{\lambda}^{\text{ff}}(\lambda)(H). \quad (6.88)$$

Substitution into (6.87) gives

$$z_{\text{eff}} = \frac{1}{n_e} \sum_{i,z} z_i^2 n_z^i = \frac{\sum_{i,z} z_i^2 n_z^i}{\sum_{i,z} z_i n_z^i}. \quad (6.89)$$

z_{eff} is some kind of mean charge, which is used as measure for the impurity contamination of such plasmas. $z_{\text{eff}} = 1$ thus describes the pure hydrogen plasma.

Bremsstrahlung has a maximum at a wavelength λ_{\max} which solely depends on the temperature. $d\varepsilon_{\lambda}^{\text{ff}}(\lambda)/d\lambda = 0$ yields the relation given by (6.1).

The absorption coefficient by the process of *inverse* bremsstrahlung is derived by considering a plasma in complete thermodynamic equilibrium. In this case, the source function defined as the ratio of emission and absorption coefficients (p. 12) is simply Planckian, i.e., it is identical to the spectral radiance of a blackbody:

$$\frac{\varepsilon_{\nu}^{\text{ff}}(\nu)}{\kappa_{\text{net}}^{\text{ff}}(\nu)} = S_{\nu}^{\text{ff}}(\nu) = L_{\nu}^B(\nu, T) = \frac{2h\nu^3}{c^2} \frac{1}{e^{(h\nu/k_B T)} - 1}. \quad (6.90)$$

Similar to the case of line radiation (6.21), the *net* absorption coefficient $\kappa_{\text{net}}^{\text{ff}}(\nu)$ has to be used which accounts for stimulated emission.

$$\kappa_{\text{net}}^{\text{ff}}(\nu) = \kappa^{\text{ff}}(\nu) \left[1 - e^{-(h\nu/k_B T_e)} \right]. \quad (6.91)$$

Combining (6.83), (6.90), and (6.91) leads to

$$\kappa^{\text{ff}}(\lambda) = \frac{1}{2hc^2} \frac{32\sqrt{\pi} c (\alpha a_0)^3 E_R}{3\sqrt{3}} \times n_e n_z z^2 \left(\frac{E_R}{k_B T_e} \right)^{1/2} \lambda^3 \xi^{\text{ff}}(z, T_e, \lambda), \quad (6.92)$$

or

$$\kappa^{\text{ff}}(\lambda) = 3.45 \times 10^{-57} \frac{n_e}{\text{m}^{-3}} \frac{n_z}{\text{m}^{-3}} z^2 \left(\frac{E_R}{k_B T_e} \right) \left(\frac{\lambda}{\text{nm}} \right)^3 \xi^{\text{ff}}(z, T_e, \lambda) \text{ m}^{-1}. \quad (6.93)$$

The absorption coefficient increases rapidly with wavelength and hence also the optical depth in plasmas. As a consequence, plasmas of not too low density will become blackbody radiators at long wavelengths (see Fig. 6.1).

Also at long wavelengths, plasma effects become noticeable first when the density increases. Obvious is the influence of the dielectric dispersion

as the frequency of the radiation approaches the plasma frequency $\nu_{pe} = \sqrt{e^2 n_e / 4\pi^2 \epsilon_0 m_e}$, [241]. The wavelength region to observe this is thus around λ_{pe} given by

$$\lambda_{pe}^2 n_e = \frac{\pi}{r_e}, \quad \text{or} \quad \left(\frac{\lambda_{pe}}{\mu\text{m}} \right)^2 \frac{n_e}{\text{m}^{-3}} = 1.115 \times 10^{27}. \quad (6.94)$$

The detailed behavior of the radiation in the vicinity of λ_{pe} depends on the effects of collisions in the dispersion function of the plasma. Further modifications by high-density effects are discussed in [8].

We now turn to bremsstrahlung from plasmas with non-Maxwellian and anisotropic velocity distributions. Examples are high-energy tails in ECR-discharges [242] and in tokamaks during radio-frequency heating [11], runaway electrons [243], energetic electron beams in laser-produced plasmas [244] and in micro-pinches [245]. Although the spectral emission coefficient can be calculated for known distributions and cross-sections in several approximations, the general inversion of the emission spectrum to derive the distribution function poses serious problems if the distribution is also anisotropic. For the case of a one-dimensional distribution of high energy yet non-relativistic electron beams an analytic solution has been given by [246].

At low temperatures, plasmas are usually weakly ionized and bremsstrahlung by electron–atom and electron–molecule collisions plays a role because of the low density of ions. The continua are typically in the visible and infra-red spectral regions. In contrast to the bremsstrahlung by electron–ion collisions, where the electron moves in the Coulomb field of the ions, the emission during an electron–neutral collision is sensitive to details of short-range interactions. The incoming electron polarizes the atomic system, and when it relaxes a photon is emitted. Hence, the emission depends strongly on the neutral species.

A short review of the subject can be found, for example, in [247]. If $\sigma^{\text{ffa}}(E_{\text{kin}}, h\nu)$ is the cross-section for the emission of a photon $h\nu$ by an incoming electron of energy E_{kin} , the spectral emission coefficient is given by

$$\varepsilon_{\nu}^{\text{ffa}}(\nu) = \frac{h\nu}{4\pi} n_e n_a \int_{h\nu}^{\infty} v \sigma^{\text{ffa}}(E_{\text{kin}}, h\nu) f_e(E_{\text{kin}}) dE_{\text{kin}}, \quad (6.95)$$

where n_a is the density of the neutral species. $\sigma^{\text{ffa}}(E_{\text{kin}}, h\nu)$ is related to the cross-section $\sigma_{ea}(E_{\text{kin}})$ of momentum transfer between the electron and the neutral species. For inert gases [248] suggests, for example,

$$\sigma^{\text{ffa}}(E_{\text{kin}}, h\nu) = \frac{8}{3\pi} \frac{\alpha}{m_e c^2} \left(1 - \frac{h\nu}{2E_{\text{kin}}} \right) \left(1 - \frac{h\nu}{E_{\text{kin}}} \right)^{1/2} E_{\text{kin}} \sigma_{ea}(E_{\text{kin}}). \quad (6.96)$$

Insertion into (6.95) allows thus to calculate the spectral emission coefficient numerically with given $\sigma_{ea}(E_{\text{kin}})$. Other authors [249] assume billiard ball-type collisions and employ

$$\sigma^{\text{ffa}}(E_{\text{kin}}, h\nu) = \sigma_{ea}(E_{\text{kin}}). \quad (6.97)$$

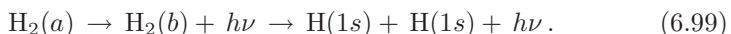
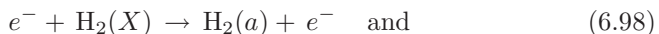
Choosing a constant average value $\sigma_{ea}(T_e)$ for the cross-section, (6.95) can be integrated. The most accurate calculations have been performed so far for the e^- -H collision in [250]. Large cross-sections, for example, exist for e^- -Hg collisions [251], an important emission process in high-pressure mercury lamps.

6.3.3 Negative Ion and Molecular Continua

A number of atoms and molecules can capture an electron to form a negative ion, usually with only a single bound state. This *attachment* process is identical to radiative recombination and results in the emission of a corresponding continuum with an edge. Hence, the spectral emission coefficient $\varepsilon_\nu^{\text{fb}}(\nu)$ can be derived in the same way as that for recombination of ions, Chap. 6.3.1. The photo-detachment cross-section $\sigma_-(g \rightarrow E_{\text{kin}})$ simply has to be inserted into (6.69), $n_{z+1}(g)$ becomes the density n_a of the neutral atoms, and $g_z(q)$ the statistical weight of the single level of the negative ion. g_{z+1} has to be replaced by the partition function of the atom. Attachment or binding energies of negative ions are found in [252].

Negative ions play a role in some laboratory and technical plasmas of rather low temperature, the emission due to H^- -ions also in solar and stellar plasmas. The attachment energy for the hydrogen atom is about 0.7542 eV, which fixes the edge of the emission at 1644 nm. It is common to refer to both attachment continuum and free-free continuum by electron hydrogen-atom collisions together as H^- -continuum. Both emission and absorption coefficients can be found in [7].

Continuous emission of molecular origin is emitted from discharges with excimer molecules and ions, from low-pressure arcs operated in hydrogen and deuterium (for example, deuterium lamps, p. 80), and was also identified in magnetic mirror confined plasmas during gas fueling with hydrogen [253]. We illustrate the typical emission process for the case of the hydrogen molecule. Figure 6.6 shows the potential curves for the ground state $X^1\Sigma_g^+$ and two excited states $a^3\Sigma_g^+$ and $b^3\Sigma_u^+$, the latter being repulsive. Data are from [254]. Electron collisions excite the molecule from vibrational levels of the singlet ground state X to levels of the triplet bound state a from which it can, however, radiatively decay only to the *unbound* excited state b , the transition to the ground state being spin forbidden: a photon is emitted and the molecule dissociates into two ground state atoms. The reactions are written as



Since the state b is unbound, a continuum of final molecular states exists and thus a bound-free continuum of photon energies, also known as *dissociative* continuum. A complete set of data for its calculation is presented in [255],

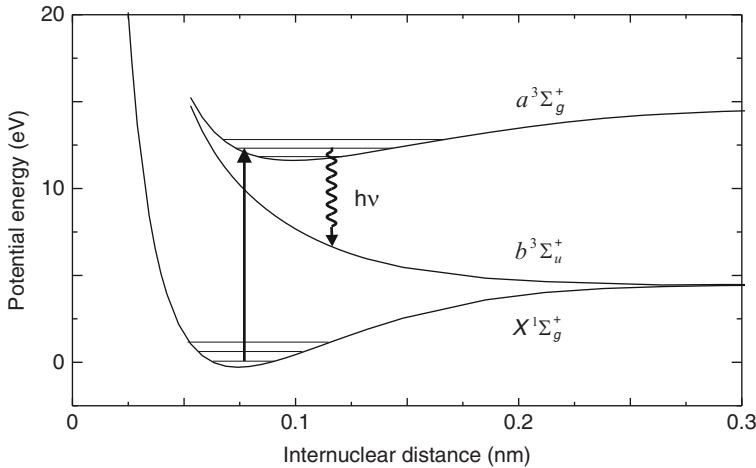
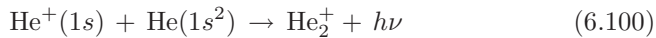


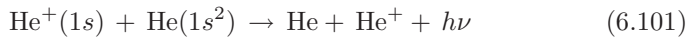
Fig. 6.6. Potential curves for the hydrogen molecule

together with continua for the spectral region 160–300 nm. Additional continuum branches via excitation of further electronic states (for example the $c^1\Pi_u$ state) are possible [256], and continuum emission is observable between 120–600 nm. For information on excimer radiation in high-pressure rare gas discharges one may consult [257].

In addition to the emission triggered by electron collisions also collisions with ions can lead to the emission of continua. In this context, [258] analyzes the processes of photo-association



and of radiative charge exchange



in low-temperature helium plasmas.

6.3.4 Rate Coefficients for Radiative Recombination

For modeling the kinetics of the population of atomic levels (see Chap. 8) of an ion of charge (z), the populating events per unit time into each level (q) must be known, and these rates $R_z^{\text{rr}}(\rightarrow q)$ for radiative recombination are obtained by integrating (6.64) over the energy distribution (respectively the velocity distribution) of the electrons:

$$\begin{aligned} R_z^{\text{rr}}(\rightarrow q) &= n_{z+1}(g) n_e \int_0^\infty \sigma_{z+1}(E_{\text{kin}} \rightarrow q; \nu) v f_e(E_{\text{kin}}) dE_{\text{kin}} \\ &= n_{z+1}(g) n_e \alpha_{z+1}^{\text{rr}}(\rightarrow q). \end{aligned} \quad (6.102)$$

$n_e \alpha_{z+1}^{\text{rr}}(\rightarrow q)$ represents the probability of such a process at the ion density $n_{z+1}(g)$. $\alpha_{z+1}^{\text{rr}}(\rightarrow q)$ is called rate coefficient for radiative recombination, and by the definition of the distribution function it is practically an average of $(v\sigma)$ over the velocity distribution. Since in most plasmas this function is Maxwellian, all rate coefficients are a function of the electron temperature T_e . Specific calculations are certainly necessary for non-Maxwellian plasmas.

The total rate coefficient for radiative recombination to an ion of charge (z) is simply given by the sum

$$\alpha_{z+1}^{\text{rr}} = \sum_q \alpha_{z+1}^{\text{rr}}(\rightarrow q). \quad (6.103)$$

Equation (6.65) connects recombination rates (6.102) and free-bound emission coefficient, and the rate coefficient becomes

$$\alpha_{z+1}^{\text{rr}}(\rightarrow q) = \int_{\nu_{q\infty}}^{\infty} \frac{4\pi \varepsilon_{\nu}^{\text{fb}}(\nu)}{h\nu} \frac{1}{n_{z+1}(g) n_e} d\nu. \quad (6.104)$$

Taking now only one term (n_q) of the sum of (6.71), one obtains for the recombination of a bare nucleus ($z + 1 = Z$) into a hydrogenic shell with the principal quantum number (n_q)

$$\begin{aligned} \alpha_{z+1}^{\text{rr}}(\rightarrow n_q) &= 4\pi \frac{64\sqrt{\pi}(\alpha a_0)^3 E_R}{3\sqrt{3}} \times Z^4 \left(\frac{E_R}{k_B T_e} \right)^{3/2} \frac{1}{n_q^3} \exp\left(\frac{Z^2 E_R}{n_q^2 k_B T_e}\right) \\ &\times \int_{\nu_{q\infty}}^{\infty} \frac{1}{h\nu} \exp\left(-\frac{h\nu}{k_B T_e}\right) G_{n_q}^{\text{bf}}(\nu) d\nu. \end{aligned} \quad (6.105)$$

We introduce a frequency-averaged Gaunt factor $\overline{G}_{n_q}^{\text{bf}}$ and integrate the equation:

$$\begin{aligned} \alpha_{z+1}^{\text{rr}}(\rightarrow n_q) &= \frac{4\pi}{h} \frac{64\sqrt{\pi}(\alpha a_0)^3 E_R}{3\sqrt{3}} \times Z^4 \left(\frac{E_R}{k_B T_e} \right)^{3/2} \frac{1}{n_q^3} \exp\left(\frac{Z^2 E_R}{n_q^2 k_B T_e}\right) \\ &\times E_1\left(\frac{Z^2 E_R}{n_q^2 k_B T_e}\right) \overline{G}_{n_q}^{\text{bf}}. \end{aligned} \quad (6.106)$$

$E_1(y)$ is the exponential integral of index 1 defined by

$$E_1(y) = + \int_y^{\infty} \frac{\exp(-x)}{x} dx. \quad (6.107)$$

The numerical value of the coefficient is

$$\frac{4\pi}{h} \frac{64\sqrt{\pi}(\alpha a_0)^3 E_R}{3\sqrt{3}} = 5.20 \times 10^{-20} \text{ m}^3 \text{s}^{-1}. \quad (6.108)$$

The dependence on the principal quantum number reveals, that radiative recombination is preferentially into the ground state, in contrast to three-body recombination, where recombination into high-lying levels dominates (see Chap. 7.3). The rate coefficient decreases with temperature, and for high temperatures we have [7]

$$\alpha_{z+1}^{\text{rr}}(\rightarrow n_q) \propto (k_B T_e)^{-3/2} \quad \text{for } k_B T_e \gg \frac{Z^2 E_R}{n_q^2}. \quad (6.109)$$

For low temperatures, where radiative recombination indeed plays a role, the exponential integral can be approximated by [7]

$$\int_y^\infty \frac{\exp(-x)}{x} \approx \frac{\exp(-y)}{y}. \quad (6.110)$$

and (6.106) becomes

$$\begin{aligned} \alpha_{z+1}^{\text{rr}}(\rightarrow n_q) &= 5.20 \times 10^{-20} \frac{Z^2}{n_q} \left(\frac{k_B T_e}{E_R} \right)^{-1/2} \overline{G}_{n_q}^{\text{bf}} \text{ m}^3 \text{s}^{-1} \\ \text{for } k_B T_e &\leq \frac{1}{5} \frac{Z^2 E_R}{n_q^2}. \end{aligned} \quad (6.111)$$

When introducing the ionization energy of each hydrogenic level into (6.106), the scaling law with temperature is evident:

$$\alpha_Z^{\text{rr}}(T_e) \approx Z \alpha_H^{\text{rr}} \left(\frac{T_e}{Z^2} \right). \quad (6.112)$$

Seaton [259] summed up the rate coefficients into all levels of the hydrogenic ions and expanded the Gaunt factor arriving at

$$\begin{aligned} \alpha_{z+1}^{\text{rr}}(T_e) &= 5.20 \times 10^{-20} Z \left(\frac{Z^2 E_R}{k_B T_e} \right)^{1/2} \\ &\times \left[0.4288 + \frac{1}{2} \ln \left(\frac{Z^2 E_R}{k_B T_e} \right) + 0.4638 \left(\frac{Z^2 E_R}{k_B T_e} \right)^{-1/3} \right] \text{ m}^3 \text{s}^{-1}, \end{aligned} \quad (6.113)$$

which should be in error by less than 3% for $k_B T_e / Z^2 \leq 100 \text{ eV}$.

Rate coefficients for *non-hydrogenic* ions are usually derived by applying the hydrogenic approximation to recombination into all excited levels but calculating recombination toward the ground state via the Milne relation from photoionization cross-sections (6.63). One certainly must account for the presence of other bound electrons with the same principal quantum number, which reduces the rate coefficient: according to [8] this is done by multiplying the rate coefficient with a factor $(1 - m/2n_q^2)$, where m is the number of bound electrons in the shell (n_q).

A number of specific calculations have been reported. Many have been fitted to two, three, and four parameter formulae (for example, see [260]). A rather extensive set of theoretical recombination data has become available only recently and is even accessible online [261].

Collisional Processes

7.1 Introductory Remarks

The population of atomic, molecular, and ionic levels is changed by collisions with electrons, atoms, ions, and molecules, the strength of each possible process being characterized by a respective cross-section σ . If we consider a beam of test particles of velocity v and density n_b impinging on a thin slab of target atomic species at rest of density $n_z(q)$ in the atomic state (q), the rate of transitions into a state (p) of the same or another ionization stage of the species is given by

$$R(q \rightarrow p) = \frac{dn_z(p)}{dt} \Big|_{q \rightarrow p} = \sigma(v)v n_b n_z(q) . \quad (7.1)$$

The cross-section is a function of the beam velocity, or more precisely of the relative velocity between beam and target particles; its unit is m^2 .

In a plasma particles display velocity distributions $f(\mathbf{v})$ and the rate for a process involving two species (1) and (2) is given by substituting $n_b = n_1 f_1(\mathbf{v}_1) d\mathbf{v}_1$, $n_z = n_2 f_2(\mathbf{v}_2) d\mathbf{v}_2$, $v = |\mathbf{v}| = |\mathbf{v}_1 - \mathbf{v}_2|$ into (7.1), and integrating over the velocity space:

$$R(q \rightarrow p) = \frac{dn_z(p)}{dt} \Big|_{q \rightarrow p} = n_1 n_2 \int_{\mathbf{v}_1, \mathbf{v}_2} \sigma(v) v f_1(\mathbf{v}_1) f_2(\mathbf{v}_2) d^3 \mathbf{v}_1 d^3 \mathbf{v}_2 . \quad (7.2)$$

The quantity

$$\langle \sigma v \rangle = \int_{\mathbf{v}_1, \mathbf{v}_2} \sigma(v) v f_1(\mathbf{v}_1) f_2(\mathbf{v}_2) d^3 \mathbf{v}_1 d^3 \mathbf{v}_2 \quad (7.3)$$

is called *rate coefficient* of the process; its unit is $\text{m}^3 \text{s}^{-1}$ for binary collisions. If both f_1 and f_2 are Maxwellian at a temperature T , integrals can be performed by changing variables to the center of mass system. In the case of electron collisions, the target species can be even considered stationary in practically all cases because of the high velocities of the electrons. The high velocity is also responsible, that usually electron collisions dominate.

7.2 Collisional Excitation and Deexcitation by Electron Impacts

In theoretical calculations of electron impact excitation very often the *collision strength* Ω is preferred instead of the cross-section σ . It is dimensionless and defined by

$$\Omega(q \rightarrow p; E_{\text{kin}}) = g(q) \frac{\sigma(q \rightarrow p; v)}{\pi a_0^2} \frac{E_{\text{kin}}}{E_R}. \quad (7.4)$$

E_{kin} is the relative kinetic energy of the incoming electron, v its relative velocity. E_R is again the Rydberg energy (6.57), and for the atomic unit of the cross-section πa_0^2 see (6.56). The advantage is that Ω is symmetric with respect to the direct and the inverse process (see later), and in regard to the atomic structure it is additive. $g(q)$ is the statistical weight of the lower level, i.e., $g(q) = (2S+1)(2L+1)$ for LS-coupling, or $g(q) = (2J+1)$ if fine structure is taken into account.

$$\Omega(q \rightarrow p; E_{\text{kin}1}) = \Omega(p \rightarrow q; E_{\text{kin}2}) \quad (7.5)$$

with $E_{\text{kin}2} = E_{\text{kin}1} - [E(p) - E(q)]$. In tabulations cross-sections or collision strengths very often are quoted as function of the kinetic energy in units of the threshold energy for excitation $E_{qp} = E(p) - E(q)$, i.e., as function of

$$u = \frac{E_{\text{kin}}}{E_{qp}}. \quad (7.6)$$

The cross-section thus is obtained from the collision strength by the relation

$$\sigma(q \rightarrow p; u) = \frac{1}{E_{qp}/E_R} \frac{\Omega(q \rightarrow p; u)}{g(q)} \frac{1}{u} \pi a_0^2. \quad (7.7)$$

For plasmas with a Maxwellian energy distribution of the electrons the rate coefficient for electron impact excitation may be written in terms of the collision strength after substituting (6.67) and (7.4) into (7.3)

$$\begin{aligned} X(q \rightarrow p; T_e) &= \langle \sigma v \rangle = \frac{2\alpha c \pi a_0^2}{\sqrt{\pi} g(q)} \left(\frac{E_R}{k_B T_e} \right)^{1/2} \\ &\times \int_{E_{qp}/k_B T_e}^{\infty} \Omega(q \rightarrow p) \exp\left(-\frac{E_{\text{kin}}}{k_B T_e}\right) d\left(\frac{E_{\text{kin}}}{k_B T_e}\right). \end{aligned} \quad (7.8)$$

Some authors give the integral in their tabulations and designate it by *effective collision strength* or *rate parameter* γ :

$$\gamma(q \rightarrow p; T_e) = \int_{E_{qp}/k_B T_e}^{\infty} \Omega(q \rightarrow p) \exp\left(-\frac{E_{\text{kin}}}{k_B T_e}\right) d\left(\frac{E_{\text{kin}}}{k_B T_e}\right). \quad (7.9)$$

The excitation rate coefficient thus is written as

$$X(q \rightarrow p; T_e) = 2.172 \times 10^{-14} \frac{1}{g(q)} \left(\frac{E_R}{k_B T_e} \right)^{1/2} \gamma(q \rightarrow p; T_e) \text{ m}^3 \text{s}^{-1}. \quad (7.10)$$

In cases of nearly constant collision strength, Ω may be replaced by an average collision strength $\bar{\Omega}$; the integral can then be readily evaluated and leads to

$$X(q \rightarrow p; T_e) = 2.172 \times 10^{-14} \frac{\bar{\Omega}}{g(q)} \left(\frac{E_R}{k_B T_e} \right)^{1/2} \exp\left(-\frac{E_{qp}}{k_B T_e}\right). \quad (7.11)$$

The corresponding deexcitation rate coefficients are obtained via the principle of detailed balance (p. 139):

$$X(p \rightarrow q; T_e) = X(q \rightarrow p; T_e) \frac{g(q)}{g(p)} \exp\left(\frac{E_{qp}}{k_B T_e}\right). \quad (7.12)$$

During the last decades the rapidly increasing availability of computing power stimulated, and still does, the calculation of electron impact excitation cross-sections for many atoms, ions, and molecules. In principle, the calculation of cross-sections is more difficult than that of radiative transition probabilities since the full Coulomb interaction between bound and free electrons must be considered. The problem cannot be solved exactly, and several approximations are successfully employed; for details see, for example, [222, 262–264]. A number of experimental studies have certainly been carried out and cross-sections have been determined, but by quantity they are behind theory. Nevertheless, where available they are crucial for checking the accuracy and reliability of the theoretical calculations and in this regard benchmarking experiments are indispensable in the future. Available cross-sections are found in several databases (see Appendix B.1), in [262], and are continuously published in the literature. Reviews for ions along isoelectronic sequences are reported in [265].

In the following, we briefly summarize the most important theoretical methods. The obtained accuracy depends on the representation used for the target wavefunctions and the type of scattering approximation chosen.

The simplest theoretical approach for neutral atoms is the first Born approximation, which considers the incident electron as a plane wave. This gives a cross-section $\sigma \rightarrow 0$ at the threshold energy $E_{\text{kin}} = E_{qp}$, and a maximum at about $E_{\text{kin}} = (2 - 3) E_{qp}$. In the case of positive ions, the effect of the long-range Coulomb field is so powerful that Coulomb waves have to be taken for the incident and scattered electron. The approach is known as Coulomb–Born approximation and gives a finite cross-section at threshold, which is even maximum there. This is illustrated in Fig. 7.1 which shows the cross-sections for excitation $1s \rightarrow 2p$ in hydrogen (H I) and hydrogenic argon (Ar XVIII). The Born approximation gives the main dependencies of the cross-sections on atomic constants [222].

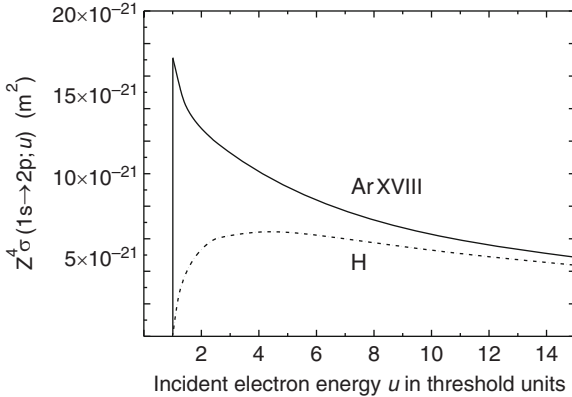


Fig. 7.1. Cross-sections for excitation $1s \rightarrow 2p$ in hydrogen obtained with the plane wave Born exchange approximation [266] and for hydrogenic argon calculated in the distorted wave approximation employing the LANL physics codes [267]

The Bethe approximation holds for high electron energies; collisions with large impact parameters dominate and the colliding electron remains outside the atom most of the time. The asymptotic formula for allowed (dipole) transitions ($\Delta L = \pm 1, \Delta S = 0$) is

$$\sigma(q \rightarrow p; u) = 4 \left(\frac{E_R}{E_{qp}} \right)^2 f(q \rightarrow p) \frac{\ln(bu)}{u} \pi a_0^2 \quad \text{for } u \gg 1, \quad (7.13)$$

where b is a numerical parameter of the order of unity.

The corresponding Bethe limit for optically forbidden electric monopole and quadrupole transitions is

$$\sigma(q \rightarrow p; u) = 4 \left(\frac{E_R}{E_{qp}} \right)^2 b' \frac{1}{u} \pi a_0^2 \quad \text{for } u \gg 1. \quad (7.14)$$

For intercombination transitions ($\Delta S = 1$), which can occur only by electron exchange [268], one obtains for high electron energies

$$\sigma(q \rightarrow p; u) = 4 \left(\frac{E_R}{E_{qp}} \right)^2 b'' \frac{1}{u^3} \pi a_0^2 \quad \text{for } u \gg 1. \quad (7.15)$$

b' and b'' are again numerical constants. The dependence of the cross-sections on the energy is thus characteristic for the type of transition and can be used in the spectroscopic diagnostics.

Seaton [269] introduced the Gaunt factor $G(u)$ in his calculations and arrived at a cross-section formula similar to (7.13) valid for allowed dipole transitions. This was put to practical use by Van Regemorter [270], who analyzed all experimental and theoretical data known at that time and replaced

$G(u)$ by an effective empirical Gaunt factor $\overline{G}(u)$ now also simply called *g-bar-factor*, yielding

$$\sigma(q \rightarrow p; u) = \frac{8\pi}{\sqrt{3}} \left(\frac{E_R}{E_{qp}} \right)^2 f(q \rightarrow p) \frac{1}{u} \overline{G}(u) \pi a_0^2. \quad (7.16)$$

This semiempirical formula is commonly referred to as Seaton's and Van Regemorter's \overline{G} or effective Gaunt factor approximation and, because of its simplicity, it is the most widely employed formula if no specific calculations or experimental measurements are available. Where such data exist they definitely should be preferred. One must keep in mind, that the above approximation *can not* be applied to other than allowed dipole transitions.

Fisher et al. [274] analyzed experimentally studied transitions in atoms with *LS*-coupling scheme and suggest an effective Gaunt factor

$$\overline{G}(u) = \left(0.33 - 0.3 \frac{1}{u} + 0.08 \frac{1}{u^2} \right) \ln u \quad (7.17)$$

for $\Delta n = 0$ transitions, and

$$\overline{G}(u) = \left(0.276 - 0.18 \frac{1}{u} \right) \ln u \quad (7.18)$$

for $\Delta n > 0$ transitions.

For ions first tabulations of $\overline{G}(u)$ quoted threshold values $\overline{G}(1) = 0.2$ [271]. However, numerous advanced calculations and experiments revealed soon that this is wrong especially for $\Delta n = 0$ excitations, for which threshold values are typically in the range $\overline{G}(1) = 0.6 - 1.0$ [272]. Hence this reference should be consulted, see also [273].

Rate coefficients $X(q \rightarrow p)$ are obtained in this approximation by substituting (7.16) into (7.7) and that equation into (7.8). With the introduction of an averaged Gaunt factor

$$P\left(\frac{E_{qp}}{k_B T_e}\right) = \frac{\int_{E_{qp}/k_B T_e}^{\infty} \overline{G}\left(\frac{E_{kin}}{E_{qp}}\right) \exp\left(-\frac{E_{kin}}{k_B T_e}\right) d\left(\frac{E_{kin}}{k_B T_e}\right)}{\int_{E_{qp}/k_B T_e}^{\infty} \exp\left(-\frac{E_{kin}}{k_B T_e}\right) d\left(\frac{E_{kin}}{k_B T_e}\right)}, \quad (7.19)$$

the rate coefficients for allowed transitions in the effective Gaunt factor approximation thus may be written

$$X(q \rightarrow p; T_e) = 16 \sqrt{\frac{\pi}{3}} \alpha c \pi a_0^2 f(q \rightarrow p) \left(\frac{E_R}{E_{qp}} \right) \\ \times \left(\frac{E_R}{k_B T_e} \right)^{1/2} \exp\left(-\frac{E_{qp}}{k_B T_e}\right) P\left(\frac{E_{qp}}{k_B T_e}\right), \quad (7.20)$$

with the constant factor

$$16\sqrt{\frac{\pi}{3}} \alpha c \pi a_0^2 = 3.15 \times 10^{-13} \text{ m}^3 \text{s}^{-1}. \quad (7.21)$$

Values for $P(E_{qp}/k_B T_e)$ from the original publication [270] are also cited in [262, 271]. Mewe [268] analyzed four isoelectronic sequences and gave improved values for both \bar{G} and P employing a four-parameter formula.

Early the Born and Coulomb–Born approximations have been used extensively. Exchange is included in the so-called Coulomb–Born–Oppenheimer approximation. The most widely employed approaches are now the Distorted Wave and the Close-Coupling approximation. The first one considers more accurate wavefunctions for the incident and scattered electrons and is thought to be accurate to about 25%. In the more elaborate close-coupling approximation the scattering electron sees individual target electrons, the channels are coupled and a set of integro-differential equations is solved. A widely used variant employs the R-matrix method which treats the wavefunctions differently in the core and outer region [276]. Uncertainties better than 10% are quoted. Close-coupling calculations also reveal a rich structure of pronounced resonances on the cross-sections; they are due to resonant excitation via intermediate states [264].

Applying the Bethe approximation (7.13)–(7.15) to hydrogenic ions by introducing $E_{qp} = Z^2 E_R (1/n_q^2 - 1/n_p^2)$ suggests a scaling for ions with $u = \text{const}$

$$Z^4 \sigma(q \rightarrow p; u) \approx \text{const}, \quad \text{respectively,} \quad Z^2 \Omega(q \rightarrow p; u) \approx \text{const}. \quad (7.22)$$

This has been exploited by Sampson and collaborators who have done extensive calculations in several approximations and give their results in terms of a scaled hydrogenic collision strength $[Z^2 \Omega_H(q \rightarrow p)]_{Z \rightarrow \infty}$:

$$\Omega(q \rightarrow p) = \frac{[Z^2 \Omega_H(q \rightarrow p)]_{Z \rightarrow \infty}}{Z_{\text{eff}}^2}. \quad (7.23)$$

Z_{eff} is an effective nuclear charge, which also accounts for screening by other bound electrons if (7.23) is applied to hydrogenic levels of other ions. From a whole series of publications see [277], for example.

Experimental cross-sections are usually measured by crossing a beam of atoms, molecules, or ions with an electron beam of variable energy [278]. The number of excitation events typically is obtained from the number of emitted photons or from the number of beam electrons showing the respective energy loss. Collinear merged electron and ion beams have been used to measure absolute cross-sections of multiply charged ions in a small energy range above threshold [279]. One major advantage is the high detection sensitivity near unity.

Electron-beam ion traps (EBITs) permit now cross-section measurements for very highly ionized species and have been successfully employed for that

purpose [280, 281]. A completely different approach does not yield cross-sections but rate coefficients [282, 283]: line emission from ions in suitable plasmas, which are well diagnosed (preferably by Thomson scattering), is measured absolutely and interpreted in terms of excitation rate coefficients. This is straightforward and of reasonable certainty only if the emission of a line depends essentially on one excitation channel, like for example, in the corona limit (p. 142). The technique is sometimes referred to as the plasma spectroscopy method.

We now turn to excitation characteristics of some isoelectronic sequences which are frequently used for diagnostic purposes or in some applications.

Hydrogen-Like Ions

Early calculations have been reviewed in [265]. Later Fisher et al. [275] compared $n_q l_q \rightarrow n_p l_p$ cross-sections calculated in the convergent close-coupling and Coulomb–Born with exchange approximations with each other and gave the total $n_q \rightarrow n_p$ cross-sections by summing over l_p and statistically averaging over l_q . By comparison with the effective Gaunt factor formula employing the l -averaged hydrogenic oscillator strength $f(n_q \rightarrow n_p)$ they determined an effective Gaunt factor as fit to all their data:

$$\bar{G}(u) = 0.349 \ln u + 0.0988 + 0.455 \frac{1}{u}, \quad (7.24)$$

They also compared their calculations with a semiempirical formula originally proposed in [262]. They rewrote it in the form

$$\sigma(n_q \rightarrow n_p; u) = \frac{\pi a_0^2}{Z^4} \frac{n_q^7 \sqrt{n_p}}{(n_p^2 - n_q^2)^2} \frac{1}{u} F(u) \quad (7.25)$$

and obtain $F(u)$ for each calculation by a fitting procedure. As best fit again to all calculations they suggest

$$F(u) = 14.5 \ln u + 4.15 + 9.15 \frac{1}{u} + 11.9 \frac{1}{u^2} - 5.16 \frac{1}{u^3}. \quad (7.26)$$

The authors quote an accuracy of better than 50% for any incident electron energy and better than 30% for $u < 2$.

Cross-sections to high levels decrease rapidly with increasing principal quantum number. This is seen when considering the $1s \rightarrow n_p$ excitation. Substitution of the hydrogenic oscillator strength into (7.13) or (7.16) gives for high n_p

$$\sigma(1s \rightarrow n_p) n_p^3 \approx \text{const.} \quad (7.27)$$

Collisions redistributing populations between highly excited neighboring levels $n_q \rightarrow n_q + 1$ are important for establishing statistical population of the levels in a plasma (see Chap. 8). Sobel'man et al. [262] give cross-sections and

rate coefficients for neutral hydrogen and hydrogen-like ions. For the latter the rate coefficient is

$$X(n_q \rightarrow n_q + 1; T_e) = 10^{-14} \frac{n_q(n_q+1)^3}{Z^3} \left(\frac{Z^2 E_R}{k_B T_e} \right)^{1/2} \times \exp\left(\frac{E_{qp}}{k_B T_e}\right) \Phi(Z, k_B T_e) \text{ m}^3 \text{s}^{-1}. \quad (7.28)$$

The function $\Phi(Z, k_B T_e)$ is tabulated for hydrogen-like ions and for neutral hydrogen ($Z = 1$). For high n_q usually $E_{qp} \ll k_B T_e$, and if we approximate $\Phi \approx 4$, then we obtain for estimates to within a factor of 2 the simple relation

$$Z^3 X(n_q \rightarrow n_q + 1) \left(\frac{k_B T_e}{Z^2 E_R} \right)^{1/2} = 4 \times 10^{-14} n_q^4 \text{ m}^3 \text{s}^{-1} \quad (7.29)$$

in the range $0.1 < k_B T_e / Z^2 E_R < 1$. For nonhydrogenic ions effective charge and effective quantum number have to be used.

Helium-Like Ions

Helium and helium-like ions offer specific diagnostic possibilities because of the high-lying metastable level 2^3S_1 of the triplet system, the metastable level 2^1S_0 being of minor impact. Although excitation cross-sections to the singlet and to the triplet system are of the same magnitude close to threshold, they differ strongly at high energies as is readily seen in the Bethe limit, (7.13) and (7.15). Figure 7.2 shows the cross-sections for the transitions $1s^2 1S \rightarrow 1s2p^1P$ and $1s^2 1S \rightarrow 1s2p^3P$ in HeI. The difference is crucial in all cases where energetic electron beams (non-Maxwellian tails of the distribution function,

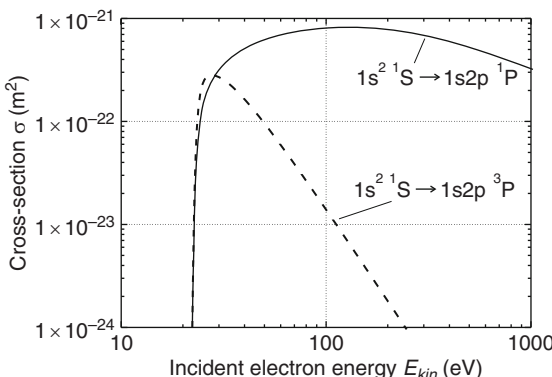


Fig. 7.2. Cross-sections for excitation in HeI [284]

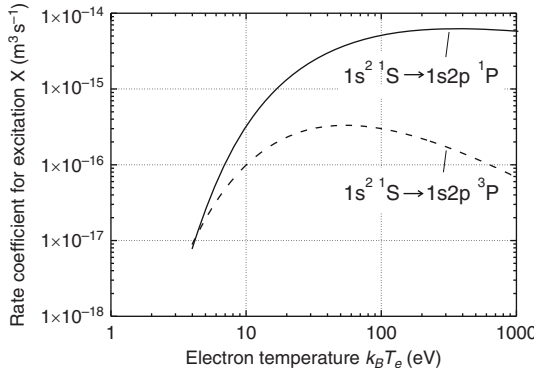


Fig. 7.3. Rate coefficients X for excitation in HeI [284]

respectively) are present. Figure 7.3 shows the difference in the corresponding rate coefficients X in a Maxwellian plasma.

Due to the extremely low decay rates from the $n = 2$ triplet levels to the ground state, see Table 6.4, the population densities in these levels are very high, and as a consequence collisional excitation from these levels to higher levels plays an important role. Collisional coupling of higher levels of the same principal quantum number n by $nl \rightleftharpoons n(l \pm 1)$ transitions occurs with increasing electron density and increasing n . For estimates of these transitions (without spin change) a high-temperature limit rate coefficient is useful, which has been derived in line broadening calculations [286]:

$$\begin{aligned} X(l \rightarrow l - 1) &\simeq 3 \left(\frac{2\pi m_e}{k_B T_e} \right)^{1/2} \left(\frac{\hbar}{m_e} \right)^2 \frac{n^2 l (n^2 - l^2)}{2l + 1} \ln \left(\frac{2}{n^2} \frac{k_B T_e}{E_{qp}} \right) \quad (7.30) \\ &\simeq 6.5 \times 10^{-14} \frac{1}{\sqrt{k_B T_e / E_R}} \frac{n^2 l (n^2 - l^2)}{2l + 1} \ln \left(\frac{2}{n^2} \frac{k_B T_e}{E_{qp}} \right) \text{ m}^3 \text{s}^{-1}. \end{aligned}$$

The most recent comprehensive and critical assessment of cross-sections is given in [285], where also references to previous compilations are found. The recommended cross-section data are presented by analytic fit functions.

The relatively high population densities of the metastable levels decrease with increasing nuclear charge along the isoelectronic sequence as the transition probabilities from these levels to the ground state increase rapidly. Figure 7.4 illustrates the excitation cross-section of resonance and intercombination line for ArXVII; they have been computed in the distorted wave approximation employing the Los Alamos Atomic Physics Codes [267]. Cross-sections of helium-like ions are collected and assessed in several data banks. We cite only one more recent publication where references to earlier calculations are found [287].

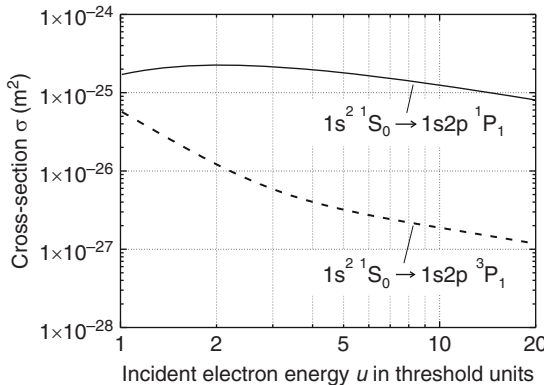


Fig. 7.4. Cross-sections for excitation of the resonance and intercombination line in ArXVII

Lithium-Like Ions

The lithium-like isoelectronic sequence is characterized by low-lying levels $2\ ^2P_{1/2}$ and $2\ ^2P_{3/2}$ which are strongly populated in many plasmas. Hence collisional excitation from these levels is important.

Cross-sections are naturally found in data bases and in the literature. A critical assessment of theoretical and experimental collision strengths with a recommendation of best data was given by [288]. More recently, Fisher et al. [289] presented easy to use cross-sections based on their computations by convergent close-coupling and Coulomb–Born with exchange approximations up to the principal quantum number $n_p = 4$. Here, it is probably useful to point out that the $2s \rightarrow 4f$ collisional octupole excitation rate with $\Delta l = 3$ is of the same magnitude as the dipole rate; this was observed when studying the emission from NeVIII ions in a plasma [290].

Inner-shell excitation leads to doubly excited states which may auto-ionize or radiatively decay. The emission gives so-called satellites to lines of the helium-like ion spectrum which are conveniently exploited for diagnostics. Cross-sections are found in [291, 292].

Neon-Like Ions

Because of the closed-shell configuration neon-like ions exist over a large temperature range like helium-like ions. The particular interest in this ionization stage, however, originates in the achievement of lasing in the soft x-ray region employing these ions. Population inversion between 3p and 3s levels becomes possible due to a strong monopole excitation $2p \rightarrow 3p$ and fast radiative decay of the 3s levels. Collision strengths may be found, for example, in [293].

Argon

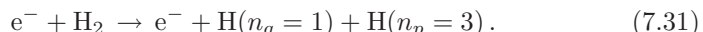
Argon has become one of the most important elements since it is the working gas in many technical plasma devices. Collisional data are spread and very often only cross-sections by the effective Gaunt factor approximation are employed. In a recent analysis available cross-sections have been assessed and a coherent set of nonanalytical cross-sections is proposed [294].

Molecules

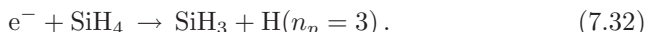
Theoretical calculations of electron impact excitation cross-sections are rather difficult because of the complexity of the molecular structure. For this reason, calculations are rare. Quantum mechanical approximations are those which are applied to atoms and ions, i.e., Born, close-coupling and distorted-wave approximations and the R-matrix method [212]. In the absence of any data, the effective Gaunt factor approximation (7.16) (7.20) for dipole allowed transitions is most useful.

Cross-sections for rotational excitations are relatively small; for hydrogen they are typically in the range $10^{-21} - 10^{-20} \text{ m}^2$. Cross-sections for vibrational excitation $v \rightarrow v'$ are even smaller, in the absence of resonances they are typically of the order of 10^{-22} m^2 . In many cases population of an excited level by electron impact occurs via intermediate steps. It is then customary to characterize the total probability by a *photon emission cross-section* σ_{em} , which may even include the branching ratio of the transition probabilities; it is mostly obtained experimentally.

A rather common process in molecules is that of *collisional dissociative excitation*. Two examples are given below: for the hydrogen molecule, which plays a role in low-temperature plasmas as well as in the cold boundary of fusion plasmas, and for the silane molecule, which is employed in plasma processing technologies. Excitation is via purely dissociative states of the molecules; the following represents only one of the fragmentation channels:



More details are given in [284, 295]. Silane has also several fragmentation channels, one is



Other channels lead to different SiH_y fragments, which can also be in excited states. A comprehensive data set with critical assessment is found in [296], the equivalent for hydrocarbons in [297, 298].

7.3 Electron Impact Ionization and Three-Body Recombination

Direct ionization of atoms, molecules and ions by electron impact occurs from the ground state (g) of the species as well as from excited states (q) to usually the ground state of the next ionization stage. The process is written symbolically



The probability is characterized again like in the case of excitation by a corresponding cross-section $\sigma_z(q; E_{\text{kin}})$ which depends on the kinetic energy of the impacting electron. The rate coefficients for plasmas are obtained by integrating the product cross-section times velocity over the velocity (energy) distribution function of the electrons: $S_z = \langle \sigma_z v \rangle$, see Sect. 7.1. In case of a Maxwellian distribution, the rate coefficient is a function of the electron temperature, $S_z = S_z(q; T_e)$.

The reverse reaction is known as *three-body or collisional recombination*. It involves two electrons: the energy gained by capture of one electron is transferred to the second one, which effectively means heating this electron; this effect is commonly referred to as *recombination heating*.

The theoretical treatment of ionization is more complex than that of excitation because of the double-continuum electron final state. One has to resort again to approximations. A rough estimate, however, is already obtained by the classical calculation of Thomson who obtained [299]

$$\sigma_z(n_q; u) = 4 \xi_{n_q} \left(\frac{E_R}{E_{z,n_q\infty}} \right)^2 \frac{u-1}{u^2} \pi a_0^2. \quad (7.34)$$

ξ_{n_q} is the number of electrons in the n_q -subshell, and $u = E_{\text{kin}}/E_{z,n_q\infty}$ is the kinetic energy of the impacting electrons in units of the ionization energy $E_{z,n_q\infty}$ of this subshell. Although this cross-section has the wrong dependence for $u \rightarrow 0$ and the wrong asymptotic behavior ($\sigma \sim 1/u$ instead of $\sigma \sim \ln u/u$ like for allowed excitation transitions), it predicts a correct scaling law for $u = \text{const}$ in agreement with quantum theories

$$(E_{z,n_q\infty})^2 \sigma_z(n_q; u) \simeq \text{const}, \quad \text{i.e.,} \quad Z^4 \sigma_z(n_q; u) \simeq \text{const} \quad (7.35)$$

for hydrogen-like ions. Scaling is very useful for interpolation or extrapolation along isoelectronic sequences.

For the rate coefficients, one obtains

$$(E_{z,n_q\infty})^{3/2} S_z \left(n_q; \frac{k_B T_e}{E_{z,n_q\infty}} \right) \simeq \text{const}, \quad \text{i.e.,} \quad Z^3 S_z \left(n_q; \frac{k_B T_e}{E_{z,n_q\infty}} \right) \simeq \text{const}. \quad (7.36)$$

Approximations employed in quantum mechanical calculations are those also used for electron impact excitation, p. 117, i.e., plane wave Born, Coulomb-Born, Born exchange, distorted wave, and close coupling approximations. These methods are complemented by a number of semi-empirical and semi-classical approaches [300–302].

Experimental cross-sections are primarily obtained in crossed-beams experiments [303]. Examples of cross-sections thus measured for hydrogen-like ions from BV to OVIII are found in [304]. Toward higher ionized species such methods are limited as suitable high-current ion and electron beams start to become unavailable. Electron beam ion traps (EBITs) allow now the extension to high-Z elements. Cross-section measurements of hydrogen-like iron and molybdenum, for example, are reported [305].

Rate coefficients have been derived from the analysis of suitable lines emitted specifically from transient plasmas. The principle is discussed in [282, 283]. The disadvantage (or advantage ?) is that *effective* ionization rates are obtained which include ionization from excited, especially from metastable levels, and hence may depend on the electron density and on collisions with other plasma particles, see Chap. 10.1.

Guided by theoretical considerations a number of fit-formulae have been proposed to describe analytically theoretical and experimental cross-sections and rate coefficients. These formulae then are taken as reference to assess the reliability of new theoretical and experimental data. One of the most widely used semiempirical formula is that of Lotz [306], which is attractive because of its simplicity, yet gives reasonable results. For *hydrogen-like ions* he proposed

$$\sigma_z(n_q; u) = 2.76 \left(\frac{E_R}{E_{z,n_q\infty}} \right)^2 \frac{\ln u}{u} \pi a_0^2 = 2.76 \frac{n_q^4}{Z^4} \frac{\ln u}{u} \pi a_0^2. \quad (7.37)$$

Cross-sections increase strongly with principal quantum number n_q . The corresponding rate coefficients are with

$$y = \frac{E_{z,n_q\infty}}{k_B T_e} \quad (7.38)$$

$$S_z(n_q; y) = 6.0 \times 10^{-14} \left(\frac{E_R}{E_{n_q\infty}} \right)^{3/2} y^{-1/2} e^{-y} f(y) \text{ m}^3 \text{s}^{-1} \quad (7.39)$$

$$f(y) = y e^y \text{Ei}(-y) \approx y \ln \left(1 + \frac{0.562 + 1.4 y}{y(1 + 1.4 y)} \right), \quad y > 0. \quad (7.40)$$

$\text{Ei}(-y)$ is the exponential integral. $f(y)$ is approximated to within 5% by the right-hand side of (7.40) revealing that it is a weak function of y [302]. This in turn also shows that the rate coefficients for ionization from excited states tend to scale like $S_z(n_q) \propto n_q^4$. For ionization from high Rydberg levels $y \ll 1$, and the exponential integral can be approximated by [8]

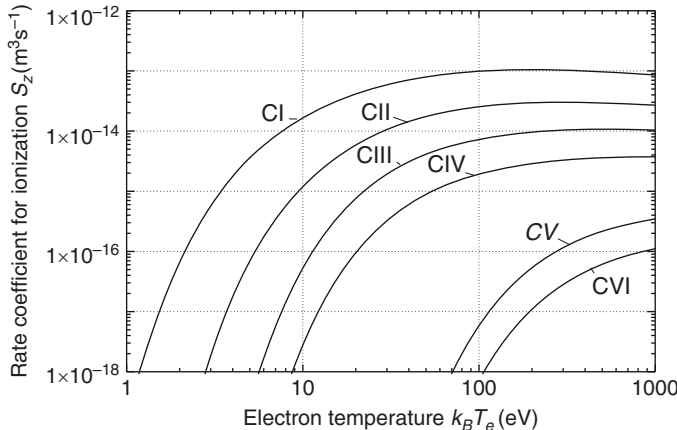


Fig. 7.5. Rate coefficients S_z for ionization according to [306]

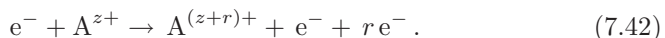
$$\text{Ei}(-y) \approx \left(\ln \frac{1}{y} - 0.577 \right) \quad (7.41)$$

indicating that the above scaling becomes weaker and is closer to $S_z(n_q) \propto n_q^2$.

Lotz expanded his formula to neutral atoms and to their ionization stages, thereby including ionization from inner shells. This ionization channel can be important for atoms and ions with only a few electrons in the outer subshell and an inner shell of comparable ionization energy with many electrons. Fitting parameters for cross-sections and rate coefficients are given in [307, 308]. Figure 7.5 illustrates these rate coefficients for carbon and its ions.

The most recent assessment of known experimental and theoretical ionization cross-sections from H to Ge is given in [309] and for Kr and Mo in [310]. The authors employed a four parameter fitting formula which was proposed by Younger [311] on the basis of his calculations in the distorted-wave-exchange approximation. They took into account the inner-shell excitation to doubly excited states, which may autoionize, by adding additional terms with parameters to the fitting formula. Excitation–autoionization is important especially in some heavier species and may exceed direct ionization by an order-of-magnitude. A discussion can be found in [312], for example. Cross-sections and rate coefficients for direct and indirect ionization are additive.

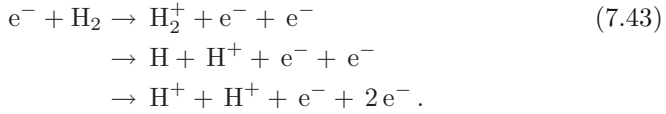
Direct multiple ionization described by



may play a role when neutral atoms or their low charge states are suddenly exposed to high temperatures in a plasma. For a review [302] may be consulted. A recent analysis of double ionization is found in [313].

Electron impact ionization of molecules is complex because of many possible fragments which can be even in various excited (vibrational) states. For

the hydrogen molecule, for example, three ionization channels exist:



Cross-section data are given in [284, 314]. Direct ionization as well as various dissociative ionization channels are discussed and assessed in [297] for the hydrocarbons CH_y and CH_y^+ ($y = 1 - 4$), and for the silane family SiH_y in [296].

Direct *electron impact ionization* and *three-body recombination* are inverse processes, and in a plasma at thermodynamic equilibrium their rates must be equal (principle of detailed balance): hence, the rate coefficient for recombination is directly related to that for ionization.

$$n_e S_z(q \rightarrow g) n_z(q) = n_e^2 \alpha_{z+1}^{\text{cr}}(g \rightarrow q) n_{z+1}(g). \quad (7.44)$$

$$\alpha_{z+1}^{\text{cr}}(g \rightarrow q) = \frac{n_z(q)}{n_e n_{z+1}(g)} S_z(q \rightarrow g). \quad (7.45)$$

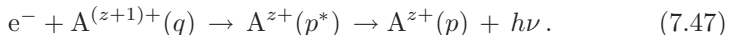
The Saha equation (8.12) links the density of the ions in the level (q) of the ionization stage (z) to the density of the ions in the ground state (g) of the ionization stage ($z+1$), and (7.45) becomes

$$\alpha_{z+1}^{\text{cr}}(g \rightarrow q) = \frac{1}{2} \frac{g_z(q)}{g_{z+1}(g)} \left(\frac{2\pi\hbar^2}{m_e k_B T_e} \right)^{3/2} \exp\left(\frac{E_{z,q\infty}}{k_B T_e}\right) S_z(q). \quad (7.46)$$

Applying this relation to *hydrogen-like* ions (7.39–7.41) reveals that three-body recombination is preferentially into excited states in contrast to radiative recombination where the ground state is preferred. With $g_z(n_q) = 2n_q^2$ we have $\alpha_{z+1}^{\text{cr}}(g \rightarrow n_q) \propto n_q^6$ changing to $\alpha_{z+1}^{\text{cr}}(g \rightarrow n_q) \propto n_q^4$ for Rydberg states.

7.4 Dielectronic Recombination and Autoionization

The importance of *dielectronic recombination* was first quantitatively elaborated on by Burgess in analyzing the emission from the solar corona [315, 316]. It is a two-step process:



A fast incoming electron is resonantly captured into a doubly excited state (p^*) by simultaneously exciting one electron. This state will either autoionize thus canceling the capture or it will decay to a lower singly excited level of the ion finalizing the capture. Figure 7.6 illustrates the process. Dielectronic recombination thus depends on the capture cross-section and on the branching ratio for the radiative transition. In contrast to the other recombination

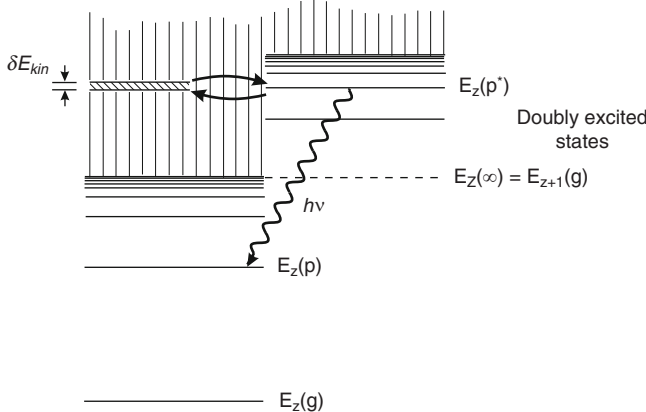


Fig. 7.6. Scheme of dielectronic recombination

processes, where electrons of all kinetic energies can participate, this capture is resonant, i.e., only electrons in an energy interval δE_{kin} can be captured which is given by the lifetime τ_{p^*} of the doubly excited autoionizing state (9.14):

$$\delta E_{\text{kin}} = \frac{\hbar}{\tau_{p^*}} = \hbar [A(p^* \rightarrow) + A_a(p^* \rightarrow)], \quad (7.48)$$

where $A_a(p^* \rightarrow)$ is the autoionization probability and $A(p^* \rightarrow)$ the *total* probability of stabilizing transitions.

Dielectronic capture and autoionization are inverse processes and hence again the rates are equal at thermodynamic equilibrium according to the principle of detailed balance.

$$n_e n_{z+1}(g) \alpha_{z+1}^{\text{cap}}(g \rightarrow p^*) = n_z(p^*) A_a(p^*). \quad (7.49)$$

The capture rate coefficient $\alpha_{z+1}^{\text{cap}}(g \rightarrow p^*)$ is given by the total capture cross-section times the velocity times δE_{kin} , or more precisely by

$$\alpha_{z+1}^{\text{cap}}(g \rightarrow p^*) = \int_0^\infty \sigma^{\text{cap}}(g \rightarrow p^*) v f_e(E_{\text{kin}}) dE_{\text{kin}}, \quad (7.50)$$

where the cross-section has a Lorentzian shape with the full width at half maximum of δE_{kin} . With (8.12) we obtain

$$\begin{aligned} \alpha_{z+1}^{\text{cap}}(g \rightarrow p^*) &= \frac{1}{2} \frac{g_z(p^*)}{g_{z+1}(g)} \left(\frac{2\pi\hbar^2}{m_e k_B T_e} \right)^{3/2} \\ &\times \exp \left(-\frac{(E_z(p^*) - E_{z+1}(g))}{k_B T_e} \right) A_a(p^* \rightarrow). \end{aligned} \quad (7.51)$$

Multiplication with the branching ratio for stabilizing transitions gives the rate coefficient for dielectronic recombination:

$$\alpha_{z+1}^{\text{dr}}(g \rightarrow p^*) = \alpha_{z+1}^{\text{cap}}(g \rightarrow p^*) \frac{A(p^* \rightarrow)}{A_a(p^* \rightarrow) + A(p^* \rightarrow)}. \quad (7.52)$$

The total dielectronic recombination rate coefficient $\alpha_{z+1}^{\text{dr}}(g)$ is finally obtained by summing over all possible doubly excited autoionizing states. The large number of these states (indeed, entire Rydberg series) results in the significance of this recombination process. If a large number of ions are in a metastable state, corresponding recombination from that state must be certainly considered as well.

Discussions of theoretical calculations with approximate formulae are found in [8, 9, 222, 262, 317]. Hahn assessed all then available data and proposed rate formulae according to the excitation mode [318]. An earlier evaluation is available for ions along isoelectronic sequences [319].

The most recent and extensive calculations have been and are still being published by Badnell and coworkers in a whole series for isoelectronic sequences. Starting with [320] an easily accessible data base is available. One of the last publications is on the helium isoelectronic sequence [321]. Total and partial (i.e., final-state level-resolved) rate coefficients from the ground and the metastable state are given. For practical applications the total rate coefficients are fitted to a formula

$$\alpha_{z+1}^{\text{dr}}(g) = \frac{1}{T_e^{3/2}} \sum_{i=1}^k C_i \exp\left(-\frac{E_i}{T_e}\right). \quad (7.53)$$

with $k \leq 5$. The coefficients are given in tabular form with C_i in units of $\text{K}^{3/2} \text{cm}^3 \text{s}^{-1}$ and T_e and E_i in units of K. α_{z+1}^{dr} is in units of $\text{cm}^3 \text{s}^{-1}$.

External electric fields can enhance dielectronic recombination. They mix nearly degenerated l sublevels and reduce thus the autoionization probability, resulting in increased recombination [322]. The effect has been verified by several experiments. A magnetic field perpendicular to the electric field enhances the recombination still further, whereas a parallel magnetic field has no influence [323].

Parallel to the theoretical calculations advances in the measurement of rate coefficients are impressive. Crossed and merged electron and ion beams have been used [324] as well as facilities like storage rings [325], electron beam ion traps and sources [326]. The plasma spectroscopic approach derives the total rate coefficients from the time behavior of the line emission in transient plasmas (e.g., [327, 328]), or partial rate coefficients from the intensity of the stabilizing transitions after dielectronic capture (e.g., [329]).

Figure 7.7 illustrates the relevance of dielectronic versus radiative recombination for the helium-like ion OVII forming lithium-like OVI. Only at low electron temperatures radiative recombination dominates, otherwise dielectronic recombination is by far the stronger channel. The ionization rate coefficient from the ground state of OVII–OVIII is shown for comparison.

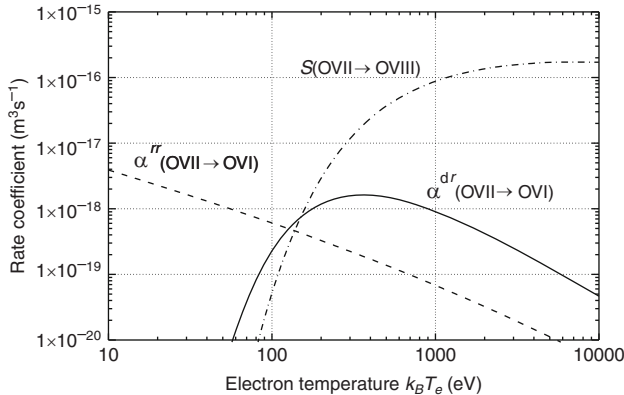
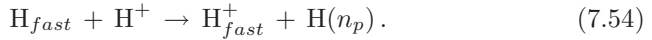


Fig. 7.7. Total rate coefficients for dielectronic and radiative recombination from the ground state of OVII; the ionization rate coefficient is shown for comparison

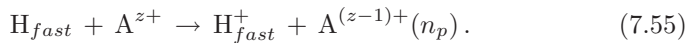
7.5 Charge Exchange Processes

The importance of charge exchange even in hot plasmas was realized in the context of neutral beam heating of fusion plasmas. The basic reaction for energetic hydrogen (or deuterium) beams is



The target proton captures the electron from the fast atom into a level n_p .

The energetic hydrogen beam also interacts with impurity ions of the plasma, transferring the atomic electron into an excited level of the target ion according to



In effect, this is nothing else but a further recombination process, which has to be accounted for and which may influence the ionization balance and ionization dynamics, respectively. This was recognized in tokamaks [330] as well in pinch plasmas [331].

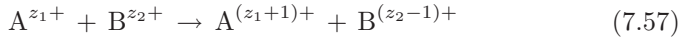
The process is resonant, charge exchange into one particular level having a high cross-section, the probability of capture into neighboring levels being low. For the case of a bare nucleus, the ionization energy of the recombined hydrogenic ion should be equal to the ionization energy of the hydrogen atom, in a crude picture resulting in $n_p \approx Z$ for atoms in the ground state. More precise calculations yield the principal quantum number of the captured level [332]

$$n_p \cong Z^{0.768}. \quad (7.56)$$

This reveals that for heavy bare nuclei in hydrogen plasmas charge exchange is into *high* n_p -levels; hydrogen atoms in excited states even leading to the

population of much higher levels of the target ion. Since moreover levels of higher angular momentum, which cannot decay directly to the ground state, are preferred in the capture process, the decay is via subsequent $\Delta n = -1$ transitions at long wavelengths; these can be, for example, in the visible and hence convenient for diagnostic purposes (p. 182).

Large cross-sections have been reported not only for quasi-resonant charge exchange collisions



between multiply charged ions [333], but also for nonresonant charge exchange between specific ion pairs [334]. Reasonable estimates of the cross-sections can be obtained by the classical overbarrier model.

The body of theoretical calculations is large, and methods and approximations are presented in [332, 335]. The standard experimental technique employs crossed ion beams (for example, see [336]).

7.6 Ion and Atom Impact Excitation and Ionization

Proton collisions resulting in excitation and ionization can play a role in high-temperature plasmas. Because of the large mass ratio between proton and electron the relative energy transfer in a collision is small and the maximum cross-section is reached, therefore, at impact energies, which are typically three orders-of-magnitude higher than those for the corresponding electron impact. The magnitude of the cross-section though can be comparable to or even larger than that by the electrons. Figure 7.8 shows as example the cross-section for the excitation of the level 2^1P from the ground state in HeI by electron and proton impact:

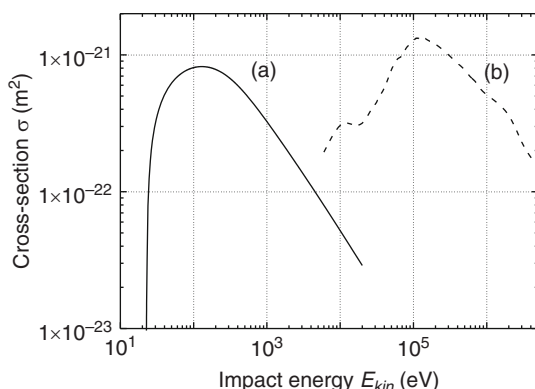


Fig. 7.8. Cross-section for the excitation of the transition $1s^2 1S_0 \rightarrow 1s2p 1P$ in HeI by (a) electron [284] and (b) by proton impact [337]

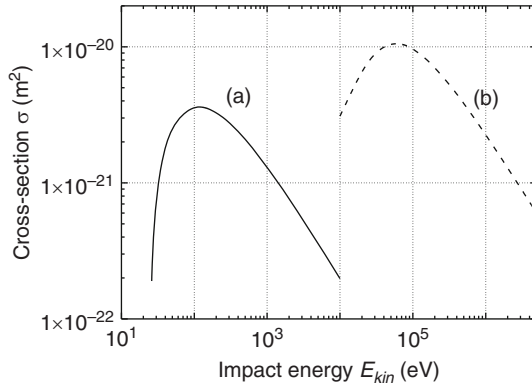


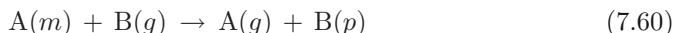
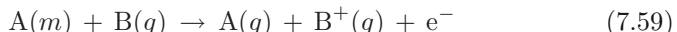
Fig. 7.9. Cross-section for impact ionization of HeI by (a) electrons [341] and (b) by protons [342]

There is *no* excitation of the triplet levels from the ground state since it requires the exchange of spin between electrons.

It is obvious that proton collisions will start to become important for transitions between close fine structure levels where $E_{\text{kin}} \gg E_{qp}$ or $k_B T_i \gg E_{qp}$, respectively. This has been recognized for fine structure transitions in the ground configuration but also in excited states of many ions; see [338], where theoretical calculations as well as experimental results are assessed. Further cross-sections and rate coefficients are found, e.g., in [211, 339, 340].

For ionization by proton impact the energy scaling is similar. Figure 7.9 illustrates the cross-sections for ionization of HeI.

In low-temperature plasmas of atomic species with high-lying metastable levels Penning ionization and excitation can influence the level populations. The three most relevant reactions between two atomic (or molecular) species A and B are listed below where (m) denotes the metastable level, (g) the ground state, and (p) is again an excited state.



The excitation energy of the metastable state (m) must be higher than half the ionization energy for process (7.58) also called “chemo-ionization”, and larger than the ionization energy of species B in process (7.59) known as Penning ionization. B can be also a molecule. Unfortunately, reliable cross-section data are scarce [343, 344]. Argon and helium atoms in their metastable states are the most common representatives of species A.

Kinetics of the Population of Atomic Levels in Plasmas

8.1 Introductory Remarks

The kinetics of the local population of atomic states (p) of ions of charge (z) in plasmas is governed by coupled rate equations of the type

$$\frac{dn_z(p)}{dt} = -R_z(p \rightarrow) + R_z(\rightarrow p) + \Gamma_z(p), \quad (8.1)$$

where $R_z(p \rightarrow)$ and $R_z(\rightarrow p)$ represent the sums of all rates of possible radiative and collisional transitions out of the level (p) and into the level, respectively, and $\Gamma_z(p)$ is the external flux of level- p population by diffusion and convection. It is obvious, that a general solution is practically impossible not only because of the large number of transitions which have to be considered but also for the fact that for many transitions the probabilities and rate coefficients are not known with sufficient accuracy. It is therefore a common approach to reduce the number of rate equations to a set of tractable size by taking into account only the most relevant processes and by considering the pertinent time scales. These so-called *collisional-radiative models* may differ for different atomic and ionic species and certainly for molecules, and they depend on the regime of plasma parameters.

The longest time constant to reach steady-state population for an excited level (p) is given by the lifetime for pure radiative decay $\tau = 1/A_z(p \rightarrow)$. Since in atomic systems these are typically very short compared to changes of the plasma conditions, usually $dn_z(p)/dt = 0$ can be assumed; the time dependence needs to be kept only for metastable levels (m) and ground states (g), which reach steady-state by ionization and recombination on longer time scales. The influx of level population $\Gamma_z(p)$ is low and even negligible in most cases. If it becomes relevant, this is also true for the ground state and metastable levels.

Radiative relaxation times for the ground state vibrational levels of molecules are typically long, too, and the above quasi-steady-state approximation may not be appropriate.

For very high and very low densities the collisional-radiative models approach simple equilibria and steady-state balances, which will be discussed in the following sections.

8.2 Thermodynamic Equilibrium Relations

A plasma and radiation field confined in a fictitious box with an inner wall at constant temperature T will be in thermodynamic equilibrium with the wall, i.e., its physical state is completely determined by T . This means:

- The radiation field is given by Planck's law.
- The energy (velocity) distribution of each species of particles corresponds to a classical Maxwell–Boltzmann distribution (usually simply called Maxwell distribution); for very high electron densities n_e , when the thermal de Broglie wavelength of the electrons becomes larger than their mean distance, quantum effects come into play and the electrons obey a Fermi–Dirac distribution.
- The ratio of the population densities in two states (p) and (q) $< (p)$ of an ion (atom, molecule) with the energies $E_z(p)$ and $E_z(q)$ is given by the Boltzmann distribution

$$\frac{n_z(p)}{n_z(q)} = \frac{g_z(p)}{g_z(q)} \exp\left[-\frac{E_z(p) - E_z(q)}{k_B T}\right]. \quad (8.2)$$

- The rates of pairs of inverse processes are equal – *principle of detailed balance*.

Summation of (8.2) over all states of the ion gives the total density n_z of the ionization stage (z). Equation (8.2) becomes

$$\frac{n_z(p)}{n_z} = \frac{g_z(p)}{U_z(T)} \exp\left[-\frac{E_z(p) - E_z(g)}{k_B T}\right], \quad (8.3)$$

where $U_z(T)$ is the internal partition function of the ionization stage:

$$U_z(T) = \sum_{i=g}^{\infty} g_z(i) \exp\left[-\frac{E_z(i) - E_z(g)}{k_B T}\right]. \quad (8.4)$$

For the ground state (g) (8.3) simplifies to

$$\frac{n_z(g)}{g_z(g)} = \frac{n_z}{U_z(T)}. \quad (8.5)$$

In the limit of noninteracting particles the partition function of the total system is just the product of the partition functions of all species (ions). It is a fundamental thermodynamic quantity from which other thermodynamic

quantities can be deduced. Unfortunately, the partition function of an individual ion diverges mathematically since the number of levels goes to infinity when approaching the ionization limit and the statistical weight increases with $g_z(n_p) = 2n_p^2$, where n_p is the principal quantum number.

In a plasma, however, each ion is subject to the Coulomb field of all other ions and of the electrons, which results in a lowering of the ionization energy $E_z(\infty) - E_z(g)$ (sometimes also called *continuum lowering*) of the isolated ion and thus in a finite number of bound states. This truncation of the sum removes the divergence of (8.4). Several calculations have been reported, a more recent detailed analysis is given by Griem in Sect. 7.3 of [8]. He quotes the reduction as

$$\Delta E_z(\infty) = -z E_R \text{ Min} \left(\frac{2a_0}{\varrho'_D}, \frac{3a_0}{2R_0} \right), \quad (8.6)$$

i.e., the smallest of the two values in the bracket should be taken. a_0 is the Bohr radius, ϱ'_D the Debye shielding factor (radius),

$$\varrho'_D = \sqrt{\frac{\epsilon_0 k_B T}{e^2 (n_e + \sum_z z^2 n_z)}}, \quad (8.7)$$

and R_0 is the ion-sphere radius defined by

$$\frac{4\pi}{3} R_0^3 n_z = 1. \quad (8.8)$$

The maximum principal quantum number n_{max} for bound states just below the reduced ionization limit is obtained from

$$\Delta E_z(\infty) = -\frac{z^2 E_R}{n_{max}^2}. \quad (8.9)$$

The calculation of partition functions is discussed in Sect. 7.4 of [8], and tabulations for a number of atoms and ions are given as function of T for various $\Delta E_z(\infty)$ in [345].

The Boltzmann distribution (8.2) can be extended to continuum states by considering those as states of free electrons. If one defines dn_e as the density of electrons with energies in the interval E_{kin} to $E_{kin} + dE_{kin}$ and the statistical weight dg_e as the number of free electron states in that energy interval, the Boltzmann ratio can be written

$$\frac{dn_e}{dg_e} = \frac{n_z(q)}{g_z(q)} \exp \left(-\frac{E_{kin} - E_z(q)}{k_B T} \right). \quad (8.10)$$

dg_e is calculated by considering the plane wavefunctions of the free electrons and counting the number of possible eigenmodes in a normalization

volume [7]. It leads to

$$dg_e = 2 \frac{g_{z+1}(g)}{n_{z+1}(g)} \left(\frac{m_e}{2\pi\hbar^2} \right)^{3/2} \left(\frac{E_{\text{kin}}}{\pi} \right)^{1/2} dE_{\text{kin}}. \quad (8.11)$$

Substitution into (8.10) and integration over all electron energies yields

$$\frac{n_{z+1}(g) n_e}{n_z(q)} = 2 \frac{g_{z+1}(g)}{g_z(q)} \left(\frac{m_e k_B T}{2\pi\hbar^2} \right)^{3/2} \exp\left(-\frac{E_{z,g\infty}}{k_B T}\right), \quad (8.12)$$

where $E_{z,g\infty} = E_z(\infty) - E_z(q)$ is the ionization energy of the level q . This equation connects the population density of an excited level of the ion (z) with the ground state density of the next ionization stage. Substitution of both densities by the *total* densities n_z and n_{z+1} employing (8.3) gives

$$\frac{n_{z+1} n_e}{n_z} = 2 \frac{U_{z+1}(T)}{U_z(T)} \frac{1}{\lambda_B^3} \exp\left(-\frac{E_{z,g\infty}}{k_B T}\right), \quad (8.13)$$

where we have now introduced the thermal de Broglie wavelength of the electron

$$\lambda_B = \left(\frac{2\pi\hbar^2}{m_e k_B T} \right)^{1/2}. \quad (8.14)$$

As numerical value equation we may write (8.13)

$$\frac{n_{z+1}/\text{m}^{-3}}{n_z/\text{m}^{-3}} \frac{n_e}{\text{m}^{-3}} = 6.034 \times 10^{27} \frac{U_{z+1}(T)}{U_z(T)} \left(\frac{k_B T}{\text{eV}} \right)^{3/2} \exp\left(-\frac{E_{z,g\infty}}{k_B T}\right). \quad (8.15)$$

At higher densities, when plasma effects have to be taken into account, the right-hand side of (8.13) becomes also density dependent via the lowering of the ionization energies (8.6) of both stages (z) and ($z+1$). Both (8.12) and (8.13) are known as Saha equation, also called Saha–Eggert equation. The right-hand side of (8.13) is sometimes referred to as Saha function.

The distribution of the ionization stages (charge state distribution) is obtained by calculation of (8.13) for all adjacent ions with the condition that all densities give the total density n_i of the species (i)

$$n_i = \sum_{z=0}^Z n_z. \quad (8.16)$$

For one-component plasmas charge neutrality demands:

$$n_e = \sum_{z=1}^Z z n_z. \quad (8.17)$$

Equation (8.13) reveals that at constant temperature ionization equilibria shift to lower ionization stages with increasing electron density n_e .

In the kinetic picture, this is easily understood: three-body recombination increases much faster ($\propto n_e^2$) than collisional ionization ($\propto n_e$). Viewed differently: the temperature range, where one ionization stage exists, and hence the temperature of maximum abundance $T_{z,max}$ shift to lower values.

Every atomic process discussed in Chaps. 6 and 7 has its inverse, and in thermodynamic equilibrium the rates in both directions are equal. This *principle of detailed balance* is very useful since the rate coefficient of only one of the inverse processes need to be known. As an example we apply it to the electron collisions (excitation and de-excitation) between two levels:

$$n_z(q) n_e X_z(q \rightarrow p) = n_z(p) n_e X_z(p \rightarrow q). \quad (8.18)$$

With $n_z(p)/n_z(q)$ given by the Boltzmann distribution (8.2) one obtains

$$X_z(p \rightarrow q) = \frac{g_z(q)}{g_z(p)} X_z(q \rightarrow p) \exp\left(+\frac{E_z(p) - E_z(q)}{k_B T_e}\right). \quad (8.19)$$

In analogy the rate coefficient for three-body recombination is obtained from the rate coefficient for ionization by employing the Saha equation (8.12), see p. 129, and the rate coefficient for dielectronic capture from the autoionization probability, p. 130. It is important to realize, that these relations between the rate coefficients of reverse processes do not depend on the population densities of the levels.

In thermodynamic equilibrium, the principle of detailed balance also holds for any energy interval of the Maxwell distribution of the electrons. This links the cross-sections. The relation between the cross-sections for photoionization and radiative recombination is known as Milne formula (6.63). The equation connecting cross-sections for de-excitation with those for excitation is given by

$$\sigma_z(p \rightarrow q; u) = \frac{g_z(q)}{g_z(p)} \frac{u+1}{u} \sigma_z(q \rightarrow p; u+1), \quad (8.20)$$

and it is known as Klein–Rosseland formula [262]. u is here the kinetic energy of the electrons incident on the upper level (p) in units of the excitation energy. In principle, (8.20) follows also directly from the collision strengths of direct and reverse process being equal (7.5).

8.3 Local Thermodynamic Equilibrium

Complete thermodynamic equilibrium is never reached in laboratory plasmas, however, it will exist in the interior of stars. Radiation usually escapes readily from plasmas thus leading to radiation fields inside the plasma below the Planckian radiant energy density.

Nevertheless, at high plasma densities collisions will be so frequent, that they maintain steady-state population densities according to the Boltzmann

relation and a distribution of the ionization stages given by the Saha equation. These conditions represent a powerful concept referred to as *local thermodynamic equilibrium*, abbreviated LTE. Since electron collisions are much faster than ion collisions, they will establish the equilibrium; a Maxwellian energy distribution of the electrons is naturally the prerequisite. Hence, it is the electron temperature which is relevant and which has to be employed in the thermodynamic equations of the preceding section. The ion temperature may be different. Plasmas in LTE are sometimes synonymously referred to as *collision dominated* (CD).

For complete LTE in a steady-state plasma to prevail for the population densities of all levels of an ion, Griem [346] suggested that the electron collisional rate across the *largest energy gap* in the term system should be higher than the corresponding radiative rate by at least a factor of ten.

$$n_z(p) n_e X_z(p \rightarrow q) \geq 10 n_z(p) A_z(p \rightarrow q). \quad (8.21)$$

The population will thus deviate from the Boltzmann value by less than 10%. Assuming that the radiative decay is by a dipole transition according to (6.28),

$$A_z(p \rightarrow q) = \frac{2 r_e}{\hbar^2 c} \frac{g(q)}{g(p)} f(q \rightarrow p) [E_z(p) - E_z(q)]^2, \quad (8.22)$$

and the deexcitation rate coefficient is given by the effective Gaunt factor approximation, (7.20) combined with (8.19),

$$X_z(p \rightarrow q) = 16 \sqrt{\frac{\pi}{3}} \alpha c \pi a_0^2 \frac{g_z(q)}{g_z(p)} f(q \rightarrow p) \frac{E_R}{E_{qp}} \left(\frac{E_R}{k_B T_e} \right)^{1/2} P \left(\frac{E_{qp}}{k_B T_e} \right), \quad (8.23)$$

one arrives at [7]

$$n_e \geq \frac{5}{16\pi} \sqrt{\frac{3}{\pi}} \left(\frac{\alpha}{a_0} \right)^3 \left(\frac{E_z(p) - E_z(q)}{E_R} \right)^3 \left(\frac{k_B T_e}{E_R} \right)^{1/2} \frac{1}{P(E_{qp}/k_B T_e)}. \quad (8.24)$$

Taking the lowest value of the averaged Gaunt factor for ions, $P = 0.2$, the requirement for complete LTE can be written

$$\frac{n_e}{m^{-3}} \geq 1.4 \times 10^{20} \left(\frac{E_z(p) - E_z(q)}{eV} \right)^3 \left(\frac{k_B T_e}{eV} \right)^{1/2}. \quad (8.25)$$

For a hydrogen plasma of $k_B T_e = 5 \text{ eV}$ this requires $n_e \geq 3.3 \times 10^{23} \text{ m}^{-3}$. This condition can be relaxed if the lower level (q) is the ground state (g) and the respective resonance transition ($p \rightarrow g$) becomes optically thick; re-absorption of the emitted radiation provides additional coupling of both levels.

It is difficult to derive a corresponding general condition for two ionization stages being described by the Saha equation. Three-body recombination

should be much stronger than energy-dissipating radiative and dielectronic recombination together:

$$n_{z+1}(g) n_e^2 \alpha_{z+1}^{\text{cr}}(g \rightarrow g) \geq 10 n_{z+1}(g) n_e [\alpha_{z+1}^{\text{rr}}(g \rightarrow g) + \alpha_{z+1}^{\text{dr}}]. \quad (8.26)$$

At low temperatures radiative recombination dominates, at high temperatures dielectronic recombination, see Fig. 7.7. For the low-temperature regime, Salzmann [317] cites a condition

$$\frac{n_e}{\text{m}^{-3}} \geq 1 \times 10^{20} \left(\frac{E_z(\infty) - E_z(g)}{\text{eV}} \right)^{5/2} \left(\frac{k_B T_e}{\text{eV}} \right)^3, \quad (8.27)$$

where $E_z(\infty) - E_z(g)$ is now the ionization energy of the lower stage.

More precise conditions for the existence of LTE are obtained by analyzing the solution of collisional radiative models, Sect. 8.5, with respect to deviations from LTE at increasing electron densities [347]. For hydrogen and hydrogen-like ions this was done in detail by Fujimoto and McWhirter [348]. They compare their results with the approximate criteria usually applied.

For *transient* plasmas with rapidly changing density and temperature the respective time scales to reach steady-state must be considered for the above conditions to apply. These are the effective ionization time calculated from a collisional radiative model in a rapidly heated ionizing plasma, and the recombination relaxation time determined essentially by three-body recombination in a recombining plasma. In spatially inhomogeneous plasmas, the scale length of the variation of plasma parameters must be compared with the diffusion velocity times the appropriate relaxation time [8].

With decreasing electron density, collisions become less frequent and populations will start to deviate from a Boltzmann distribution first between levels separated by the largest energy gap, which is in hydrogen-like and helium-like ions between the ground state and the first excited state. The higher levels will still be populated according to the Boltzmann distribution and connected to the ground state density of the next ionization stage by the Saha equation. Since the level structure of the higher levels resembles that of hydrogen-like ions, it is justified to carry out the considerations for one-electron systems. Griem [7] defined a level (principal quantum number n_{th}) as *thermal limit*, for which the collisional depopulation rate is ten times the radiative decay rate. All higher levels are thus described by the Boltzmann distribution. This is an extremely useful concept and it is referred to as *partial local thermodynamic equilibrium*, briefly PLTE.

If we take the radiative decay probability given by (6.47) and the collisional depopulation from level n_{th} to $(n_{\text{th}} + 1)$ approximated to within a factor of 2 by (7.29), we obtain with $Z - 1 = z$ a condition for PLTE to hold for all levels $n_p > n_{\text{th}}$ of an ion of charge state (z)

$$\frac{n_e}{\text{m}^{-3}} \geq 1.1 \times 10^{24} \frac{(z+1)^6}{n_{\text{th}}^{17/2}} \left(\frac{k_B T_e}{\text{eV}} \right)^{1/2}. \quad (8.28)$$

The thermal limit for a given electron density thus is

$$n_{\text{th}} \approx 670 (z+1)^{12/17} \left(\frac{n_e}{\text{m}^{-3}} \right)^{-2/17} \left(\frac{k_B T_e}{\text{eV}} \right)^{1/17}. \quad (8.29)$$

Griem [8] gives the factor of (8.29) to 840, and Fujimoto and McWhirter [348] obtain in their detailed treatment of hydrogen-like ions with nuclear charge $Z = z + 1$

$$n_{\text{th}} \approx 590 (z+1)^{0.73} \left(\frac{n_e}{\text{m}^{-3}} \right)^{-0.133} \left(\frac{k_B T_e}{\text{eV}} \right)^{0.1}. \quad (8.30)$$

PLTE can be extended to include doubly excited states above the ionization limit [349]. In this case, the collisional depopulation rate should be at least ten times faster than the autoionization and radiative decay rates of the doubly excited levels.

In ions with a group of low-lying excited levels like, for example, in the iso-electronic sequences of lithium and beryllium, a Boltzmann distribution between these levels and the ground state can be maintained down to some lower density limit in addition to PLTE of the populations of the higher levels. In any case, this must be checked for each specific ion by considering the relevant collisional and radiative rates. Corresponding considerations definitely apply to the vibrational and rotational levels of the ground state of molecules.

Fine structure levels of excited states are usually more closely spaced than the levels of neighboring principal quantum numbers. Hence, they remain coupled by collisions with decreasing electron density even as collisional coupling to the other levels has ceased. Due to the small energy spacing, the ratio of the population densities corresponds simply to the ratio of the statistical weights of the levels (8.2). The magnitude of the collisional coupling in relation to the radiative decay can be estimated with (7.30). In hot plasmas collisional coupling between close fine structure levels inclusive those of the ground configuration of highly ionized atoms may be due to collisions by protons, p. 134.

In transient plasmas the validity conditions for PLTE can be drastically different. For rapidly ionizing and recombining plasmas corresponding investigations were carried out in [347] and [348]. A critical discussion and analysis are also found in [8].

8.4 Corona Equilibrium

The corona approximation originally acquired the name from its application to the solar corona. The basic assumption is that at very low electron densities collisional processes have become very weak compared to radiative ones. As a consequence, depopulation of excited levels is only by radiative decay, population by electron collisions. In steady-state, we may write for the population

density of a level (p)

$$n_z(p) A_z(p \rightarrow) = n_e \sum_q n_z(q) X_z(q \rightarrow p). \quad (8.31)$$

With $A_z(p \rightarrow q) \gg n_e X(p \rightarrow q)$, and hence also $A_z(p \rightarrow q) \gg n_e X(q \rightarrow p)$, the population densities $n_z(q)$ of all excited levels are very low relative to that of the ground state, perhaps with the exception of metastable levels. In the strict corona approximation it is assumed, therefore, that all ions of an ionization stage are in the ground state and population of the upper levels is only by electron collisions from the ground state. The population density of a level (p) thus is in steady-state

$$\frac{n_z(p)}{n_z(g)} = \frac{n_e X_z(g \rightarrow p)}{A_z(p \rightarrow)} \ll 1, \quad (8.32)$$

and the emission coefficient of a line becomes according to (6.5)

$$\varepsilon_z(p \rightarrow q) = \frac{h\nu_{pq}}{4\pi} \frac{A_z(p \rightarrow q)}{A_z(p \rightarrow)} n_e X_z(g \rightarrow p) n_z(g). \quad (8.33)$$

For the first resonance line $A_z(p \rightarrow) = A_z(p \rightarrow g)$, and the equation simplifies to

$$\varepsilon_z(p \rightarrow q) = \frac{h\nu_{pq}}{4\pi} n_e X_z(g \rightarrow p) n_z(g), \quad (8.34)$$

i.e., the emission rate in photon units is simply given by the excitation rate from the ground state.

In contrast to LTE, the electron density and excitation rates must be known, and the temperature dependence is now via the rate coefficient for excitation. This strict original definition of the *coronal excitation equilibrium* is usually relaxed in two aspects. First, radiative cascading transitions from higher levels after excitation from the ground state are considered and incorporated into an *effective* excitation rate coefficient $X_{z,\text{eff}}(g \rightarrow p)$. According to Fujimoto [9] the cascading contribution is around 20% and is nearly independent of the principal quantum number. Second, excitation from a metastable level (m) or from a low-lying first excited level is included if they are strongly populated:

$$\begin{aligned} \varepsilon_z(p \rightarrow q) &= \frac{h\nu_{pq}}{4\pi} \frac{A_z(p \rightarrow q)}{A_z(p \rightarrow)} \\ &\times n_e [X_{z,\text{eff}}(g \rightarrow p) n_z(g) + X_{z,\text{eff}}(m \rightarrow p) n_z(m)]. \end{aligned} \quad (8.35)$$

With

$$n_z(g) + n_z(m) = n_z \quad \text{and} \quad \beta = \frac{n_z(m)}{n_z(g)} \quad (8.36)$$

the emission coefficient is

$$\begin{aligned}\varepsilon_z(p \rightarrow q) = & \frac{h\nu_{pq}}{4\pi} \frac{A_z(p \rightarrow q)}{A_z(p \rightarrow)} \\ & \times n_e n_z \left[\frac{1}{1 + \beta} X_{z,\text{eff}}(g \rightarrow p) + \frac{\beta}{1 + \beta} X_{z,\text{eff}}(m \rightarrow p) \right].\end{aligned}\quad (8.37)$$

The time constant to reach steady state with respect to the ground state is naturally the radiative life time of the upper level, $\tau = 1/A(p \rightarrow)$.

Since the coronal approximation can never be satisfied for very high levels, McWhirter [350] defined a validity regime for coronal population of hydrogen-like ions by requesting that for the level with the principal quantum number $n_q = 6$ the radiative decay rate should be larger than the sum of all collisional transitions out of that level. He obtained

$$\frac{n_e}{m^{-3}} \leq 6 \times 10^{16} (z+1)^6 \frac{k_B T_e}{\text{eV}} \exp \left[\frac{0.1 (z+1)^2}{k_B T_e / \text{eV}} \right]. \quad (8.38)$$

The corona regime for the charge state distribution was originally defined by assuming the energy-conserving three-body recombination to be negligible compared to energy-dissipating radiative recombination. This certainly holds for hydrogen-like ions, and in steady-state both processes are balanced. $n_e S_z n_z = n_e \alpha_{z+1}^{\text{rr}} n_{z+1}$ results in

$$\frac{n_{z+1}}{n_z} = \frac{S_z}{\alpha_{z+1}^{\text{rr}}}. \quad (8.39)$$

The corona ionization equilibrium is independent of the electron density and the ratio of the ion densities is a function of the electron temperature through the rate coefficients. It is not a universal function like the Saha function of LTE but depends on the specific ions. An estimate for coronal charge distribution to hold was given in [351]

$$\frac{n_e}{m^{-3}} \leq 4 \times 10^{15} \frac{1}{z+1} \left(\frac{k_B T_e}{\text{eV}} \right)^4. \quad (8.40)$$

The importance of dielectronic recombination was recognized only later and coronal charge state distribution is now preferably defined with its inclusion:

$$\frac{n_{z+1}}{n_z} = \frac{S_z}{\alpha_{z+1}^{\text{rr}} + \alpha_{z+1}^{\text{dr}}}. \quad (8.41)$$

An estimate of the validity range is provided by [317]:

$$\frac{n_e}{m^{-3}} \leq 1 \times 10^{18} \left(\frac{k_B T_e}{\text{eV}} \right)^3 \left(\frac{E_{z,g\infty}}{k_B T_e} \right)^{5/2}. \quad (8.42)$$

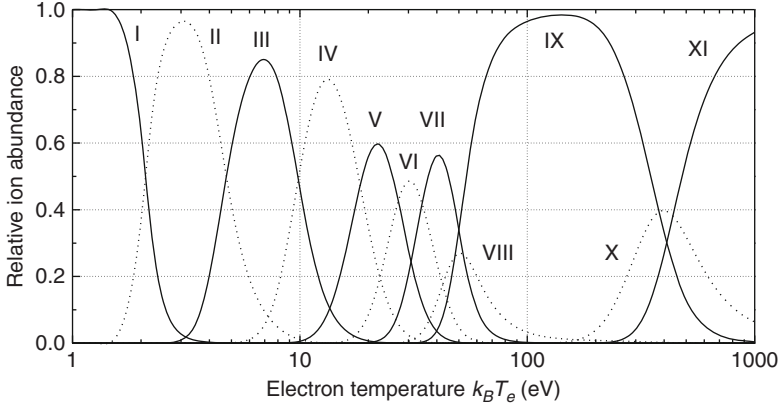


Fig. 8.1. Distribution of the ionization stages of neon in the corona approximation as function of the electron temperature, from [352]

From (8.41) it is obvious that with increasing electron density the three-body recombination term has to be added in the denominator, and this pushes the ionization equilibrium to lower ionization stages till Saha equilibrium with its density dependence is fully reached.

Figure 8.1 shows the charge state distribution for neon in the corona limit as function of the electron temperature. The helium-like ionization stage (Ne IX) exists over the largest temperature range. This deserves specific attention since it becomes relevant when using this ionization stage for diagnostic purposes. It holds quite generally also for other ions with a closed shell like, for example, neon-like ions.

For transient plasmas the coupled set of equations must be solved:

$$\begin{aligned} \frac{dn_z}{dt} = & n_e S_{z-1} n_{z-1} - n_e S_z n_z \\ & + n_e (\alpha_{z+1}^{\text{rr}} + \alpha_{z+1}^{\text{dr}}) n_{z+1} - n_e (\alpha_z^{\text{rr}} + \alpha_z^{\text{dr}}) n_z . \end{aligned} \quad (8.43)$$

If a plasma is heated rapidly to a temperature T_e , it is in an *ionizing regime* with respect to an ionization stage (z) if its temperature of maximum abundance is $T_{e,z\max} \ll T_e$; recombination is negligible as can be readily seen also on the example of Fig. 7.7. The time history of the abundance of such ions thus is solely determined by the ionization rates:

$$\frac{1}{n_z} \frac{dn_z}{dt} = n_e \left(\frac{n_{z-1}}{n_z} S_{z-1} - S_z \right) . \quad (8.44)$$

On the decaying part of the abundance $n_{z-1}/n_z \ll 1$, and the exponential section reflects directly the ionization rate to the next ionization stage:

$$\frac{1}{n_z} \frac{dn_z}{dt} = - n_e S_z . \quad (8.45)$$

In a rapidly cooled plasma ions are correspondingly in a recombining regime, and for $T_e \ll T_{e,z\max}$ (8.43) may be written as

$$\frac{1}{n_z} \frac{dn_z}{dt} = n_e \left[\frac{n_{z+1}}{n_z} (\alpha_{z+1}^{\text{rr}} + \alpha_{z+1}^{\text{dr}}) - (\alpha_z^{\text{rr}} + \alpha_z^{\text{dr}}) \right]. \quad (8.46)$$

The time history of the various ions is essentially determined by recombination rates.

8.5 Collisional Radiative Models

The first approach to a manageable *collisional radiative* (CR) *model* for the population densities of an ion (atom, molecule) is to solve (8.1) taking into account the following processes (omitting photoexcitation and photoionization):

- Electron collisional transitions out of the level (p) and into the level from all other levels of the ion
- Radiative decay to all lower levels and cascading contributions from all higher levels
- Collisional ionization to the ground state (g) of the next ionization stage ($z+1$) and three-body recombination from that state
- Radiative recombination and dielectronic recombination

$$\begin{aligned} \frac{dn_z(p)}{dt} = & - n_z(p) \sum_{q \neq p} n_e X_z(p \rightarrow q) + \sum_{q \neq p} n_z(q) n_e X_z(q \rightarrow p) \\ & - n_z(p) \sum_{q < p} A_z(p \rightarrow q) + \sum_{r > p} n_z(r) A_z(r \rightarrow p) \\ & - n_z(p) n_e S_z(p \rightarrow g) + n_{z+1}(g) n_e^2 \alpha_{z+1}^{\text{cr}}(g \rightarrow p) \\ & + n_{z+1}(g) n_e \alpha_{z+1}^{\text{rr}}(g \rightarrow p) \\ & + n_{z+1}(g) n_e \alpha_{z+1}^{\text{dr}}(g \rightarrow p). \end{aligned} \quad (8.47)$$

For the derivative of the ground state density $n_z(g)$, in principle, terms with ionization from and recombination into levels of the lower ionization stage ($z-1$) should be added. They are redundant only for neutral atoms (molecules), but a corresponding equation holds for $n_{z+1}(g)$.

Mathematically this set of rate equations (8.47) describes the dynamics of the population vector $\mathbf{n}_z = \{n_{z+1}(g), \dots, n_z(p), \dots, n_z(g)\}$,

$$\frac{d}{dt} \begin{pmatrix} n_{z+1}(g) \\ \vdots \\ n_z(p) \\ \vdots \\ n_z(g) \end{pmatrix} = \begin{pmatrix} 0 & \dots & n_e S_z(p \rightarrow g) & \dots & \dots \\ \vdots & \vdots & \vdots & \vdots & \vdots \\ \dots & \dots & \dots & \dots & \dots \\ \vdots & \vdots & \vdots & \vdots & \vdots \\ \dots & \dots & \dots & \dots & \dots \end{pmatrix} \begin{pmatrix} n_{z+1}(g) \\ \vdots \\ n_z(p) \\ \vdots \\ n_z(g) \end{pmatrix}, \quad (8.48)$$

and the matrix contains all radiative and collisional transition probabilities.

As discussed on p. 135, excited states reach quasi-steady state on very short time scales compared to the changes of the densities of the ground states and metastable states and of the plasma parameters. This allows a realistic approximation where the time variation is kept only for the ground states and perhaps metastable states, and all excited levels are considered being in quasi-equilibrium with their ground state: $dn_z(p)/dt = 0$ for $p > g$. This implies that they follow instantaneously the variation of the ground-state density.

Therefore, the matrix equation may be replaced by a set of coupled linear equations which can be solved for assumed input ground-state densities $n_z(g)$ and $n_{z+1}(g)$. The results are substituted into (8.47) for the ground-state density leading to an equation of the type

$$\frac{dn_z(g)}{dt} = -n_e n_z(g) S_z^{\text{eff}}(T_e, n_e) + n_e n_{z+1}(g) \alpha_{z+1}^{\text{eff}}(T_e, n_e). \quad (8.49)$$

S_z^{eff} and $\alpha_{z+1}^{\text{eff}}$ are called *collisional-radiative ionization* and *recombination coefficients*, and both are functions of electron temperature and density. S_z^{eff} takes into account multi-step excitation and deexcitation followed finally by ionization, and discounts electrons which return to the ground state. Likewise $\alpha_{z+1}^{\text{eff}}$ accounts for all recombination processes ending in the ground state.

At low electron densities the time-dependent corona model is retrieved from (8.47) and (8.49), and at high electron densities the populations of the CR model reflect the Boltzmann distribution and in steady-state the Saha–Eggert equation, i.e., LTE is reached.

The first model was developed for hydrogen and hydrogen-like ions by Bates, Kingston and McWhirter [354]. They recognized that in steady state the excited-level population may be written as the sum of two terms

$$n_z(p) = C_0(p, n_e, T_e) n_{z+1}(g) + C_1(p, n_e, T_e) n_z(g), \quad (8.50)$$

where the first term represents the effective downward contribution from the ground state of the ion ($z + 1$) to the population of the level (p), and the second term the upward contribution of the ground state of the ion (z) by all routes. In *transient* plasmas, the *upward flow of excited-state populations* dominates for ions in the ionizing regime, the *downward population flow* for ions in the recombination regime.

It is customary to normalize the population densities to their Saha–Boltzmann population density (superscript SB) which the levels would have for that temperature. Equation (8.50) therefore can be written as [353]

$$\frac{n_z(p)}{n_z^{\text{SB}}(p)} = r_0(p) + r_1(p) \frac{n_z(g)}{n_z^{\text{SB}}(g)}. \quad (8.51)$$

The population coefficients $r_0(p)$ and $r_1(p)$ are determined from the collisional and radiative processes specified in (8.47) of the preceding page. They are functions of electron density and temperature. $r_1(p)$ characterizes the upward excitation component of the excited-level populations, $r_0(p)$ the recombining

component. Extensive calculations for hydrogen $z = 0$ and hydrogenic ions $z = Z - 1$ have been carried out, and tabulations of r_0 , r_1 , S_z^{eff} , and α_z^{eff} have been published for a range of density and temperature [353–356]. The results for hydrogen-like ions are given as functions of reduced temperature Θ_e and density η_e :

$$\Theta_e = \frac{T_e}{(z+1)^2} \quad \text{and} \quad \eta_e = \frac{n_e}{(z+1)^7}. \quad (8.52)$$

This scaling follows from the exponent of the Boltzmann factor (8.2) and from the ratio of collisional excitation and radiative decay, (7.20) and (6.46):

$$\frac{k_B T_e}{(z+1)^2 E_R} \propto \frac{T_e}{(z+1)^2} \quad \text{and} \quad \frac{n_e X(g \rightarrow p)}{A(p \rightarrow g)} \propto \frac{n_e}{(z+1)^7}. \quad (8.53)$$

A CR model of the above type was extensively employed by van der Mullen [347] and Fujimoto [9] to study in great detail several aspects of the population kinetics for various regimes of the plasma parameters. The thermal limit for PLTE as given by (8.30) for steady-state plasmas is one immediate result: it is simply the principal quantum number n_{th} of the level (p), for which $n_z(p)/n_z^{\text{SB}}(p)$ approaches 1, according to Griem [7], for example, to better than 10%. Naturally, a condition for complete LTE is retrieved correspondingly. As earlier mentioned on p. 142, thermal limits for ionizing and recombining plasmas were obtained as well.

For levels above the thermal limit $n_p \geq n_{\text{th}}$ the population coefficients obey the simple relation

$$r_0(p) + r_1(p) = 1. \quad (8.54)$$

An interesting observation is the behavior of the excited-state population $n_z(p)$ of levels with principal quantum number n_p in cases of *transient* plasmas. At PLTE conditions (high densities) the population densities per statistical weight, $n_z(p)/g_z(p)$, are nearly constant as the exponential factor is practically constant for a given (sufficiently high) temperature (8.3). In an ionizing plasma this changes as the overpopulation of the ground state is relieved by ladder-like excitation-ionization to the continuum and ground state of the next ion: this excitation flow yields a power law [357, 358]

$$\frac{n_z(p)}{g_z(p)} \propto n_p^{-6}. \quad (8.55)$$

The analytical analysis reveals that the distribution of the overpopulation specified by the true population minus the Saha population has the same form as the Maxwellian distribution of the free electrons [358].

In a rapidly recombining plasma the overpopulation [$n_{z+1}(g) - n_{z+1}^{\text{SB}}(g)$] of the ion $(z+1)$ flows correspondingly ladder-like downward and establishes

a n_p^{-6} -distribution only for low-lying levels [9]. For higher-lying levels Byron et al. [359] had already observed that the down-flow through the excited-level space reaches a *bottleneck* level with the principal quantum number

$$n_B = \left(\frac{(z+1)^2 E_R}{3k_B T_e} \right)^{1/2}, \quad (8.56)$$

which is now sometimes referred to as Byron's limit. For levels below n_B deviations from PLTE become more likely. More detailed discussions are found in [7, 9, 347].

A number of collisional-radiative models have been reported, in many cases adapted to specific needs. We shall mention only some examples of broader interest. In the model for hydrogen-like ions by Ljepojevic et al. [360, 361] fine structure components were treated separately and proton collisions between the fine structure levels were included. This is necessary for hydrogen-like ions in tokamak plasmas and solar flares.

A generalized collisional-radiative model has been setup by Summers et al. [362] that includes dielectronic recombination and accounts for metastable levels, which requires a detailed specific classification of the level structure for both recombining and recombined ions. Bundling of levels was used whenever meaningful. Atomic structure data and radiative and collisional data are taken from the ADAS data bank inclusive code packages [363].

Several models of varying complexity have been setup for helium-like ions because of their usefulness in diagnostic applications, especially at low and intermediate densities [364–367]. Dielectronic capture from hydrogen-like ions and inner shell excitation from lithium-like and beryllium-like ions were included as were charge exchange with neutral hydrogen and particle transport, and even a non-Maxwellian velocity distribution was allowed for. In a series of models for neutral helium is that by Goto [368] the most up-to-date one.

A model for lithium-like ions is discussed in [369]. Argon is the working gas for many technically used plasmas and a number of models are applied. We cite [343] as a more recent example, and for neon [370].

An extremely useful tool is provided by the FLYCHK code [371], which allows steady-state and time-dependent calculations of population and charge-state distributions from low to high-Z elements. Photoexcitation and photoionization are included as well. The code is maintained at the National Institute of Standards and Technology (NIST) and can be used interactively through the internet [372]. It is continuously improved and extended.

Photoexcitation of lines by self-absorption requires, in general, the inclusion of the radiation transport equation (2.26) into the system of equations. A simple approximation, however, makes use of the fact that re-absorption reduces the number of emitted photons from the upper level and accounts for

that formally by reducing the spontaneous transition probability:

$$A(p \rightarrow q) \Rightarrow A(p \rightarrow q) \theta(\tau_0). \quad (8.57)$$

The reduction factor $\theta(\tau_0)$ is called *escape factor*, and it depends on the optical depth τ_0 at the center λ_0 of the line profile, the shape of the line profile $\mathcal{L}(\lambda)$, and certainly also on the geometry of the plasma. The FLYCHK code makes use of this formalism.

The escape factor may be defined as the flux of photons of a line emanating from the surface of the plasma divided by the total rate of photons emitted within the plasma, which is equivalent to the mean probability that a photon emitted anywhere in the plasma into any direction leaves the plasma directly.

Initially, the escape factor was introduced by Holstein [373, 374] and Biberman [375]. The concept has been critically reviewed and extensively analyzed by Irons [376–378]. Holstein treated the problem in terms of a Boltzmann-type integro-differential equation. For an infinitely long cylinder of diameter D and for the case of a Gaussian line profile a good approximation for the escape factor is [377, 379]

$$\begin{aligned} \theta(\tau_0) &= \frac{1.60}{(\tau_0/2) \sqrt{\pi \ln(\tau_0/2)}} && \text{for } \tau_0 \geq 8, \\ \theta(\tau_0) &\approx \exp(-\tau_0/4.84) && \text{for } \tau_0 \leq 8, \end{aligned} \quad (8.58)$$

with the optical depth along the diameter $\tau_0 = \kappa^L(\lambda_0) \mathcal{L}_G(\lambda_0) D$, (2.25), (6.15), (9.3). The first equation is Holstein's asymptotic result for large optical depth. The factor in the exponent for the lower optical depth regime was adjusted to have continuity at $\tau_0 = 8$. For the corresponding case of a Lorentz profile the approximation is

$$\begin{aligned} \theta(\tau_0) &= \frac{1.59}{\sqrt{\pi \tau_0/2}} && \text{for } \tau_0 \geq 5 \\ \theta(\tau_0) &\approx \exp(-\tau_0/8.82) && \text{for } \tau_0 \leq 5. \end{aligned} \quad (8.59)$$

(Please note that many authors define the optical depth from the axis to the surface. Hence, their optical depth is half of τ_0 as defined earlier.) Other calculations exist for the plane-parallel slab geometry and for spheres.

Only a few calculations of escape factors have been reported for Stark-broadened line profiles, see for example [380]. For more complicated geometries and differentially moving plasmas, where varying Doppler shifts have to be accommodated, Monte Carlo simulations of the photon transport in the plasma are quite suitable [381, 382].

Escape factors have been studied also experimentally. Usually atoms in a gas cell or atoms of a beam were excited by a laser or an electron beam and the radiative decay was monitored, for example [379].

We finally mention collisional-radiative models for molecules. They are certainly more complex but increasingly needed to understand plasmas near the wall and in divertors of fusion devices on the one hand, and technical plasmas on the other hand. Sawada and Fujimoto included the molecular hydrogen in their hydrogen model [383]. A general analysis was reported in [384]. For air plasmas at atmospheric pressure a CR model has been proposed in [385].

Line Broadening

9.1 Profile Functions

The shapes of lines are described by line shape functions \mathcal{L} in frequency ν , angular frequency ω , wavelength λ , or wavenumber units σ . In theoretical calculations the angular frequency ω is usually preferred. \mathcal{L} is normalized:

$$\int_{\text{line}} \mathcal{L}(\omega) d\omega = 1. \quad (9.1)$$

Naturally, experimental profiles are given as function of wavelength or wavenumber. When converting into wavelength, the wavelength factor results in an inherent asymmetry of a profile which is symmetric in ω :

$$\mathcal{L}(\omega) d\omega = \mathcal{L}(\lambda) d\lambda \quad \Rightarrow \quad \mathcal{L}(\lambda) = \frac{2\pi c}{\lambda^2} \mathcal{L}(\omega). \quad (9.2)$$

The full width at half maximum (FWHM) in wavelength units shall be denoted by $\Delta\lambda_{1/2}$, the center wavelength by λ_0 .

The two most common shapes are represented by Gaussian and Lorentzian functions with the FWHM as parameter given by $\Delta\lambda_{1/2}^G$ and $\Delta\lambda_{1/2}^L$, respectively:

$$\mathcal{L}_G(\lambda; \Delta\lambda_{1/2}^G) = \sqrt{\frac{4 \ln 2}{\pi}} \frac{1}{\Delta\lambda_{1/2}^G} \exp \left[-4 \ln 2 \left(\frac{\lambda - \lambda_0}{\Delta\lambda_{1/2}^G} \right)^2 \right], \quad (9.3)$$

$$\mathcal{L}_L(\lambda; \Delta\lambda_{1/2}^L) = \frac{1}{\pi} \frac{\Delta\lambda_{1/2}^L/2}{(\lambda - \lambda_0)^2 + (\Delta\lambda_{1/2}^L/2)^2}. \quad (9.4)$$

Convolution of both functions yields a Voigt line shape

$$\begin{aligned} \mathcal{L}_V(\lambda - \lambda_0; \Delta\lambda_{1/2}^G, \Delta\lambda_{1/2}^L) &= \mathcal{L}_G(\lambda - \lambda_0; \Delta\lambda_{1/2}^G) * \mathcal{L}_L(\lambda - \lambda_0; \Delta\lambda_{1/2}^L) \\ &= \int_{-\infty}^{\infty} \mathcal{L}_G(\lambda' - \lambda_0) \mathcal{L}_L(\lambda - \lambda') d\lambda' \\ &= \frac{1}{\Delta\lambda_{1/2}^G} \sqrt{\frac{4 \ln 2}{\pi}} V(x, a). \end{aligned} \quad (9.5)$$

$V(x, a)$ is called Voigt function [386] given by

$$V(x, a) = \frac{a}{\pi} \int_{-\infty}^{\infty} \frac{e^{-t^2}}{a^2 + (x - t)^2} dt. \quad (9.6)$$

The wavelength variable x is normalized to the halfwidth of the Gaussian profile by

$$x = \frac{\lambda - \lambda_0}{\Delta\lambda_{1/2}^G} 2\sqrt{\ln 2}, \quad (9.7)$$

and the parameter a of the Voigt function, which specifies the relative importance of Gaussian and Lorentzian component, is defined by

$$a = \frac{\Delta\lambda_{1/2}^L}{\Delta\lambda_{1/2}^G} \sqrt{\ln 2}. \quad (9.8)$$

(The apparently odd definition containing a factor $\sqrt{\ln 2}$ is due to the original normalization by the Doppler ($1/e$)-width.)

In Fig. 9.1, three line shapes of equal halfwidth are illustrated, the Voigt profile with equal width of Gaussian and Lorentzian component. Far-extending wings are characteristic of Lorentz profiles in contrast to the more centered Gaussian ones. Voigt profiles are dominated by the Gaussian component near the center (core), and resemble the Lorentzian component on the wings.

Convolution of two Gaussian profiles gives again a Gaussian profile with the halfwidth

$$(\Delta\lambda_{1/2}^G)^2 = (\Delta\lambda_{1/2}^{G1})^2 + (\Delta\lambda_{1/2}^{G2})^2, \quad (9.9)$$

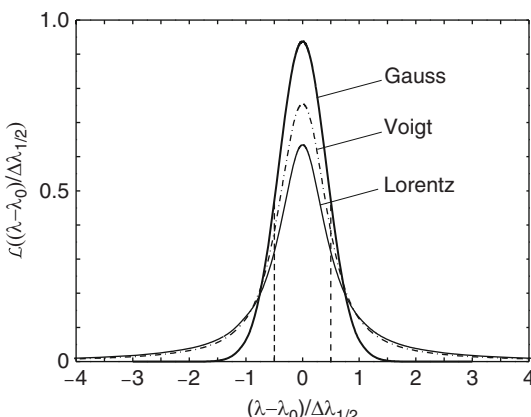


Fig. 9.1. Gaussian, Lorentzian and Voigt profiles of equal halfwidth $\Delta\lambda_{1/2}$

and convolution of two Lorentz profiles results in a Lorentzian with

$$\Delta\lambda_{1/2}^L = \Delta\lambda_{1/2}^{L1} + \Delta\lambda_{1/2}^{L2}. \quad (9.10)$$

As long as the order of convolution does not matter, the convolution of two Voigt function also gives a Voigt function, where the squared halfwidth of the Gaussian component is given by the sum of the squared Gaussian halfwidths, and the halfwidth of the Lorentzian component is the sum of the respective individual components.

Originally Voigt profiles have been widely tabulated (e.g., [387]), in the meantime many computational methods have been reported [388]. If only the width of a Voigt profile is of interest, this may be obtained to an accuracy of about 1% by a simple relation [389]

$$\Delta\lambda_{1/2}^V \approx \left[\left(\frac{\Delta\lambda_{1/2}^L}{2} \right)^2 + (\Delta\lambda_{1/2}^G)^2 \right]^{1/2} + \frac{\Delta\lambda_{1/2}^L}{2}. \quad (9.11)$$

A modification of this equation leads even to an accuracy of 0.02% [390].

Absorption within the plasma modifies the profile of lines leaving the plasma. Since this is a cumulative effect along the line of sight and hence depends on the spatial characteristics of the plasma, respective profile functions must be calculated individually for each case by solving the equation of radiative transfer, Sect. 9.2.7.

9.2 Broadening Mechanisms

9.2.1 Natural Broadening

The energy levels of excited states in atomic systems are not infinitely sharp but have to replaced by an energy distribution due to the finite lifetime of the levels, Fig. 9.2. Heisenberg's uncertainty principle connects the uncertainty ΔE of the energy E of any atomic system with the uncertainty Δt of the time intervals during which corresponding measurements of the energy can be carried out. If ΔE and Δt are defined as the standard deviations of the respective distributions, the uncertainty principle demands

$$\Delta E \Delta t \geq \hbar/2. \quad (9.12)$$

For quasi-stationary states (p) with $\Delta E(p) \ll E(p)$ the equal sign holds (state of maximum certainty), and with $\Gamma_p = 2 \Delta E(p)$ one obtains for every state

$$\Gamma_p \tau_p = \hbar, \quad (9.13)$$

where $\Delta t = \tau_p = 1/A(p \rightarrow)$, since for an exponential distribution of the time intervals the standard deviation equals the mean which is defined as the

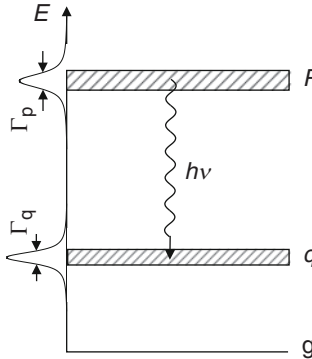


Fig. 9.2. Natural width of excited energy levels

lifetime τ_p of the state, Sect. 6.2.1. The energy distribution is Lorentzian with the full halfwidth Γ_p , which leads to a Lorentzian line shape of the transition between levels (p) and (q) with a halfwidth

$$\Delta\omega_{1/2} = \frac{\Gamma_p + \Gamma_q}{\hbar} = \frac{1}{\tau_p} + \frac{1}{\tau_q} = A(p \rightarrow) + A(q \rightarrow). \quad (9.14)$$

A rigorous quantum mechanical treatment can be found, for example, in [8]. In wavelength units the relative width becomes

$$\frac{\Delta\lambda_{1/2}}{\lambda_{pq}} = \frac{\lambda_{pq}}{2\pi c} [A(p \rightarrow) + A(q \rightarrow)]. \quad (9.15)$$

For the case of the hydrogen Lyman-alpha line the relative natural width is 4×10^{-8} , which is indeed negligible. Along the isoelectronic sequence it scales with Z^2 , i.e., it becomes about 3×10^{-5} for the Lyman-alpha line of FeXXVI; this still is small compared with the Doppler width since such high ionization stages in plasmas are reached only at high temperatures.

9.2.2 Doppler Broadening

Any motion of an emitter leads to a Doppler shift of the angular frequency ω_{pq} of its emitted wave which is given for nonrelativistic velocities by

$$\frac{\omega - \omega_{pq}}{\omega_{pq}} = \frac{v_x}{c}, \quad (9.16)$$

where v_x is the velocity component in the direction x of emission and c is the speed of light. The emission of an ensemble of emitters with a one-dimensional velocity distribution $f_a(v_x)$ in that direction thus results in a profile of the originally monochromatic line. Substituting (9.16) into

$$\mathcal{L}_D(\omega)d\omega = f_a(v_x)dv_x \quad (9.17)$$

gives the Doppler profile

$$\mathcal{L}_D(\omega) = \frac{c}{\omega_{pq}} f_a \left(c \frac{\omega - \omega_{pq}}{\omega_{pq}} \right) \quad (9.18)$$

The profile mirrors exactly the velocity distribution in the direction x . For a Maxwellian distribution $f_a(v_x)$ of temperature T_a the line shape function (9.18) becomes simply a Gaussian (9.3) with a halfwidth

$$\Delta\omega_{1/2}^G = \omega_{pq} \sqrt{8 \ln 2 \frac{k_B T_a}{m_a c^2}}, \quad (9.19)$$

or in wavelength units

$$\frac{\Delta\lambda_{1/2}^G}{\lambda_{pq}} = \sqrt{8 \ln 2 \frac{k_B T_a}{m_a c^2}} = 7.715 \times 10^{-5} \sqrt{\frac{k_B T_a / \text{eV}}{m_a / \text{u}}}. \quad (9.20)$$

m_a is the mass of the emitters and “u” the atomic mass unit.

9.2.3 Pressure Broadening by Neutral Particles

Ambient particles influence the emission process of radiators resulting in broadening and shift of their spectral lines. Both effects depend on particle density and velocity (i.e., temperature), and hence the generally used designation *pressure broadening* makes sense.

Perturbation by atoms and molecules plays a role only in low-temperature weakly ionized plasmas and, in many cases, even there it is negligible compared with the perturbation by charged particles. Interaction with atoms of the *same* kind results in resonance broadening, if either the lower (q) or the upper state (p) of the emitted line is the upper level of a resonance transition, i.e., the level is connected to the ground state (g) by an allowed dipole transition (frequency ω_{qg} or ω_{pg} , oscillator strength $f(g \rightarrow q)$ or $f(g \rightarrow p)$). The interaction between perturber and radiator then is well approximated by a dipole–dipole potential $V(R) \sim 1/R^3$, where R is their separation; this leads to a Lorentzian profile with negligible shift and a halfwidth given by [8, 391]

$$\Delta\omega_{1/2} \approx 4\pi \left(\frac{g(g)}{g(p)} \right)^{1/2} r_e c^2 \frac{1}{\omega_{pg}} f(g \rightarrow p) n_a(g). \quad (9.21)$$

$n_a(g)$ is the density of ground-state atoms. Changing to wavelength units this equation may be written as numerical value equation for a line with wavelength λ_{pq} as

$$\frac{\Delta\lambda_{1/2}}{\lambda_{pq}} \approx 9 \times 10^{-34} \sqrt{\frac{g(g)}{g(p)}} f(g \rightarrow p) \frac{\lambda_{pq}}{\text{nm}} \frac{\lambda_{pg}}{\text{nm}} \frac{n_a(g)}{\text{m}^{-3}}. \quad (9.22)$$

Although negligibly small in most cases, this *resonance broadening* can be predominant at extreme conditions like they prevail, for example, in high-intensity discharge (HID) lamps [392].

To a first approximation the interaction by unlike neutral particles is described by a Van der Waals potential $V(R) = \hbar C_6/R^6$ and the line shape in the core is also Lorentzian. The Van der Waals interaction constant C_6 is specific to each pair of atoms/molecules.

In the impact approximation (see Sect. 9.2.4) one obtains a halfwidth of the line [262, 393]

$$\Delta\omega_{1/2} \approx 8.08 C_6^{2/5} v^{3/5} n_b, \quad (9.23)$$

where v is the mean relative velocity between radiator of mass m_a and perturber of mass m_b . n_b is the density of the perturbers, and v is given by

$$v = \left(\frac{8k_B T}{\pi \mu} \right)^{1/2} \quad \text{with the reduced mass} \quad \frac{1}{\mu} = \frac{1}{m_a} + \frac{1}{m_b}. \quad (9.24)$$

The interaction constant C_6 is probably best determined from experiments, for example [394], but it can also be calculated by

$$C_6 = \frac{e^2}{4\pi\epsilon_0} \frac{1}{\hbar} \alpha_d |\langle R_p^2 \rangle - \langle R_q^2 \rangle|. \quad (9.25)$$

Its unit is $[C_6] = \text{m}^6 \text{s}^{-1}$. α_d is the dipole polarizability of the perturbers ($[\alpha_d] = \text{m}^3$), and $\langle R_p^2 \rangle$ and $\langle R_q^2 \rangle$ are the mean-square radii of the levels (p) and (q) of the emitter. For some atoms α_d and $\langle R^2 \rangle$ are found in tabulations, for example [70, 395], otherwise they can be calculated in the hydrogenic (one electron system) approximation, [393]. With the reduced mass μ in units of u, (9.23) may now be written

$$\frac{\Delta\lambda_{1/2}}{\lambda_{pq}} \approx 8.5 \times 10^{-17} \frac{\lambda_{pq}}{\text{nm}} \left(\frac{C_6}{\text{m}^6 \text{s}^{-1}} \right)^{2/5} \left(\frac{T/\text{K}}{\mu/\text{u}} \right)^{3/10} \frac{n_b}{\text{m}^{-3}}. \quad (9.26)$$

The lines are also red-shifted by

$$\Delta\lambda_{shift} \approx \frac{\Delta\lambda_{1/2}}{2.75}. \quad (9.27)$$

With C_6 of the order of $10^{-40} \text{ m}^6 \text{s}^{-1}$ and $n_b = 1 \times 10^{24} \text{ m}^{-3}$ it is evident that Van der Waals broadening is negligible in most plasmas like resonance broadening. A review on broadening by nonresonant collisions is given in [396].

9.2.4 Stark Broadening

Pressure broadening of spectral lines by charged particles (electrons and ions) usually dominates in plasmas and is termed Stark broadening. It naturally depends on the atomic structure of the emitting atom or ion and, since the

atomic structure exhibits many regularities and similarities, one can expect this also for broadening and shift.

The standard reference is the monograph by Griem [286]. Later developments are analyzed in [8], and a more recent summary and a critical review are given in [397] and [398]. The biannual conference series with conference proceedings – *International Conference on Spectral Line Shapes* – is the forum for current activities and progress. A spectral line broadening bibliographic database is maintained at the National Institute of Standards and Technology (NIST) and is accessible via the internet [399].

The complexity of the broadening is obvious since the perturbation of the line emission is by long-range Coulomb interaction with many charged particles in the plasma. With the plasma field $\mathbf{E}(t)$ at the position of a radiator and the dipole moment operator $\mathbf{Q}^{(1)} = -e\mathbf{r}$ for the radiating bound electron, the interaction Hamiltonian is

$$\Delta H = -e\mathbf{r} \cdot \mathbf{E}(t), \quad (9.28)$$

where the electric field strength is given by

$$\mathbf{E}(t) = \frac{1}{4\pi\epsilon_0} \sum_i z_i e \frac{\mathbf{r}_i(t)}{[r_i(t)]^3} - \frac{1}{4\pi\epsilon_0} \sum_j e \frac{\mathbf{r}_j(t)}{[r_j(t)]^3}. \quad (9.29)$$

$\mathbf{r}_i(t)$ and $\mathbf{r}_j(t)$ are the positions of the ions and electrons of the plasma, and z_i is the charge state of the ions. Monopole and higher multipole terms in ΔH can be neglected in most cases [8]. In principle, the time-dependent Schrödinger equation with ΔH added must be solved. A general solution is impossible, but consideration of relevant time scales leads to two approximations which are successfully employed: the impact and the quasistatic approximation.

Impact Approximation

The impact approximation bases on the realization that the electric field produced by electrons varies rapidly as electrons pass a neutral atom on straight-line paths or ions on hyperbolic trajectories. The paths are fixed, any back-reaction is usually neglected. The effect on the system thus can be treated as collision, in the classical picture changing abruptly the phase of an emitted electromagnetic wave train. In the case of random collisions, the Fourier transform reveals a Lorentzian line shape. This collisional effect can readily be depicted also from the uncertainty principle (9.13) and the discussion in Sect. 9.2.1: collisions simply shorten the lifetime of levels thus leading to respective broadening.

One distinguishes weak and strong collisions. At large impact parameters the phase change of the wave train is small but many collisions contribute and hence they usually dominate. With decreasing impact parameter the phase change increases and when it becomes larger than 1 radian, one talks of strong

collisions. They are rare and can be treated usually as correction. The impact parameter for the phase change 1 radian is called Weisskopf radius.

The starting point for most calculations of the width (FWHM) of an *isolated* line in angular frequency units is the fundamental formula as given by Baranger [400] for a transition from an upper level (p) to a lower level (q):

$$\begin{aligned}\Delta\omega_{1/2} = n_e \int_0^\infty v f_e(v) & \left(\sum_{p' \neq p} \sigma_{pp'}(v) + \sum_{q' \neq q} \sigma_{qq'}(v) \right) dv \\ & + n_e \int_0^\infty v f_e(v) \left(\int |\phi_p(\theta, v) - \phi_q(\theta, v)|^2 d\Omega \right) dv.\end{aligned}\quad (9.30)$$

The first term gives the contributions to the line width from inelastic collisions (cross-section σ) connecting upper and lower level with other perturbing levels (p') and (q'), respectively. Integration is over the electron velocity distribution $f_e(v)$ thus yielding corresponding rate coefficients. The second term reveals contributions by elastic collisions: $\phi_p(\theta, v)$ and $\phi_q(\theta, v)$ are elastic scattering amplitudes for the target ion in upper and lower state, and integration is over the scattering angle θ , $d\Omega$ being the element of the solid angle. In this approximation, both contributions are proportional to the electron density n_e . The approach is intriguing for the mere fact that it relates the line width to atomic collision cross-sections, and theoretical methods discussed in Chap. 7 can thus be used, although refinements like including high partial waves of the colliding electron are necessary [8].

A semiclassical approach pioneered by Griem et al. [401] has been most extensively applied to line broadening calculations [8, 402, 403]. Relatively quick calculations are possible by a semiempirical method employing effective Gaunt factors [404]. These were analyzed for that application by Hey and Breger [405, 406]. Both approaches were modified in [407].

Recent calculations of electron impact broadening now turn to fully quantum mechanical close-coupling calculations, see for example [408, 409].

When perturbation of the lower state (q) can be neglected, (9.30) simplifies to the so-called one-state version [8],

$$\Delta\omega_{1/2} \cong n_e X(p). \quad (9.31)$$

$X(p)$ stands for the sum of all elastic and inelastic collisional rate coefficients. The error thus introduced is small in most cases [8]. The equation also provides some scaling. Since collisions with neighboring fine structure levels usually will be strongest, we employ (7.30) in the preceding equation and obtain for $k_B T_e \gg E_{qp}$

$$\Delta\omega_{1/2} \propto \frac{n_e}{(T_e)^x} \quad \text{with} \quad 0.2 < x < 0.5. \quad (9.32)$$

The impact approximation also leads to a shift $\Delta\omega_s$ which reduces in the one-state version to

$$\Delta\omega_s \cong \frac{\hbar}{m_e} n_e \operatorname{Re} [\phi(0)]_{av}, \quad (9.33)$$

where $\phi(0)$ is the forward scattering amplitude and the average is taken over the Maxwell distribution of the electrons.

Quasistatic Approximation

In the quasistatic approximation, the electric field produced by the ions is considered constant at the location of the radiator during the emission process. This *plasma microfield* splits and shifts upper and lower level by the Stark effect. Perturbation theory gives for simple cases the respective line shift

$$\Delta\omega_{pq}(E) = C_{pq}^{(k)} E^m, \quad (9.34)$$

where $m = 1$ and $m = 2$ hold for linear and quadratic Stark effect, respectively, and (k) designates the Stark component. Since the field is characterized by a distribution, all components are smeared resulting accordingly in a line profile.

The first calculation of the ion microfield distribution was carried out by Holtsmark [410] who assumed all plasma ions to be statistically independent and contributing to the field according to the first term of (9.29). Neglecting external magnetic and electric fields, the microfield thus is isotropic. It is customary in the literature to designate the microfield by \mathbf{F} . The Holtsmark distribution is

$$H(\beta) = \frac{2}{\pi} \beta \int_0^\infty dx \sin(\beta x) \exp(-x^{3/2}) \quad (9.35)$$

with the normalized field strength

$$\beta = \frac{F}{F_0} \quad \text{and} \quad \int_0^\infty H(\beta) d\beta = 1. \quad (9.36)$$

F_0 is the Holtsmark field strength defined by

$$F_0 = 2.603 \frac{ze}{4\pi\epsilon_0} n_z^{2/3}, \quad \text{respectively} \quad \frac{F_0}{V/m} = 3.748 \times 10^{-9} z \left(\frac{n_z}{m^{-3}} \right)^{2/3}. \quad (9.37)$$

The integral cannot be evaluated analytically, it must be computed numerically. For the strong field part $\beta \gg 1$ of the distribution, which determines the largest shifts $\Delta\omega$ and hence the wings of a line, an asymptotic expansion yields

$$H(\beta) \sim \frac{1.496}{\beta^{5/2}}. \quad (9.38)$$

This limit corresponds to the *nearest neighbor approximation* which bases on the assumption that the field on a radiator is solely determined by the nearest ion. The weak-field part $\beta \ll 1$ of the distribution, on the other hand, reflects the superposition of the fields from many distant perturbers.

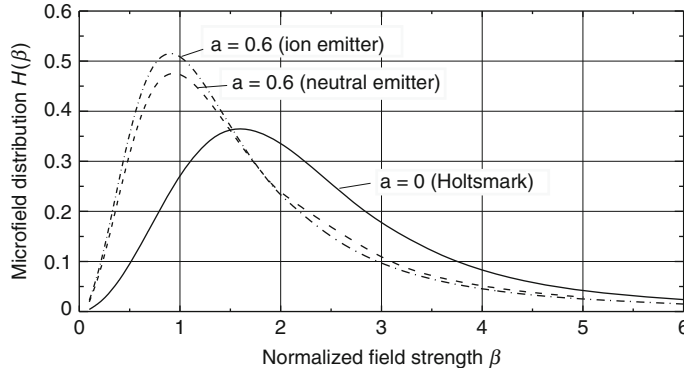


Fig. 9.3. Microfield distributions for $a = 0.6$ for a neutral and a singly charged ion emitter, and for the Holtsmark distribution $a = 0$

The mean ion-produced microfield in the plasma is obtained by averaging β over the Holtsmark distribution

$$\bar{\beta} = \int_0^\infty \beta H(\beta) d\beta, \quad (9.39)$$

which gives according to [286]

$$\bar{F} \approx 3.38 F_0. \quad (9.40)$$

More sophisticated distributions take into account ion–ion correlations and shielding of the perturber charges by plasma particles, an effect known as Debye shielding. We illustrate the respective influence in Fig. 9.3 which shows microfield distributions calculated by Hooper [411] for $z = 1$. They depend on a dimensionless parameter a defined by

$$a = \frac{R_0}{\rho_D}. \quad (9.41)$$

R_0 is the ion-sphere radius (8.8) and ρ_D the Debye radius in the form

$$\rho_D = \sqrt{\frac{\epsilon_0 k_B T}{e^2 n_e}}. \quad (9.42)$$

The distribution differs slightly for cases where the emitter is a neutral atom or an ion, since in the second case the emitter ion repels the perturber ions. The Holtsmark distribution is shown for comparison: it corresponds to a large Debye radius, i.e., to $a = 0$.

For each Stark component (k) of a line, profile and microfield distribution are connected via

$$\mathcal{L}^{(k)}(\omega - \omega_{pq}) d\omega = H(\beta) d\beta. \quad (9.43)$$

For a line subject to linear Stark effect one obtains with (9.34), i.e., $\omega - \omega_{pq} = C_{pq}^{(k)} F_0 \beta$,

$$\mathcal{L}^{(k)}(\omega - \omega_{pq}) = \frac{1}{C_{pq}^{(k)} F_0} H\left(\frac{\omega - \omega_{pq}}{C_{pq}^{(k)} F_0}\right). \quad (9.44)$$

Summation of all components gives the final line profile in the quasistatic approximation.

The profile on the wings of the line thus decays as

$$\mathcal{L}(\omega - \omega_{pq}) \propto \frac{1}{(\omega - \omega_{pq})^{5/2}}. \quad (9.45)$$

This is somewhat faster than the decay of a Lorentzian profile, $\propto 1/(\omega - \omega_{pq})^2$.

For high-density strongly coupled plasmas Hooper's approach is not suitable anymore; reasonable results for this regime were obtained by the adjustable-parameter exponential approximation (APEX) method [412]. More recent calculations employ Monte-Carlo simulations but present analytic formulas that reproduce the calculated microfield distribution for ion-ion coupling parameters Γ from 0 to 100 [413]. Γ is defined by

$$\begin{aligned} \Gamma &= \frac{1}{4\pi\epsilon_0} \frac{z^2 e^2}{R_0 k_B T}, \quad \text{respectively,} \\ \Gamma &= 2.32 \times 10^{-9} z^2 \left(\frac{n_z}{\text{m}^{-3}}\right)^{1/3} \left(\frac{k_B T}{\text{eV}}\right)^{-1}. \end{aligned} \quad (9.46)$$

Hooper's distributions can be used for $\Gamma \leq 1$. Further calculations are discussed in [8], and a more recent review on microfield distributions is given in [414].

Hydrogen and Hydrogen-Like Ions

Hydrogen lines are certainly the most studied ones. Due to the degeneracy of the energy levels they are subject to the linear Stark effect which is much stronger than the quadratic Stark effect. Indeed, the shifts by the particle-produced fields are usually so large that the quasistatic approximation – shift larger than the inverse duration of the corresponding ion-atom collision – is quite valid. Electron collisions must certainly be accounted for and this is done by introducing impact broadening for each shifted Stark component and convolving that with the microfield distribution.

Approximate widths of lines emitted by hydrogen and hydrogen-like ions of nuclear charge Z can be obtained in the quasistatic approximation. Starting with the linear Stark coefficient for the components (k) of a line [286],

$$C_{pq}^{(k)} \simeq \frac{3}{2} \frac{4\pi\epsilon_0}{e} \frac{1}{Z} \frac{\hbar}{m_e} [n_p(n'_p - n''_p) - n_q(n'_q - n''_q)], \quad (9.47)$$

where n' and n'' are parabolic quantum numbers of upper and lower level of the line, one introduces an effective Stark coefficient $\overline{C_{pq}}$ for the total line by proper averaging over all Stark components [262, 415],

$$\overline{C_{pq}} \approx \left(\frac{3}{8}\right)^{2/3} \frac{3}{2} \frac{4\pi\epsilon_0}{e} \frac{1}{Z} \frac{\hbar}{m_e} (n_p^2 - n_q^2). \quad (9.48)$$

With the mean Holtsmark field strength \overline{F} (9.40) one obtains a full halfwidth $\Delta\omega_{1/2} = 2\overline{\Delta\omega_{pq}}$ of the line profile,

$$\Delta\omega_{1/2} \approx 13.7 \frac{\hbar}{m_e} \frac{z}{Z} (n_p^2 - n_q^2) n_z^{2/3}. \quad (9.49)$$

(Keep in mind, that Z refers to the nuclear charge of the emitting ion and z to the charge of the perturber ions). In wavelength units we may write the equation

$$\frac{\Delta\lambda_{1/2}}{\lambda_{pq}} \approx 8.4 \times 10^{-22} \frac{\lambda_{pq}}{\text{nm}} (n_p^2 - n_q^2) \frac{z}{Z} \left(\frac{n_z}{\text{m}^{-3}}\right)^{2/3}. \quad (9.50)$$

The widths do not depend on the temperature in this approximation because the ions are considered static. The actual widths are usually smaller since the Holtsmark distribution neglects ion-ion interactions and Debye screening. The tendency to smaller widths is also evident from the field distributions of Fig. 9.3, which reveal lower mean fields with decreasing Debye length. Both effects introduce a weak temperature dependence.

As example, the short review on the broadening of the hydrogen Balmer- α line [416] mirrors quite vividly the progress of both theory and experiment during a period of about 50 years. Modern theory for lines of hydrogenic species starts with combining quasistatic and impact broadening [417], the approach now usually referred to as *Standard Theory*. It was continuously improved with fewer approximations. Other theoretical approaches emerged as well like, for example, the frequency fluctuation model, a relaxation model, the so-called unified theory, the model microfield method, a Green's function approach, computer simulation methods, and the so-called Generalized Theory by Oks [418]. Some particulars of this approach are still subject of controversial disputes [419, 420].

Naturally, also experimental studies of line shapes advanced and details of both experiments and theoretical approaches are found in the monographs by Griem [8, 286] and in a more recent book by Oks [421] which is solely on the broadening of hydrogen and hydrogen-like ions.

Although spectroscopic observations of lines seem straightforward and can be done with sufficient precision, for *bench-marking* measurements they rely on sufficient homogeneity of the plasma, independent diagnostics of the plasma parameters, no self-absorption of the lines, and reliable identification of the continuous background radiation. The observation of total line profiles is certainly desirable for comparison with theoretical calculations, for diagnostic

purposes the determination of the halfwidths suffices. In principle, line shifts can be used for that purpose too, but they are usually less accurate.

Plasma sources employed for systematic investigations of hydrogen Balmer lines range from rf-discharges at low densities of 10^{19} m^{-3} [422] via shock tubes and wall-stabilized arcs [423] at intermediate densities to pinch discharges like the gas-liner pinch operated at high densities of up to 10^{25} m^{-3} [424]. In this device, the species of interest (“test gas”) are emitted from a homogeneous plasma region along the axis of the pinch column with no cold boundary, the plasma parameters are obtained by collective Thomson scattering, and optical depth of the lines and continuous background emission can be checked by varying independently the concentration of the test gas atoms (ions) down to zero.

The achievable quality of line profiles in the gas-liner pinch is illustrated in Fig. 9.4. It shows the P_α -line of HeII emitted from a discharge in hydrogen with helium added as test gas. The background is determined from discharges without helium and it is from continuum radiation and from the wing of the nearby H_β -line of hydrogen. Background and best-fit Voigt profile are indicated. The unshifted position of the line is marked and clearly reveals a red-shift.

Theoretical line profiles for hydrogen and hydrogen-like helium are found, for example, in Table I of Griem [286], and for hydrogen in [426], these being calculated according to the model microfield method. It is customary to express the profiles $\mathcal{L}(\alpha)$ in these tables in terms of reduced wavelengths $\alpha = |\lambda - \lambda_{pq}|/F_0$, where F_0 is again the Holtsmark field strength.

Since the halfwidth suffices to derive the electron density from a line as pointed out above, most theoretical calculations quote only its value and compare it with experiments and vice versa. One could suppose that the hydrogen

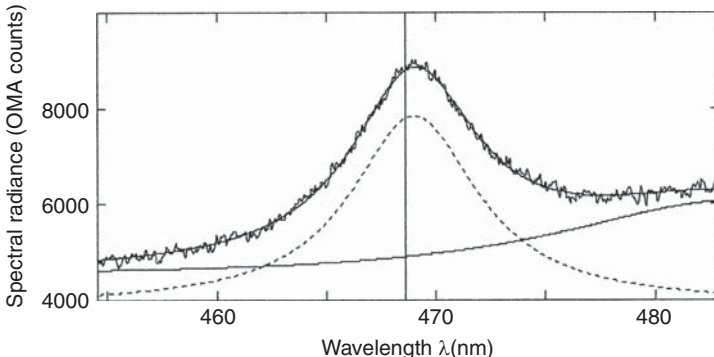


Fig. 9.4. Experimental profile of the P_α -line of HeII at 468.6 nm from [425]. The plasma parameters from Thomson scattering are $n_e = 3.5 \times 10^{24} \text{ m}^{-3}$ and $k_B T_e = 6.8 \text{ eV}$. The dashed line gives the best-fit Voigt profile, and the full line shows the background

Balmer-alpha line H_α at 656.28 nm is the first line to employ for diagnostics but unfortunately due to its unshifted central component it is rather sensitive to ion dynamics. Nevertheless, at high electron densities of 10^{23} m^{-3} to 10^{25} m^{-3} experiments and calculations with the frequency fluctuation model [424] suggest the following approximation neglecting the weak temperature dependence:

$$\frac{\Delta\lambda_{1/2}}{\text{nm}} \approx 2.8 \times 10^{-17} \left(\frac{n_e}{\text{m}^{-3}} \right)^{0.72}. \quad (9.51)$$

The most widely employed line is the H_β -transition at 486.13 nm with a central dip. Ion dynamics influences essentially only this dip, and the line is also less sensitive to optical depths effects. Recently recommended halfwidths [427], which are consistent with earlier results [286], are represented by

$$\frac{\Delta\lambda_{1/2}}{\text{nm}} \simeq 1.03 \times 10^{-15} \left(\frac{n_e}{\text{m}^{-3}} \right)^{0.681}. \quad (9.52)$$

The weak temperature dependence becomes noticeable at low temperatures, say below 0.5 eV, and if necessary full tables must be consulted. Uncertainties of the halfwidths should be below 10%. Halfwidths for high principal quantum number hydrogen Balmer lines, which are observed in radio-frequency discharges and tokamak edge plasmas, can be found in [428].

Detailed investigations are also available for the Paschen lines of He II; they are still in a convenient wavelength range, the widths are narrower, and the ion emits at higher temperatures. A critical analysis of theoretical calculations and of new and previous measurements was reported for the P_α -line at 468.56 nm in [425]. Neglecting again the weak temperature dependence a semiempirical relation slightly modified from that originally proposed by Pittman and Fleurier [429] is the best fit to all reliable data, especially at high densities:

$$\frac{\Delta\lambda_{1/2}}{\text{nm}} \simeq 2.74 \times 10^{-20} \left(\frac{n_e}{\text{m}^{-3}} \right)^{0.831}. \quad (9.53)$$

The uncertainty is about $\pm 10\%$.

The corresponding relation for the He II P_β -line at 320.31 nm proposed in [430] is

$$\frac{\Delta\lambda_{1/2}}{\text{nm}} \simeq 9.78 \times 10^{-18} \left(\frac{n_e}{\text{m}^{-3}} \right)^{0.74}. \quad (9.54)$$

Shifts for both lines were analyzed in [425] as well.

With increasing principal quantum number n_p of the upper level lines of a spectral series become broader and simultaneously move closer as the spacing of the levels decreases. At some principal quantum number their widths will be broader than their spacing and they practically merge, producing a quasi continuum that passes into the true recombination continuum. Assuming quasistatic Stark broadening Inglis and Teller [431] used the above condition to derive a relation for the principal quantum number $n_{p,max}$ of the upper level

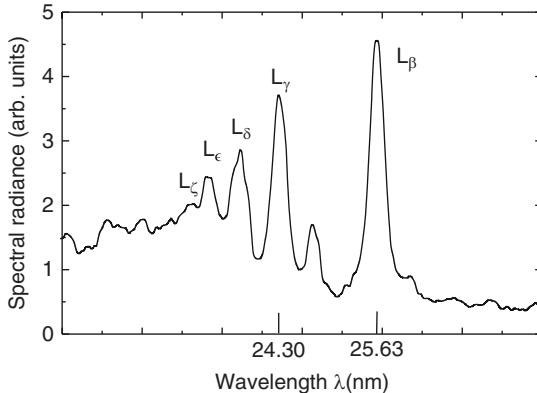


Fig. 9.5. Lyman series of He II emitted from a hydrogen pinch plasma seeded with helium [433]; from Thomson scattering $n_e = 3 \times 10^{24} \text{ m}^{-3}$ and $k_B T_e = 8 \text{ eV}$

of the last line (Inglis–Teller limit) which is still resolvable. We combine (9.49) with the energy separation of levels ($n_{p,max}$) and ($n_{p,max}+1$),

$$\hbar \Delta\omega_{1/2} \approx Z^2 E_R \left(\frac{1}{n_{p,max}^2} - \frac{1}{(n_{p,max} + 1)^2} \right), \quad (9.55)$$

and obtain

$$\lg \frac{n_z}{\text{m}^{-3}} \approx 29.12 + 4.5 \lg Z - 1.5 \lg z - 7.5 \lg n_{p,max}. \quad (9.56)$$

Just the observation of the last line thus allows an easy estimate of the perturber density n_z . A classical example can be seen in Fig. 5 of [432] which shows all members of the Balmer series of hydrogen as emitted from a wall-stabilized arc at several plasma conditions. Figure 9.5 illustrates the merging of the Lyman series of He II emitted from a hydrogen plasma ($z = 1$) with a small amount of helium ($Z = 2$). The last resolvable line is L_ϵ with $n_{p,max} = 6$, and the Inglis–Teller limit gives the estimate $n_e = 4.4 \times 10^{24} \text{ m}^{-3}$, which is reasonable in comparison with the value obtained by Thomson scattering.

Isolated Lines of Atoms and Ions

Stark broadening of well-isolated lines of atoms and ions is predominantly by electron impact with small contributions due to the quadratic Stark effect by the microfield (and possibly quadrupole interactions) which induces shifts of upper and lower levels. The static contribution is even smaller for ions compared with the contribution to neutral atom lines, so it may be neglected in many cases. Following Griem (p. 97 of [286]) halfwidths and shifts of the

lines from neutral atoms can be written by approximate formulas:

$$\Delta\omega_{1/2} \approx 2w + 1.75A(1 - 0.75R)2w, \quad (9.57)$$

$$\Delta\omega_s \approx d \pm 2.00A(1 - 0.75R)w. \quad (9.58)$$

w is the electron impact half halfwidth usually employed in theoretical calculations and d is the electron impact shift at the line maximum. Due to the asymmetry of the lines the shift is slightly different at the halfwidth of the line. The parameter A is a measure of the ion contribution and R , the Debye shielding parameter defined by

$$\begin{aligned} R = \frac{R_0}{\varrho_D} &= (36\pi)^{1/6} \left(\frac{e^2}{4\pi\epsilon_0 k_B T_e} \right)^{1/2} n_e^{1/6} \equiv a \\ &= 8.34 \times 10^{-5} \left(\frac{k_B T_e}{\text{eV}} \right)^{-1/2} \left(\frac{n_e}{\text{m}^{-3}} \right)^{1/6}, \end{aligned} \quad (9.59)$$

measures the influence of Debye shielding and ion-ion correlations. R is identical to Hooper's parameter a employed in his microfield distributions (9.41). The sign in the shift equation is equal to the low velocity limit of d . For both equations the parameters A and R should be in the following ranges:

$$0.05 \leq A \leq 0.5 \quad \text{and} \quad R \leq 0.8. \quad (9.60)$$

For $A > 0.5$, forbidden components begin to overlap and the transition to the linear Stark effect sets in.

Tabulations of calculated electron widths w' (in Å) and ion broadening parameters A (both tagged in the following with the index "tab" for clarity) are given for a number of atoms in Griem [286] (Table IV) for an electron density of 10^{22} m^{-3} . With the scalings $w \propto n_e$ and $A \propto n_e^{1/4}$ the parameters for other densities are readily derived:

$$\frac{w'}{\text{\AA}} = 10^{-22} \frac{w_{\text{tab}}}{\text{\AA}} \frac{n_e}{\text{m}^{-3}} \quad \text{and} \quad A = 3.16 \times 10^{-6} A_{\text{tab}} \left(\frac{n_e}{\text{m}^{-3}} \right)^{1/4}. \quad (9.61)$$

The full halfwidth of a line thus may be written

$$\begin{aligned} \frac{\Delta\lambda_{1/2}}{\text{nm}} &\approx 2 \times 10^{-23} \frac{w_{\text{tab}}}{\text{\AA}} \frac{n_e}{\text{m}^{-3}} \\ &\times \left[1 + 5.53 \times 10^{-6} A_{\text{tab}} \left(\frac{n_e}{\text{m}^{-3}} \right)^{1/4} (1 - 0.75R) \right]. \end{aligned} \quad (9.62)$$

For singly ionized atoms, ion broadening is negligible in most cases ($A \rightarrow 0$). Table V of [286] gives half halfwidths w_{tab}^* for an electron density of 10^{23} m^{-3} ; full halfwidths are thus obtained from

$$\frac{\Delta\lambda_{1/2}}{\text{nm}} \approx 2 \times 10^{-24} \frac{w_{\text{tab}}^*}{\text{\AA}} \frac{n_e}{\text{m}^{-3}} \quad (9.63)$$

Quite a number of more recent theoretical calculations and detailed studies have been reported since then, specifically also for lines of multiply ionized atoms. This is also true for experimental investigations. Both are discussed in [8] and [397], a critical review of experimental halfwidths and shifts is found in [398].

Experimental investigations of specific transitions along the isoelectronic sequence, of analogous transitions in homologous atoms, and of spectral series are intriguing since they may reveal regularities and similarities which can be concealed in theoretical calculations due to the number of necessary approximations. Respective studies of available width and shift data were reported in [434] and [435]. One more recent example are systematic measurements of the $3p \rightarrow 3s$ doublet in lithium-like ions up to NeVIII carried out on a pulsed arc [436] and on a pinch discharge [437, 438]. With increasing nuclear charge of the ions deviations from latest quantum mechanical width calculation increase [408], a puzzle not yet resolved.

Lines with close-by *forbidden* transitions offer specific advantages, especially also in the presence of collective fields (see Chap. 10). The best-known examples are the transitions $4^1D \rightarrow 2^1P$ at 492.193 nm and $4^3D \rightarrow 2^3P$ at 447.148 nm with the forbidden components $4^1F \rightarrow 2^1P$ and $4^3F \rightarrow 2^3P$. At low electron densities these are extremely weak, and the allowed line is practically isolated. Figure 9.6 shows the gross structure of the line profile at intermediate densities. It may be characterized by the halfwidth $\Delta\lambda_{1/2}$ of the allowed transition, by the separation of allowed and forbidden component $\Delta\lambda_{sep} = \lambda_a - \lambda_f$, and by the ratio of the maxima of forbidden and allowed component in the line shape function, i.e., $\mathcal{L}(\lambda_f)/\mathcal{L}(\lambda_a)$.

With increasing electron density Stark mixing of the wavefunctions of the upper levels occurs and the intensity of the forbidden component increases correspondingly. In addition, the lines shift apart, broaden and overlap, and transition from quadratic to linear Stark effect sets in. A quick estimate of the electron density may be obtained simply from the peak intensity ratio of

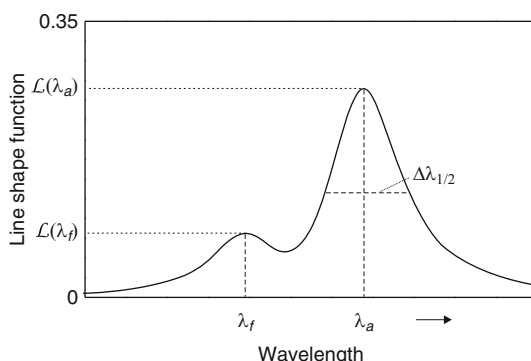


Fig. 9.6. Gross structure of a line with forbidden component

forbidden and allowed component. Neglecting the weak temperature dependence, the ratio for the $4^3D, ^3F \rightarrow 2^3P$ transitions, for example, is in the density interval $(1 \times 10^{20} - 3 \times 10^{21}) \text{ m}^{-3}$

$$\frac{\mathcal{L}(\lambda_f)}{\mathcal{L}(\lambda_a)} \approx 6 \times 10^{-23} \frac{n_e}{\text{m}^{-3}}. \quad (9.64)$$

One should keep in mind that the instrument function may modify the ratio [439].

A number of theoretical and experimental studies of lines with forbidden components have been reported and are discussed in [8]. For the most up-to-date information we refer again to the NIST bibliographic database [399].

Forbidden transitions in polar diatomic molecules like BCl and CS have been successfully employed for electric field measurements too, [440, 441]. The field mixes the wavefunctions of the Λ -doublet sublevels of each rotational level of a ${}^1\Pi$ electronic state so that, after excitation of one sublevel by a laser, emission of a line in a forbidden branch becomes feasible.

We conclude this chapter by comments on macroscopic electric fields, which are usually absent in plasmas due to shielding effects. Just for that reason, however, they exist in the sheath region in front of electrodes and walls, where they produce sufficient Stark splitting of Rydberg levels. Due to the low electron densities in those regions, the levels are too weakly populated for observable emission, and the respective investigations are done, therefore, by laser spectroscopic techniques, e.g., [442].

9.2.5 Effects of Collective Fields

The first investigation of the influence of oscillating electric fields on line profiles was reported by Blochinzew [443], and the effect is very often referred to as *dynamic* or *high-frequency* Stark effect. In plasmas, such fields are usually connected with plasma (Langmuir) oscillations in the high-frequency range and with ion-acoustic oscillations at low frequencies. Blochinzew solved the Schrödinger equation for the hydrogen atom in a monochromatic rf-field and found that lines split into a number of components separated from the line center by multiples of the frequency of the field. In thermal plasmas this line splitting, however, is never observed, since broadening by the microfield by far dominates. In turbulent plasmas, on the other hand, oscillations can be excited several orders of magnitude above their thermal level, and the dynamic Stark effect then manifests itself by *satellites* on the line and its wings. Corresponding observations on the Balmer lines of hydrogen in a turbulent heating experiment as well as theoretical calculations for the presence of both quasistatic and oscillating fields were reported, for example, in [444]. Line profile calculations for hydrogenic ions are also presented in [445]. For further theoretical and experimental investigations the reader is referred to the monographs of Oks [446] and Griem [8, 286].

Low-frequency turbulent electric fields will not show up as satellites, but lead to corresponding broadening of the lines in addition to the always present broadening by the microfield and by the Doppler effect. In principle, such turbulent field broadening can be extracted from the line profile if the electron density, which determines the intrinsic Stark broadening component, is known and the Doppler component is obtained from lines not prone to quasistatic broadening: assuming a trial field distribution function for the turbulent field, the corresponding profile is convolved with the thermal Stark profile and the Doppler profile, and the best fit is found. First identification of such broadening was reported in [447]: comparison of the P_α - and P_β -lines of HeII allowed estimates of the turbulent field. The higher the principal quantum number of the upper level in a line series, the stronger is broadening by the turbulent field (9.47) whereas relative Doppler broadening remains constant (9.20).

The assumption of the trial function for the turbulent field is a minor problem. In case of fully developed isotropic turbulence, the electric field distribution will be a three-dimensional Gaussian according to the central limit theorem. In most other cases, a Rayleigh distribution is probably a better approximation [448] though it is close to a Gaussian.

One-dimensional wave fields are best studied by making use of the polarization of emitted hydrogen and hydrogenic ion lines: Stark splitting and polarization properties are different for σ ($\Delta m = \pm 1$) and π ($\Delta m = 0$) components emitted parallel and perpendicular to the wave field [449]. This simply leads to a different width of the line profile which thus depends on the direction of observation. An example of such investigations is found in [450]. A novel approach which needs no assumption on the distribution function has been proposed by Alexiou et al. [451]: they extract the autocorrelation function from the experimental line profile, which must be of good quality and must cover a fair part of the line wings, and arrive thus at the mean turbulent field strength.

At high plasma densities level shifts due to the quasistatic ion microfield may come into resonance with the wavefield resulting in *dips* on the line profile, each dip being straddled by two maxima [446]. They were indeed observed and studied systematically, for example, on the L_α -line of hydrogen emitted from a gas-liner pinch [452]. With the electron density obtained from Thomson scattering it was verified over the density range 5×10^{23} to $2.5 \times 10^{24} \text{ m}^{-3}$ that the separation of both first-order dips corresponds to $2\omega_{pe}$ and that of the second-order dips to $4\omega_{pe}$. Although originally assumed that thermally excited Langmuir waves are sufficient for the observation of these dips, it is argued in [8], that plasma waves excited above thermal level are necessary.

Another structure now called *x-dip* yet not connected with collective fields was observed on the blue wing of the H_α -line of hydrogen in a dense helium plasma [453]. The dip was reproducible and did not vary with the electron density. It was proposed that it is caused by a charge exchange process. Further theoretical considerations are found in [421].

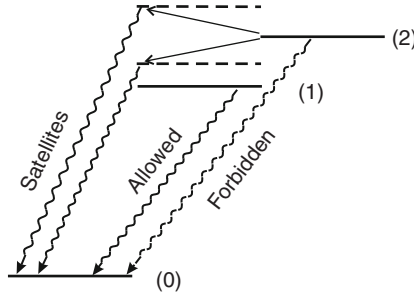


Fig. 9.7. Level scheme for satellite emission

The other Stark broadening method for wave field measurements has been put forward by Baranger and Mozer [454] and was first realized by Kunze and Griem [455] in a theta pinch discharge. The method utilizes three suitable levels of an atomic system designated by (0), (1) and (2) with one allowed ($\Delta l = \pm 1$) and one forbidden ($\Delta l = 0, \pm 2$) transition as illustrated in Fig. 9.7. Two such often employed systems are, for example, the levels 4^1D , 4^1F and 2^1P , and 4^3D , 4^3F and 2^3P in HeI. The separation in angular frequency units ω_{12} between levels 1 and 2 is small.

Without any oscillating field, the typical emission profile is that of Fig. 9.6. With a high-frequency electric field at ω_{pe} present, where the index (pe) may indicate oscillations at the electron plasma frequency, two effects are observed: two satellite lines appear symmetrically spaced by ω_{pe} around the forbidden transition, and the separation between allowed and forbidden transition increases. The satellites can be viewed each as a two-quantum transition: absorption of a plasmon $\hbar\omega_{pe}$ to a virtual level and emission of the far satellite with the photon energy $\hbar(\omega_{10} + \omega_{pe})$, and emission of a plasmon together with the emission of the near satellite with the photon energy $\hbar(\omega_{10} - \omega_{pe})$. The transition probability for the satellites was calculated by second-order perturbation theory. Due to the small energy separation of the levels (1) and (2) these are practically populated according to their statistical weights, and the emission coefficient of the satellites is, therefore, usually given normalized to that of the total allowed transition [8, 454],

$$S_{+-} \approx \frac{3}{8} \frac{l_>}{2l_1 + 1} \left(\frac{4\pi\epsilon_0 \hbar n_1}{m_e e (z+1)} \right)^2 \frac{n_1^2 - l_>^2}{|\omega_{12} \pm \omega_{pe}|^2} E_{rms}^2, \quad (9.65)$$

where $E_{rms} = \sqrt{\langle E(t)^2 \rangle_{av}}$ is the root mean square average of the oscillating field. (z) is the charge state of the ion, n_1 the principal quantum number of the upper level of the allowed line, and $l_>$ is the larger one of the two angular momenta l_1 and l_2 .

With increasing strength of the oscillating field higher order terms must be considered in the perturbation treatment [8]. This reveals that the magnitude

of the satellites changes: the near satellite decreases and the far one becomes stronger. In addition higher order satellites emerge. At first, satellites separated from the allowed line by $2\omega_{pe}$ can be seen, their relative magnitude given by

$$S_{2\pm} \approx \frac{1}{2} S_+ S_- \left(\frac{\omega_{12} \pm \omega_{pe}}{\omega_{pe}} \right)^2. \quad (9.66)$$

Next, satellites at $3\omega_{pe}$ should appear around the forbidden line, etc.

The emission of weak satellites as well as of the allowed and forbidden line can be enhanced by pumping the upper level (1) or any other close-by level of the same principal quantum number n_1 with laser radiation [456] thus increasing the population densities of the upper levels, which equilibrate quickly by collisions. Since pumping is along the laser beam only, the enhanced emission is localized and spatially resolved observation is feasible. The highest sensitivity is certainly achieved by scanning the satellites, forbidden and allowed line with a tunable dye laser. In a model experiment with lithium atoms in a microwave field satellites up to $7\omega_{pe}$ around the forbidden line and up to $6\omega_{pe}$ around the allowed line could be identified [457]. Lithium atoms are the other most widely employed species. Polarization of the satellites is yet another quantity, which can be tapped to obtain information on the type of waves propagating in the plasma [458].

The interpretation of the shape of the satellites is difficult because of the forbidden component which can be enhanced by low-frequency turbulence. Also, the dynamic Stark effect produces a shift of the allowed line in addition to the usual Stark shifts: the correction is given in [8] as

$$\Delta\omega_s \approx 2(S_+ S_-)^{1/2} \omega_{12}. \quad (9.67)$$

On the experimental side, attention has to be paid to the possibility of H_2 and He_2^* molecular lines mocking satellites. Indeed this was observed in several plasmas, for example, in the afterglow of a laser-produced helium plasma [459] and in a low-pressure after-glow discharge in hydrogen [460]. The problem was analyzed in [461]. In principle, however, such difficulties in the interpretation of observations can be eliminated by just looking for the presence of other molecular lines and/or by checking if satellites change their wavelength with density or stay fixed as molecular lines will do.

Intense oscillating fields due to the laser beam itself are present also in laser-produced plasmas and can induce the corresponding satellites around dipole forbidden components displaced by the laser frequency. They have been identified by several groups, see e.g., [462]. Their intensity is a measure of the local laser field in the plasma. These satellites should not be confused with true plasma satellites at ω_{pe} identified on He-like lines emitted in the X-ray region from laser-produced plasmas [463]: at the high plasma densities the electric microfield is so strong, that the He-like energy levels are effectively degenerate and linear Stark broadening occurs.

9.2.6 Magnetic Field Effects

Magnetic fields split the energy levels of atomic systems and hence the spectral lines, an effect known as Zeeman effect. For weak magnetic fields, i.e., the magnetic interaction is smaller than the spin-orbit interaction, each level with the total angular momentum quantum number J splits into $(2J + 1)$ states characterized by the magnetic quantum number M . The dipole transitions between such two states obey the selection rules $\Delta M = 0, \pm 1$. π -components ($\Delta M = 0$) do not emit along the magnetic field direction and are linearly polarized parallel to the field when observed perpendicular to the field. σ -components ($\Delta M = \pm 1$) are circularly polarized in the direction of the field, and linearly polarized in the direction perpendicular to it, with the plane of polarization perpendicular to the field.

The energy shift of the states is given by

$$\Delta E = M g \mu_B B, \quad (9.68)$$

where μ_B is the Bohr magneton, B is the magnetic flux density (magnetic field), and g_L is the Landé factor. It depends on the type of coupling; in LS -coupling it is given by

$$g_L(J, L, S) = 1 + \frac{J(J+1) - L(L+1) + S(S+1)}{2J(J+1)}. \quad (9.69)$$

For the energy shift of the Zeeman components of a transition between an upper level (p) and a lower level (q) one thus obtains

$$\Delta E_{pq} = [M_p g_L(p, J, L, S) - M_q g_L(q, J, L, S)] \mu_B B, \quad (9.70)$$

or in wavelength units

$$\frac{\Delta\lambda_{pq}}{\text{nm}} = 4.669 \times 10^{-8} [M_q g_L(q, J, L, S) - M_p g_L(p, J, L, S)] \left(\frac{\lambda}{\text{nm}} \right)^2 \frac{B}{\text{T}}. \quad (9.71)$$

Historically, this multi-component pattern is referred to as anomalous Zeeman effect. The simplest case is for $g_L(p) = g_L(q) = 1$ with one unshifted π -component and two shifted σ -components. This holds for singlet systems $S = 0$, the pattern is known as Lorentz triplet, and one talks of the normal Zeeman effect.

With increasing magnetic field the Paschen-Back regime is reached, where the magnetic interaction becomes larger than the spin-orbit interaction breaking the spin-orbit coupling. Each electric dipole multiplet $(SL)_p \rightarrow (SL)_q$ splits into three components, an undisplaced central component and two symmetrically shifted components. The selection rules are

$$\Delta M_S = 0 \quad \text{and} \quad \Delta M_L = 0, \pm 1, \quad (9.72)$$

and for the shift between the triplets we have

$$\Delta E_{pq} = \Delta M_L \mu_B B, \quad (9.73)$$

Both Paschen–Back and Lorentz triplets are given by the same relation. At still higher magnetic fields the quadratic Zeeman effect may become significant.

The relative intensities of the components of a Zeeman pattern can be calculated, for example, see [214, 221]. As aide-mémoire we write the splitting (9.73) in angular frequency units

$$\Delta\omega_{pq} = \Delta M_L \frac{\mu_B}{\hbar} B = \frac{1}{2} \omega_{ce} \Delta M_L, \quad (9.74)$$

where $\omega_{ce} = eB/m_e$ is the electron cyclotron frequency: Zeeman splittings are always of the order of ω_{ce} .

In plasmas, each Zeeman component is broadened by Stark and by Doppler effect. Since Doppler width and Zeeman splitting scale differently with wavelength, (9.20) and (9.71),

$$\frac{\Delta\lambda^{split}}{\Delta\lambda_{1/2}^G} \propto \lambda_{pq} \frac{B}{(k_B T_z / m_z)^{1/2}}, \quad (9.75)$$

it is obvious to select long-wavelength transitions for magnetic field measurements and, whenever possible, preferably in heavy ions. For that reason, magnetic dipole transitions within the ground state of heavy ions (p. 98) have been employed in fusion devices [464, 465]. Since Doppler broadening still dominated and does in most hot plasmas, the polarization properties of σ -and π -components had to be utilized.

Especially low ion temperatures prevail in the outer edge of fusion plasmas and within a divertor. For these conditions profiles for the Lyman and Balmer lines of hydrogen and deuterium have been calculated and studied including Zeeman splitting, which is here observable; for example see [466–469].

In plasmas of higher density usually Stark broadening dominates and use has to be made again of the polarization to extract information on the magnetic field. Direct Zeeman splitting of the CV 2p → 2s triplet lines was observed in a plasma focus device with fields of the order of 100 T [470] and in laser-produced plasmas for fields up to 20 T [471].

An elegant novel approach was suggested and experimentally tested in [472]. The authors exploit the fact that different fine structure components experience different splitting. Since Doppler broadening and Stark broadening are practically the same for the components, this results in a different width of the lines even if Doppler or Stark broadening dominates.

We finally note that the high-frequency Stark effect was also extended to include a static magnetic field [473].

Atoms/ions moving with a velocity v across a magnetic field experience the Lorentz electric field

$$\mathbf{E} = \mathbf{v} \times \mathbf{B}, \quad (9.76)$$

in their rest frame. This naturally leads to corresponding additional Stark splitting. The effect is known as *motional Stark effect* and was pointed out already by Drawin et al. [474], although its significance was recognized only much later when the emission from energetic hydrogen beams injected into tokamak plasmas for heating was analyzed [475]. The Balmer H_α -line, for example, splits into nine principal components with distinct polarization, the fractional polarization of the line being a measure of the magnetic field pitch angle. Zeeman splitting by the magnetic field is usually much smaller than the Stark splitting [8]. Detailed atomic physics modeling of the Stark–Zeeman spectrum of deuterium Balmer- α line for both beam into plasma and into gas is presented in [476].

The motional Stark effect on energetic helium atoms was studied on forbidden lines in the visible [477]. As discussed on p. 169, the intensity of the forbidden line increases with the electric field and hence here with the magnetic field.

9.2.7 Broadening due to Self-Absorption

As absorption starts to play a role it is strongest at the maximum of a line and weak on the wings, and hence results in effective broadening of lines leaving the plasma. The effect is often referred as *opacity broadening*. The profiles are obtained by solving the equation of radiative transfer, Sect. 2.4. This is only straightforward for homogenous plasmas. Figure 9.8 illustrates the effect of absorption on the line profiles from a homogeneous plasma slab for several optical depth $\tau_0 = \tau(\lambda_0)$, where the local emission and absorption profiles are identical and are (a) Gaussian and (b) Lorentzian. The radiance of each line is

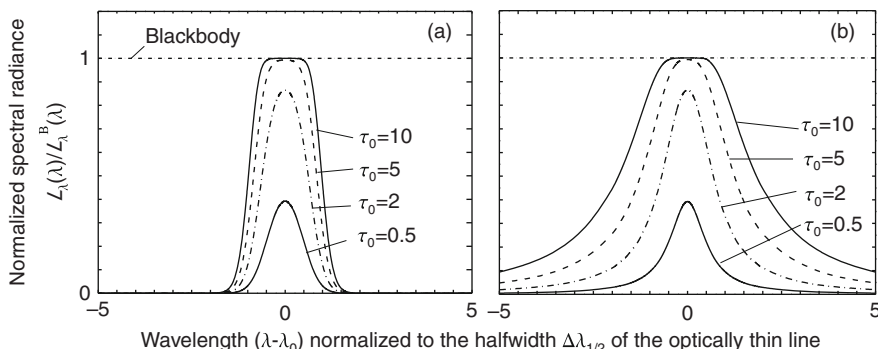


Fig. 9.8. Examples of line shapes of optically thick lines, (a) Gaussian, (b) Lorentzian. τ_0 is the optical depth at the line center

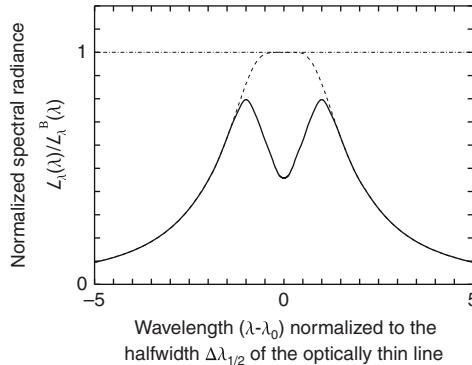


Fig. 9.9. Example of a self-reversed line profile

normalized to the blackbody limit, and the wavelength is given in units of the halfwidth of the optically thin line. With increasing optically depth the lines reach the blackbody limit. In case (a) the halfwidth of the optically thick line increases only slowly with the optical depth in contrast to (b), where the line broadens strongly with τ_0 and develops wide wings through which radiation can escape from the plasma.

For many plasmas the approximation of a homogeneous plasma is not meaningful as a central dip in the line profile appears caused by absorption in cooler boundary regions. The phenomenon is known as *self-reversal* [478, 479]. This is illustrated in Fig. 9.9 for a Lorentzian profile of the emission coefficient. The spectral radiance is normalized again to that of a blackbody at the maximum temperature. The dashed line gives the profile for a homogeneous plasma of optically depth $\tau_0 = 10$, see Fig. 9.8. The condition for the two maxima of the self-reversed line follows from

$$\frac{dL_\lambda(\lambda)}{d\lambda} = \frac{dL_\lambda(\lambda)}{d\tau(\lambda)} \frac{d\tau(\lambda)}{d\lambda} = 0 \quad \text{and is} \quad \frac{dL_\lambda(\lambda)}{d\tau(\lambda)} = 0. \quad (9.77)$$

Pure spectral lines in absorption are observed when external continuum radiation traverses a plasma and the emission coefficients of the lines are negligible. For low optical depth the line shapes of the absorption coefficients are obtained, i.e., a Gaussian, Lorentzian or Voigt profile, to stay with the examples above. The profiles with increasing optical depth are won by simply employing the Beer–Lambert law (2.21). Figure 9.10 shows the shapes of normalized absorption lines for several optical depths τ_0 at the maximum of the absorption coefficient. The area of the absorption profile in units of wavelength given by

$$W(\lambda_0) = \int_{\text{line}} \frac{L_\lambda^{\text{in}}(\lambda) - L_\lambda^{\text{trans}}(\lambda)}{L_\lambda^{\text{in}}(\lambda)} d\lambda \quad (9.78)$$

is used to characterize the total absorption. It is called *equivalent width* since it corresponds to the width of a fictitious rectangular absorption line of

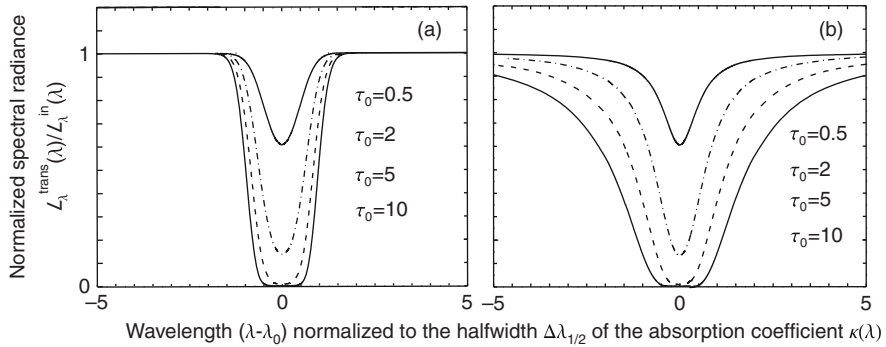


Fig. 9.10. Absorption profiles for several optical depths τ_0 at the center wavelength of the absorption coefficient of (a) Gaussian and (b) Lorentzian shape. $L_\lambda^{\text{in}}(\lambda)$ is the spectral radiance of the incident continuum radiation, $L_\lambda^{\text{trans}}(\lambda)$ that of the radiation leaving the plasma

$L_\lambda^{\text{trans}} = 0$ at λ_0 having the same area. The background continuum provides a convenient reference for $W(\lambda_0)$.

The equivalent width is extensively employed in astronomical studies and has been calculated there for many cases. Since it depends on the total number of absorbing atoms $n(q)$ in the lower level (q) of a line along the line of sight (path length l) and on the absorption cross-section, it is usually given as function of $n(q) f(q \rightarrow p) l$, which is referred to as *curve of growth*.

Tables for the halfwidths of opacity broadened emission lines are given, for example, in [480] for spatially constant source functions. For inhomogeneous plasmas with self-reversal in the profile, no general solutions are possible. One approach by Bartels [481] (reviewed in [478]) assumes LTE and a parabolic radial temperature profile. The model by Karabourniotis et al. is independent of the existence of LTE and employs a one-parameter power law for the source function [479].

Diagnostic Applications

10.1 Verification of Atomic Data

Plasmas provided the first information on ions. Spectra measured with high precision yielded their level structure and they continue to do as our knowledge, especially of multiply ionized heavy atoms, is poor [482].

Well diagnosed plasmas allow the verification of theoretical atomic data as well as the measurement of data not yet accessible by other techniques. Self-consistency among data obtained by a larger number of studies under different plasma conditions offers an additional route to assess the reliability.

The derivation of *transition probabilities*, especially of multiply ionized atoms, from the radiance of emission lines has been and is still being pursued. Prerequisites are several critical factors [220]:

- Absolute calibration of the radiance of the lines, see Sect. 5.2
- Knowledge of the length of the emitting plasma layer
- Absence of self-absorption; in cases of low optical depth corrections can be applied
- Knowledge of the population density of the upper level

The last quantity is certainly the most crucial one, and it is accessible when LTE or PLTE has been established, see Sect. 8.3. The accuracy of branching ratios of transition probabilities for lines from the same upper level is only limited by the accuracy of the radiometric calibration. The investigation of multiplets provides tests for the validity of LS-coupling and thus guides theoretical calculations [483].

At low electron densities the corona population model holds, where the population densities are practically determined by electron induced transitions. Hence the radiances of the spectral lines contain information on the relevant electron collisional rate coefficients, which thus can be extracted within some limits [282, 283]. Excitation rates from the ground state are readily obtained employing (8.34) when the upper levels of lines are essentially populated by collisions from the ground state, i.e., excitation from other

low-lying levels, collisional mixing between close-by levels, and cascading contributions are weak. If low-lying excited levels are strongly populated and have, in addition, a high statistical weight like the metastable level in beryllium-like ions, excitation rates from such levels can be derived with somewhat lower accuracy, see (8.35).

Rather sophisticated modeling of a spectrum or part of a spectrum as it is done for the K-spectra of helium-like ions, for example, allows self-consistent checks of the employed rates for excitation, radiative and dielectronic recombination, and innershell excitation [484]. Introduced to large fusion-oriented plasmas by Bitter et al. [485], those methods are now employed in a number of devices. A review and details may be found in [366].

Transient plasmas offer further possibilities [282, 283]. In the ionizing regime, where recombination is negligible, the time histories of the ions in their successive ionization stages are solely determined by the ionization rate coefficients which can thus be derived (8.44). Plasmas in the recombination regime are correspondingly governed by recombination rates (8.45). One should keep in mind, however, that in principle *effective* rate coefficients in a specific plasma environment are deduced. This can be an advantage but is naturally disadvantageous for comparison with cross-section measurements.

Measurements of the shape of spectral lines in well known plasmas, especially of their width and shift, as function of density and temperature play an important role in plasma spectroscopy and are indispensable to advance and refine theoretical calculations, as was discussed in Chap. 9.

10.2 Measurements of Particle Densities

10.2.1 Particle Densities from Line Emission

Absolute measurements of the radiances $L(p \rightarrow q)$ of optically thin emission lines always give the density $n_z(p)$ of the species in the upper level (p) of the transition, after the local emission coefficient $\varepsilon_z(p \rightarrow q)$ of the line has been obtained, see Sect. 2.3. According to (6.5)

$$n_z(p) = \frac{4\pi \varepsilon_z(p \rightarrow q)}{h\nu_{pq} A_z(p \rightarrow q)}. \quad (10.1)$$

In the limit of LTE total local densities $n_z(\mathbf{r})$ of an ionization stage (z) can thus be deduced, when the partition function $U_z(T)$ is available and the temperature T_e has been determined. Equation (8.3) gives

$$\begin{aligned} n_z &= \frac{n_z(p)}{g_z(p)} U_z(T_e) \exp\left[+\frac{E_z(p) - E_z(q)}{k_B T_e} \right] \\ &= \frac{4\pi \varepsilon_z(p \rightarrow q)}{h\nu_{pq} A_z(p \rightarrow q)} \frac{U_z(T_e)}{g_z(p)} \exp\left[\frac{h\nu_{pq}}{k_B T_e} \right]. \end{aligned} \quad (10.2)$$

In case of high-lying upper levels (p) in PLTE with the ground-state (g) of the next ionizations stage ($z+1$), its ground state density $n_{z+1}(g)$ is retrieved from a line. Employing the Saha–Eggert equation (8.12) leads to the total density

$$n_{z+1}(g) = \frac{4\pi \varepsilon_z(p \rightarrow g)}{h\nu_{pq} A_z(p \rightarrow q)} \frac{2g_{z+1}(g)}{g_z(p)} \frac{1}{n_e} \left(\frac{m_e k_B T_e}{2\pi \hbar^2} \right)^{3/2} \exp\left(-\frac{E_{z,p\infty}}{k_B T_e}\right). \quad (10.3)$$

Now, in addition to T_e also n_e must be known. It certainly has to be checked that the conditions for LTE and PLTE, respectively, are complied with, Sect. 8.3.

Naturally also high-lying doubly excited states (p^*) of an ion of charge z , which decay to a singly excited state by a so-called satellite transition, can be in PLTE with their ionization limit [349]. Since this limit corresponds to a singly excited level of the next ionization stage ($z+1$), the satellite transition gives the density of that level through the Saha–Eggert relation.

In the other limit of sufficiently low electron densities for the corona approximation to be applicable, where excitation of a level is essentially only from the ground state (g) by electron collisions, the electron density n_e , the electron temperature T_e , and the excitation rate coefficient $X_z(g \rightarrow p)$ must be known. Since the population densities of the excited levels are low, the total density $n_z \simeq n_z(g)$ holds. Equation (8.32) thus yields from a transition $(p) \rightarrow (q)$

$$\begin{aligned} n_z &= \frac{A_z(p \rightarrow)}{n_e X_z(g \rightarrow p)} n_z(p) \\ &= \frac{4\pi \varepsilon_z(p \rightarrow q)}{h\nu_{pq} A_z(p \rightarrow q)} \frac{A_z(p \rightarrow)}{n_e X_z(g \rightarrow p)}. \end{aligned} \quad (10.4)$$

Forbidden transitions of the M1-type between fine structure levels of the ground state of highly ionized species are a special case. As mentioned on p. 98, the green and red iron lines emitted by Fe XIV and Fe XV, respectively, were originally observed in the solar corona and successfully used for its analysis. Now, such lines emitted from a number of elements are utilized in fusion plasmas [232]. Electron and proton collisions within the ground state are usually fast enough even at the low electron densities of such plasmas that the population densities of the fine structure levels are according to PLTE, i.e., here simply according to the statistical weights of the levels, because of their small energy separation. Given the statistical weight $g(p_i)$ of a fine structure level (p_i), the density of an ionization stage is obtained simply by summation over all levels (p_i):

$$\begin{aligned} n_z \simeq n_z(g) &= \frac{n(p_i)}{g(p_i)} \sum_j g(p_j) \\ &= \frac{4\pi \varepsilon_z(p_i \rightarrow q)}{h\nu_{p_i q} A_z(p_i \rightarrow q)} \frac{1}{g(p_i)} \sum_j g(p_j). \end{aligned} \quad (10.5)$$

The great advantage from the experimentalist's point of view is the fact, that many of these transitions are in the visible and near ultraviolet. Their radiative transition probabilities are certainly very small, but the ground state population is high, and hence they are observable.

10.2.2 Particle Densities Employing Injected Fast Beams

Charge exchange processes (p. 132) allow the measurement of the density of fully stripped ions which do not radiate and are thus not detectable. Usually energetic neutral hydrogen or deuterium beams, which are injected into the plasmas for heating, are also used for that purpose [486, 487]. The process is represented by (7.55). If the beam density is given by n_b and the ion density in the plasma by n_{z+1} , the population density $n_z(p)$ of a selectively populated level (p) of the recombined ion z is

$$n_z(p) = \frac{\langle \sigma^{cx}(v) v \rangle n_{z+1} n_b}{A(p \rightarrow)} \quad (10.6)$$

where $\sigma^{cx}(v)$ is the cross-section as function of the relative velocity v between ion and beam particle, and the average is over the velocity distribution function of the ions. In practice, however, v is equal to the velocity v_b of the beam particles since this is high, and there is thus no need of averaging. From the emission of a line $(p) \rightarrow (q)$ we derive

$$n_{z+1} = \frac{4\pi \varepsilon_z(p \rightarrow q)}{h\nu_{pq}} \frac{A(p \rightarrow)}{\sigma^{cx}(v_b) v_b n_b}. \quad (10.7)$$

Recombination is selectively into levels with high principal quantum number n_p and there into large angular momentum states l . As a consequence, emission is preferably by $\Delta n_p = -1$ transitions, which are at long wavelengths; however, possible collisional mixing between the fine structure levels should be accounted for. Observation perpendicular to the neutral beam yields spatially resolved results, a great advantage of this *active spectroscopy* method with beams.

Of utmost importance is the possibility to measure the density of α -particles produced in burning plasmas. Their velocity is much higher than that of typical neutral beam atoms, $v_\alpha \gg v_b$, and hence only the cross-section at the α -particle velocity is needed.

Fast lithium beams have been successfully employed to study the distribution of light ions in the edge region of fusion oriented plasmas [488, 489].

A recent detailed review of the diagnostic possibilities with beams is found in [490]. It includes extensive references to work published so far.

10.2.3 Density of Molecules

Due to the complexity of molecular spectra the determination of molecular densities is naturally far more difficult. Emission lines (bands) give again

the densities of the upper levels, i.e., vibrational and rotational populations in electronically excited states. Collisional radiative models to connect these populations with that of the ground state are rare, p. 151, although for a number of chemical reactions already the population densities in excited states may be the ones of interest. For some molecules (e.g., CH and C₂), the coronal approximation suffices.

In molecular hydrogen or deuterium, the Fulcher bands ($d\ ^3\Pi_u \rightarrow a\ ^3\Sigma_g^+$) in the triplet system, which emit in the convenient wavelength interval 590–640 nm, are one of the most intense transitions. CR models connect the upper levels with the levels of the ground state [383, 491]. When taking the ratio Balmer H_γ-line to Fulcher transitions, the electron density cancels and the ratio H/H₂ is readily obtained [492]. A novel technique was developed by combining CR models for the atom, the molecule, and the negative hydrogen ion H[−]. It was found that the line ratio H_α/H_β yields the ratio H[−]/H [493].

10.2.4 Actinometry

Since modeling of some plasmas especially of those containing reactive species is extremely difficult because of the large number of participating processes with even mostly unknown reaction rates, a technique known as *actinometry* is frequently employed. It was first introduced in [494] to a (CF₄)-plasma. It is based on the addition of a gas (actinomer) with well-known excitation characteristics to the plasma at a well-known concentration n_{act} , which should be low enough as not to influence the processes in the plasma. The intensity ratio of a suitable actinomer line and of a transition in the atom, molecule or ion to be measured thus gives the unknown density $n_x(g)$. In the low-density limit the corona approximation holds for the population densities of both species and

$$\frac{n_x}{n_{act}} = const \frac{\varepsilon_x}{\varepsilon_{act}} \frac{X_{act}(T_e)}{X_x(T_e)}. \quad (10.8)$$

If the excitation energies of both lines are about equal, even the temperature dependence in the ratio of the excitation functions drops out. In general, however, collisional radiative models must be employed for both species, and most actinometry systems have even been calibrated by other methods. Argon is most frequently used as actinomer. Some other actinometry systems are O/Ar [495, 496], Cl₂/Ar and Cl/Ar [497], N/Ar [498, 499], where the references are either examples or more recent publications.

10.2.5 Particle Densities from Absorption Measurements

Measurements of the absorption of resonance lines yield directly the density of the ground state of the respective species, and hence should be preferable for that reason. The classical approach is to employ an external incoherent

broadband source much brighter than the plasma. The Beer–Lambert law

$$L_\lambda(x = l, \lambda) = L_\lambda(x = 0, \lambda) \exp(-\kappa(\lambda)l), \quad (10.9)$$

where the plasma is assumed to be homogeneous and the incident radiation enters the plasma at $x = 0$ and leaves it at $x = l$, gives the line absorption coefficient $\kappa(\lambda)$ if induced emission from the upper level is negligible, i.e., the population of the upper level is small. After integration over the absorption profile the integrated line absorption coefficient $\kappa^L(\lambda_{gp})$ is retrieved, which is related to the ground state density by (6.25):

$$n_z(g) = \frac{\kappa^L(\lambda_{gp})}{\pi \lambda_{gp}^2 r_e f(g \rightarrow p)}. \quad (10.10)$$

Xenon and deuterium lamps are usually employed as broadband sources, since many atoms have their resonance lines already in the vacuum ultraviolet spectral region, let alone those of ions with increasing charge state. One example is reported in [500]. The unavailability of suitable sources for all spectral regions limits the wide application of absorption spectroscopy, and the method becomes insensitive as the absorption (optical depth of the resonance line) becomes too large.

Alternatively, a source is employed which emits the identical resonance line (resonance lamp) [501]. Conventional theory taking into account the line profile of the incident radiation is applicable for the analysis [502]. A variant method uses the plasma to be studied also as light source: a spherical mirror placed behind the plasma reflects the resonance line back into the plasma, thus nearly doubling the optical depth. Reflectance of the mirror and transmittance of windows must be accounted for, as must be the effect that, due to the larger optical depth, the line profile of the additional emerging component is broader [503], see also Fig. 9.10.

For the application of tunable lasers we refer to the relevant literature, e.g., [1].

10.2.6 Ratio of Particle Densities from the Spectra of Helium-like Ions

K-spectra of heavy helium-like ions play a role in the diagnostics of hot plasmas and hence will be discussed specifically. Their great advantage is the fact that the lines of interest are close in wavelength, thus avoiding the necessity for even relative calibration of the spectroscopic system. The first detailed spectra were obtained from a tokamak and reported for Fe XXV [485]. Figure 10.1 shows a corresponding spectrum for Ar XVII [330]. In addition to the resonance (w), intercombination (y), and forbidden (x, z) lines, which were addressed already on p. 97, a number of satellites are seen that correspond to transitions from doubly excited states. They follow either dielectronic capture and are called dielectronic satellites (for example, the k-satellite and the

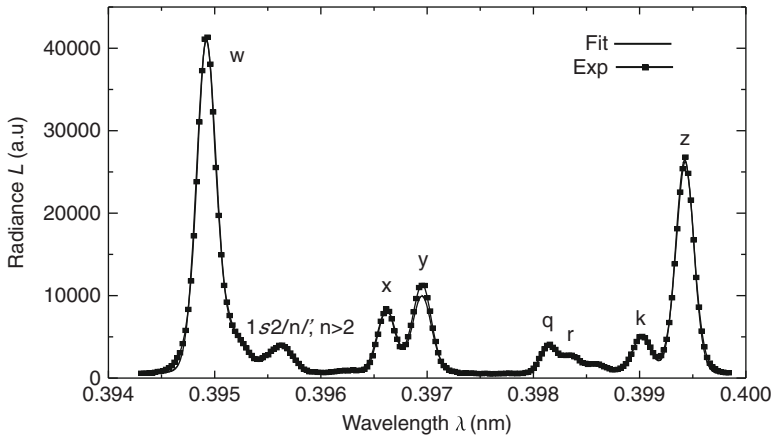


Fig. 10.1. Spectrum of helium-like argon from [330]

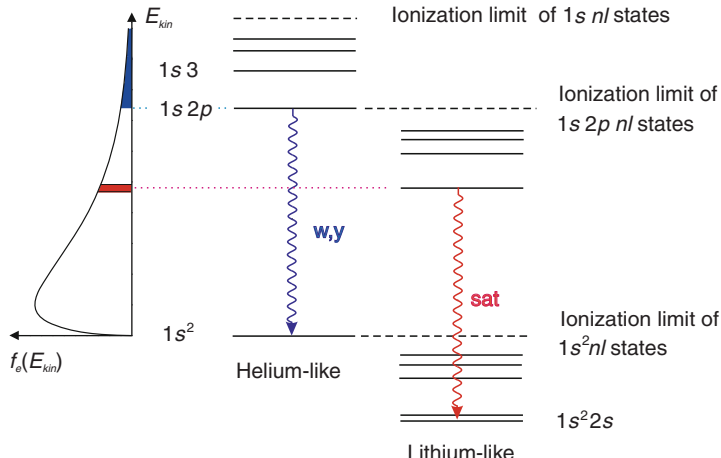


Fig. 10.2. Schematic energy level diagram of helium-like and lithium-like ions

$1s2lnl$, $n > 2$, satellites), or the upper level is populated by innershell excitation like the q - and r -satellites. Gabriel labeled all relevant satellites by a letter, and his notation is now in common use [227].

Figure 10.2 shows a schematic partial energy level diagram, an extension of Fig. 6.4 now including doubly excited states of the lithium-like ion. Collisional excitation to the singly-excited $1s2p$ levels is from the ground state by all electrons above the excitation energy (shaded region); population of doubly-excited levels by dielectronic capture is a resonant process and is only by electrons in a narrow energy interval corresponding to the width of the levels, see p. 130. As a first approximation, we consider now only the dominant excitation process for the lines. The resonance (w) line is collisionally excited

from the ground state and its emission coefficient hence is given by

$$\varepsilon_w \propto n_e X_w(T_e) n_{\text{He}}(g), \quad (10.11)$$

where $X_w(T_e)$ is the excitation rate coefficient. For a dielectronic satellite one may write (p. 131)

$$\varepsilon_{\text{sat}}^{\text{dr}} \propto n_e \alpha_{\text{He}}^{\text{dr}}(T_e) n_{\text{He}}(g), \quad (10.12)$$

and thus the ratio of the emission coefficients is a sole function of the electron temperature

$$\frac{\varepsilon_{\text{sat}}^{\text{dr}}}{\varepsilon_w} = F_1(T_e). \quad (10.13)$$

Satellites due to innershell excitation have the dependence

$$\varepsilon_{\text{sat}}^{\text{in}} \propto n_e X^{\text{in}}(T_e) n_{\text{Li}} \quad (10.14)$$

and their intensity with respect to that of the resonance line is

$$\frac{\varepsilon_{\text{sat}}^{\text{in}}}{\varepsilon_w} \propto F_2(T_e) \frac{n_{\text{Li}}}{n_{\text{He}}}. \quad (10.15)$$

This ratio thus gives the density ratio of the lithium-like and helium-like ionization stages with the electron temperature derived from the dielectronic satellite ratio.

The z-line is essentially populated by recombination of the hydrogen-like ion, and this gives

$$\frac{\varepsilon_z}{\varepsilon_w} \propto F_3(T_e) \frac{n_{\text{H}}}{n_{\text{He}}}, \quad (10.16)$$

i.e., the density ratio of the hydrogen-like and helium-like ionization stages is obtained. In the case of Ar, attention must be paid to a dielectronic satellite labeled (j) that is at the same wavelength position as the z-line. For other helium-like ions like Fe it is clearly separated. Sophisticated population models include collisional mixing between higher levels, cascading and charge exchange, p. 180.

10.3 Temperature Measurements

10.3.1 Atom, Molecule, and Ion Temperature

The particle temperature T_z characterizes the velocity distribution function, if that is Maxwellian. In this case each emission line broadened by the Doppler effect has a Gaussian shape, its halfwidth yielding the temperature (9.20). If other broadening mechanisms like pressure and Zeeman broadening, as well as broadening by the instrument function, are also effective, the true Gaussian component has to be retrieved by some de-convolution procedure, see Sect. 9.1

and Sect. 10.4.1. Available routines for fitting a Voigt function to an experimental profile give automatically the Gaussian and Lorentzian components. If possible, however, one certainly should choose lines with weak pressure (Stark) broadening.

In the boundary region of fusion plasmas the high magnetic field produces a Zeeman pattern of impurity lines usually by the Paschen–Back effect, the components being convolved with the Doppler profile [504]. Using the polarization characteristics aids separating the Zeeman components [465].

Again charge exchange of fast hydrogen or lithium beams with bare nuclei as discussed in Sect. 10.2.2 can be utilized to derive now even the local temperature of these nuclei from Doppler broadened line profiles of the hydrogenic stage. Naturally drifts are obtained as well in all cases and non-Maxwellian components show up in the profile if existing, although it is always difficult to measure accurately low-intensity wings above continuous background radiation. In the literature, these measurements are found under the heading charge-exchange spectroscopy.

10.3.2 Electron Temperature

Line Ratios

The most straightforward approach to obtain the electron temperature from line emission is possible if the population densities of the upper levels of two lines are in PLTE, i.e. if they are connected by the Boltzmann factor (8.2). In this case the ratio of the emission coefficients of two lines at λ_{pq} and $\lambda_{p'q'}$ is simply given by

$$\frac{\varepsilon_z(p \rightarrow q)}{\varepsilon_z(p' \rightarrow q')} = \frac{\lambda_{p'q'}}{\lambda_{pq}} \frac{A_z(p \rightarrow q)}{A_z(p' \rightarrow q')} \frac{g_z(p)}{g_z(p')} \exp\left[-\frac{E_z(p) - E_z(p')}{k_B T_e}\right]. \quad (10.17)$$

It is a sole function of the electron temperature T_e , but as the exponential function reveals, this dependence is most sensitive for $k_B T_e < E_z(p) - E_z(p')$. Hence lines should be selected which have a large energy separation of the upper levels. The accuracy can naturally be increased by observing several lines. In this case it is convenient to derive the population density $n_z(p)$ of the upper levels of all lines with (10.1) and to plot the logarithm of the densities divided by the statistical weight, i.e., of $n_z(p)/g(p)$, as function of the energy $E_z(p)$ of the levels: such a plot is called *Boltzmann plot*, a straight line with slope given by $k_B T_e$. This method has the advantage that lines, which are optically thick, can be identified by a large deviation of their data points from the straight line fit, always provided that the transition probabilities of the observed lines are known with sufficient accuracy, see Sect. 6.2.3. Otherwise, the final accuracy of the temperature is determined by the accuracy of the relative spectral sensitivity calibration of the spectroscopic system (Sect. 5.2) and the noise on the radiance signal of the observed spectral lines.

One always has to check if indeed the assumption of a Boltzmann distribution (PLTE) is justified for the upper levels. In steady-state plasmas the corresponding condition (8.29) should be fulfilled. However, as discussed on p. 148, in transient plasmas the upward or downward excitation flow results in different distributions of the population densities, and equilibrium may not be reached even if the steady-state conditions seem to indicate that.

The population densities of the rotational and vibrational levels of electronically excited states of molecules obtained from line emission are usually characterized by *rotational and vibrational temperatures*, which are deduced by fitting a Boltzmann distribution. Both temperatures are quite formally defined and can differ strongly from the electron temperature in plasmas where the population of these molecular states is governed by processes other than electron collisions.

In this context, a comment may be appropriate on the concept *excitation temperature* T_{exc} . As earlier, this variable is also used to describe the population distribution of excited atomic levels, and it is again obtained by fitting a Boltzmann distribution to the existing population densities. It has no physical meaning, but nevertheless it is often quoted for technical plasmas. Only in case of LTE it equals the electron temperature T_e .

One possibility to extend the temperature range is to observe two lines of consecutive ionization stages, since the energy separation $E_{z+1}(p) - E_z(p') = E_{z+1, gp} + E_{z,p' \infty}$ of the upper levels thus is large. Employing the Saha–Eggert equation (8.12) for the population $n_z(p')$ of the upper level (p') of the line in the ion (z) and the Boltzmann relation (8.2) for the population $n_{z+1}(p)$ of the upper level (p) in the ion ($z+1$) one arrives at

$$\frac{\varepsilon_{z+1}(p \rightarrow q)}{\varepsilon_z(p' \rightarrow q')} = \frac{\lambda_{p'q'}}{\lambda_{pq}} \frac{A_{z+1}(p \rightarrow q)}{A_z(p' \rightarrow q')} \frac{g_{z+1}(p)}{g_z(p')} \times \frac{2}{n_e} \left(\frac{m_e k_B T_e}{2\pi\hbar^2} \right)^{3/2} \exp \left[-\frac{E_{z+1}(p) - E_z(p')}{k_B T_e} \right]. \quad (10.18)$$

The condition for LTE to hold for two ionization stages is fulfilled only in a few cases like, for example, in plasmas of high density for the neutral atom and its first ionization stage. One example given in [8] for densities above 10^{24} m^{-3} is the ratio of the He II line at 486.6 nm and the He I line at 587.6 nm. Further examples for LTE-plasmas are cited in [505]. One drawback is certainly the additional dependence of the ratio on the electron density n_e , which now must be known.

A number of variants can be used for lower densities. One class of line pairs may be described as follows: the upper level (p) of the line in the ion ($z+1$) is in PLTE with the ground state of the ion ($z+2$), the upper level (p') of the second line in the ion z is in PLTE with the ground state of the ion ($z+1$), and both ground states are in coronal equilibrium: $n_{z+2}/n_{z+1} = S_{z+1}/\alpha_{z+2}$. Employing again the Saha–Eggert equation yields

$$\frac{\varepsilon_{z+1}(p \rightarrow q)}{\varepsilon_z(p' \rightarrow q')} = \frac{\lambda_{p'q'}}{\lambda_{pq}} \frac{A_{z+1}(p \rightarrow q)}{A_z(p' \rightarrow q')} \frac{g_{z+1}(p)}{g_z(p')} \frac{g_{z+1}(g')}{g_{z+2}(g)} \times \frac{S_{z+1}}{\alpha_{z+2}} \exp\left[\frac{E_{z+1,p\infty} - E_{z,p'\infty}}{k_B T_e}\right]. \quad (10.19)$$

The line ratio is again a sole function of the electron temperature since ionization S_{z+1} and recombination rate coefficients α_{z+2} are also sole functions of T_e in this approximation. However, now these rate coefficients must be known. With increasing density they may be replaced by collisional-radiative rate coefficients, see p. 147, and a density dependence thus introduced, too.

Another class of line pairs is characterized by a low-lying level (p') of the line in the ion (z) being in PLTE with the ground state (g') of this ion, and the upper level (p) in the ion ($z+1$) being in PLTE with the ground state of the ion ($z+2$). Using the Boltzman relation between (p') and (g'), the Saha-Eggert equation for (p), and connecting the ground states of the ions ($z+1$) and ($z+2$) by the corona equation for ionization equilibrium, one obtains

$$\frac{\varepsilon_{z+1}(p \rightarrow q)}{\varepsilon_z(p' \rightarrow q')} = \frac{\lambda_{p'q'}}{\lambda_{pq}} \frac{A_{z+1}(p \rightarrow q)}{A_z(p' \rightarrow q')} \frac{g_{z+1}(p)}{g_z(p')} \frac{g_z(g')}{g_{z+2}(g)} \times \frac{n_e}{2} \left(\frac{2\pi\hbar^2}{m_e k_B T_e}\right)^{3/2} \frac{S_{z+1}}{\alpha_{z+2}} \frac{S_z}{\alpha_{z+1}} \exp\left[\frac{E_{z+1,p\infty} + E_{z,g'p'}}{k_B T_e}\right]. \quad (10.20)$$

We recall that $E_{z+1,p\infty}$ is the ionization energy of the level (p) and $E_{z,g'p'}$ the excitation energy of the level (p'). As this level is low-lying, it is usually strongly populated and ionization from the level has to be taken into account, i.e., S_z should be replaced again by a collisional radiative ionization rate coefficient S_z^{eff} . Examples of such intensity ratios are given in [7] and [506] for C IV and C III lines.

At low electron densities the *coronal population model* holds, i.e., excitation by electron collisions and depopulation of the levels by radiative decay (Sect. 8.4). The ratio of the emission coefficients of two lines within one ion thus is given by

$$\frac{\varepsilon_z(p \rightarrow q)}{\varepsilon_z(p' \rightarrow q')} = \frac{\lambda_{p'q'}}{\lambda_{pq}} \frac{A_z(p \rightarrow q)}{A_z(p \rightarrow)} \frac{A_z(p' \rightarrow)}{A_z(p' \rightarrow q')} \frac{X_z(g \rightarrow p)}{X_z(g \rightarrow p')} . \quad (10.21)$$

It is independent of the electron density, the dependence on the electron temperature is through the excitation rate coefficients which must now be known. If two lines are considered the upper levels of which are excited by a dipole transition from the ground state, the rate coefficients in the effective Gaunt factor approximation (p. 119) give

$$\frac{\varepsilon_z(p \rightarrow q)}{\varepsilon_z(p' \rightarrow q')} = \frac{\lambda_{p'q'}}{\lambda_{pq}} \frac{A_z(p \rightarrow q)}{A_z(p \rightarrow)} \frac{A_z(p' \rightarrow)}{A_z(p' \rightarrow q')} \frac{f_z(g \rightarrow p)}{f_z(g \rightarrow p')} \frac{E_{z,gp}}{E_{z,gp'}} \times \exp\left(\frac{E_{z,gp} - E_{z,gp'}}{k_B T_e}\right) \frac{P(E_{z,gp}/k_B T_e)}{P(E_{z,gp'}/k_B T_e)} . \quad (10.22)$$

This suggests again to select lines with a large energy difference $E_{z, gp} - E_{z, gp'}$ of the upper levels. For high accuracy, cascading contributions may have to be included.

Lithium-like ions are one example. Suitable lines are the $3p \rightarrow 3s$ and $3p \rightarrow 2s$ transition on the one hand and the $2p \rightarrow 2s$ transition from the lower level on the other hand, all with very well known transition probabilities. The only drawback is of experimental nature: the lines are in rather different wavelength regions.

The dependence of the line ratios on plasma parameters becomes quickly more complex with increasing electron density, especially if metastable levels (or even low-lying levels) are involved, which are highly populated. Spectra of helium-like ions are characteristic for that, and they usually can be described only by collisional-radiative population models.

Spectra of neutral helium demand specific attention due to the extreme longevity of the metastable levels, which in low-density discharges may even depopulate severely by collisions with the walls and with other atoms or molecules. At very low electron densities, say below $n_e \leq 10^{16} \text{ m}^{-3}$, the corona population model holds and (10.21) may be applied to ratios of singlet to triplet lines. The method was originally proposed by Cunningham (a discussion is found in [350]) and makes use of the fact that the excitation cross-sections for singlet and triplet levels and hence also the excitation rates differ strongly (see p. 122) for high collision energies. Suitable line ratios are thus sole functions of the electron temperature. Lines employed were the transitions $4^3S \rightarrow 2^3P$ at 471.32 nm and $4^1D \rightarrow 2^1P$ at 492.19 nm, however, it is safer to use lines with upper S-levels since they are least affected by collisional mixing with levels of equal principal quantum number n_p . For that reason, we suggest to use the lines $4^3S \rightarrow 2^3P$ at 471.32 nm and $4^1S \rightarrow 2^1P$ at 504.77 nm. Figure 10.3 gives the ratio in the corona limit, i.e.,

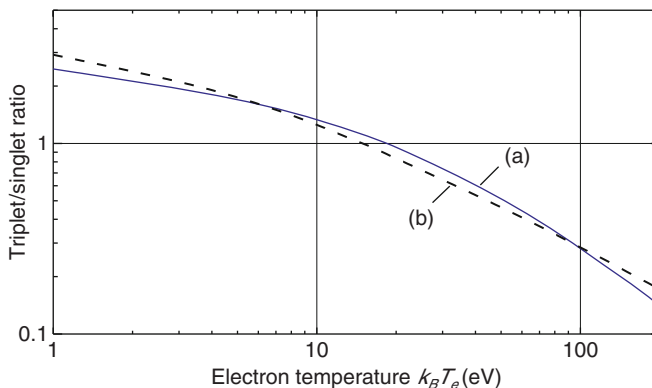


Fig. 10.3. Ratios of HeI lines (a) $4^3S \rightarrow 2^3P$ at 471.32 nm and $4^1S \rightarrow 2^1P$ at 504.77 nm, and (b) $4^3S \rightarrow 2^3P$ at 471.32 nm and $4^1D \rightarrow 2^1P$ at 492.19 nm, in the corona limit

Table 10.1. Line pairs in He I suitable for diagnostics

	Transition	λ_1 (nm)	Transition	λ_2 (nm)	Parameter obtained
(a)	$3^3S \rightarrow 2^3P$	706.52	$3^1S \rightarrow 2^1P$	728.14	T_e
(b)	$3^1D \rightarrow 2^1S$	667.82	$3^1S \rightarrow 2^1P$	728.14	n_e
(c)	$4^3S \rightarrow 4^3P$	471.32	$4^1S \rightarrow 2^1P$	504.77	T_e

for $n_e \leq 10^{16} \text{ m}^{-3}$, employing the most recent critically assessed cross-section data [285].

With increasing electron density, however, excitation and ionization from the metastable levels and collisional redistribution between the levels become strong and the lines are, in addition, density dependent. Collisional radiative models, which may also include radiative transport, give the emission coefficients of the lines as function of electron density *and* temperature. By taking ratios of lines, pairs can be found which depend strongly only on *one* parameter, perhaps only for some limited range of the other plasma parameter. They are thus suited for diagnostics. Some examples are given in Table 10.1. Attention should be paid to lines ending at the 2^1S and 2^3S metastable levels since they are the first ones to become affected by self-absorption, besides lines to the ground state, of course. More recent studies of such line ratios have been reported in [507, 508], and in context with thermal helium beams for the boundary diagnostics of tokamaks in [509]. Due to the finite ionization time injected beam atoms exist at much higher temperatures than in discharge plasmas. The authors quote a usable parameter range $10 \text{ eV} < k_B T_e < 250 \text{ eV}$ in the density range $2.0 \times 10^{18} \text{ m}^{-3} < n_e < 2.0 \times 10^{19} \text{ m}^{-3}$.

In their K-spectra helium-like ions provide a method employing close-by lines as shown on p. 186: the ratio of the emission coefficients of dielectronic satellites and the resonance line (upper level (p')) is a sole function of the electron temperature. Introduced by Gabriel [227], the ratio is written using (7.52)

$$\frac{\varepsilon_{z-1,sat}^{\text{dr}}(p^* \rightarrow q)}{\varepsilon_{z,w}(p' \rightarrow g')} = \frac{\lambda_w}{\lambda_{\text{sat}}} \frac{A_{z-1}(p^* \rightarrow q)}{A_{z-1}(p^* \rightarrow)} \frac{\alpha_z^{\text{dr}}(g' \rightarrow p^*)}{X_z(g' \rightarrow p')} . \quad (10.23)$$

Spectra of helium-like ions up to Ni have been used [510], and even that of Kr has already been observed [511]. Higher accuracy of the ratios is obtained by including cascading transitions or by modeling the total K-spectrum, p. 180.

Non-thermal components of the electron energy distribution like high energy tails will certainly modify any triplet to singlet ratio: whereas they hardly influence the excitation of triplet levels due to the small asymptotic cross-section, they strongly affect the excitation of singlet levels. This influence of hot electrons on He I lines was demonstrated in a plasma divertor simulation experiment [512]. Non-Maxwellian components certainly leave corresponding

signatures also on spectra of highly ionized atoms in high-temperature plasmas. An example is the ratio of the $3p \rightarrow 1s$ resonance and intercombination line in helium-like ions [513], or the above ratio (10.23) of dielectronic satellites and resonance line, only the latter being enhanced by a high-energy tail [514].

Because in the corona approximation all electrons with energies above the excitation energy participate (see Fig. 10.2), the population densities and hence the emitted lines indeed reflect to some extent the shape of the energy distribution function above threshold. A general inversion procedure, however, is not possible. Nevertheless, some information may already be obtained by observing a number of lines with differing excitation energies and by assuming a mathematical function of the distribution with few adjustable parameters, which are varied till the population model fits the observations. Ideally, the whole emission spectrum should be used. This was done with the visible spectrum of a neon glow discharge [370]. The analysis employed the Bayesian probability theory.

In some cases, trace gases may be added in order to have sufficient lines with different threshold excitation [515]. They are usually inert gases, but also the emission from molecules in nitrogen discharges was utilized [516–518]. The population distribution of the vibrational levels in this case even gives information on the low-energy part of the distribution function.

An interesting line ratio method was proposed and applied to laser-produced plasmas by Marjoribanks et al. [519]. They employed the ratio of identical transitions emitted from isoelectronic ions of different elements. Deficiencies in the kinetic model for the population densities and in the collisional rates should cancel to first order in the ratio of lines and thus lead to reasonable accuracies, see also [8].

As soon as lines become *optically thick*, none of the preceding methods is applicable. In a homogeneous plasma, the profiles of optically thick lines develop a flat top and the spectral radiance approaches that of a blackbody, see p. 154. The absolute value of the spectral radiance thus gives the electron temperature via Planck's law (5.2) and, to be more precise, in a real plasma at the optical depth $\tau \approx 1$ according to (2.32).

Resonance lines are usually the transitions to become truly optically thick. In order to verify the optical thickness it is advised to select at least doublet lines whose radiance differs at low optical depth. With increasing optical depth the lines broaden, their spectral radiance becomes equal [520], a sign of large optical thickness, and they finally may even merge to one broad line [137].

Optically thick lines from plasmas with gradients are characterized by self-reversal, p. 177. In cases of LTE and cylindrical symmetry, the temperature can be deduced from the maxima of the reversed profiles. The theory was developed by Bartels [481] and reviewed in [478, 521]. He showed that the radiance of the two maxima is about 80% of the blackbody radiance at the temperature which exists at $\tau \approx 2$.

Line to Continuum Ratio

For hydrogen plasmas and pure plasmas containing only the hydrogenic and fully stripped ions the ratio of suitable line intensities to the underlying continuum provides a convenient and accurate temperature diagnostic. No calibration of the optical system is necessary. If lines are selected with the upper level in PLTE with the bare nuclei, the population density is given by the Saha–Eggert equation (8.12), and bremsstrahlung and recombination continuum by (6.81) and (6.72). The ratio for a continuum interval $\Delta\lambda$ underneath the line is then a sole function of the temperature:

$$\frac{\varepsilon_z(p \rightarrow q)}{\int_{\lambda_{pq}-\Delta\lambda/2}^{\lambda_{pq}+\Delta\lambda/2} (\varepsilon^{\text{ff}} + \varepsilon^{\text{fb}}) d\lambda} = f(T_e). \quad (10.24)$$

For lines ending at high principal quantum numbers (n_q) even the recombination contribution becomes negligible, since it scales with $1/n_q^3$. Ratios for the Balmer lines of hydrogen are given in [7]. A lower temperature limit for this method is enforced by the H⁻-continuum (p. 109) which, depending on the density, becomes strong below 1.5 eV.

In helium plasmas easily accessible candidates are the HeII P _{α} - and P _{β} -lines at 468.6 and 320.3 nm. For PLTE to hold for the upper levels, the electron densities should be, according to (8.26), above $2 \times 10^{21} \text{ m}^{-3}$ or 10^{20} m^{-3} , respectively. For contributions by singly ionized helium atoms to bremsstrahlung and recombination radiation to be negligible, temperatures must be above about 8 eV.

The method can, in principle, be extended to lower temperatures if the He⁺ contributions are properly accounted for. The ratio becomes a rather strong function of the electron temperature but also density dependent due to the changing degree of ionization. Ratios are given for several electron densities in [522]. At temperatures below about 3 eV bare helium nuclei and their contributions to the continuum radiation are practically absent, and ratios of HeI lines to underlying continua become the ratios of choice. Useable ratios are also given in [7].

Several applications to argon plasmas have been reported, e.g. in [523]. The upper levels of selected lines ought definitely to be in PLTE with the ground state of Ar II, and for the calculation of the continuum newest Biberman factors ξ^{fb} and ξ^{ff} should be taken for (6.78) and (6.83). A study of the free-bound factor has been reported in [524], and for the free–free part, the Gaunt factor tables of Karzas and Latter [236] seem adequate so far.

Recombination Edges

As illustrated in Fig. 6.5 for a hydrogen plasma, recombination continua are characterized by discontinuities which occur as a consequence of recombination into subsequent shells. Plasmas should be purely hydrogenic for

contributions to the continuum from other ionization stages to be negligible. If one measures the continuum at the wavelength λ_1 and λ_2 in wavelength intervals $\Delta\lambda_1$ and $\Delta\lambda_2$ on each side of a discontinuity, one obtains from (6.72) and (6.81)

$$\frac{[\varepsilon^{\text{fb}}(\lambda_1) + \varepsilon^{\text{ff}}(\lambda_1)] \Delta\lambda_1}{[\varepsilon^{\text{fb}}(\lambda_2) + \varepsilon^{\text{ff}}(\lambda_2)] \Delta\lambda_2} = f(T_e), \quad (10.25)$$

i.e., the ratio is a function of the electron temperature. Unfortunately, the discontinuity is never sharp because of the smooth transition between the end of a line series and the continuum, e.g., see Fig. 9.5. It is customary, therefore, to choose the wavelengths λ_1 and λ_2 at some suitable distance from the discontinuity which also allows to avoid possible impurity lines [525], or one extrapolates the continuum to the position of the discontinuity. Continuum ratios at the Lyman and Balmer limit are given in [8]. Because of the limited applicability this temperature diagnostic is not routinely used.

Short- and Long-Wavelength Continuum

Continuum emission covers the whole spectral region from short to long wavelengths, its spectral shape being illustrated in Fig. 6.1. At long wavelengths it is solely bremsstrahlung. As the absorption coefficient increases strongly with wavelength, $\kappa^{\text{ff}}(\lambda) \propto \lambda^3$ according to (6.93), the plasma will finally become optically thick, and the spectral radiance at the surface approaches the Planck function. For low-density plasmas this will be at very long wavelengths (microwave and radio-frequency region) depending, of course, on the size of the plasma and on the temperature. For dense pinch discharges [526] and laser-produced plasmas this can be in the infrared and even in the visible spectral region. The temperature of nonideal metal plasmas was obtained in this way [527]. It suffices to fit either the relative spectral radiance to a Planck function or to measure the spectral radiance at one wavelength absolutely by comparison with a radiometric standard source (Chap. 5.2). One has to keep in mind that the temperature corresponds to the plasma layer where the optical depth is about $\tau \approx 1$; see the discussion of optically thick lines on p. 192.

At very short wavelengths the spectral emission coefficient $\varepsilon_\nu(\nu)$ as function of frequency of both bremsstrahlung and recombination radiation displays a dependence $\exp(-h\nu/k_B T_e)$, i.e., it is an extremely strong function of the temperature, (6.81) and (6.71). A logarithmic plot of the spectral radiance vs frequency (photon energy) thus yields a straight line, its slope given by the temperature. In long-lived magnetically confined hot plasmas, where photon counting techniques combined with pulse height analysis are usually employed, respective graphs are thus intrinsically obtained, and perturbations by impurity lines from heavy elements are readily identified [528]. An example of laser-produced plasmas is shown in [529].

Non-Maxwellian tails of the distribution function show up as tails on the short-wavelength spectrum. Unfortunately, since such distribution functions are usually anisotropic and each electron produces a bremsstrahlung spectrum, an inversion is difficult [11].

A convenient approach to measure the electron temperature employs thin metallic absorber foils, p. 30, placed in front of a detector. Metal and foil thickness are chosen such that in addition to radiation at all long wavelengths also short-wavelength line radiation is absorbed as well. The ratio of the integrated radiation transmitted through *two* different foils is a sole function of the electron temperature [530], which is thus readily obtained by comparing an experimental ratio with computed ones.

Ratio of Ionization Stages and Time Behavior

In steady-state low-density plasmas the distribution of the ionization stages of an element is a function of the electron temperature only, the concentrations being given by the corona relation (8.39). As illustrated in Fig. 8.1, each ionization stage (z) exists in a temperature range around the electron temperature of maximum abundance $T_{e,z\max}$. An estimate of T_e can thus simply be obtained from observing the mere existence of an ion. With increasing electron density the ion distribution becomes also dependent on the electron density and $T_{e,z\max}$ of the charge states shifts to lower temperatures: a temperature estimate requires now the knowledge of n_e .

The electron density must be known also in transient ionizing plasmas. The time constant τ of disappearance of an ionization stage (approximately its lifetime) is given by $\tau = 1/n_e S_z$ according to (8.45). An estimate of T_e is thus obtained from τ using the ionization rate coefficient S_z .

10.4 Measurements of the Electron Density

10.4.1 Electron Densities from Line Profiles

General Considerations

The width of plasma-broadened lines is a convenient quantity for the derivation of the electron density, Sect. 9.2.4, and such measurements are widely employed [286]. In principle, the shift of lines may be used as well if theoretical calculations have been verified with sufficient accuracy; however, shift calculations are usually less accurate as they are easily affected by fairly fine effects of even differing sign [531].

Experimental profiles contain broadening by the Doppler effect and by the instrument function too, and the part solely due to the plasma environment has to be retrieved by a de-convolution process; see, for example, [532, 533], p. 155 and Sect. 10.3.1. A forward approach may also be quite

satisfactory: a theoretical line profile is assumed and convolved with the instrument function and with a Gaussian Doppler profile according to the atom/ion temperature, and a least-square fit to the *entire* experimental profile yields the most likely half-width and shift. In general, the achievable accuracy of the obtained electron density is limited by the accuracy of the theoretical profiles and their experimental verification.

An advice of caution is appropriate at this point. In a number of low-pressure discharges operated in hydrogen, in hydrogen-inert gas mixtures or even in water-vapor, excessive Doppler broadening of hydrogen Balmer lines has been observed, e.g., [534, 535] and references therein. This broadening is caused by fast hydrogen atoms which are produced by fast ions reflected as neutrals from the metal electrodes after the ions had been accelerated in the boundary sheath in front. Neglect of such broadening in the de-convolution process leads to Stark profiles which are too small and thus to electron densities too low.

It is certainly desirable that selected lines are free of close-by neighboring lines, although curve fitting procedures allow, at least to some extent, separation into individual components or lines.

A clear determination of the continuum background is mandatory. For that accurate measurements of the profile wings are needed, but curve fitting can again be very useful in identifying the background. In cases where tracer gases are added for the density determination, discharges without those gases give the shape of the background.

Transitions to the ground state (g) or to a metastable level (m) are first prone to self-absorption because of their high population density. However, since the optical depth at the line center is $\tau(\lambda_0) \propto n_z(g) f(g \rightarrow p) \mathcal{L}(\lambda_0)$, also strong lines with a large f-value are easily affected and possibly should be avoided. The optical depth may be checked by placing a mirror behind the observed plasma volume thus practically doubling the optical depth and identifying its influence in this way, or one simply observes several lines with differing strengths and checks their relative radiance against expected theoretical ratios.

Hydrogen and Hydrogen-like Ions

At low temperatures lines from hydrogen atoms are the most useful ones because of the large linear Stark effect, and at high temperatures only lines from hydrogen-like ions may show sufficient broadening for the same reason. The Balmer lines of hydrogen are in the convenient visible spectral region and are the most investigated ones. A very weak temperature dependence is an additional advantage. The Balmer-alpha line at 656.28 nm can be used up to densities of 10^{25} m^{-3} [424], its halfwidth given by (9.51). Halfwidths of the H $_{\beta}$ -line at 486.13 nm are described by (9.52).

For low electron densities as are typical for radiofrequency discharges ($n_e \approx 10^{19} \text{ m}^{-3}$) and the edge plasma of fusion experiments ($n_e \approx 10^{21} \text{ m}^{-3}$),

recent calculations provide new halfwidths for high principal quantum number Balmer lines [428]. Observation of the widths of a whole line series certainly increases the reliability of the measurement. Examples of such applications are found in [536] and [537], respectively.

Lines between high Rydberg levels of hydrogen show sufficient Stark broadening even at the very low electron densities of interstellar plasmas and clouds. They are in the radio-frequency region and are usually referred to as radio recombination lines since the upper levels are populated by recombination. They are an indispensable tool for the radioastronomer [538]. The strongest lines are between Rydberg levels $n_p = n + 1$ and $n_q = n$ and are designated as $H\alpha$ -lines. Most recent Stark parameters are found in [539].

The next species along the iso-electronic sequence is He II. The widths of the Paschen lines P_α at 468.56 nm and P_β at 320.31 nm have also been well established and provide densities to an uncertainty of about 10%, (9.53) and (9.54).

For lines from highly ionized hydrogen-like species one usually has to rely on theoretical calculations which in most cases have not been verified experimentally to sufficient accuracy [8, 398, 399].

Isolated Lines

The list of isolated lines emitted by atoms and nonhydrogenic ions, the profiles of which have been studied theoretically and/or experimentally, is steadily increasing, and for available broadening parameters the reader should consult, as already suggested on p. 168, the NIST bibliographic line broadening data base [399] as well as [286] and [398].

For lines emitted by ions the halfwidths scale linearly with the electron density n_e according to broadening by electron collisions (9.32); for lines from atoms a slightly increased dependence is possible due to ion contributions, p. 168. For optimum accuracy of the derived densities the temperature should be known, although the dependence is usually weak (9.32) and accounted for in the tables of Griem [286], which give the halfwidths employing (9.62) and (9.63).

Helium

Helium deserves specific attention since it is often employed as discharge gas and popular as trace element to plasmas. Furthermore, lines ending at the $n = 2$ singlet and triplet levels are also conveniently in the visible spectral region for observation. Due to the metastability of the lower levels 2^1S and 2^3S , their population densities are high. With increasing electron density this also holds for the 2^1P and 2^3P levels due to collisional coupling of all $n = 2$ levels, and self-absorption of corresponding lines has to be watched for, too.

The most recent calculations for He I have been published by Omar et al. [540] for dense plasmas (5×10^{21} to $5 \times 10^{23} \text{ m}^{-3}$) and compared with experimental and theoretical investigations reported in the literature. General

agreement is observed, consolidating the reliability of these line profiles for density diagnostics. Adler and Piel [439] focused in their experiment at lower densities (10^{20} to $3 \times 10^{21} \text{ m}^{-3}$) on the transitions $4^1\text{D} \rightarrow 2^1\text{P}$ and $4^3\text{D} \rightarrow 2^3\text{P}$ at 492.193 nm and 447.148 nm, respectively, with their forbidden components $4^1\text{F} \rightarrow 2^1\text{P}$ and $4^3\text{F} \rightarrow 2^3\text{P}$. In case low radiance at low densities does not permit high-resolution measurements, the simple intensity ratio of forbidden to allowed transition gives a reasonable electron density value employing (9.64).

Like the high-principal quantum number Balmer lines of H I discussed in p. 197, the corresponding transitions in He I also allow measurements at low densities. First calculations for triplet lines of the diffuse series $1s\,nd\,{}^3\text{D} \rightarrow 1s2p\,{}^3\text{P}$ have been reported and applied to spectra obtained from the outer region of the divertor of the JET tokamak [541].

Argon

Argon is probably the most widely used filling gas in discharges for technical applications. Recent calculations of Stark broadening parameters of visible Ar I lines are presented in [542]. They are compared with published experimental values and other theoretical calculations. One strong, well isolated, and for diagnostics well suited transition is the line $4p' \rightarrow 4s$ at 696.54 nm. We cite a relation given in [543]

$$\frac{\Delta\lambda_{1/2}}{\text{nm}} = 8.50 \times 10^{-25} \left(\frac{1}{k_{\text{B}}T_{\text{e}}/\text{eV}} \right)^{0.37} \frac{n_{\text{e}}}{\text{m}^{-3}}, \quad (10.26)$$

which should be accurate to better than 10% for electron densities up to $n_{\text{e}} \approx 3 \times 10^{23} \text{ m}^{-3}$.

Extensive measurements of profiles of Ar II lines are found in [544] for the density range 0.2 to $2.0 \times 10^{23} \text{ m}^{-3}$, with comments in [398]. In general, the uncertainties are around 25% on the average. Recent measurements extended the range up to $9 \times 10^{23} \text{ m}^{-3}$, for some lines [545].

10.4.2 Electron Densities from the Ratio of Lines

Examination of the line ratios (10.17)–(10.22) in Sect. 10.3.2, which are used for electron temperature measurements, reveals that only the ratio of lines of two subsequent ionization stages with the upper levels being in equilibrium (10.18) can directly lead to the electron density n_{e} if the temperature has been determined by another method. As mentioned previously, the strong requirement of LTE is normally fulfilled even at high densities only for atoms and their first ionization stage.

Starting from low electron densities of the pure corona limit, where no electron density dependence between the relative populations of excited levels and hence of emitted lines exists, such a dependence can be introduced with increasing electron density for some levels (p') of atoms and ions when collisional depopulation rates become comparable to the radiative decay rates.

The second line has to be selected from a level (p), which still decays essentially by radiation in order for the ratio to be density dependent. As soon as the collisional depopulation of this level becomes noticeable too, the density dependence disappears. Each ratio hence is sensitive only in a restricted density regime.

The population densities of both upper levels (p) and (p') are given to a first approximation through

$$n_z(g) n_e X_z(g \rightarrow p) \simeq n_z(p) A(p \rightarrow), \quad (10.27)$$

$$n_z(g) n_e X_z(g \rightarrow p') \simeq n_z(p') [A(p' \rightarrow) + n_e X_z(p' \rightarrow)], \quad (10.28)$$

where $X_z(p' \rightarrow)$ represents the sum of all collisional rate coefficients out of level (p'). The ratio of both lines thus is

$$\begin{aligned} \frac{\varepsilon_z(p \rightarrow q)}{\varepsilon_z(p' \rightarrow q')} &\simeq \frac{\lambda_{p'q'}}{\lambda_{pq}} \frac{A_z(p \rightarrow q)}{A_z(p \rightarrow)} \frac{A_z(p' \rightarrow)}{A_z(p' \rightarrow q')} \frac{X_z(g \rightarrow p)}{X_z(g \rightarrow p')} \\ &\times \left[1 + n_e \frac{X_z(p' \rightarrow)}{A_z(p' \rightarrow)} \right]. \end{aligned} \quad (10.29)$$

For low electron densities the coronal limit is retrieved. Collisional depopulation is usually strongest to close-by levels, where the energy separation between the levels is very small in comparison to the electron temperature. In this case the temperature dependence of $X_z(p' \rightarrow)$ is weak, i.e., it is practically negligible. If furthermore upper levels are selected for which the excitation rate coefficients have a similar temperature dependence, the respective ratio also does not depend on the electron temperature. Equation (10.29) simplifies to

$$\frac{\varepsilon_z(p \rightarrow q)}{\varepsilon_z(p' \rightarrow q')} \simeq \text{const} \left[1 + n_e \frac{X_z(p' \rightarrow)}{A_z(p' \rightarrow)} \right]. \quad (10.30)$$

More accurate line ratios valid over a large density regime are naturally obtained by calculating the population densities $n_z(p)$ and $n_z(p')$ within the frame of a kinetic collisional radiative model.

As example, we again consider ions of the helium isoelectronic sequence, p. 97 and p. 185. At low densities the $n = 2$ triplet levels are strongly populated, making intercombination (y) and forbidden (z) lines to the ground state observable despite lower transition probabilities. With increasing electron density collisional coupling with the $n = 2$ singlet levels and ionization out of the levels reduces the population density, thus introducing the density dependence with respect to the resonance line.

The density dependence of the ratio resonance to intercombination line in O VII and C V was studied quite early in pinch discharges [546, 547]. Gabriel and Jordan [548] analyzed the line emission in C V to Ne IX over 12 orders of magnitude in the density and identified thus the usable density regimes. Extensions to heavier helium-like ions are reviewed, for example, in [549]. In helium the intercombination line is not observable due to the very low

transition probability. Density-sensitive line ratios, however, have been identified for transitions between excited levels in HeI like the line ratio (b) in Table 10.1 on p. 191.

Suitable ratios have been found also in a number of other multiply ionized atoms, for example, in the boron [550, 551], nitrogen [552], oxygen [553], sodium and copper [554] isoelectronic sequences and in nickel-like tungsten [555]. For ratios in ArI we refer to [556].

A different possibility is offered by dielectronic satellites of the resonance line L_α of hydrogen-like ions: the relative populations of doubly excited triplet states due to dielectronic capture are modified by collisional transitions from nearby autoionizing levels. Hence, such line ratios of satellites depend on the electron density and can be used for its measurement [549, 553]. One advantage is obvious: self-absorption, which often influences the radiance of resonance lines, is absent; the lower levels of the satellites are excited states.

A method for low pressure nitrogen plasmas utilizing ratios of molecular lines has been investigated in [557]; it is based upon a detailed kinetic model for the nitrogen molecule [558]. The principle is as follows: the distribution of the population densities of the vibrational states of the ground state is a sensitive function of the electron density in some cases, and this distribution determines the population distribution of the vibrational levels of the excited state $C^3\Pi_u$. Hence, measurements of the optical transitions from all relevant levels of that state allow conclusions on the electron density. Unfortunately the method is suboptimal as the electron and the gas temperature are required for the analysis. We conclude by referring to [516]. The authors showed that the emission coefficient of the N_2^+ molecular band gives the electron density.

For the experimentalist the great advantage of line ratio methods is obvious: only a relative spectral sensitivity calibration of the detection system is required. Caution is advised if two lines far apart in wavelength are used: as pointed out on p. 35, in some devices reflection of radiation from the wall can contribute, and the reflectivity is usually wavelength dependent. The true line ratio is thus modified.

10.4.3 Electron Densities from the Continuum Emission at Long Wavelengths

The emission coefficient of bremsstrahlung (6.81) for plasmas of completely stripped atoms ($n_e = Zn_Z$) is given at *long* wavelengths, $h\nu < 0.05 k_B T_e$, where also recombination radiation is negligible, by

$$\varepsilon_\lambda^{\text{ff}}(\lambda) \simeq 4.108 \times 10^{-37} \times \frac{(n_e/\text{m}^{-3})^2}{(k_B T_e/E_R)^{1/2}} \times \frac{Z}{(\lambda/\text{nm})^2} G^{\text{ff}}(T_e, \lambda) \frac{\text{W}}{\text{m}^3 \text{nm sr}}. \quad (10.31)$$

It is a strong function of the electron density n_e and a weak function of the electron temperature T_e , since also the Gaunt factor $G^{\text{ff}}(T_e, \lambda)$ changes only slowly with T_e . Hence a crude measurement of T_e allows already the derivation

of reasonable electron densities from absolute continuum measurements. For that reason corresponding investigations have been carried out particularly on hydrogen plasmas, $Z = 1$, where the Gaunt factor varies at long wavelengths in the range $G^{\text{ff}}(T_e, \lambda) = 3.0 \pm 1.3$ [236].

With impurities present in the hydrogen plasma their contributions to the emission coefficient must be accounted for (6.87). As discussed in p. 107, it is common to characterize the impurity content by an effective ionic charge z_{eff} which is the ratio of the actual emission to that of a pure hydrogen plasma [559, 560].

Due to the generally less known Biberman factors $\xi^{\text{ff}}(z, T_e, \lambda)$ (6.83), density measurements of other than hydrogen plasmas employing the continuum emission are rare and difficult to interpret. Bremsstrahlung due to electron-atom collisions can be important (p. 108), particularly in technical plasmas. An example of such electron density measurements is presented in [561].

10.4.4 Electron Densities from Other Spectroscopic Observations

A couple of other methods are available, which allow more or less accurate measurements in very specific cases. The derivation of the electron density simply from the identification of the last observable member (Inglis–Teller limit) of a line series must certainly be listed here (9.56). This method is indeed rather useful and reasonably accurate at low electron densities when high principal quantum number lines can be observed.

In p. 195 the time of disappearance of an ionization stage $\tau = 1/n_e S_z$ in rapidly ionizing plasmas was considered for the determination of the electron temperature. τ may be used alternatively for a measurement of the electron density if the temperature is already known otherwise. The measurement becomes indeed very simple if atoms or ions are observed for which the electron temperature is much higher than the ionization energy, say $k_B T_e \geq 10 E_{ion}$. In those cases the ionization rate coefficient S_z is practically independent of the electron temperature. This was exploited, for example, in [562] where several suitable elements (Li, Ba, Mg, and Ca) were added as trace elements to the filling gas of a plasma opening switch.

Such measurements are also carried out in the diagnostics of the boundary plasma in fusion-oriented plasmas with injected thermal or superthermal lithium beams [563], the ionization energy of Li I being $E_{ion} = 5.39 \text{ eV}$. The atoms penetrate into a plasma of increasing temperature, and the local τ can be deduced, in principle, from the local “attenuation” of the beam atoms if the beam velocity is known. A further advantage of lithium is the strong Li I resonance doublet $2p^2P \rightarrow 2s^2S$ at 670.78 nm, for which the excitation rate coefficient becomes practically also independent of the temperature. The emission coefficient of the line reflects thus directly the ground state density of the lithium atoms.

When energetic Li-beams (10 keV and higher) are employed [563, 564], additional ionization by charge exchange must be considered, too.

10.5 Electric and Magnetic Field Measurements

10.5.1 Magnetic Fields

The knowledge of the magnetic field is crucial especially for magnetic confinement devices, as it allows to obtain the profile of the current density \mathbf{j} via the fourth Maxwell equation, $\mu_0 \mathbf{j} = \nabla \times \mathbf{B}$.

As discussed in Sect. 9.2.6 the magnetic field splits the energy levels of atomic systems and hence of emitted lines by the Zeeman effect. To make things complicated, Doppler broadening dominates in many cases in hot plasmas, and Stark broadening in plasmas of high electron density. The polarization characteristics help in identifying the Zeeman components.

This was exploited in early measurements on plasmas where the Doppler width was larger than the Zeeman splitting. A method originally developed for field measurements of the sun by Babcock [565] was applied to pinch discharges [566, 567]. The principle is based on the analysis of the left and the right circularly polarized component of Paschen-Back or Lorentz triplets which overlap due to large Doppler broadening. Hence only the shift between both profiles is used, which is directly proportional to the magnetic field. Originally the emission close to the inflexion points of both profiles was measured and compared, nowadays the total line profile is readily recorded with available multichannel detectors, resulting in higher accuracy. At very high fields as observed in plasma focus devices [470] the Zeeman splitting may exceed Doppler broadening.

For direct observation of polarization-separated Zeeman components in hot plasmas one has to turn to long-wavelength transitions in heavy ions, where Doppler broadening may be sufficiently small (9.75). Seely et al. [568] suggested to employ forbidden magnetic dipole transitions (see p. 98), and first applications to a tokamak were reported in [569] analyzing the Ti XVII line at 383.4 nm. Such measurements are being carried out since also in other fusion-oriented devices, e.g., [465].

Doping with elements, which have suitable lines, was employed in plasmas where Stark broadening dominates [570]. In any case, high accuracy measurements of the line profiles are necessary if the magnetic field is deduced from Zeeman components broadened by Doppler or Stark effects.

A very promising and rather general method was advanced recently [428], see p. 175, which is applicable to multiplet lines even if they are predominantly broadened by Stark or Doppler effect. It utilizes the fact that Zeeman splitting of fine structure components differs (9.71), whereas Doppler and Stark broadening are practically the same. The width difference thus is directly related to the Zeeman splitting and hence to the magnetic field.

Energetic neutral Li-beams were introduced by McCormick et al. [571] and provided for some time the main diagnostic tool for the measurement of *local* magnetic fields in hot plasmas. A list of such applications as well as of various experimental techniques is found in [490]. High energies are needed for deep

penetration into the plasma. The method uses the observation of the strong resonance transition $2^2P \rightarrow 2^2S$ at 670.8 nm, which splits into a Paschen-Back triplet above $B \sim 1$ T. The polarization characteristics depend on the angle between magnetic field and direction of observation here as well.

At very high fields, where the Zeeman components are split sufficiently to be resolved, one can do without the polarization analysis and rely on a precision measurement of the line ratio between the σ and π components; this ratio depends on the above angle between the magnetic field and the direction of observation [572].

A method first reported in [475] and now widely applied to fusion devices is based on the motional Stark effect which fast neutral atoms experience in the magnetic field of a plasma, p. 176, [490]. In most devices they are present because energetic beams (velocity v_b) of hydrogen or deuterium atoms are injected for the purpose of heating the plasma. Of course, special diagnostic beams of optimized velocity may be employed, too. The observed transition is usually the Balmer- α line of hydrogen at 656.28 nm. The Lorentz field $\mathbf{E} = \mathbf{v}_b \times \mathbf{B}$ splits upper and lower levels by the linear Stark effect, and as a consequence the emitted line ($n_p = 3 \rightarrow n_q = 2$) is split into 15 components of which only nine are practically observable [224]. The lines have characteristic polarization properties: six components ($\Delta m = 0$ transitions or π lines) are linearly polarized parallel to the electric field vector, the remaining three lines ($\Delta m = \pm 1$ transitions or σ lines) are polarized perpendicular to the electric field. Zeeman splitting by the magnetic field can be ignored [573]. Since the beam emission is Doppler shifted depending on the direction of observation, Balmer- α emission from the edge plasma is easily identified and discarded.

Excitation is primarily by proton collisions from the ground state. Detailed collisional-radiative modeling, however, is mandatory to obtain quantitatively accurate line emission coefficients. This particularly requires the inclusion of charge exchange and electron collisions [476], and consideration of collisions to the individual m-substates [574].

Most recent applications analyze the line splitting as well as intensity ratios of π and σ components to retrieve both the magnitude of the magnetic field and its direction [575].

Fast helium beams offer some simple alternative for a limited parameter range. The Lorentz field produces shifts and mixes the wave functions of close-by levels, thus increasing the transition probability of dipole forbidden lines [477]. Hence, line shifts and the ratios of forbidden to allowed lines can be used for magnetic field measurements.

10.5.2 Electric Fields

Electric fields are measured, in principle, by the Stark effect on emitted lines. As mentioned on p. 170, macroscopic fields are usually absent in plasmas due to shielding effects, of course with the exception of some special cases. The always present plasma microfield is mirrored in the broadening of lines

emitted by hydrogen and hydrogenic ions, p. 163. Electric fields in the sheath region of plasmas and in front of electrodes split Rydberg levels sufficiently for observation, but the population of these high-lying levels may have to be increased by laser pumping for emission lines to become detectable [442].

The observation of forbidden lines to measure electric fields has been widely applied to a number of plasma devices. Both HeI and LiI atoms have been injected into the plasma, lithium very often by laser blow-off from a solid target. Again, for strong line emission, which allows a detailed analysis of the Stark broadened line profiles, the population of the upper levels has to be enhanced by laser pumping from lower levels [576, 577]. In principle, in this case one has to count on that the population densities of the upper levels equilibrate fast enough. In [578], the field in the cathode fall region of a glow discharge was deduced from the shift between allowed and forbidden components of several HeI lines.

The emission of forbidden transitions in polar diatomic molecules is likewise influenced by the Stark mixing of upper levels, p. 170. Again, after pumping upper levels by a laser, the ratio of forbidden to allowed transition gives the electric field strength.

High radial electric fields are expected in tokamaks, when large toroidal rotation velocities and pressure gradients exist. They have to be accounted for in the analysis of a Balmer- α line profile broadened by the motional Stark effect (p. 203), and thus they can be deduced. First successful attempts have been reported [579].

Turbulent electric fields of low frequencies show up as additional broadening in the line profiles of hydrogen and hydrogen-like ions, p. 171. Comparison of the profiles of a line series allows the elimination of the Doppler component in the analysis [447].

High-frequency electric fields usually are at the electron plasma frequency ω_{pe} , and in turbulent plasmas they are easily excited several orders of magnitude above thermal level. They first show up as two satellites displaced symmetrically by ω_{pe} around a forbidden component close to a strong allowed transition; details are discussed in p. 172. Transitions in HeI and LiI are very suitable and have been widely used. The ratio of satellite to allowed line gives directly E_{rms}^2 according to (9.65). With increasing field strength the relation becomes non-linear, and higher order satellites appear: satellites at $2\omega_{pe}$ around the allowed line, and at $3\omega_{pe}$ around the forbidden one. Pumping the upper levels by a laser increases the sensitivity of the method. Further possibilities which can be used in special cases are discussed in [8, 446].

A

Appendix

A.1 List of Symbols

Symbol	Definition
a_0	Bohr radius
A	Area
A	Ion broadening parameter
A_{tab}	Tabulated ion broadening parameter
A_E	Area of entrance slit
A_p	Surface of plasma
$A(p \rightarrow q)$	Transition probability from upper level (p) to lower level (q)
$A(p \rightarrow)$	Total transition probability from upper level (p) to <i>all</i> lower levels
$A_H(p \rightarrow q)$	Transition probability in hydrogen atoms
$A_a(p^* \rightarrow)$	Autoionization probability of doubly excited state (p^*)
$B(p \rightarrow q)$	Einstein coefficient for radiative transition from level (p) to level (q)
B	Magnetic induction
c	Speed of light in vacuum
C	Capacitance
C_6	Van der Waals interaction constant
d	Groove spacing of a grating
d_{hkl}	Spacing of lattice planes of crystals
D	Optical density
e	Elementary charge
E	Irradiance
E	Electric field strength
$E(p)$	Energy of an atomic system in level (p)
$E_{z,qp}$	Energy difference between levels (q) and (p) of the ion of charge (z)
$E_{z,\infty}$	Ionization energy of level (q) of the ion of charge (z)

E_1	Electric dipole transition
E_2	Electric quadrupole transition
E_H	Ionization energy of the hydrogen atom
E_R	Rydberg energy
E_{kin}	Kinetic energy
f	Focal length
f	Frequency of electrical systems
f_{bw}	Frequency bandwidth
$f(q \rightarrow p)$	Absorption oscillator strength
$f_e(E_{\text{kin}})$	Energy distribution function of electrons
F_0	Holtsmark field strength
FWHM	Full width between half maximum points
\mathcal{F}	Finesse
g	Designation of ground state
$g(p), g_z(p)$	Statistical weight of level (p) in ion (z)
$g_L(J, L, S)$	Lande factor
G	Gain of detectors
$G_{nq}^{\text{bf}}(\nu)$	Gaunt factor, bound-free
G^{ff}	Gaunt factor, free-free
$G(u)$	Gaunt factor for electron collisions between levels (q) and (p)
$\overline{G}(u)$	Effective Gaunt factor for electron collisions
h	Planck constant
\hbar	Planck constant over 2π
H	Fluence
H	Hamilton operator
$H(\beta)$	Holtsmark distribution of reduced field strength β
I	Radiant intensity
I	Current
I_A	Anode current
I_c	Photocurrent
I_d	Dark current
$\mathcal{I}(\lambda)$	Instrument function, apparatus function
J	Total angular momentum
\mathcal{J}	Rotational quantum number of molecules
k_B	Boltzmann constant
L	Radiance
L	Angular momentum
$L_\lambda, L_\nu, L_\omega$	Spectral radiance
$L_\lambda^B(\lambda, T)$	Spectral radiance of blackbody
$\mathcal{L}(\lambda), \mathcal{L}(\nu), \mathcal{L}(\omega)$	Line shape function
m	Order of diffraction
m, M	Magnetic quantum number
m_a	Mass of atoms, ions, molecules
m_z	Mass of ions of charge (z)

m_e	Mass of the electron
m_N	Mass of the nucleus
m_u	Atomic mass constant
M1	Magnetic dipole transition
$\mathbf{M}^{(k)}$	Magnetic multipole operator
n	Principal quantum number
n	Index of refraction
N	Total number of grooves of a grating
n_a	Density of neutral species
n_e	Electron density
n_z	Density of ions of charge state (z)
$n_z(p)$	Population density of level (p) of ions of charge state (z)
$n_z^{\text{SB}}(p)$	Saha–Boltzmann population density of level (p)
n_p	Principal quantum number of upper level (p)
n_q	Principal quantum number of lower level (q)
p	Designation of upper atomic level
p^*	Designation of doubly excited states
P^{fb}	Power loss per unit volume by recombination radiation
P^{ff}	Power loss per unit volume by bremsstrahlung
$P(E_{qp}/k_B T_e)$	Averaged Gaunt factor
q	Designation of lower atomic level
$q(v', v'')$	Franck–Condon factor between vibrational levels (v') and (v'')
Q	Electric charge
$\mathbf{Q}^{(k)}$	Electric multipole operator
r	Radius
\mathbf{r}	Position vector
r_e	Classical electron radius
r_0, r_1	Population coefficients
R	Plasma radius
R	Resistance
R	Debye shielding parameter
R_0	Ion sphere radius
$R(\lambda)$	Reflectance, wavelength dependent
$R_e(\alpha', \alpha'')$	Electronic transition matrix element between the electronic states (α') and (α'') of a molecule
$R_z^{\text{rr}}(\rightarrow q)$	Rate of radiative recombination into level (q) of ion (z)
$R(q \rightarrow p)$	Rate of transitions from level (q) to level (p)
$R(p \rightarrow)$	Total rate of all transitions out of level (p)
$R(\rightarrow p)$	Total rate of all transitions into level (p)
s	Second
\mathcal{R}	Resolution
\mathcal{R}_2	Radon transformation
S	Signal of detector
$S_{+,-}$	Relative emission coefficient of plasma satellites

$S(\lambda)$	Spectral sensitivity of detectors and instruments
$S_\lambda, S_\nu, S_\omega$	Source function
$S(p \rightarrow q)$	Line strength for transition (p) to (q)
$S(\mathcal{J}', \mathcal{J}'')$	Hönle–London factor
$S_z(q \rightarrow p)$	Rate coefficient for ionization from level (q) of ion (z) to level (p) of ion ($z + 1$)
$T(\lambda)$	Transmittance, wavelength dependent
T	Temperature
T_b	Brightness temperature
T_e	Electron temperature
$T_{e,z\max}$	Electron temperature of maximum abundance of ion (z) in corona equilibrium
T_z	Temperature of ions of charge state (z)
T_r	Rise time of a detector signal
$\mathbf{T}^{(k)}$	Multipole operator
u	Radiant energy density
u	Kinetic energy in units of excitation energy
u	Unit of atomic mass
$u_\lambda, u_\nu, u_\omega$	Spectral radiant energy density
U	Voltage
$U_z(T)$	Internal partition function of ionization stage (z)
v	Velocity
v_b	Beam velocity
V	Electric potential
V_A	Anode Potential
$V(R)$	Van der Waals potential
$V(x.a)$	Voigt function
w	Half line width
w_{tab}	Tabulated half line width
w_{en}	Width of entrance slit
w_{ex}	Width of exit slit
$W(\lambda_0)$	Equivalent width of an absorption line at λ_0
$X(q \rightarrow p)$	Rate coefficient for collisional transitions from level (q) to level (p)
$X(p \rightarrow)$	Sum of all collisional rate coefficients out of level (p)
z	Charge of ion
Z	Nuclear charge
$\alpha(\lambda)$	Absorption coefficient of solid materials, wavelength dependent
α_B	Brewster angle
$\alpha_{z+1}^{\text{cap}}(g \rightarrow p^*)$	Rate coefficient for dielectronic capture from ground state (g) of ion ($z + 1$) into doubly excited state (p^*) of ion (z)

$\alpha_{z+1}^{\text{dr}}(g \rightarrow p^*)$	Rate coefficient for dielectronic recombination from ground state (g) of ion ($z + 1$) into doubly excited state (p^*) of ion (z)
$\alpha_{z+1}^{\text{dr}}(g)$	Total rate coefficient for dielectronic recombination from ground state (g) of ion ($z + 1$) to all levels of ion (z)
$\alpha_{z+1}^{\text{rr}}(\rightarrow q)$	Rate coefficient for radiative recombination of ion ($z + 1$) into level (q) of ion (z)
$\alpha_{z+1}^{\text{cr}}(g \rightarrow p)$	Rate coefficient for three-body recombination from the ground state (g) of the ion ($z + 1$) into the level (p) of the ion (z)
β	Reduced micro-field strength
$\gamma(q \rightarrow p)$	Effective collision strength or rate parameter for transitions from level (q) to level (p)
Γ	Ion-ion coupling parameter
Γ_p	Energy width of atomic level (p)
$\Gamma_z(p)$	External flux of level-p population
δ	Secondary-emission coefficient of dynodes
$\Delta\lambda_{1/2}$	Full width of a line profile
$\Delta\lambda_F$	Free spectral range
ε	Emission coefficient
$\varepsilon_\lambda, \varepsilon_\nu, \varepsilon_\omega$	Spectral emission coefficient
$\varepsilon(p \rightarrow q)$	Emission coefficient from upper level (p) to lower level (q)
$\varepsilon_\lambda^{\text{fb}}, \varepsilon_\nu^{\text{fb}}, \varepsilon_\omega^{\text{fb}}$	Spectral-emission coefficient of free-bound transitions
$\varepsilon_\lambda^{\text{ff}}, \varepsilon_\nu^{\text{ff}}, \varepsilon_\omega^{\text{ff}}$	Spectral-emission coefficient of free-free transitions
$\varepsilon_\lambda^{\text{ffa}}, \varepsilon_\nu^{\text{ffa}}, \varepsilon_\omega^{\text{ffa}}$	Spectral-emission coefficient of bremsstrahlung by electron-atom collisions
$\varepsilon_{\text{sat}}^{\text{dr}}$	Emission coefficient of a dielectronic satellite
$\varepsilon_{\text{sat}}^{\text{in}}$	Emission coefficient of an innershell satellite
ϵ_0	Electric constant
$\epsilon(\lambda, T)$	Emissivity of solids
$\eta(\lambda)$	Spectral quantum efficiency
$\theta(\tau_0)$	Escape factor
$\kappa(\lambda), \kappa(\nu), \kappa(\omega)$	Absorption coefficient
$\kappa^L(\nu_{pq})$	Line absorption coefficient of transition (p) to (q)
$\kappa^{\text{ff}}(\lambda)$	Absorption coefficient by inverse bremsstrahlung
$\kappa_{\text{net}}^{\text{ff}}(\lambda)$	Net absorption coefficient by inverse bremsstrahlung accounting for stimulated emission
λ	Wavelength
λ_{pq}	Wavelength of lines between levels (p) and (q)
λ_{vac}	Wavelength in vacuum
λ_B	Thermal de Broglie wavelength of electrons

$\lambda_{\text{B}1}$	Blaze wavelength of gratings
$\Lambda_{\text{loss}}^{\text{fb}}$	Electron energy loss constant by radiative recombination
$\Lambda_{\text{loss}}^{\text{ff}}$	Electron energy loss constant by bremsstrahlung
μ_e	Mobility of free electrons
μ_0	Magnetic permeability in vacuum, magnetic constant
μ_B	Bohr magneton
ν	Frequency of a radiative transitions
ν_{pq}	Frequency of a radiative transition from level (p) to level (q)
ν_{pe}	Electron plasma frequency
ξ^{bf}	Bibermann factor for free–bound transitions
ξ^{ff}	Bibermann factor for bremsstrahlung
ϱ_D	Electron Debye radius
$\varrho_{D'}$	Electron and ion Debye radius
σ	Spectroscopic wavenumber
σ	Electric conductivity
$\sigma(q \rightarrow p)$	Cross-section for transitions from level (q) to level (p) by collisions
$\sigma(\nu)$	Cross-section for absorption
$\sigma^{Kr}(n_q \rightarrow E_{\text{kin}})$	Kramers cross-section for photo-absorption
$\sigma^L(\nu_{qp})$	Cross-section for absorption of a line at ν_{qp}
σ^{cx}	Cross-section for charge exchange
τ	Optical depth
τ	Lifetime
τ_p	Lifetime of level (p) of an atomic system
ϕ	Radiant flux density
Φ	Radiant flux (radiant power)
Ψ_p	Wavefunction of level (p)
ω	Angular frequency
ω_{pe}	Electron plasma frequency
Ω	Solid angle
$\Omega(q \rightarrow p)$	Collision strength from level (q) to level (p)

B

Appendix

B.1 Data Centers

In the following selected institutions are listed that maintain data centers providing useful information via the internet on atomic data; some even allow online calculations.

Weizmann Institute, Israel – Plasma gate database

URL: <http://plasma-gate.weizmann.ac.il/DBfAPP.html>

A catalogue lists all major databases with hyperlinks.

National Institute of Standards and Technology (NIST), USA

URL: <http://physics.nist.gov/PhysRefData/contents-atomic.html>

Critically evaluated data and bibliographies on atomic spectra, wavelengths, transition probabilities, and line shapes.

Naval Research Laboratory (NRL), USA

URL: <http://wwwsolar.nrl.navy.mil/chianti.html>

Database CHIANTI: it consists of a critically evaluated set of up-to-date atomic data.

Paris Observatory, France

URL: <http://stark-b.obspm.fr/index.php>

Database of calculated widths and shifts of isolated lines of atoms and ions due to electron and ion collisions.

International Atomic Energy Agency (IAEA), Vienna, Austria

URL: <http://www-amdis.iaea.org>

The Atomic and Molecular Data Information System (AMDIS) contains recommended and evaluated data for atomic and molecular collisions and an atomic and molecular bibliographic retrieval system.

National Institute for Fusion Science (NIFS), Japan

URL: <https://dbshino.nifs.ac.jp>

Contains cross sections and rate coefficients for ionization, excitation, and recombination by electron impact, charge transfer by heavy particle collisions, and collision processes of molecules.

Havard-Smithonian Center for Astrophysics, USA

URL: <http://www.adsabs.harvard.edu>

The SAO/NASA Astrophysics Data System (ADS) maintains three bibliographic databases.

University of Strathclyde, UK

URL: <http://www.adas.ac.uk>

The Atomic Data and Analysis Structure (ADAS) is an interconnected set of computer codes and data collections for modeling the radiating properties of ions and atoms in plasmas. General access is provided to ADAS members. A selected set of data is openly available at <http://open.adas.ac.uk>.

Institute for Spectroscopy, Troitsk, Russia

URL: <http://das101.isan.troitsk.ru/BIBL.HTM>

The data bank BIBL contains a bibliography on atomic data for plasma physics, atomic physics, and astrophysics.

C

Appendix

C.1 Atomic Constants and Quantities

The table contains numerical values of atomic constant and quantities which are frequently needed. They are taken from [13].

Quantity	Symbol	Value	Unit
Speed of light in vacuum	c	299,792,458	m s^{-1}
Mass of electron	m_e	9.109 382 15	$\times 10^{-31} \text{ kg}$
		5.485 799 094	$\times 10^{-4} \text{ u}$
	$m_e c^2$	0.510 998 910	MeV
Mass of proton	m_p	1.672 621 64	$\times 10^{-27} \text{ kg}$
		1.007 276 467	u
	$m_p c^2$	938.272 01	MeV
Mass of neutron	m_n	1.674 927 21	$\times 10^{-27} \text{ kg}$
		1.008 664 916	u
	$m_n c^2$	939.565 346	MeV
Atomic mass unit	$1 \text{ u} = m_u$	1.660 538 782	$\times 10^{-27} \text{ kg}$
	uc^2	931.494 028	MeV
Elementary charge	e	1.602 176 487	$\times 10^{-19} \text{ C}$
Electric constant	ϵ_0	8.854 187 817	$\times 10^{-12} \text{ F m}^{-1}$
Magnetic constant	μ_0	4π	$\times 10^{-7} \text{ N A}^{-2}$
Boltzmann constant	k_B	1.380 650 4	$\times 10^{-23} \text{ J K}^{-1}$
Avogadro constant	N_A	6.022 141 79	$\times 10^{23} \text{ mol}^{-1}$
Rydberg constant	R_∞	10 973 731.568 53	m^{-1}
Rydberg energy	E_∞	13.605 691 9	eV
Hartree energy	E_h	27.211 383 9	eV
Ionization energy of H	E_H	13.598 433	eV

Quantity	Symbol	Value	Unit
Planck constant	h	6.626 068 96	$\times 10^{-34}$ J s
Planck constant over 2π	\hbar	1.054 571 63	$\times 10^{-34}$ J s
Fine-structure constant	α	7.297 352 538	$\times 10^{-3}$
Bohr radius	a_0	5.291 772 086	$\times 10^{-11}$ m
Classical electron radius	r_e	2.817 940 289	$\times 10^{-15}$ m
Compton wavelength	λ_c	2.426 310 218	$\times 10^{-12}$ m
Unit of atomic cross-sections	πa_0^2	8.797 355 3	$\times 10^{-21}$ m ²
Thomson cross-section	σ_{Th}	0.665 245 856	$\times 10^{-28}$ m ²
Bohr magneton	μ_B	5.788 381 756	$\times 10^{-5}$ eV T ⁻¹

C.2 Some Atomic Relations

Useful relations between between atomic quantities.

$$\begin{aligned}
 \text{Speed of light in vacuum} & \quad 1 = \mu_0 \epsilon_0 c^2 \\
 \text{Fine structure constant} & \quad \alpha = \frac{e^2}{4\pi\epsilon_0 \hbar c} = \frac{e^2}{2\epsilon_0 hc} = \frac{\mu_0 c e^2}{2h} \\
 \text{Rydberg constant} & \quad R_\infty = \frac{m_e e^4}{8\epsilon_0^2 h^3 c} = \frac{m_e c \alpha^2}{2h} \\
 \text{Rydberg energy} & \quad E_\infty = R_\infty hc = \frac{1}{2} m_e (\alpha c)^2 \\
 \text{Hartee energy} & \quad E_h = 2 E_\infty \\
 \text{Rydberg constant of H atom} & \quad R_H = R_\infty \frac{m_p}{m_p + m_e} \\
 \text{Bohr radius} & \quad a_0 = \frac{4\pi\epsilon_0 \hbar^2}{m_e e^2} = \frac{1}{\alpha} \frac{\hbar}{m_e c} \\
 \text{Classical electron radius} & \quad r_e = \frac{e^2}{4\pi\epsilon_0 m_e c^2} = \alpha^2 a_0 \\
 \text{Thomson cross-section} & \quad \sigma_{\text{Th}} = \frac{8\pi}{3} r_e^2 = \frac{8}{3} \alpha^4 \pi a_0^2 \\
 \text{Bohr magneton} & \quad \mu_B = \frac{e\hbar}{2m_e}
 \end{aligned} \tag{C.1}$$

References

1. W. Demtröder, *Laser Spectroscopy*, 3rd edn. (Springer, Berlin, 2003)
2. K. Muraoka, M. Maeda, *Laser Aided Diagnostics of Plasmas and Gases* (Institute of Physics Publishing, Bristol, 2001)
3. H.-J. Kunze, in *The Laser as a Tool for Plasma Diagnostics*, ed. by W. Lochte-Holtgreven. *Plasma Diagnostics* (North-Holland, Amsterdam, 1968), pp. 550–616
4. A.W. DeSilva, G.C. Goldenbaum, in *Plasma Diagnostics by Light Scattering*, ed. by H.R. Griem, R.H. Lovberg. *Methods of Experimental Physics*, vol 9 (Academic Press, New York, 1970), pp. 61–113
5. J. Sheffield, *Plasma Scattering of Electromagnetic Radiation* (Academic Press, New York, 1975)
6. S.H. Glenzer, W.E. Alley, K.G. Estabrook, J.S. De Groot, M.G. Haines, J.H. Hammer, J.-P. Jadaud, B.J. MacGowan, J.D. Moody, W. Rozmus, L.J. Suter, T.L. Weiland, E.A. Williams, *Phys. Plasma* **6**, 2117 (1999)
7. H.R. Griem, *Plasma Spectroscopy* (McGraw-Hill, New York, 1964)
8. H.R. Griem, *Principles of Plasma Spectroscopy* (Cambridge University Press, Cambridge, 1997)
9. T. Fujimoto, *Plasma Spectroscopy* (Clarendon Press, Oxford, 2004)
10. A. Thorne, U. Litzén, S. Johannson, *Spectrophysics – Principles and Applications* (Springer, Berlin, 1999)
11. I.H. Hutchinson, *Principles of Plasma Diagnostics* (Cambridge University Press, Cambridge, 1987)
12. W. Lochte-Holtgreven (ed.), *Plasma Diagnostics* (North-Holland, Amsterdam, 1968)
13. National Institute of Standards and Technology (NIST), USA.
<http://www.physics.nist.gov/PhysRefData/contents-atomic.html>
14. C. Cowley, W.L. Wiese, J. Fuhr, L.A. Kuznetsova, in *Spectra*, ed. by A.N. Cox. Allen's Astrophysical Quantities 4th edn. (Springer, New York, 1999), pp. 55–93
15. G. Herzberg, *Spectra of Diatomic Molecules* (Van Nostrand, New York, 1959)

16. G. Herzberg, *Electronic Spectra of Polyatomic Molecules* (Van Nostrand, New York, 1966)
17. Harvard Smithsonian Center for Astrophysics, USA. <http://www.hitran.com>
18. Le Système International d'Unités, *The International Systems of Units* (Bur. Intl. Poids et Mesures, Sèvres France, 1998)
19. Yu.E. Voskoboinikov, N.G. Preobrazhenskii, Optic. Spectros. (USSR) **60**, 111 (1999)
20. K.T. Walsh, J. Fielding, M.B. Long, Optic. Lett. **25**, 457 (2000)
21. N. Gottardi, J. Appl. Phys. **50**, 2647 (1979)
22. H. Soltwisch, Rev. Sci. Instrum. **57**, 1939 (1986)
23. H.K. Park, Plasma Phys. Contr. Fusion **31**, 2035 (1989)
24. Y. Nagayama, A.W. Edwards, Rev. Sci. Instrum. **63**, 4757 (1992)
25. A.M. Cormack, J. Appl. Phys. **34**, 2722 (1963)
26. F. Natterer, F. Wuebbeling, *Mathematical Methods in Image Reconstruction* (SIAM, Philadelphia, 2001)
27. J. Cooper, Rep. Prog. Phys. **29**, 35 (1966)
28. R.A. Sawyer, *Experimental Spectroscopy* (Dover, New York, 1963)
29. F.A. Jenkins, H.E. White, *Fundamentals of Optics* (McGraw-Hill, New York, 1957)
30. J.A.R. Samson, *Techniques of Vacuum Ultraviolet Spectroscopy* (Wiley, New York, 1967)
31. G.W. Stroke, in *Diffraction Gratings*, ed. by S. Flügge. Handbuch der Physik, vol 29 (Springer, Berlin, 1967)
32. E.G. Loewen, E. Popov, *Diffraction Gratings and Applications* (Marcel Dekker, New York, 1997)
33. T. Namioka, in *Diffraction Gratings*, ed. by J.A.R. Samson, D.L. Ederer. Vacuum Ultraviolet Spectroscopy I (Academic Press, San Diego, 2000), pp. 347–377
34. H. Haber, J. Opt. Soc. Am. **40**, 153 (1950)
35. F. Masuda, H. Noda, T. Namioka, J. Spectros. Soc. Jpn. **27**, 211 (1978)
36. L. Poletto, R.J. Thomas, Appl. Optic. **43**, 2029 (2004)
37. T. Harada, T. Kita, Appl. Optic. **19**, 3987 (1980)
38. W.R. Hunter, in *Multilayer Gratings*, ed. by J.A.R. Samson, D.L. Ederer. Vacuum Ultraviolet Spectroscopy I (Academic Press, San Diego, 2000), pp. 379–399
39. J.F. Seely, C.M. Brown, D.L. Windt, S. Donguy, B. Kjornrattanawanich, Appl. Optic. **43**, 1463 (2004)
40. H. Bräuniger, P. Predehl, K.P. Beuermann, Appl. Optic. **18**, 368 (1979)
41. S. Sailaja, V. Arora, S.R. Kumbhare, P.A. Naik, P.D. Gupta, D.A. Fedin, A.A. Rupasov, A.S. Shikanov, Meas. Sci. Technol. **9**, 1462 (1998)
42. E. Fill, K.-H. Stephan, P. Predehl, G. Pretzler, K. Eidmann, A. Saeman, Rev. Sci. Instrum. **70**, 2597 (1999)
43. W.L. Bragg, Proc. Camb. Philos. Soc. **17**, 43 (1912)
44. N.G. Alexandropoulos, G.G. Cohen, Appl. Spectros. **28**, 155 (1974)

45. E.P. Bertin, *Principles and Practice of X-Ray Spectrometric Analysis* (Plenum, New York, 1975)
46. A. Burek, Space Sci. Instrum. **2**, 53 (1976)
47. B.L. Henke, E.M. Gullikson, J. Kerner, A.L. Oren, R.L. Blake, J. X Ray Sci. Technol. **2**, 17 (1990)
48. R. Barnsley, S.N. Lea, A. Patel, N.J. Peacock, in *UV and X-Ray Spectroscopy of Astrophysical and Laboratory Plasmas*, ed. by E.H. Silver, S.M. Kahn (Cambridge University Press, Cambridge, 1993), pp. 513–520
49. B.L. Henke, P.A. Jannink, Rev. Sci. Instrum. **56**, 1537 (1985)
50. M. Ohler, M. Sanchez del Rio, A. Tuffanelli, M. Gambaccini, A. Taibi, A. Fantini, G. Pareschi, J. Appl. Cryst. **33**, 1023 (2000)
51. H.H. Johann, Z. Phys. **69**, 185 (1931)
52. G. Bogren, Ark. Fys. **3**, 515 (1951)
53. D.N. Nikogosyan, *Properties of Optical and Laser Related Materials: A Handbook* (Wiley, Chichester, 1997)
54. W.R. Hunter, S.A. Malo, J. Phys. Chem. Solid. **30**, 2739 (1969)
55. B.L. Henke, E.M. Gullikson, J.C. Davis, Atom. Data Nucl. Data Table **54**, 181 (1993)
56. D.F. Heath, P.A. Sacher, Appl. Optic. **5**, 937 (1966)
57. G. Hass, W.R. Hunter, Appl. Optic. **9**, 2101 (1970)
58. H.U. Fahrbach, A. Eberhagen, Radiat. Eff. **65**, 127 (1982)
59. R.C. Elton, D.-M. Billings, J. Grun, F.C. Young, C.K. Manka, B.H. Ripin, H.R. Burris, J. Resnick, D.J. Ripin, J.R. Millard, J. Appl. Phys. **74**, 5432 (1993)
60. M. Baudaz, A. Peacock, D. Fuchs, T. Lederer, P. Müller, F. Scholze, G. Uhm, V.-P. Vittanen, R. Mutikainen, Rev. Sci. Instrum. **66**, 2570 (1995)
61. SCHOTT catalogue: *Optical Filters – Glass Filters* (Schott AG, Mainz, Germany, 2005)
62. W.R. Hunter, in *Windows and Filters*, ed. by J.A.R. Samson, D.L. Ederer. Vacuum Ultraviolet Spectroscopy I (Academic Press, San Diego, 2000), pp. 305–346
63. W.R. Hunter, D.W. Angel, R. Tousey, Appl. Optic. **4**, 895 (1965)
64. Center for X-Ray Optics, Lawrence Berkely National Laboratory, USA. <http://www-cxro.lbl.gov>
65. M. Zukic, D.G. Torr, J.F. Spann, M.R. Torr, Appl. Optic. **29**, 4293 (1990)
66. W.R. Hunter, in *Polarization*, ed. by J.A.R. Samson, D.L. Ederer. Vacuum Ultraviolet Spectroscopy I (Academic Press, San Diego, 2000), pp. 227–255
67. P.H. Berning, G. Hass, R.P. Madden, J. Opt. Soc. Am. **50**, 586 (1960)
68. E.D. Palik (ed.), *Handbook of Optical Constants* (Academic Press, New York, 1985)
69. D.E. Gray (ed.), *American Institute of Physics Handbook* (McGraw-Hill, New York, 1972)

70. D.R. Lide (ed.), *CRC Handbook of Chemistry and Physics*, 82nd edn. (CRC Press, New York, 2001–2002)
71. J.T. Cox, G. Hass, J.B. Ramsey, W.R. Hunter, *J. Opt. Soc. Am.* **63**, 435 (1973)
72. W.R. Hunter, in *Reflectance Spectra of Single Materials*, ed. by J.A.R. Samson, D.L. Ederer. Vacuum Ultraviolet Spectroscopy I (Academic Press, San Diego, 2000), pp. 205–226
73. A.G. Michette, *Optical Systems for Soft X Rays* (Plenum Press, New York, 1986)
74. E. Spiller, in *Reflecting Optics: Multilayers*, ed. by J.A.R. Samson, D.L. Ederer. Vacuum Ultraviolet Spectroscopy I (Academic Press, San Diego, 2000), pp. 271–288
75. A.D. Stokes, *J. Opt. Soc. Am.* **57**, 1100 (1967)
76. Y.-K. Pu, Z.-D. Yu, Z.-G. Guo, *Phys. Plasma* **12**, 113301 (2005)
77. P. Kirkpatrick, A.V. Baez, *J. Opt. Soc. Am.* **38**, 766 (1948)
78. R.D. Guenther, *Modern Optics* (Wiley, New York, 1990)
79. H. Wolter, *Ann. Phys.* **10**, 94 (1952)
80. V.L. Kantsyrev, R. Bruch, R. Phaneuf, N.G. Publicover, *J. X Ray Sci. Technol.* **7**, 139 (1997)
81. S. Wilkins, A.W. Stevenson, K.A. Nugent, H. Chapman, S. Steenstrup, *Rev. Sci. Instrum.* **60**, 1026 (1989)
82. A.N. Brunton, G.W. Fraser, J.E. Less, I.C.E. Turcu, *Appl. Optic.* **36**, 5461 (1997)
83. G.J. Price, A.N. Brunton, G.W. Fraser, M. Bavdaz, M.W. Beijersbergen, J.-P. Boutot, R. Fairbend, S.-O. Flyckt, A. Peacock, E. Tomaselli, *Nucl. Instrum. Meth. Phys. Res. A* **490**, 290 (2002)
84. R.L. Lucke, S.E. Thonnard, *Appl. Optic.* **37**, 616 (1998)
85. J.K. Pribram, C.M Penchina, *Appl. Optic.* **7**, 2005 (1968)
86. P. Lindblom, *Anal. Chim. Acta* **380**, 353 (1999)
87. M. Koike, in *Normal Incidence Monochromators and Spectrometers*, ed. by J.A.R. Samson, D.L. Ederer. Vacuum Ultraviolet Spectroscopy II (Academic Press, San Diego, 2000), pp. 1–20
88. A.M. Maletta, P.M. Johnson, *Rev. Sci. Instrum.* **71**, 3653 (2000)
89. V.A. Soukhanovskii, D. Stutman, M. Finkenthal, H.W. Moss, R. Kaita, R. Majeski, *Rev. Sci. Instrum.* **72**, 3270 (2001)
90. A.P. Shevelko, L.A. Shmaenok, S.S. Churilov, R.K.F.J. Bastiaensen, F. Bijlkirk, *Phys. Scripta* **57**, 276 (1998)
91. R.X. Li, P.Z. Fan, Z.Z. Xu, Z.Q. Zhang, P.X. Lu, *Opt. Eng.* **33**, 2366 (1994)
92. G. Tondello, *Opt. Acta* **26**, 357 (1979)
93. W. Biel, G. Bertschinger, R. Burhenn, R. König, E. Jourdain, *Rev. Sci. Instrum.* **75**, 3268 (2004)
94. K. Eidmann, M. Kühne, P. Müller, G.D. Tsakiris, *J. X Ray Sci. Technol.* **2**, 259 (1990)

95. E.E. Fill, T. Schlegel, J. Steingruber, J. Zhang, in *X-ray Lasers 1992*, ed. by E.E. Fill (Inst. Phys. Conf. Ser. No. 125, London, 1992), pp. 423–426
96. A. Schulz, R. Burhenn, F.B. Rosmej, H.-J. Kunze, J. Phys. D Appl. Phys. **22**, 659 (1989)
97. B. Yaakobi, A.J. Burek, IEEE J. Quant. Electron. **QE-19**, 1841 (1983)
98. A. Pak, G. Gregori, J. Knight, K. Campbell, D. Price, B. Hammel, O.L. Landen, S.H. Glenzer, Rev. Sci. Instrum. **75**, 3747 (2004)
99. R. Barnsley, U. Schumacher, E. Källne, H.W. Morsi, G. Rupprecht, Rev. Sci. Instrum. **62**, 889 (1991)
100. U. Schumacher, E. Källne, H.W. Morsi, G. Rupprecht, Rev. Sci. Instrum. **60**, 562 (1989)
101. P. Platz, J. Ramette, E. Belin, C. Bonnelle, A. Gabriel, J. Phys. E Sci. Instrum. **14**, 448 (1981)
102. K.W. Hill, M. Bitter, M. Tavernier, M. Diesso, S. von Goeler, G. Johnson, L.C. Johnson, N.R. Sauthoff, N. Schechtmann, S. Sesnic, F. Tenney, K.M. Young, Rev. Sci. Instrum. **56**, 1165 (1985)
103. P. Beiersdorfer, S. von Goeler, M. Bitter, K.W. Hill, R.A. Hulse, R.S. Walling, Rev. Sci. Instrum. **60**, 895 (1989)
104. F. Walden, H.-J. Kunze, A. Petoyan, A. Urnov, J. Dubau, Phys. Rev. E **59**, 3562 (1999)
105. J. Weinheimer, I. Ahmad, O. Herzog, H.-J. Kunze, G. Bertschinger, W. Biel, G. Borchert, M. Bitter, Rev. Sci. Instrum. **72**, 2566 (2001)
106. L.M. Belyaev, A.B. Gil'varg, Y.A. Mikhailov, S.A. Pikuz, G.V. Sklizkov, A. Ya. Faenov, S.I. Fedotov, Sov. J. Quant. Electron. **7**, 67 (1977)
107. M. Bitter, K. Hill, L. Roquemore, P. Beiersdorfer, D. Thorn, M.F. Gu, Rev. Sci. Instrum. **74**, 1977 (2003)
108. T. Johansson, Z. Phys. **82**, 507 (1933)
109. B.S. Fraenkel, M. Bitter, J. X Ray Sci. Technol. **9**, 29 (2001)
110. Y. Cauchois, J. Physique et Rad. **3**, 320 (1932)
111. R. Beier, H.-J. Kunze, Z. Phys. A **285**, 347 (1978)
112. L. van Hám̄os, Ann. Phys. **17**, 716 (1933)
113. T.A. Hall, J. Phys. E Sci. Instrum. **17**, 110 (1984)
114. S.A. Pikuz, T.A. Shelkovenko, M.D. Mitchell, K.M. Chandler, J.D. Douglass, R.D. McBride, D.P. Jackson, D.A. Hammer, Rev. Sci. Instum. **77**, 10F309 (2006)
115. E. Källne, J. Källne, E.S. Marmar, J.E. Rice, Phys. Scripta **31**, 551 (1985)
116. A.P. Shevelko, Y.S. Kasyanov, O.F. Yakushev, L.V. Knight, Rev. Sci. Instrum. **73**, 3458 (2002)
117. O. Renner, T. Missala, P. Sondhauss, E. Krouský, E. Förster, C. Chenais-Popovics, O. Rancu, Rev. Sci. Instrum. **68**, 2393 (1997)
118. O. Renner, M. Kopecký, J.S. Wark, H. He, E. Förster, Rev. Sci. Instrum. **66**, 3234 (1995)

119. A.P. Thorn, M.R. Howells, in *Interferometric Spectrometers*, ed. by J.A.R. Samson, D.L. Ederer. Vacuum Ultraviolet Spectroscopy II (Academic Press, San Diego, 2000), pp. 73–106
120. G. Herandez, *Fabry-Perot Interferometers* (Cambridge University Press, Cambridge, 1986)
121. J. Cooper, J.R. Greig, J. Sci. Instrum. **40**, 433 (1963)
122. B.C. Smith, *Fundamentals of Fourier Transform Infrared Spectroscopy* (CRC Press, Baton Rouge, 1996)
123. K. Tamasaku, T. Ishikawa, M. Yabashi, Appl. Phys. Lett. **83**, 2994 (2003)
124. J. Howard, Appl. Optic. **41**, 197 (2002)
125. J. Chung, R. König, J. Howard, M. Otte, T. Klinger, Plasma Phys. Contr. Fusion **47**, 919 (2005)
126. A. Brablec, D. Trunec, F. Šťastný, J. Phys. D Appl. Phys. **32**, 1870 (1999)
127. G.M. Petrov, J. Quant. Spectros. Radiat. Tran. **72**, 281 (2002)
128. H.-J. Kunze, *Physikalische Meßmethoden*, in German (Teubner, Stuttgart, 1986); Russian edn. *Metodi fizicheskikh ismerenii* (MIR Publisher, Moscow, 1989)
129. P. Lee, J. Gernhardt, C.J. Armentrout, R.T. Snider, Rev. Sci. Instrum. **59**, 883 (1988)
130. R.J. Keyes (ed.), *Optical and Infrared Detectors* (Springer, Berlin, 1977)
131. G. Beck, Rev. Sci. Instrum. **47**, 537 (1976)
132. R.H. Kingston, *Detection of Optical and Infrared Radiation* (Springer, Berlin, 1978)
133. R. Lincke, in *Vacuum Ultraviolet Spectroscopy*, ed. by W. Lochte-Holtgreven. Plasma Diagnostics (North-Holland, Amsterdam, 1968), pp. 347–423
134. G.F. Knoll, *Radiation Detection and Measurement*, 3rd edn. (Wiley, New York, 1999)
135. M. Nikl, Meas. Sci. Technol. **17**, R37 (2006)
136. J.L. Wiza, Nucl. Instrum. Meth. **162**, 587 (1979)
137. F. Böttcher, J. Musielok, H.-J. Kunze, Phys. Rev. A **36**, 2265 (1987)
138. D.G. Simons, G.W. Fraser, P.A.J. de Korte, J.F. Pearson, L. de Jong, Nucl. Instrum. Meth. Phys. Res. A **261**, 579 (1987)
139. G.R. Carruthers, Appl. Optic. **27**, 5157 (1988)
140. O.H.W. Siegmund, E. Everman, J. Hull, J.V. Vallerga, M. Lampton, Appl. Optic. **27**, 4323 (1988)
141. O.H.W. Siegmund, M. Lampton, R. Raffanti, W. Herrick, Nucl. Instrum. Meth. Phys. Res. A **310**, 311 (1991)
142. B.K.F. Young, R.E. Stewart, J.G. Woodsworth, J. Bailey, Rev. Sci. Instrum. **57**, 2729 (1986)
143. B.A. Hammel, L.E. Ruggles, Rev. Sci. Instrum. **59**, 1828 (1988)
144. E.L. Dereniak, D.G. Crowe, *Optical Radiation Detectors* (Wiley, New York, 1984)

145. E.M. Gullikson, R. Korde, L.R. Canfield, R.E. Vest, J. Electron Spectros. Relat. Phenom. **80**, 313 (1996)
146. L.R. Canfield, in *Photodiode detectors*, ed. by J.A.R. Samson, D.L. Ederer. Vacuum Ultraviolet Spectroscopy II (Academic Press, San Diego, 2000), pp. 117–138
147. K. Brau, S. von Goeler, M. Bitter, R.D. Cowan, D. Eames, K. Hill, N. Sauthoff, E. Silver, W. Stodiek, Phys. Rev. A **22**, 2769 (1980)
148. J.E. Rice, K. Molvig, H.I. Helava, Phys. Rev. A **25**, 1645 (1982)
149. S.M. Gruner, M.W. Tate, E.F. Eikenberry, Rev. Sci. Instrum. **73**, 2815 (2002)
150. M.J. Renzi, M.W. Tate, A. Ercan, S.M. Gruner, E. Fontes, C.F. Powell, A.G. Macphee, S. Narayanan, J. Wang, Y. Yue, R. Cuenca, Rev. Sci. Instrum. **73**, 1621 (2002)
151. J.A.R. Samson, G.N. Haddad, Phys. Rev. Lett. **33**, 875 (1974)
152. J.A.R. Samson, J. Opt. Soc. Am. **54**, 6 (1964)
153. A.G. Michette, C.J. Buckley, *X-Ray Science and Technology* (Institute of Physics Publishing, Bristol, 1993)
154. K.W. Hill, S. von Goeler, M. Bitter, L. Campbell, R.D. Cowan, B. Fraenkel, A. Greenberger, R. Horton, J. Hovey, W. Roney, N.R. Sauthoff, W. Stodiek, Phys. Rev. A **19**, 1770 (1979)
155. G. Charpak, R. Bouclier, T. Bressani, J. Favier, Č. Zupančič, Nucl. Instrum. Meth. **65**, 217 (1968)
156. R.A. Boie, J. Fischer, Y. Inagaki, F.C. Merritt, V. Radeka, L.C. Rogers, D.M. Xi, Nucl. Instrum. Meth. **201**, 92 (1982)
157. G.C. Smith, J. Synchrotron. Radiat. **13**, 172 (2006)
158. F. Sauli, Nucl. Intrum. Meth. Phys. Res. A **386**, 531 (1997)
159. S.H. Moseley, J.C. Mather, D. McCammon, J. Appl. Phys. **56**, 1257 (1984)
160. D. McCammon, W. Cui, M. Juda, J. Morgenthaler, J. Zhang, R.L. Kelley, S.S. Holt, G.M. Madejski, S.H. Moseley, A.E. Szymkowiak, Nucl. Instrum. Meth. Phys. Res. A **326**, 157 (1993)
161. J. Reader, C.J. Sansonetti, R.D. Deslattes, Appl. Optic. **39**, 637 (2000)
162. A. Ben-Kish, A. Fisher, E. Cheifetz, J.L. Schwob, Rev. Sci. Instrum. **71**, 2651 (2000)
163. S.G. Gales, C.D. Bentley, Rev. Sci. Instrum. **75**, 4001 (2004)
164. K. Danzmann, M. Günther, J. Fischer, M. Kock, M. Kühne, Appl. Optic. **27**, 4947 (1988)
165. K. Bergmann, G. Schriever, O. Rosier, M. Müller, W. Neff, R. Lebert, Appl. Optic. **38**, 5413 (1999)
166. W. Biel, G. Bertschinger, R. Burhenn, R. König, E. Jourdain, Rev. Sci. Instrum. **77**, 10F305 (2006)
167. U. Schumacher, K. Asmussen, G. Fussmann, T. Liebsch, R. Neu, Rev. Sci. Instrum. **67**, 2826 (1996)
168. K. Anhalt, J. Hartmann, D. Lowe, G. Machin, M. Sadli, Y. Yamada, Metrologia **43**, S78 (2006)

169. N. Sasajima, H.W. Yoon, C.E. Gibson, V. Khromchenko, F. Sakuma, Y. Yamada, *Metrologia* **43**, S109 (2006)
170. D. Lowe, Y. Yamada, *Metrologia* **43**, S135 (2006)
171. J. Schwinger, *Phys. Rev.* **75**, 1912 (1949)
172. D.L. Ederer, E.B. Saloman, S.C. Ebner, R.P. Madden, *J. Res. NBS-A. Phys. Chem.* **79A** 761 (1975)
173. B. Wende, *Metrologia*, **32**, 419 (1995/1996)
174. E. Hinnov, F. Hofmann, *J. Opt. Soc. Am.* **53**, 1259 (1963)
175. M. Mumma, *J. Opt. Soc. Am.* **62**, 1459 (1972)
176. J.C. De Vos, *Physica* **20**, 690 (1954)
177. R.E. Larrabee, *J. Opt. Soc. Am.* **49**, 619 (1959)
178. H. Magdeburg, U. Schley, *Z. Angew. Phys.* **20**, 465 (1966)
179. A.T. Hattenberg, *Appl. Optic.* **6**, 95 (1967)
180. E. Pitz, *Appl Optic.* **10**, 813 (1971)
181. D. Einfeld, D. Stuck, *Z. Naturforsch.* **33a**, 502 (1978)
182. W.R. Ott, K. Behringer, G. Gieres, *Appl. Optic.* **14**, 2121 (1975)
183. K. Behringer, P. Thoma, *Appl. Optic.* **18**, 2586 (1979)
184. J.M. Bridges, W.R. Ott, *Appl. Optic.* **16**, 367 (1977)
185. D. Einfeld, K. Grützmacher, D. Stuck, *Z. Naturforsch.* **34a**, 233 (1979)
186. R.C. Preston, C. Brookes, F.W.J. Clutterbuck, *J. Phys. E Sci. Instrum.* **13**, 1206 (1980)
187. R.D. Saunders, W.R. Ott, J.M. Bridges, *Appl. Optic.* **17**, 593 (1978)
188. E. Tegeler, *Nucl. Instrum. Meth. Phys. Res. A* **282**, 706 (1989)
189. P.J. Key, R.C. Preston, *J. Phys. E Sci. Instrum.* **13**, 866 (1980)
190. D. Einfeld, D. Stuck, *Optic. Comm.* **19**, 297 (1976)
191. P. Sperfeld, K.D. Stock, K.-H. Raatz, B. Nawo, J. Metzdorf, *Metrologia* **40**, S111 (2003)
192. J. Hollandt, M. Kühne, B. Wende, *Appl. Optic.* **33**, 68 (1994)
193. C. Heise, J. Hollandt, R. Kling, M. Kock, M. Kühne, *Appl. Optic.* **33**, 5111 (1994)
194. A. Gottwald, M. Richter, G. Ulm, U. Schühle, *Rev. Sci. Instrum.* **76**, 023101 (2005)
195. G. Balloffet, J. Romand, B. Vodar, *C. R. Acad. Sci.* **262**, 4139 (1961)
196. M. Kühne, D. Stuck, E. Tegeler, *Appl. Optic.* **21**, 3919 (1982)
197. J. Fischer, M. Kühne, B. Wende, *Appl. Optic.* **23**, 4252 (1984)
198. J. Fischer, M. Kühne, B. Wende, *Metrologia* **23**, 179 (1986/87)
199. M. Kühne, *Appl. Optic.* **21**, 2124 (1982)
200. G. Boldt, *Space Sci. Rev.* **11**, 728 (1970)
201. P.J. Key, R.C. Preston, *Appl. Optic.* **16**, 2477 (1977)
202. H.-J. Kunze, W.D. Johnston III, *Phys. Rev. A* **3**, 1384 (1971)
203. R. König, K.-H. Kolk, H.-J. Kunze, *Phys. Scripta* **48**, 9 (1993)
204. K.-D. Zastrow, J.H. Brzozowski, *Phys. Fluid B* **5**, 4099 (1993)
205. J.Z. Klose, W.L. Wiese, *J. Quant. Spectros. Radiat. Tran.* **42**, 337 (1989)
206. B. Denne, E. Hinnov, *J. Opt. Soc. Am. B* **1**, 699 (1984)
207. J.F.M Aarts, F.J. de Heer, *J. Opt. Soc. Am.* **58**, 1666 (1968)

208. N.K. Bibinov, D.O. Bolshukhin, D.B. Kokh, A.M. Pravilov, I.P. Vinogradov, K. Wiesemann, *Meas. Sci. Technol.* **8**, 773 (1997)
209. H.G. Kuhn, *Atomic Spectra* (Academic Press, New York, 1969)
210. P.H. Heckmann, E. Träbert, *Introduction to the Spectroscopy of Atoms* (North-Holland, Amsterdam, 1989)
211. V.P. Shevelko, *Atoms and their Spectroscopic Properties* (Springer, Heidelberg, 1997)
212. S.V. Khristenko, A.I. Maslov, V.P. Shevelko, *Molecules and Their Spectroscopic Properties* (Springer, Berlin, 1998)
213. P.F. Bernath, *Spectra of Atoms and Molecules* (Oxford University Press, New York, 1995)
214. B.W. Shore, D.H. Menzel, *Principles of Atomic Spectra* (Wiley, New York, 1968)
215. R.D. Cowan, *The Theory of Atomic Structure and Spectra* (University of California Press, Berkeley, 1981)
216. D.L. Huestis, in *Radiative Transition Probabilities*, ed. by G.W.F. Drake. *Atomic, Molecular, and Optical Physics Handbook* (AIP Press, Woodbury, 1996), pp. 394–410
217. H.R. Griem, Y.W. Huang, J.-S. Wang, J.C. Moreno, *Phys. Fluid B* **3**, 2019 (1991)
218. S. Suckewer, *Phys. Fluid B* **3**, 2437 (1991)
219. S. Glenzer, J. Musielok, H.-J. Kunze, *Phys. Rev. A* **44**, 1266 (1991)
220. W.L. Wiese, *Phys. Scripta* **T65**, 188 (1996)
221. I.I. Sobelmann, *Atomic Spectra and Radiative Transitions* (Springer, Berlin, 1979)
222. V.P. Shevelko, L.A. Vainshtein, *Atomic Physics for Hot Plasmas* (Institute of Physics Publishing, Bristol, 1993)
223. W.L. Wiese, M.W. Smith, B.M. Glenon, *Atomic Transition Probabilities, vol I Hydrogen through Neon* (Nat. Bur. Standards, NSRDS-NBS 4, Washington, DC, 1966)
224. H.A. Bethe, E.E. Salpeter, *Quantum Mechanics of One- and Two-Electron Atoms* (Springer, Berlin, 1957)
225. W.L. Wiese, A. W. Weiss, *Phys. Rev.* **175**, 50 (1968)
226. M.W. Smith, W.L. Wiese, *Astrophys. J. Suppl. Ser.* **23**, 103 (1971)
227. A.H. Gabriel, *Mon. Not. R. Astron. Soc.* **160**, 99 (1972)
228. H.F. Beyer, V.P. Shevelko, *Introduction to the Physics of Highly Charged Ions* (Institute of Physics Publishing, Bristol, 2003)
229. W.R. Johnson, D.R. Plante, J. Sapirstein, *Adv. Atom. Mol. Opt. Phys.* **35**, 355 (1995)
230. B. Denne, E. Hinnov, S. Suckewer, S. Cohen, *Phys. Rev. A* **28**, 206 (1983)
231. P. Beiersdorfer, E. Träbert, E.H. Pinnington, *Astrophys. J.* **587**, 836 (2003)
232. V. Kaufmann, J. Sugar, *J. Phys. Chem. Ref. Data* **15**, 321 (1986)

233. I.I. Tupitsyn, A.V. Volotka, D.A. Glazov, V.M. Shabaev, G. Plunien, J.R. Crespo López-Urrutia, A. Lapierre, J. Ullrich, Phys. Rev A **72**, 062503 (2005)
234. G.A. Martin, W.L. Wiese, Phys. Rev. A **76**, 699 (1976)
235. H.A. Kramers, Phil. Mag. **46**, 836 (1923)
236. W.J. Karzas, R. Latter, Astrophys. J. Suppl. **6**, 167 (1961)
237. A. Burgess, M.J. Seaton, Mon. Not. R. Astron. Soc. **120**, 121 (1961)
238. G. Peach, Mem. R. Astron. Soc. **71**, 13 (1967)
239. G.V. Marr, *Photoionization Processes in Gases* (Academic Press, New York, 1967)
240. D. Hofsaess, J. Quant. Spectros. Radiat. Tran. **19**, 339 (1978)
241. G. Bekefi, *Radiation Processes in Plasmas* (Wiley, New York, 1966)
242. K. Bernhardi, K. Wiesemann, Plasma Phys. **24**, 867 (1982)
243. J. Wesson, *Tokamaks* (Oxford University Press, Oxford, 2004)
244. J.P. Matte, M. Lamoureux, C. Möller, R.Y. Yin, J. Delettrez, J. Virmont, T.W. Johnston, Plasma Phys. Contr. Fusion **30**, 1665 (1988)
245. K.N. Koshelev, N.R. Pereira, J. Appl. Phys. **69**, R21 (1991)
246. K.E. Voss, N.J. Fisch, Phys. Fluid B **4**, 762 (1992); Erratum, Phys. Fluid B **5**, 659 (1993)
247. K.T.A.L. Burm, Plasma Source Sci. Technol. **13**, 387 (2004)
248. W. Kasýanow, A. Starostin, Sov. Phys. JETP **21**, 193 (1965)
249. F. Cabannes, J. Chapelle, in *Spectroscopic Plasma Diagnostics*, ed. by M. Venugopalan. Reactions under Plasma Conditions, vol I, chap 7 (Wiley-Interscience, New York, 1971)
250. K.L. Bell, K.A. Berrington, J. Phys. B Atom. Mol. Phys. **20**, 801 (1987)
251. J.E. Lawler, J. Phys. D Appl. Phys. **37**, 1532 (2004)
252. H. Hotop, W.C. Lineberger, J. Phys. Chem. Ref. Data **14**, 731 (1985)
253. T.G. Moran, Phys. Rev. E **51**, 3464 (1995)
254. T.E. Sharp, At. Data **2**, 119 (1971)
255. U. Fantz, B. Schalk, K. Behringer, New J. Phys. **2**, 7 (2000)
256. H. Abgrall, E. Roueff, X. Liu, D.E. Shemansky, Astrophys. J. **481**, 557 (1997)
257. C.K. Rhodes (ed.), *Excimer Lasers* (Springer, Berlin, 1979)
258. A.A. Mihajlov, A.M. Ermolaev, M.S. Dimitrijevic, J. Quant. Spectros. Radiat. Tran. **50**, 227 (1993)
259. M.J. Seaton, Mon. Not. R. Astron. Soc. **119**, 81 (1959)
260. D.A. Verner, G.J. Ferland, Astrophys. J. Suppl. Ser. **103**, 467 (1996)
261. N.R. Badnell, Astrophys. J. Suppl. Ser. **167**, 334 (2006)
262. I.I. Sobel'man, L.A. Vainshtein, E.A. Yukov, *Excitation of Atoms and Broadening of Spectral Lines* (Springer, Berlin, 1995)
263. R.J.W. Henry, Phys. Rep. **68**, 1 (1981)
264. R.J.W. Henry, Rep. Prog. Phys. **56**, 327 (1993)
265. J. Lang, Spec. Ed., At. Data Nucl. Data Table, **57**(1/2), 1–7 (1994)
266. P.M. Stone, Y.-K. Kim, J.P. Desclaux, J. Res. Natl. Inst. Stand. Technol. **107**, 327 (2002)

267. Los Alamos National Laboratory, Los Alamos, New Mexico, USA.
<http://aphysics2.lanl.gov/cgi-bin/ION/runlanl08d.pl>
268. R. Mewe, Astron. Astrophys. **20**, 215 (1972)
269. M.J. Seaton, in *The Theory of Excitation and Ionization by Electron Impact*, ed. by D.R. Bates. Atomic and Molecular Physics (Academic Press, New York, 1962), p. 375
270. H. Van Regemorter, Astrophys. J. **136**, 906 (1962)
271. C.W. Allen, *Astrophysical Quantities* (University of London, Athlone Press, London, 1964)
272. S.M. Younger, W.L. Wiese, J. Quant. Spectros. Radiat. Tran. **22**, 161 (1979)
273. D.H. Sampson, H.L. Zhang, Phys. Rev A **45**, 1556 (1992)
274. V.I. Fisher, V.A. Bernshtam, H. Golten, Y. Maron, Phys. Rev. A **53**, 2425 (1996)
275. V.I. Fisher, Y.V. Ralchenko, V.A. Bernshtam, A. Goldgirsh, Y. Maron, L.A. Vainshtein, I. Bray, H. Golten, Phys. Rev. A **55**, 329 (1997)
276. P.G. Burke, A. Hibbert, W.D. Robb, J. Phys. B Atom. Molec. Phys. **4**, 153 (1971)
277. L.B. Golden, R.E.H. Clark, S.J. Goett, D.H. Sampson, Astrophys. J. Suppl. Ser. **45**, 603 (1981)
278. G.H. Dunn, in *Colliding Beams*, ed. by B. Bederson, V.M. Cohen, F.M.J. Pichanik. Atomic Physics, vol I (Plenum, New York, 1069), p. 417
279. E.W. Bell, X.Q. Guo, J.L. Forand, K. Rinn, D.R. Swenson, J.S. Thompson, G.H. Dunn, M.E. Bannister, D.C. Gregory, R.A. Phaneuf, A.C.H. Smith, A. Müller, C.A. Timmer, E.K. Wählén, B.D. DePaola, D.S. Belić, Phys. Rev. A **49**, 4585 (1994)
280. R.E. Marrs, M.A. Levine, D.A. Knapp, J.R. Henderson, Phys. Rev. Lett. **60**, 1715 (1988)
281. K.L. Wong, P. Beiersdorfer, K.J. Reed, D.A. Vogel, Phys. Rev. A **51**, 1214 (1995)
282. H.-J. Kunze, Space Sci. Rev. **13**, 565 (1972)
283. H.R. Griem, J. Quant. Spectros. Radiat. Tran. **40**, 403 (1988)
284. R.K. Janev, W.D. Langer, K. Evans Jr., D.E. Post Jr., *Elementary Processes in Hydrogen-Helium Plasmas: Cross Sections and Reaction Rate Coefficients* (Springer, Berlin, 1987)
285. Y. Ralchenko, R.K. Janev, T. Kato, D.V. Fursa, I. Bray, F.J. de Heer, At. Nucl. Data Table **96**, 403 (2008)
286. H.R. Griem, *Spectral Line Broadening by Plasmas* (Academic Press, New York, 1974)
287. A.D. Whitford, N.R. Badnell, C.P. Ballance, M.G. O'Mullane, H.P. Summers, A.L. Thomas, J. Phys. B At. Mol. Opt. Phys. **34**, 3179 (2001)
288. R.W.P McWhirter, At. Data Nucl. Data Table **57**, 39 (1994)
289. V.I. Fisher, Y.V. Ralchenko, V.A. Bernshtam, A. Goldgirsh, Y. Maron, L.A. Vainshtein, I. Bray, Phys. Rev. A **56**, 3726 (1997)
290. H.-J. Kunze, Phys. Rev A **4**, 111 (1971)

291. D.H. Sampson, S.J. Goett, G.V. Petrou, H. Zhang, R.E.H. Clark, At. Data. Nucl. Data Table **32**, 343 (1985)
292. U.I. Safranova, M.S. Safranova, T. Kato, Phys. Scripta **54**, 68 (1996)
293. H.L. Zhang, D.H. Sampson, At. Data Nucl. Data Table **43**, 1 (1989)
294. Á. Yanguas-Gil, J. Cotrino, L.L. Alves, J. Phys. D Appl. Phys. **38**, 1588 (1995)
295. R.K. Janev, in *Collision Processes of Atomic and Molecular Hydrogen in Fusion Plasmas: The Cross-Section Data Status*, ed. by R.E.H. Clark, D.H. Reiter. Nuclear Fusion Research (Springer, Berlin, 2005)
296. R.K. Janev, D. Reiter, Contrib. Plasma Phys. **43**, 401 (2003)
297. R.K. Janev, D. Reiter, Phys. Plasma **9**, 4071 (2002)
298. R.K. Janev, D. Reiter, Phys. Plasma **11**, 780 (2004)
299. J.J. Thomson, Philos. Mag. **23**, 449 (1912)
300. S.M. Younger, in *Quantum Theoretical Methods for Calculating Ionization Cross Sections*, ed. by T.D. Märk, G.H. Dunn. Electron Impact Ionization (Springer, New York, 1985)
301. S.M. Younger, T.D. Märk, in *Semi-Empirical and Semi-Classical Approximations for Electron Ionization*, ed. by T.D. Märk, G.H. Dunn. Electron Impact Ionization (Springer, New York, 1985)
302. V.P. Shevelko, Phys. Rev. **19**, 1 (1999)
303. G.H. Dunn, in *Electron-Ion Ionization*, ed. by T.D. Märk, G.H. Dunn. Electron Impact Ionization (Springer, New York, 1985)
304. K. Aichele, U. Hartenfeller, D. Hathiramani, G. Hofmann, V. Schäfer, M. Steidl, M. Stenke, E. Salzborn, T. Pattard, J.M. Rost, J. Phys. B At. Mol. Opt. Phys. **31**, 2369 (1998)
305. H. Watanabe, F.J. Currell, H. Kuramoto, Y.M. Li, S. Ohtani, B.E. O'Rourke, X.M. Tong, Nucl. Instrum. Meth. Phys. Res. B **205**, 417 (2003)
306. W. Lotz, Astrophys. J. Suppl. Ser. **14**, 207 (1967)
307. W. Lotz, Z. Physik **216**, 241 (1968)
308. W. Lotz, Z. Physik **232**, 101 (1970)
309. M. Mattioli, G. Mazzitelli, M. Finkenthal, P. Mazzotta, K.B. Fournier, J. Kaastra, M.E. Puiatti, J. Phys. B At. Mol. Opt. Phys. **40**, 3569 (2007)
310. M. Mattioli, G. Mazzitelli, K.B. Fournier, M. Finkenthal, L. Carraro, J. Phys. B At. Mol. Opt. Phys. **39**, 4457 (2006)
311. S. Younger, J. Quant. Spectros. Radiat. Tran. **26**, 329 (1981)
312. D. Mitnik, P. Mandelbaum, J.L. Schwob, A. Bar-Shalom, J. Oreg, Phys. Rev. A **55**, 307 (1997)
313. V.P. Shevelko, H. Tawara, I. Yu. Tolstikhina, F. Scheuermann, B. Fabian, A. Müller, E. Salzborn, J. Phys. B At. Mol. Opt. Phys. **39**, 1499 (2006)
314. R. Celiberto, R.K. Janev, A. Laricchiuta, M. Capitelli, At. Nucl. Data Table **77**, 161 (2001)
315. A. Burgess, Astrophys. J. **139**, 776 (1964)
316. A. Burgess, Astrophys. J. **141**, 1588 (1964)

317. D. Salzman, *Atomic Physics in Hot Plasmas* (Oxford University Press, New York, Oxford, 1998)
318. Y. Hahn, J. Quant. Spectros. Radiat. Tran. **49**, 81 (1993)
319. M. Arnaud, R. Rothenflug, Astron. Astrophys. Suppl. Ser. **60**, 425 (1985)
320. N.R. Badnell, M.G. O'Mullane, H.P. Summers, Z. Altun, M.A. Bautista, J. Colgan, T. W. Gorczyca, D.M. Mitnik, M.S. Pindzola, O. Zatsarinny, Astron. Astrophys. **406**, 1151 (2003)
321. M.A. Bautista, N.R. Badnell, Astron. Astrophys. **466**, 755 (2007)
322. V.L. Jacobs, J. Davies, P.C. Kepple, Phys. Rev. Lett. **37**, 1390 (1976)
323. F. Robicheaux, M.S. Pindzola, Phys. Rev Lett. **79**, 2237 (1997)
324. G.H. Dunn, in *Early Dielectronic Recombination Measurements: Singly Charged Ions*, ed. by W.G. Graham, W. Frisch, Y. Hahn, J.A. Tanis. Recombination of Atomic Ions (NATO ASI Series B, Plenum Press, New York, 1992)
325. G. Kilgus, A. Habs, D. Schwalm, A. Wolf, N.R. Badnell, A. Müller, Phys. Rev. A **46**, 5730 (1992)
326. A.J. Smith, P. Beiersdorfer, K. Widmann, M.H. Chen, J.H. Scofield, Phys. Rev. A **62**, 052717 (2000)
327. H.C. Meng, P. Greve, H.-J. Kunze, T. Schmidt, Phys. Rev. A **31**, 3276 (1985)
328. R.L. Brooks, R.U. Datla, A.D. Krumbein, H.R. Griem, Phys. Rev. A **21**, 1387 (1980)
329. M. Bitter, S. von Goeler, S. Cohen, K.W. Hill, S. Sesnic, F. Tenney, J. Timberlake, U.I. Safranova, L.A. Vainshtein, J. Dubau, M. Loulergue, F. Bely-Dubau, L. Steenman-Clark, Phys. Rev. A **29**, 661 (1984)
330. O. Marchuk, G. Bertschinger, H.-J. Kunze, A. Urnov, F. Goryaev, TEXTOR-team, J. Phys. B At. Mol. Opt. Phys. **40**, 4403 (2007)
331. R.U. Datla, H.-J. Kunze, Phys. Rev. A **37**, 4614 (1988)
332. R.K. Janev, L.P. Presnyakov, V.P. Shevelko, *Physics of Highly Charged Ions* (Springer, Berlin, 1985)
333. R.K. Janev, D.S. Belic, J. Phys. B At. Mol. Phys. **15**, 3479 (1982)
334. L. Aschke, Y.V. Ralchenko, E.A. Solov'ev, H.-J. Kunze, J. Phys. IV France **11**, Pr2-547–Pr2-550 (2001)
335. B.H. Bransden, M.R.C. McDowell, *Charge Exchange and the Theory of Ion Atom Collisions* (Oxford Science Publication, Clarendon Press, London, 1992)
336. F. Melchert, S. Meuser, S. Krüdener, A. Pfeiffer, K. v. Diemar, E. Salzborn, E. Sidky, C.D. Lin, J. Phys. B At. Mol. Opt. Phys. **30**, L697 (1997)
337. F.J. de Heer, R. Hoekstra, H.P. Summer, Nucl. Fusion Suppl. **3**, 47 (1992)
338. R.S. Walling, J.C. Weisheit, Phys. Rep. **162**, 1 (1988)
339. V.G. Pal'chikov, V.P. Shevelko, *Reference Data on Multicharged Ions* (Springer, Berlin, 1995)

340. A. Burgess, J.A. Tully, J. Phys. B At. Mol. Opt. Phys. **38**, 2629 (2005)
341. Y.-K. Kim, M.E. Rudd, Phys. Rev. A **50**, 3954 (1994)
342. K.L. Bell, A.E. Kingston, J. Phys. B **2**, 653 (1969)
343. A. Bogaerts, R. Gijbels, J. Vlcek, J. Appl. Phys. **84**, 121 (1998)
344. A. Merz, M.W. Müller, M.-W. Ruf, H. Hotop, W. Mayer, M. Movre, Chem. Phys. **145**, 219 (1990)
345. H.-W. Drawin, P. Felenbok, *Data for Plasmas in Local Thermodynamic Equilibrium* (Gauthiers-Villars, Paris, 1965)
346. H.R. Griem, Phys. Rev. **131**, 1170 (1963)
347. J.A.M. van der Mullen, Phys. Rep. **191**, 109 (1990)
348. T. Fujimoto, R.W.P. McWhirter, Phys. Rev. A **42**, 6588 (1990)
349. K.N. Koshelev, O.N. Rosmej (Yartseva), F.B. Rosmej, M. Hebach, A. Schulz, H.-J. Kunze, J. Phys. B At. Mol. Opt. Phys. **25**, L243 (1992)
350. R.W.P. McWhirter, in *Spectral Intensities*, ed. by R.H. Huddlestone, S.L. Leonard. Plasma Diagnostic Techniques (Academic Press, New York, 1965)
351. R. Wilson, J. Quant. Spectros. Radiat. Tran. **2**, 447 (1962)
352. H.-J. Kunze, in *Plasma Diagnostics*, ed. by A. Dinklage, T. Klinger, G. Marx, L. Schweikhard. Plasma Physics – Confinement, Transport and Collective Effects (Springer, Berlin, 2005)
353. R.W.P. McWhirter, A.G. Hearn, Proc. Phys. Soc. **82**, 641 (1963)
354. D.R. Bates, A.E. Kingston, R.W.P. McWhirter, Proc. Roy. Soc. A **267**, 397 (1962)
355. A. Burgess, H.P. Summers, Mont. Not. R. Astron. Soc. **174**, 345 (1976)
356. L.C. Johnson, E. Hinnov, J. Quant. Spectros. Radiat. Tran. **13**, 333 (1973)
357. T. Fujimoto, J. Phys. Soc. Jpn. **47**, 273 (1979)
358. J.J.A.M. van der Mullen, B. van der Sijde, D.C. Schram, Phys. Lett. A **94**, 239 (1983)
359. S. Byron, R.C. Stabler, P.I. Bortz, Phys. Rev. Lett. **8**, 376 (1962)
360. N.N. Ljepojevic, R.J. Hutcheon, R.W.P. McWhirter, J. Phys. B At. Mol. Phys. **17**, 3057 (1984)
361. N.N. Ljepojevic, R.W.P. McWhirter, S. Volonté, J. Phys. B At. Mol. Phys. **18**, 3285 (1985)
362. H.P. Summers, W.J. Dickson, M.G. O'Mullane, N.R. Badnell, A.D. Whiteford, D.H. Brooks, J. Lang, S.D. Loch, D.C. Griffin Plasma Phys. Contr. Fusion **48**, 263 (2006)
363. University of Strathclyde, Department of Physics, Glasgow, UK. <http://adas.phys.strath.ac.uk/about.php>
364. T. Fujimoto, T. Kato, Phys. Rev. A **30**, 379 (1984)
365. F. Rosmej, J. Phys. B At. Mol. Opt. Phys. **30**, L819 (1997)
366. O. Marchuk, PhD thesis, 2004. <http://www-brs.ub.ruhr-uni-bochum.de/netahtml/HSS/Diss/MarchukOleksandr/diss.pdf>
367. L. Carraro, M. Mattioli, F. Sattin, C. Demichelis, J.T. Hogan, W. Mandl, M.E. Puiatti, P. Scarin, M. Valisa, Phy. Scripta **55**, 565 (1997)

368. M. Goto, J. Quant. Spectros. Radiat. Tran. **76**, 331 (2003)
369. T. Kawachi, T. Fujimoto, G. Csanak, Phys. Rev. E **51**, 1428 (1995)
370. D. Dodt, A. Dinklage, R. Fischer, K. Bartschat, O. Zatsarinny, D. Loffhagen, J. Phys. D Appl. Phys. **41**, 205207 (2008)
371. H.-K. Chung, M.H. Chen, W.L. Morgan, Y. Ralchenko, R.W. Lee, High Energy Density Phys. **1**, 3 (2005)
372. National Institute of Standards and Technology (NIST), USA.
<http://physics.nist.gov/PhysRefData/contents.html>
373. T. Holstein, Phys. Rev. **72**, 1212 (1947)
374. T. Holstein, Phys. Rev. **83**, 1159 (1951)
375. L.M. Biberman, Zh. Eksp. Teor. Fiz. **17**, 416 (1947)
376. F.E. Irons, J. Quant. Spectros. Radiat. Tran. **22**, 1 (1979)
377. F.E. Irons, J. Quant. Spectros. Radiat. Tran. **22**, 21 (1979)
378. F.E. Irons, J. Quant. Spectros. Radiat. Tran. **22**, 37 (1979)
379. A. Romberg, H.-J. Kunze, J. Quant. Spectros. Radiat. Tran. **39**, 99 (1988)
380. R.C. Mancini, R.F. Joyce, C.F. Hooper Jr., J. Phys. B At. Mol. Phys. **20**, 2975 (1989)
381. D. Glouchkov, K. Koshelev, A. Schulz, J. Quant. Spectros. Radiat. Tran. **81**, 191 (2003)
382. J.E. Lawler, J.J. Curry, J. Phys. D Appl. Phys. **31**, 3235 (1998)
383. K. Sawada, T. Fujimoto, J. Appl. Phys. **78**, 2913 (1995)
384. P.T. Greenland, Proc. R. Soc. Lond. A **457**, 1821 (2001)
385. P. Teulet, J.P. Sarrette, A.M. Gomes, J. Quant. Spectros. Radiat. Tran. **70**, 159 (2001)
386. B.H. Armstrong, R.W. Nicholls, *Emission, Absorption and Transfer of Radiation in Heated Atmospheres* (Pergamon Press, Oxford, 1972)
387. G.D. Finn, D. Mugglestone, J. Quant. Spectros. Radiat. Tran. **8**, 1379 (1968)
388. F. Schreier, J. Quant. Spectros. Radiat. Tran. **48**, 743 (1992)
389. E.E. Whiting, J. Quant. Spectros. Radiat. Tran. **8**, 1379 (1968)
390. J.J. Olivera, R.L. Longbothum, J. Quant. Spectros. Radiat. Tran. **17**, 233 (1977)
391. A.W. Ali, H.R. Griem, Phys. Rev. A **144**, 366 (1966)
392. J.E. Lawler, Plasma Source Sci. Technol. **13**, 321 (2004)
393. G. Traving, in *Interpretation of Line Broadening and Line Shift*, ed. by W. Lochte-Holtgreven. Plasma Diagnostics (North-Holland, Amsterdam, 1968), pp. 550–616
394. M. Born, J. Phys. D Appl. Phys. **32**, 2492 (1999)
395. A.N. Cox (ed.), *Allen's Astrophysical Quantities* (Springer, New York, 1999)
396. N. Allard, J. Kielkopf, Rev. Mod. Phys. **54**, 1103 (1982)
397. N. Konjević, Phys. Rep. **316**, 339 (1999)
398. N. Konjević, A. Lesage, J.R. Fuhr, W.L. Wiese, J. Phys. Chem. Ref. Data **31**, 819 (2002)

399. National Institute of Standards and Technology (NIST), USA.
<http://physics.nist.gov/cgi-bin/ASBib1/LineBroadBib.cgi>
400. M. Baranger, Phys. Rev. **112**, 855 (1958)
401. H.R. Griem, M. Baranger, A.C. Kolb, G. Oertel, Phys. Rev. **125**, 177 (1962)
402. S. Sahal-Bréchot, Astron. Astrophys. **1**, 91 (1969)
403. S. Sahal-Bréchot, Astron. Astrophys. **2**, 322 (1969)
404. H.R. Griem, Phys. Rev. **165**, 258 (1968)
405. J.D. Hey, P. Breger, J. Quant. Spectros. Radiat. Tran. **24**, 349 (1980)
406. J.D. Hey, P. Breger, J. Phys. B At. Mol. Opt. Phys. **22**, L79 (1989)
407. M.S. Dimitrijević, N. Konjević, J. Quant. Spectros. Radiat. Tran. **24**, 451 (1980)
408. Y.V. Ralchenko, H.R. Griem, I. Bray, J. Quant. Spectros. Radiat. Tran. **81**, 371 (2003)
409. H. Elabidi, N.B. Nessib, M. Cornille, J. Dubau, S. Sahal-Bréchot, J. Phys. B At. Mol. Opt. Phys. **41**, 025702 (2008)
410. J. Holtsmark, Ann. Phys. (Leipzig) **58**, 577 (1919)
411. C.F. Hooper, Jr., Phys. Rev. **165**, 215 (1968)
412. C.A. Iglesias, F.J. Rogers, R. Shepherd, A. Bar-Shalom, M.S. Murillo, D.P. Kilcrease, A. Calisti, R.W. Lee, J. Quant. Spectros. Radiat. Tran. **65**, 303 (2000)
413. A.Y. Potekhin, G. Chabrier, D. Gilles, Phys. Rev. E **65**, 036412 (2002)
414. A. Demura, D. Gilles, in *Spectral Line Shapes*, vol 17, ed. by E. Dalimier (Frontier Group, 2004), p. 121
415. H.R. Griem, Astrophys. J. **132**, 833 (1960)
416. H.R. Griem, Contrib. Plasma Phys. **40**, 46 (2000)
417. H.R. Griem, A.C. Kolb, K.Y. Shen, Phys. Rev. **116**, 4 (1959)
418. Ya. Ispolatov, E. Oks, J. Quant. Spectros. Radiat. Tran. **51**, 129 (1994)
419. S. Alexiou, H.R. Griem, J. Halenka, W. Olchawa, J. Quant. Spectros. Radiat. Tran. **99**, 238 (2006)
420. E. Oks, J. Quant. Spectros. Radiat. Tran. **99**, 252 (2006)
421. E. Oks, *Stark Broadening of Hydrogen and Hydrogenlike Spectral Lines in Plasmas* (Alpha Science Int., Oxford, 2006)
422. E. Ferguson, H. Schlüter, Ann Phys. **22**, 351 (1963)
423. H.R. Griem, J. Halenka, W. Olchawa, J. Phys. B At. Mol. Opt. Phys. **38**, 975 (2005)
424. S. Büscher, T. Wrubel, S. Ferri, H.-J. Kunze, J. Phys. B At. Mol. Opt. Phys. **35**, 2889 (2002)
425. S. Büscher, S. Glenzer, T. Wrubel, H.-J. Kunze, J. Phys. B At. Mol. Opt. Phys. **29**, 4107 (1996)
426. C. Stehlé, R. Hutcheon, Astron. Astrophys. Suppl. Ser. **140**, 93 (1999)
427. M.A. Gigosos, M.Á. González, V. Cardeñoso, Spectrochim. Acta Part B **58**, 1489 (2003)
428. E. Stambulnik, S. Alexiou, H.R. Griem, P.C. Kepple, Phys. Rev. E **75**, 016401 (2007)

429. T.L. Pittman, C. Fleurier, Phys. Rev. A **33**, 1291 (1986)
430. U. Ackermann, K.H. Finken, J. Musielok, Phys. Rev A **31**, 2507 (1985)
431. D.R. Inglis, E. Teller, Astrophys. J. **90**, 439 (1939)
432. W.L. Wiese, D.E. Kelleher, D.R. Paquette, Phys. Rev. A **6**, 1132 (1972)
433. Büscher, PhD thesis, 2000. <http://www-brs.ub.ruhr-unibochum.de/netahtml/HSS/Diss/BuescherStefan/diss.pdf>
434. W.L. Wiese, N. Konjević, J. Quant. Spectros. Radiat. Tran. **28**, 185 (1982)
435. W.L. Wiese, N. Konjević, J. Quant. Spectros. Radiat. Tran. **47**, 185 (1992)
436. B. Blagojević, M.V. Popvić, N. Konjević, M.S. Dimitrijević, J. Quant. Spectros. Radiat. Tran. **61**, 361 (1999)
437. S. Glenzer, N.I. Uzelać, H.-J. Kunze, Phys. Rev A **45**, 8795 (1992)
438. H. Hegazy, S. Seidel, T. Wrubel, H.-J. Kunze, J. Quant. Spectros. Radiat. Tran. **81**, 221 (2003)
439. H.G. Adler, A. Piel, J. Quant. Spetros. Radiat. Tran. **45**, 11 (1991)
440. C.A. Moore, G.P. Davis, R.A. Gottscho, Phys. Rev. Lett. **52**, 538 (1984)
441. S. Maurmann, H.-J. Kunze, V. Gavrilenko, E. Oks, J. Phys. B At. Mol. Opt. Phys. **29**, 25 (1996)
442. U. Czarnetzki, D. Luggenhölscher, V.A. Kadetov, H.F. Döbele, Pure Appl. Chem. **77**, 345 (2005)
443. D. Blochinzew, Phys. Z. Sowjetunion **4**, 501 (1933)
444. W.R. Rutgers, H.W. Kalfsbeek, Z. Naturf. **30a**, 739 (1975)
445. O. Peyrusse, Phys. Scripta **56**, 371 (1997)
446. E. Oks, *Plasma Spectroscopy – The Influence of Microwave and Laser Fields* (Springer, Berlin, 1995)
447. H.R. Griem, H.-J. Kunze, Phys. Rev. Lett. **23**, 1279 (1969)
448. E.A. Oks, G.V. Sholin, Sov. Phys. Tech. Phys. **21**, 144 (1976)
449. G.V. Sholin, E.A. Oks, Sov. Phys. Dokl. **18**, 254 (1973)
450. E. Sarid, Y. Maron, L. Troyansky, Phys. Rev. E **48**, 1364 (1993)
451. S. Alexiou, A. Weingarten, Y. Maron, M. Sarfaty, Y.E. Krasik, Phys. Rev. Lett. **75**, 3126 (1995)
452. E.A. Oks, St. Böddeker, H.-J. Kunze, Phys. Rev. A **44**, 8338 (1991)
453. St. Böddeker, H.-J. Kunze, E. Oks, Phys. Rev. Lett. **75**, 4740 (1995)
454. M. Baranger, B. Mozer, Phys. Rev. **123**, 25 (1961)
455. H.-J. Kunze, H.R. Griem, Phys. Rev. Lett. **21**, 1048 (1968)
456. C.F. Burrell, H.-J. Kunze, Phys. Rev. Lett. **29**, 1445 (1972)
457. U. Rebhahn, J. Phys. B At. Mol. Phys. **19**, 3847 (1986)
458. V.P. Gavrilenko, JETP **76**, 236 (1993)
459. G. Baravian, J. Bretagne, J. Godart, G. Sultan, Z. Physik B **20**, 255 (1975)
460. A. Piel, H. Richter, Z. Naturforsch. **34a**, 516 (1979)
461. H.W. Drawin, in *Spectral Line Shapes – Proceedings of the 5th International Conference*, ed. by B. Wende (Walter de Gruyter, Berlin, 1981), p. 527

462. R.C. Elton, H.R. Griem, B.L. Welch, A.L. Osterheld, R.C. Mancini, J. Knauer, G. Pien, R.G. Watt, J.A. Cobble, P.A. Jaanimagi, D.K. Bradley, J.A. Delettrez, R. Epstein, J. Quant. Spectros. Radiat. Tran. **58**, 559 (1997)
463. D. Riley, O. Willi, Phys. Rev. Lett. **75**, 4039 (1995)
464. U. Feldman, J.F. Seely, N.R. Sheeley, S. Suckerwer, A.M. Title, J. Appl. Phys. **56**, 2512 (1984)
465. A. Iwamae, M. Atake, A. Sakaue, R. Katai, M. Goto, S. Morita, Phys. Plasma **14**, 042504 (2007)
466. S. Günter, A. Könies, J. Quant. Spectros. Radiat. Tran. **62**, 425 (1999)
467. C.C. Chu, J.D. Hey, Contr. Plasma Phys. **40**, 597 (2000)
468. C. Stehlé, S. Brillant, G. Mathys, Eur. Phys. J. D **11**, 491 (2000)
469. J.D. Hey, C.C. Chu, Ph. Mertens, Contr. Plasma Phys. **42**, 635 (2002)
470. N.J. Peacock, B.A. Norton, Phys. Rev. A **11**, 2142 (1975)
471. E.A. McLean, J.A. Stamper, C.K. Manka, H.R. Griem, D.W. Droemer, B.H. Ripin, Phys. Fluid **27**, 1327 (1984)
472. E. Stambulchick, K. Tsigutkin, Y. Maron, Phys. Rev. Lett. **98**, 22501 (2007)
473. W.W. Hicks, R.E. Hess, W.S. Cooper, Phys. Rev. A **5**, 490 (1972)
474. H.W. Drawin, H. Henning, L. Herman, Nguyen-Hoe, J. Quant. Spectros. Radiat. Tran. **9**, 317 (1969)
475. F.M. Levinton, R.J. Fonck, G.M. Gammel, R. Kaita, H.W. Kugel, E.T. Powell, D.W. Roberts, Phys. Rev. Lett. **63**, 2060 (1989)
476. M.F. Gu, C.T. Holcomb, R.J. Jayakuma, S.L. Allen, J. Phys. D At. Mol. Opt. Phys. **41**, 095701 (2008)
477. B.A. Pohlmeier, A. Dinklage, H.-J. Kunze, J. Phys. D At. Mol. Opt. Phys. **29**, 221 (1996)
478. H. Zwicker, in *Evaluation of Plasma Parameters in Optically Thick Plasmas*, ed. by W. Lochte-Holtgreven. Plasma Diagnostics (North-Holland, Amsterdam, 1968), pp. 214–249
479. D. Karabourniotis, E. Drakakis, J.J.A.M. van der Mullen, J. Quant. Spectros. Radiat. Tran. **108**, 319 (2007)
480. S.O. Kastner, A.K. Bhatia, J. Quant. Spectros. Radiat. Tran. **58**, 217 (1997)
481. H.Z. Bartels, Z. Phys. **127**, 243 (1950); **128**, 546 (1950)
482. I. Martinson, C. Jupén, Phys. Scripta **T68**, C123 (2003)
483. S. Glenzer, H.-J. Kunze, J. Musielok, Y.-K. Kim, W.L. Wiese, Phys. Rev. A **49**, 221 (1994)
484. A.M. Urnov, F.F. Goryaev, G. Bertschinger, H.-J. Kunze, O. Marchuk, JETP Lett. **85**, 374 (2007)
485. M. Bitter, K.W. Hill, N.R. Sauthoff, P.C. Efthimion, E. Meservey, W. Roney, S. von Goeler, R. Horton, M. Goldman, W. Stodiek, Phys. Rev. Lett. **43**, 129 (1979)
486. R.C. Isler, Nucl. Instrum. Meth. Phys. Res. B **9**, 673 (1985)
487. R.J. Fonck, Rev. Sci. Instrum. **56**, 885 (1985)

488. R.P. Schorn, E. Hintz, D. Rusbüldt, F. Aumayr, M. Schneider, E. Unterreiter, H. Winter, *Appl. Phys. B* **52**, 71 (1991)
489. E. Wolfrum, J. Schweinzer, M. Reich, L.D. Horton, C.F. Maggi, *Rev. Sci. Instrum.* **77**, 033507 (2006)
490. D.M. Thomas, G.R. McKee, K.H. Burrell, F. Levinton, E.L. Foley, R.K. Fisher, *Fusion Sci. Technol.* **53**, 487 (2008)
491. U. Fantz, *Contr. Plasma Phys.* **44**, 508 (2004)
492. U. Fantz, H. Falter, P. Franzen, D. Wunderlich, M. Berger, A. Lorenz, W. Kraus, P. McNeely, R. Riedl, E. Speth, *Nucl. Fusion* **46**, S297 (2006)
493. U. Fantz, D. Wunderlich, *New J. Phys.* **8**, 301 (2006)
494. J.W. Coburn, M. Chen, *J. Appl. Phys.* **51**, 3134 (1980)
495. H.M. Katsch, A. Tewes, E. Quandt, A. Goehlich, T. Kawetzki, H.F. Döbele, *J. Appl. Phys.* **88**, (2000)
496. N. de Vries, PhD thesis, Technische Universiteit Eindhoven, The Netherlands (2008)
497. N.C.M. Fuller, I.P. Herman, V.M. Donnelly, *J. Appl. Phys.* **90**, 3182 (2001)
498. A. Ricard, J. Henriques, S. Cousty, S. Villeger, J. Amorim, *Plasma Process. Polymer* **4**, S965 (2007)
499. A. Qayyum, S. Zeb, M.A. Naveed, S.A. Ghauri, M. Zakaullah, *Plasma Dev. Oper.* **15**, 87 (2007)
500. R. Ramos, G. Cunge, M. Touzeau, N. Sadeghi, *J. Phys. D Appl. Phys.* **41**, 115205 (2008)
501. K. Sasaki, Y. Kawai, K. Kadota, *Rev. Sci. Instrum.* **70**, 76 (1999)
502. A.G. Mitchell, M.W. Zemansky, *Resonance Radiation and Excited Atoms* (Cambridge University Press, Cambridge, 1961)
503. H. Jentschke, U. Schumacher, K. Hirsch, *Contrib. Plasma Phys.* **38**, 501 (1998)
504. J.D. Hey, C.C. Chu, S. Brezinsek, P. Mertens, B. Unterberg, *J. Phys. B At. Mol. Opt. Phys.* **35**, 1525 (2002)
505. W. Neumann, in *Spectroscopic Methods of Plasma Diagnostics*, ed. R. Rompe, M. Steenbeck. *Progress in Plasmas and Gas Electronics*, vol 1 (Akademie, Berlin, 1975), pp. 1–510
506. A. Gawron, S. Maurmann, F. Böttcher, A. Meckler, H.-J. Kunze, *Phys. Rev. A* **38**, 4737 (1988)
507. N.K. Podder, J.A. Johnson III, C.T. Raynor, S.D. Loch, C.P. Ballance, M.S. Pindzola, *Phys. Plasma* **11**, 5436 (2004)
508. R.F. Boivin, S.D. Loch, C.P. Ballance, D. Branscomb, M.S. Pindzola, *Plasma Source Sci. Technol.* **16**, 470 (2007)
509. O. Schmitz, I.L. Beigman, L.A. Vainshtein, B. Schweer, M. Kantor, A. Pospieszczyk, Y. Xu, M. Krychowiak, M. Lehnens, U. Samm, B. Unterberg, TEXTOR team, *Plasma Phys. Control. Fusion* **50**, 115004 (2008)
510. K.-D. Zastrow, E. Källne, H.P. Summers, *Phys. Rev. A* **41**, 1427 (1990)

511. M. Bitter, H. Hsuan, C. Bush, S. Cohen, C.J. Cummings, B. Grek, K.W. Hill, J. Schivell, M. Zarnstorff, P. Beiersdorfer, A. Osterheld, A. Smith, B. Fraenkel, Phys. Rev. Lett. **71**, 1007 (1993)
512. A. Escarguel, F.B. Rosmej, C. Brault, T. Pierre, R. Stamm, K. Quotb, Plasma Phys. Contr. Fusion **49**, 85 (2007)
513. F.B. Rosmej, J. Phys. B At. Mol. Opt. Phys. **33**, L1 (2000)
514. R. Bartimoro, F. Bombarda, R. Giannella, Phys. Rev. A **32**, 531 (1985)
515. V.M. Donnelly, J. Phys. D Appl. Phys. **37**, R217 (2004)
516. K. Behringer, U. Fantz, J. Phys. D Appl. Phys. **27**, 2128 (1994)
517. I.P. Vinogradov, Plasma Source Sci. Technol. **8**, 299 (1999)
518. N. Bibinov, H. Halfmann, P. Awakowicz, Plasma Source Sci. Technol. **17**, 035004 (2008)
519. R.S. Marjoribanks, M.C. Richardson, P.A. Jaanimagi, R. Epstein, Phys. Rev. A **46**, R1747 (1992)
520. L. Juschkin, A. Hildebrand, H.-J. Kunze, Plasma Source Sci. Technol. **8**, 370 (1999)
521. D. Karabourniotis, in *Self-Reversed Emission Lines in Inhomogeneous Plasmas*, ed. by J.M. Proud, L.H. Luessen. Radiative Processes in Discharge Plasmas (NATO ASI Series B: Physics 149, Plenum Press, New York, 1986), pp. 171–247
522. A. Delcroix, S. Volonté, J. Phys. B Atom. Mol. Phys. **6**, L4 (1973)
523. G.J. Bastiaans, R.A. Mangold, Spectrochim. Acta B **40**, 885 (1985)
524. A.T.M. Wilbers, G.M.W. Kroesen, C.J. Timmermans, D.C. Schram, J. Quant. Spectros. Radiat. Tran. **45**, 1 (1991)
525. W.S. Cooper III, W.B. Kunkel, Phys. Fluis **8**, 482 (1965)
526. K.H. Finken, G. Bertschinger, S. Maurmann, H.-J. Kunze, J. Quant. Spetcros. Radiat. Tran. **20**, 467 (1978)
527. I. Krisch, H.-J. Kunze, Phys. Rev. E **58**, 6557 (1998)
528. B.C. Stratton, M. Bitter, K.W. Hill, D.L. Hillis, J.T. Hogan, Fusion Sci. Technol. **53**, 431 (2008)
529. M. Galanti, N.J. Peacock, J. Phys. B Atom. Mol. Phys. **8**, 2427 (1975)
530. F.C. Jahoda, E.M. Little, W.E. Quinn, G.A. Sawyer, T.F. Stratton, Phys. Rev. **119**, 843 (1960)
531. S. Alexiou, J. Quant. Spectros. Radiat. Tran. **81**, 461 (2003)
532. V. Milosavljević, G. Poparić, Phys. Rev. E **63**, 036404 (2001)
533. D. Nikolić, Z. Mijatović, S. Djurović, R. Kobilarov, N. Konjević, J. Quant. Spectros. Radiat. Tran. **70**, 67 (2001)
534. T. Babkina, T. Gans, U. Czarnetzki, Europhys. Lett. **72**, 235 (2005)
535. J. Jovović, N.M. Šišović, N. Konjević, J. Phys. D Appl. Phys. **41**, 235202 (2008)
536. R.D. Bengtson, J.D. Tannich, P.C. Kepple, Phys. Rev. A **1**, 532 (1970)
537. B.L. Welch, H.R. Griem, J. Terry, C. Kurz, B. LaBombard, B. Lipschultz, E. Marmar, G. McCracken, Phys. Plasma **2**, 4246 (1995)
538. M.A. Gordon, R.L. Sorochenko, *Radio Recombination Lines – Their Physics and Astronomical Applications* (Springer, New York, 2009)

539. M.A. Gigosos, M.Á, González, B. Talin, A. Calisti, Astron. Astrophys. **466**, 1189 (2007)
540. B. Omar, S. Günter, A. Wierling, G. Röpke, Phys. Rev. E **73**, 056405 (2006)
541. M. Koubiti, H. Capes, L. Godbert-Mouret, Y. Marandet, A. Meigs, J. Rosato, F.B. Rosmej, R. Stamm, Contrib. Plasma Phys. **45**, 661 (2006)
542. M.S. Dimitrijević, M. Christova, S. Sahal-Bréchot, Phys. Scripta **75**, 809 (2007)
543. S. Pellerini, K. Musiol, B. Pokrzewka, J. Chapelle, J. Phys. B At. Mol. Opt. Phys. **29**, 3911 (1996)
544. J.A. Aparicio, M.A. Gigosos, V.R. González, C. Pérez, M.I. de la Rosa, S. Mar, J. Phys. B At. Mol. Opt. Phys. **31**, 1029 (1998)
545. E.J. Iglesias, J. Ghosh, R.C. Elton, H.R. Griem, J. Quant. Spectros. Radiat. Tran. **98**, 101 (2006)
546. R.C. Elton, W.W. Köppendörfer, Phys. Rev. **160**, 194 (1967)
547. H.-J. Kunze, A.H. Gabriel, H.R. Griem, Phys. Rev. **165**, 267 (1968)
548. A.H. Gabriel, C. Jordan, in *Interpretation of Spectral Line Intensities from Laboratory and Astrophysical Plasmas*, ed. by E.W. McDaniel, M.R.C. McDowell. Case Studies in Atomic Collision Physics, vol 2 (North Holland, Amsterdam, 1972), pp. 209–291
549. V.A. Boiko, S.A. Pikuz, A.Ya. Faenov, J. Phys. B Atom. Mol. Phys. **12**, 1889 (1978)
550. H. Chen, P. Beiersdorfer, L.A. Heeter, D.A. Liedahl, K.L. Naranjo-Rivera, E. Träbert, M.F. Gu, J.K. Lepson, Astrophys. J. **611**, 598 (2004)
551. G.Y. Liang, G. Zhao, Astron. J. **135**, 2291, (2008)
552. G.A. Doschek, U. Feldman, J. Davis, R.D. Cowan, Phys. Rev. A **12**, 980 (1975)
553. I.Yu. Skobelev, A.V. Vinogradov, E.A. Yukov, Phys. Scripta **18**, 78 (1978)
554. U. Feldman, G.A. Doschek, J.F. Seely, J. Appl. Phys. **68**, 3947 (1990)
555. Yu. Ralchenko, J. Phys. B At. Mol. Opt. Phys. **40**, F175 (2007)
556. X.-M. Zhu, E.-C. Chen, J. Li, Y.-K. Pu, J. Phys. D Appl. Phys. **42**, 025203 (2009)
557. X.-M. Zhu, Y.-D. Pu, Z.-G. Guo, Y.-K. Pu, Phys. Plasma **13**, 123501 (2006)
558. V. Guerra, P.A. Sá, J. Loureiro, Eur. Phys. J. Appl. Phys. **28**, 125 (2004)
559. H. Meister, R. Fischer, L.D. Horton, C.F. Maggi, D. Nishijima, ASDEX Upgrade Team, C. Giroud, K.-D. Zastrow, JET-EFDA Contributors, B. Zaniol, Rev. Sci. Instrum. **75**, 4097 (2004)
560. A. Patel, P.G. Carolan, N.J. Conway, R.J. Akers, Rev. Sci. Instrum. **75**, 4944 (2004)
561. E. Iordanova, N. de Vries, M. Guillemier, J.J.A.M. van der Mullen, J. Phys. D Appl. Phys. **41**, 015208 (2008)

562. M. Sarfaty, Y. Maron, Ya.E. Krasik, A. Weingarten, R. Arad, R. Shpitalnik, A. Fruchtman, S. Alexiou, *Phys. Plasma* **2**, 2122 (1995)
563. E. Hintz, B. Schweer, *Plasma Phys. Contr. Fusion* **37**, A87 (1995)
564. K. Kadota, K. Tsuchida, Y. Kawasumi, J. Fujita, *Plasma Phys.* **20**, 1011 (1978)
565. H.W. Babcock, *Astrophys. J.* **118**, 387 (1953)
566. F. Jahoda, F.L. Ribe, G.A. Sawyer, *Phys. Rev.* **131**, 24 (1963)
567. K. Hübner, *Z. Naturf.* **19a**, 1111 (1964)
568. J.F. Seely, U. Feldman, N.R. Sheehy Jr., S. Suckewer, A.M. Title, *Rev. Sci. Instrum.* **56**, 855 (1985)
569. D. Wróblewski, H.W. Moos, W.L. Rowan, *Appl. Phys. Lett.* **48**, 21 (1986)
570. R. Shpitalnik, A. Weingarten, K. Gomberoff, Y. Krasik, Y. Maron, *Phys. Plasma* **5**, 792 (1998)
571. K. McCormick, M. Kick, J. Olivain, Proceedings of the 8th European Conference on Controlled Fusion Plasma Physics, Prague, p. 140 (1977)
572. A.A. Korotkov, P.D. Morgan, J. Vince, J. Schweinzer, JET EFDA Contributors, *Rev. Sci. Instrum.* **75**, 2590 (2004)
573. W. Mandl, R.C. Wolf, M.G. von Hellerman, H.P. Summers, *Plasma Phys. Contr. Fusion* **35**, 1373 (1993)
574. O. Marchuk, L.A. Vainshtein, I.L. Beigman, private communication
575. N.A. Pablant, K.H. Burrell, R.J. Groebner, D.H. Kaplan, C.T. Holcomb, *Rev. Sci. Instrum.* **79**, 10F517 (2008)
576. K. Takiyama, K. Kadota, T. Oda, M. Hamamoto, T. Ohgo, Y. Kamiura, K. Adati, J. Fujita, *Rev. Sci. Instrum.* **59**, 2351 (1988)
577. K. Tsigutkin, R. Doron, E. Stambulnik, V. Bernshtam, Y. Maron, A. Fruchtman, R.J. Commissio, *Phys. Rev. E* **76**, 046401 (2007)
578. M.M. Kuraca, N. Konjević, *Appl. Phys. Lett.* **70**, 1521 (1997)
579. S. Reyes Cortes, N.C. Hawkes, P. Lotte, C. Fenzi, B.C. Stratton, J. Hobirk, R. De Angelis, F. Orsitto, C.A.F. Varandas, Contributors to the EFTA-JET work program, *Rev. Sci. Instrum.* **74**, 1596 (2003)

Index

- Abel inversion, 10
- Aberration
 - spherical, 35
- Absorption coefficient, 12, 88
- Actinometry, 183
- Active spectroscopy, 182
- Air
 - index of refraction, 4
 - transmission, 3
- Airy distribution, 28, 47
- Alignment, 49
- Aperture ratio, 17
- Apodization, 49
- Apparatus profile, 16, 50
- Approximation
 - Bethe, 118
 - Born, 117
 - close-coupling, 120
 - Coulomb-Born, 117
 - Coulomb-Born-Oppenheimer, 120
 - distorted wave, 120
 - effective Gaunt factor, 119
- Array detectors, 54
- Atomic beams, 2
- Attachment continua, 109
- Autoionization, 129
-
- Balmer lines
 - high-principal quantum number, 197
- Bandwidth, 53, 59, 73
- Beam diagnostics, 182
 - helium, 191
 - lithium, 201, 203
-
- Beer-Lambert law, 29, 177, 184
- Biberman factor, 104, 105, 193
- Binning, 54
- Blackbody, 76, 85, 176, 192
- Blaze
 - angle, 19
 - wavelength, 19
- Blazing, 19
- BLIP, 65
- Bolometer, 73
- Boltzmann factor, 136, 187
- Boltzmann plot, 187
- Bragg
 - angle, 25
 - condition, 24
- Bremsstrahlung, 85
 - electron-ion encounters, 104, 200
 - electron-neutral encounters, 108
- Brewster angle for x-rays, 26
- Brightness temperature, 79
- Byron's limit, 149
-
- Calibration
 - blackbody sources, 76
 - branching ratio method, 77, 82
 - BRV source, 81
 - carbon arc, 79
 - deuterium lamp, 80
 - ECR source, 81
 - electron storage rings, 77
 - flat fielding, 78
 - hollow-cathode discharge, 75, 80
 - integrating sphere, 79

- rising effect, 78
- large-area x-ray source, 83
- laser-produced plasmas, 81
- optically thick lines, 82
- Penning discharge, 81
- sensitivity, 76
- stray light, 76
- synchrotron radiation, 77
- tungsten strip lamp, 78
- wall-stabilized arc, 79
- wavelength, 75
- Camera**
 - framing, 54
 - streak, 54
- CCD**, 54
- Charge**
 - effective ionic, 201
- Charge coupled device**, 54, 68
- Charge exchange**, 132, 182
- Charge-exchange spectroscopy**, 182, 187
- Coddington shape factor**, 35
- Collimator**
 - Soller, 37, 44
 - stacked grids, 38, 42
- Collision strength**, 116
 - effective, 116
- Collisional-radiative model (CR)**, 146
- Convolution**, 50
- Cross-section**
 - absorption, 89
 - excitation, 115
 - excitation, theoretical methods, 117
 - ionization, 126
 - Kramers, 99
 - photoionization, 99
 - scaling, 120
 - unit, 99
- Crystals**, 24
 - bent, 25
 - mosaic, 26
 - spherically bent, 27
 - toroidally bent, 27
- de Broglie wavelength thermal, 138
- De-convolution**, 51, 195
- Debye radius**, 137, 162
- Density measurements**
 - electrons, 195
 - molecules, 182
- particles, 180
- Detailed balance**
 - principle of, 117, 136, 139
- Detector**
 - gas amplification, 72
- Dispersing elements**, 15
- Dispersion**
 - angular, 16, 22
 - linear, 16
 - reciprocal linear, 16
- Distribution**
 - Boltzmann, 136
- Distribution function**
 - Maxwell, 101, 115
 - non-thermal, 191
 - velocity, 115
- Doping**, 202
- Dynamic range**, 53, 72
- Eddington Barbier relation, 14
- Efficiency**
 - conversion, 53
 - quantum, 56
- electron cyclotron frequency, 175
- Electron energy loss constant**
 - bremsstrahlung, 106
 - radiative recombination, 103
- Emission coefficient**, 6
 - spectral, 87
- Equation of radiative transfer**, 12
- Equilibrium**
 - corona, 142, 181
 - local thermodynamic (LTE), 140, 180
 - partial local thermodynamic (PLTE), 141, 181
 - thermodynamic, 136
- Escape factor**, 150
- Etendue**, 7
- Excitation**
 - argon, 125
 - autoionization, 128
 - collisional dissociative, 125
 - electron impact, 116
 - helium-like ions, 122
 - hydrogen-like ions, 121
 - lithium-like ions, 124
 - molecules, 125
 - neon-like ions, 124
 - proton impact, 133

- f-number, 17
- f-value, 90
- Fellgett's advantage, 49
- Films
 - Langmuir-Blodgett, 25
 - multilayer, 25
- Filters, 30
 - colored glass, 30
 - interference, 32
 - liquid, 31
 - long-pass, 31
 - micromesh, 32
 - narrow-band, 32
 - neutral density, 32
 - notch, 33
 - polarization, 33
- Ross, 31
- short-pass, 31
- x-ray region, 31
- Finesse, 28
- Fluence, 5
- Fourier transform spectroscopy, 48
- Free spectral range, 21, 28, 47
- Gating, 63
- Gaunt factor
 - bound-bound, 118
 - bound-free, 100
 - free-free, 105
- GEM, 72
- Grating
 - concave, 21
 - diffraction, 18
 - echelle, 20, 41
 - efficiency, 20, 22
 - holographic, 19
 - Littrow mount, 20
 - multilayer, 23
 - polarization, 22
 - ruled, 18
 - toroidal, 22
 - transmission, 23
 - varied line spacing, 22
- Grazing
 - angle, 23
 - incidence, 23
- Holtsmark field strength, 161, 165
- Image intensifier, 62
- Image plate, 73
- Inglis-Teller limit, 167, 201
- Instrument function, 16, 50
- Intensity, 5
- Interferometer
 - Fabry-Perot, 27, 47
 - Michelson, 48
 - scanning, 48
- Inversion algorithm, 10
- Ion-ion coupling parameter, 163
- Ion-sphere radius, 137, 162
- Ionization
 - collisional-radiative, 147
 - electron impact, 125
 - molecules, 128
 - Penning, 134
 - proton impact, 134
- Ionization chamber, 69
- Ionization energy, 99, 104, 106, 126, 138
 - lowering of, 137
- Ionization time
 - effective, 141
- Irradiance, 5
- Kirkpatrick-Baez arrangement, 36
- Klein-Rosseland formula, 139
- Landé factor, 174
- Laser spectroscopy, 1
- Lattice planes, 24
- Line broadening
 - by neutral particles, 157
 - collective fields, 170
 - Doppler, 156
 - impact approximation, 158, 159
 - natural, 155
 - pressure, 157
 - quasistatic approximation, 161
 - Stark broadening, 159
- Line profile functions
 - Gaussian, 153
 - Lorentzian, 153
 - Voigt, 51, 153
- Line profiles
 - argon, 198
 - equivalent width, 178
 - forbidden transitions, 169
 - helium, 197
 - hydrogen and hydrogen-like ions, 163, 196

- isoelectronic sequences, 169
- isolated lines , 168
- magnetic field effects, 174
- motional Stark effect, 176
- opacity broadening, 176
- plasma satellites, 172
- polarization, 175
- self-reversal, 177, 192
- Zeeman effect, 175
- Line ratios, 77, 179, 187
- Line shape function, 87, 153
- Line strength, 91
- Line to continuum ratio, 193
- Lines
 - optically thick, 192
- Lorentz field, 203
- Lorentz triplet, 174
- LTE, 140
- Measurement
 - current density, 202
 - electric field, 204
 - magnetic field, 202
- Microcalorimeter, 73
- Microchannel plate, 62
- Microfield, 161
- Microfield distribution
 - Holtsmark, 161
 - strongly coupled plasmas, 163
- Miller indices, 24
- Milne formula, 101, 139
- Mirrors, 33
- Molecular continua
 - dissociative, 110
- Molecular transitions, 92
 - Franck–Condon factor, 93
 - band strength, 93
 - Hönl-London factor, 93
- Monochromator, 17
 - double, 17, 41
 - double-crystal, 45
 - triple, 17, 41
 - x-ray, 44
- Mount
 - Czerny-Turner, 40
 - Eagle, 41
 - Ebert-Fastie, 39
 - grazing incidence, 42
 - Littrow, 39
- Paschen-Runge, 41
- Seya-Namioka, 41
- Wadsworth, 42
- Multiwire proportional chamber, 71
- Noise
 - 1/f, 65
 - generation-recombination, 65
 - Johnson, 55, 65
 - shot, 55
- Optical density, 32
- Optical depth, 13, 150, 176
- Optical thickness, 13
- Optics
 - capillary tubes, 36
 - Fresnel zone plates, 37
 - grazing incidence, 36
 - microchannel plates, 36
 - thick wall, 35
- Oscillator strength, 90
 - regularities, 96
- Partition function, 136
- Paschen-Back regime, 174
- Photocell, 55
- Photoconductor, 63
- Photodiode, 55, 66
 - array, 68
 - Schottky-barrier, 67
- Photoelectric effect
 - external, 55, 63
 - internal, 63
- Photomultiplier, 57
 - channel, 61
- Phototube, 55
- Pinhole camera, 10
- Planck's law, 76
- Plate factor, 16
- PLTE, 141
- Point-spread function, 36, 54
- Polarimeter, 46
- Polarization, 174
- Polychromator, 17
- Population coefficients, 147
- Population vector, 146
- Position encoding, 72
- Power loss
 - bremsstrahlung, 106
 - recombination radiation, 103

- Poynting vector, 5
- Prisms, 17
 - Glan-Taylor, 33
 - Glan-Thompson, 33
- Profile function, 87
- Proportional chamber, 70
- Radiance, 5, 8
 - spectral, 8, 76
- Radiant energy density, 5
- Radiant flux, 5
- Radiant flux density, 5
- Radiant intensity, 5
- Radiant power, 5
- Radiative loss, 5
- Radio recombination lines, 197
- Radon transformation, 11
- Rate coefficient
 - collisional-radiative, 147
 - deexcitation, 117
 - dielectronic recombination, 130
 - excitation, 115
 - experimental, 179
 - ionization, 126
 - radiative recombination, 110
 - three-body recombination, 129
- Rate parameter, 116
- Rayleigh criterion, 17, 27, 37
- Recombination
 - charge exchange, 132
 - collisional-radiative, 147
 - dielectronic, 129
 - radiative, 110
 - three-body, 129
- Recombination heating, 126
- Recombination radiation, 85, 193
- Reflectance
 - Fresnel, 29
 - multilayer systems, 34
 - normal incidence, 33
- Reflectivity
 - integrated, 26
- Resolving power, 16, 18, 20
- Responsivity, 53
- Rise time, 53
- Rowland circle, 21, 41, 42, 45
- Rydberg energy, 99
- Saha function, 138
- Saha-Eggert equation, 138, 181
- Satellite lines
 - dielectronic, 186
 - innershell excited, 186
 - plasma, 204
- Scaling laws
 - cross-section photoionization, 100
 - excitation, 120
 - ionization, 126
 - line radiation, 95
 - three-body recombination, 129
- Scintillators, 60
- Selection rules, 91
- Self-absorption, 149
- Sensitivity
 - spectral, 53
- Shafranov shift, 11
- Source function, 13
- Spectra
 - helium, 190
 - helium-like ions, 184, 191
- Spectral
 - quantities, 6
- Spectral range
 - extreme-ultraviolet, EUV, 3
 - hard x-rays, 3
 - infra-red, 2
 - soft x-rays, 3
 - ultraviolet, UV, 3
 - vacuum-uv, VUV, 3
 - visible, 2
- Spectrograph, 17
- Spectrometer
 - Cauchois, 46
 - echelle, 41
 - Johann, 45
 - Johansson, 46
 - van Hám̄os, 46
- Spectrum, 3
- Stark effect, 161
 - dynamic, 170
 - motional, 203
- Stark mixing, 169
- Stray light, 17
- Streak camera, 73
- Temperature
 - excitation, 188
 - rotational, 188
 - vibrational, 188

- Temperature measurements
 electrons, 187
 particles, 186
- Thermal limit, 141
- Thomson scattering, 1
- Throughput, 7, 17, 49
- Tomography, 11
- Transit time, 59, 65
- Transition probability, 87, 179
- Transitions
 electric dipole, 91
 forbidden, 97
 helium-like ions, 97
 intercombination, 97
 magnetic dipole, 98, 181, 202
 multipole, 91
- Transmittance, 28
 air, 29
- gases, 29
spectral, 29
- Ulbricht sphere, 79
- Virtual image, 9
- Wall effects, 36, 200
- Wavelength
 in air, 4
 in vacuum, 3
- Wavenumber, 3
- Weisskopf radius, 160
- Wien's displacement law, 85
- Windows, 28
- Wolter systems, 36
- Zeeman effect, 174, 202

Springer Series on
ATOMIC, OPTICAL, AND PLASMA PHYSICS

Editors-in-Chief:

Professor G.W.F. Drake

Department of Physics, University of Windsor
401 Sunset, Windsor, Ontario N9B 3P4, Canada

Professor Dr. G. Ecker

Ruhr-Universität Bochum, Fakultät für Physik und Astronomie
Lehrstuhl Theoretische Physik I
Universitätsstrasse 150, 44801 Bochum, Germany

Professor Dr. H. Kleinpoppen, Emeritus

Stirling University, Stirling, UK, and
Fritz-Haber-Institut
Max-Planck-Gesellschaft
Faradayweg 4–6, 14195 Berlin, Germany

Editorial Board:

Professor W.E. Baylis

Department of Physics, University of Windsor
401 Sunset, Windsor, Ontario N9B 3P4, Canada

Professor Uwe Becker

Fritz-Haber-Institut
Max-Planck-Gesellschaft
Faradayweg 4–6, 14195 Berlin, Germany

Professor Philip G. Burke

School of Mathematics and Physics
Queen's University
David Bates Building, Belfast BT7 1NN, UK

Professor R.N. Compton

Oak Ridge National Laboratory
Building 4500S MS6125
Oak Ridge, TN 37831, USA

Professor M.R. Flannery

School of Physics
Georgia Institute of Technology
Atlanta, GA 30332-0430, USA

Professor C.J. Joachain

Faculté des Sciences
Université Libre Bruxelles
Bvd du Triomphe, 1050 Bruxelles, Belgium

Professor B.R. Judd

Department of Physics
The Johns Hopkins University
Baltimore, MD 21218, USA

Professor K.P. Kirby

Harvard-Smithsonian Center for Astrophysics
60 Garden Street, Cambridge, MA 02138, USA

Professor P. Lambropoulos, Ph.D.

Max-Planck-Institut für Quantenoptik
85748 Garching, Germany, and
Foundation for Research
and Technology – Hellas (F.O.R.T.H.),
Institute of Electronic Structure
and Laser (IESL),
University of Crete, PO Box 1527
Heraklion, Crete 71110, Greece

Professor G. Leuchs

Friedrich-Alexander-Universität
Erlangen-Nürnberg
Lehrstuhl für Optik, Physikalisches Institut
Staudtstrasse 7/B2, 91058 Erlangen, Germany

Professor P. Meystre

Optical Sciences Center
The University of Arizona
Tucson, AZ 85721, USA